Comparison study of precise monitoring techniques applied to engineering specimens tested under dynamic loading

by:

Anna Maria Metheniti

Department of Civil, Environmental & Geomatic Engineering

University College London

Principal Supevisor:

Prof. Stuart Robson

May 2021

Abstract

Initially, the thesis shows a state of the art for structural health monitoring techniques and procedures. Different types of instrumentations and sensors employed under different requirements, which are presented with the view to monitor a variety of structural issues resulted by numerous conditions. It also presents examples from the literature following the proposed monitoring strategy as a novel pattern. These show how close-range digital photogrammetry and strain gauges have been employed in the past with the view to obtain strain evaluation assessments of the relevant monitored structural elements. Based on three surveys which have been carried out in a historical masonry church in Athens (Greece), the methodology of the thesis is generated with the experimental framework being also formed. Eight experiments have been carried out, five of them at the Advanced Structures Laboratory (CEGE – UCL), one at the Concrete Laboratory (CEGE – UCL) and two of them at the Earthquake and Large Structures Laboratory (EQUALS – University of Bristol). Two scale engineering specimens are employed for the experimental needs, both are scaled down using as a prototype element, the north-eastern wall of the studied church. The five experiments which are carried out in CEGE, are made on small scale masonry specimens, of $1/17^{th}$ scale and the two experiments in EQUALS are made on large scale masonry specimens, of $1/5^{th}$ scale. All the seven experiments are dynamically loaded. The only static loaded experiment is carried out at the Concrete Laboratory and it is made on a masonry specimen. Through the comparison of the two monitoring methods, close-range digital photogrammetry (CRDP) and strain gauges (SG), is concluded that both methods can capture a change in strain, on the tested specimens, when a crack is occurring.

To my parents

Contents

Table of Figures

Table of Tables

CHAPTER 1

INTRODUCTION

1.1 Heritage Structures

Important structures located within urban environments have been dealing throughout their lifespan with vibrations and/or with tunnelling-excavation activities. Such structures are the Elizabeth Tower (Big Ben) in London, the Duomo Cathedral in Milan and the Kapnikarea Chapel in Athens. The Elizabeth Tower (Big Ben) is located at the north end of the Westminster Palace in London and its construction completed in 1859. During the construction of the 18m deep New Palace Yard underground car park, which is 16m to the west of Big Ben, caused the tower to tilt. The Duomo Cathedral is located at Milan (Italy) city centre, it was built between 1386 to 1813 and the city's underground railway system is running very close to the cathedral. The Kapnikarea Chapel is a 12th century masonry church located at the historical centre of Athens (Greece), where the tube trains pass ~27m beneath the structure. During the construction period of the Athens' railway tube system, a 10mm settlement was monitored to the church. Therefore, the monitoring of such heritage structures is important for their preservation, maintenance and for the safety of their visitors.

1.2 Monitoring

When structures are malfunctioning or being out of service can result to accidents which may cause discontinuities to everyday services or even result to an accident involving human victims. A direct economic impact is reflected by the cost of reconstruction of a deficient structure and the indirect economic impact usually involves losses in other divisions of economy. The collapse of a nuclear power station or a pipeline may result in ecological pollution. Or the collapse of a historical structure (i.e. cathedrals, stone bridges, etc.) can cause cultural loss for the society.

The monitoring of structures can prevent losses and maintain a sufficient management of the durable ones. As it is a very complex procedure and requires detailed advanced planning, similarly to the construction and maintenance activities.

The collected data through the monitoring period are used to optimise the maintenance and the repair phases. More specifically, structural health monitoring (SHM) is aiming to provide in-time and accurate input for the structural condition, providing representative parameters collected during a permanent or a periodic monitoring phase, over a short or a long period of time. These parameters are usually mechanical, physical or chemical and may be monitored either to the entire structure or to a local structural level. The collected data are used to plan and design the repair activities, to increase the structure's safety, to widen the knowledge on the structure's current pathology and mainly to define if intervention is useful and needful and at which stage and level of structural deterioration. The process of SHM is usually compared to the process applied to a patient, as shown on figure 1.1.

Once all these data are collected and evaluated by the engineers, they are commonly inserted in numerical structural analysis programmes to check the structures' performances. For safety purposes, structures such as bridges and stadiums where the loading is positioned at critical places, testing before service is required. To meet structures' safe condition, monitoring system is usually installed since the beginning. Experimental tests are often carried out to understand the real performances and to compare it with the theoretical one.

The continuous monitoring allows to establish the impact of many external sources of vibrations and displacements such as tunnelling excavations, underground trains and earthquakes. The monitoring of heritage structures such as the Elizabeth Tower (Big Ben), the Duomo Cathedral and the Kapnikarea Chapel, where the cities' underground railway systems pass very close to the structures, should be continuous. Another important factor that should be considered, is the type of sensors or the monitoring techniques applied, as limited or no intervention is allowed for the monitoring of heritage structures. Therefore, the applied monitoring methods to such structures should be continuous and non-destructive.

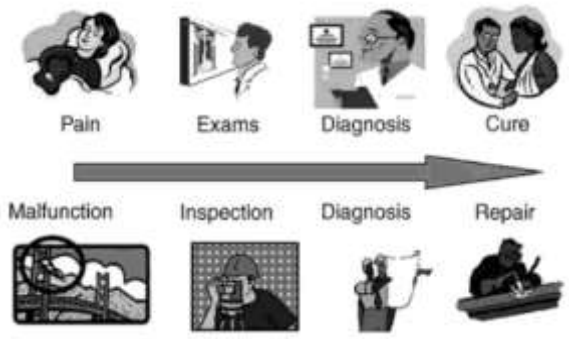

Figure 1.1: Monitoring of structure's feelings (*SMARTEC*)

1.3 Case Studies

In February 2003, during the construction works of the Channel Tunnel Rail Link (CTRL) – High Speed 1 (HS1) which was designed and built to form a new and faster route from central London to Ashford, a 10m deep hole opened above a CTRL's site in east London (Lavender Street) and managed to swallow the gardens of three residential houses. 36 hours prior to this landslip, the tunnel boring machine was excavating an 8m wide tunnel, 20m below these residential houses. To stabilise the ground and to prevent further damage, the hole was filled with concrete. Residents' frustration was mainly focused, not only to the suffering as they had to leave their premises, but to the potential lost value of their houses (*BBC 1*). However, CTRL decided to continue with the works 10 weeks after the collapse as their postponing cost was £240,000 a week (*BBC 2*).

Figure 1.2: hole created at the garden of a residential house and poured with concrete (*BBC 1*)

Similarly, in February 2003 in the 13th district of Paris, at Auguste-Perret Street, another collapse occurred, this time to a school's yard, again due to the underground tunnelling extension works for the 14th line of the Paris metro, from the Francois-Mitterand library to the Olympiades station close to the Tolbiac University (Pierre Mendès-France Centre). In addition, in December 1995, another incident occurred in the 9th district of Paris, at the Rue Papillon, close to the construction site of the future underground line RER line E. During Aeolus TBM's passage from this area, two buildings had been severely shaken and were threatened to collapse. The gigantic machine of 7.4m dia. and 8m long caused such damage to the apartments that they had to be evacuated. The 9th district contains important structures such as the Paris Opera. These two incidents happened in Paris since 1989, when the government approved the commencement of two major construction projects in the Parisian Region which would connect the north and the west part of the city. These two

projects absorbed almost all the credits intended for the public transport for Paris. The additional problems as described above extended the completion period of the project, increased the overall budget to 8 million francs – 2 million more the initial one – and caused a detrimental effect to the implementation of all other public transport projects outside Paris (*Le Monde*).

In Milan the protection and preservation of the Duomo Cathedral has been an activity of high importance. The tube trains of the city's metro system used to run with 50km/h which was reduced to 30km/h the years 1969 to 1972. In 1973 it was decided the speed limit to be further reduced to 20km/h. The speed limitation had a cost effect of 1.8 million euros (*Hellenic Ministry of Culture Reports*). The continuous monitoring of the church has been carried out with linear variable differential transformers (LVDT), fibre optics, cable extensometers, accelerometers and inclinometers. Photogrammetry has also been applied to monitor the cracks propagation (*Alba et. al., 2011*).

Another example of historical structure recorded during the construction works of the Jubilee Line Extension for London Underground, where several buildings had to be protected due to the potential damage caused by settlement. Elizabeth Tower (Big Ben) which was constructed in 1859 was one of these structures. The clock tower consists of load-bearing brickwork with stone cladding rising to a height of 61m. The construction of the 18m deep New Palace Yard underground car park (fig. 1.3), which is 16m to the west of Big Ben, caused the tower to tilt. Further analysis showed that the Big Ben would tilt even more towards the underground car park, during the combined construction of the station box and the 7.4m dia. tunnels, unless protective measures were implemented. The tower's tilt would also lead to cracking where the tower and the Palace are connected. Therefore, for the purposes of controlling the ground movement, the new technique of compensation grouting was undertaken over a 21-month period, from January 1996 until September 1997 (fig. 1.4). During this period, 122m^3 of grout was injected. In addition, a monitoring system was installed comprised of an optical and an electronically read plumb line, of prism targets attached to the clock faces and of precise levelling measurements at 4 points on the corners of Big Ben (*Mair et. al., 2001*).

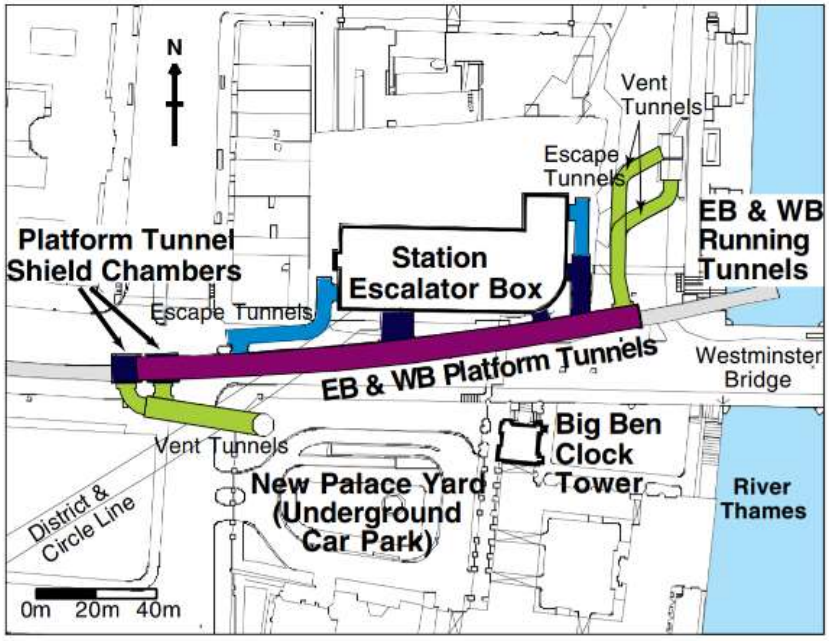

Figure 1.3: Plan of the Westminster Station & the Jubilee Line Extension; EB-eastbound, WB-westbound (*Mair et. al., 2001*)

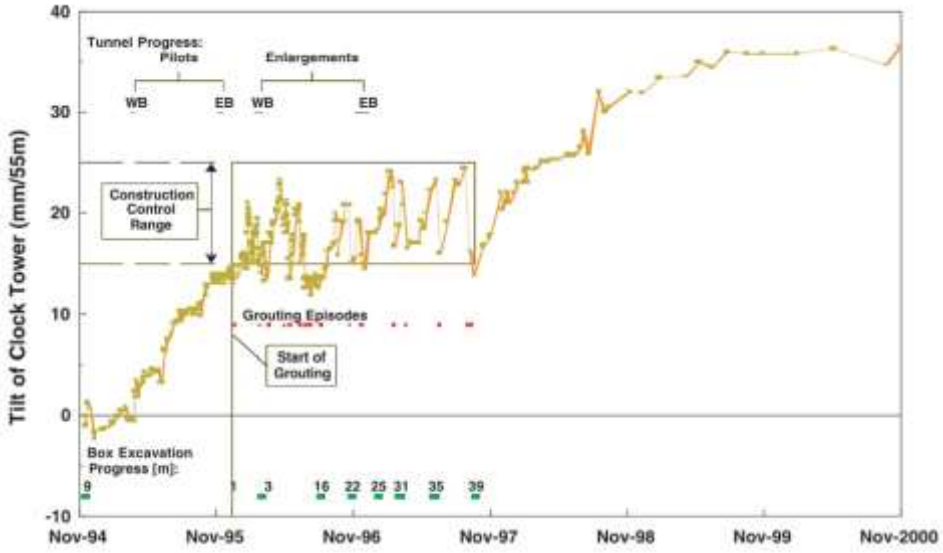

Figure 1.4: Graph showing the amount of horizontal movement of Elizabeth Tower (Big Ben) at clock face level from 1994 to 2000 (*Mair et. al., 2001*)

1.4 Literature Gap

Since the beginning of the 19th century, there is a growing political awareness for the protection of the national monuments and the ancient works of art. In 1802, the Papal Administration in Rome published a national legislation for the protection of the antiquities in the City of Rome. Since then and during the 21st century there have been a series of organisations (i.e. UNESCO, English Heritage, etc.) created for the protection of historical structures worldwide and several conferences, discussions and publications for their restoration. However, just firstly reported, in ICOMOS[1]/ISCARSAH[2] Guidelines (2003) and the Italian Guidelines for evaluation and mitigation of seismic risk to cultural Heritage (2006), one very important requirement; the selection of the appropriate monitoring technique (Lorenzoni F, 2013). The chosen monitoring method should be adequate to the issue affecting the monumental structure, to its geometry, location, and to the provided budget.

This study started with a heritage structure, the Kapnikarea Chapel in Athens. Based on the problems observed and the field studies made by the author, a monitoring plan has been proposed. Therefore, this research compares the results of two precise monitoring techniques; the photogrammetry and the strain gauge. These monitoring means are applied to small and large scale, single-leaf[3], non-reinforced masonry specimens tested under static and dynamic loading.

1.5 Structure of the Thesis

Chapter 2 is a state of the art for structural health monitoring techniques and procedures. It presents different types of instrumentations and sensors employed under different requirements with the view to monitor a variety of structural issues resulted by numerous conditions, such as environmental fluctuations, changes in deformation and loading criteria, electromagnetic and acoustic emissions. Thereafter, it presents the monitoring of masonry structures and historical constructions. It enables a two-pattern approach by showing the wide application of monitoring means and monitored factors in the laboratory and in the field. The last part of this chapter presents examples from the literature following the proposed monitoring strategy as a

[1] International Council on Monuments & Sites

[2] International Scientific Committee on the Analysis and Restoration of Structures of Architectural Heritage

[3] Single-leaf masonry specimen is consisted of masonry units joined together with mortar.

novel pattern. These show how close-range digital photogrammetry and strain gauges have been employed in the past with the view to obtain strain evaluation assessments of the relevant monitored structural elements.

Chapter 3 presents the proposed monitoring strategy which was inspired, derived and built up based on the difficulties faced and the conclusions produced by the three investigation field surveys carried out to the Kapnikarea Chapel (Athens, Greece). These three field surveys are also presented in Chapter 3. In addition, it provides justification for choosing the employed monitoring means; close range digital photogrammetry, and strain gauges. Finally, it presents the experimental set-ups for both small- and large-scale experiments, i.e. the acquisition system, the engineering specimens' construction methods and the calibration techniques, along with the followed framework.

Chapter 4 presents the thesis's diagnosis, the procedure followed and the conclusions of the two preliminary experiments. The experimental development consists of two reference tests carried out in the laboratory. It is a trial and error experiment which is made to check the small shaking table's performance (Advanced Structures Laboratory, CEGE – UCL), the acting of the masonry sample based on the proposed experimental methodology and the synchronisation of the necessary activities before, during and after the experiment. For analysing the photogrammetric data of this reference experiment the analytical softwares of Vision Measurement System and the EngVis have been employed. A second reference experiment is following with the purpose of providing a reference point for the synchronisation of the two monitoring techniques employing a simpler experimental mean, the application of static loading. The masonry specimen is tested on a compression machine and a uniaxial (y axis) loading is applied. This set up investigates the synchronisation requirements for the DSLR (nikon) cameras and it establishes the requirements for the next experiments.

Chapter 5 presents the results of the four small scale experiments carried out, showing the outcomes of the photogrammetric and the strain gauges' data. It is the part of the thesis which concludes to the practical evidence of the theoretical development through the experimental work. These experiments form two groups. Group A includes three small-scale experiments which are made with the use of the small masonry specimen and the small shaking table being actuated in the x axis with the last experiment providing a slightly alternative set-up as the specimen is facing the cameras at 45 degrees. Group B consists of one small-scale experiment, again carried out using the small masonry specimens and the small shaking table which is actuated on the z axis.

Chapter 6 presents the results of the two large scale experiments (Group C). Similarly, to Chapter 5 it shows the outcomes of the photogrammetric and the strain gauges' data. Therefore, Group C is constituted by two identical experiments carried out to a large masonry specimen and actuated on the x axis using the large shaking table facilities of the University of Bristol. This work shows the monitoring performance and the structural behaviour of engineering specimens, closer to real structures' actual size.

Chapter 7 is the thesis conclusions and future work. In this section are summarised the experimental results, the outcomes of the discussion points, the successful percentage of fitting the experimental methodology to the proposed theoretical development and the proposed future work. All these are briefly presented in a form suitable for future applicability.

CHAPTER 2

LITERATURE REVIEW

2.1 Introduction

This chapter describes the structural health monitoring discipline, addresses the types of monitoring, instrumentations and sensors and justifies the chosen monitoring techniques applied to the framework of the current research. It also explains the importance of using an appropriate monitoring strategy tailored to the structural problem being investigated.

2.2 Structural Monitoring

2.2.1 Overview

The structural health monitoring (SHM) process is a complex procedure that requires detailed planning in order to accomplish the best possible achievement. It can be performed at a local structural level or for the entire structure. The main aim of appropriately defining the SHM is the detection of any unusual structural behaviour, which requires a detailed inspection of the element/structure, a diagnosis and finally a restoration. The inspection comprises of four main steps: the detection of the damage, its localisation, its severity (quantification) and its definition, i.e. the type of damage (classification). The classification of the damage is categorised into three main groups: the mechanical where parameters such as deformation is measured, the physical where humidity is quantified and the chemical group where parameters such as steel oxidation is measured (table 2.1). Depending on the type of the structure, its condition and the monitoring requirements, different types of instrumentation and sensors are applied (Glišić et. al., 2007).

2.2.2 Instrumentation & Sensors

This section presents the most commonly used instruments and sensors, along with their advntages and disadvantages.

Monitoring Categories	*Parameters*	*Indicative Monitoring Sensors*	*Advantages*	*Limitations*
Mechanical	deformation / strain	strain gauges	small & inexpensive	need to be calibrated
		fibre optic	can measure both static and dynamic forces	fixed or embedded into the structure
		crack-meter [i.e. Moiré Tell Tale (MTT)] or crack-gauge	reusable	drilling holes on both sides of the crack
		flat-jack	no electronic device required	drilling is required for its installation
		angle: theodolite (total station)	digital display of readings	expensive
		tiltmeter or slope alert or inclinometer or pitch & roll indicator	tilt readings are obtained quickly & easily	should be mounted
	displacement	hydrostatic water level cell (HWLC)	reliable	accurate measurements require continuous density readings
		extensometer	easy to use & inexpensive	the weight of the contact extensometer itself can distort delicate-tested specimens
		shape memory alloy device (SMAD)	corrosion resistant	poor fatigue properties

		convergence meter	easy to use	fixation points required
		elevation: levelling instrument	data can be transferred to computer directly	measurements should be taken from different locations
		photogrammetry (digital image correlation) – cameras	non-intrusive	time required to process the images
		distance: laser scanner	applicable to all 2D & 3D surfaces	hardware expensive & sophisticated software required to process data
	force	load cells	long service life	presenting temperature error
	velocity/acceleration	accelerometers	lightweight	no differenation of activity type
		seismometers	well accepted piece of equipment providing in-depth knowledge about the boundaries of earthquakes	difficult interpretation of collected data
Physical	temperature	thermocouples	can be made with extremely fine wire to measure the temperature of tiny objects/gaps	low sensitivity to small temperature changes
	humidity	moisture meter	measurements are available instantly	leave 2 small hole on the surface of the monitored element
	moisture			
	sound	acoustic emission sensors (AES)	defect localization	acoustic emission signals are usually weak
		air-coupled transducers/sensor	no surface preparation required before monitoring	the analysis of the measurements is done on the diffraction of the wave reflected from the surface
		ultrasonic pulse velocity (UPV)	portability	difficulty when inspecting irregular elemets

	echo	radar sensors	can operate in different environmental conditions	expensive
Chemical	chloride concentration	smart pebble	fast, less than a few seconds can check the chloride ingress	should be inserted in the monitored element/structure
	steel oxidation	thermo-graphic camera	a big area can be scanned very quickly	cost of instrument relatively high
	timber decay	resistograph[1]	cavities can be detected	it can provide a substrate for further decay in the wood of trees with preexisting decay because the shavings from drilling are left in the hole by the device
		radiographic equipment (film ouside, source inside)	defects surface & subsurface defects	defect requires significant depth in relation to the radiation beam

Table 2.1: Parameters Usually Monitored along with the Advantages & Limitations of their equivalent indicative monitoring sensors (Glišić et. al., 2007)

[1] An electronic device which is consisted of a high-resolution needle drill capable for providing a high linear correlation of resistance between the wood's density, strength and modulus of elasticity with the measured values (Imposa et. al., 2014).

The first step in SHM is the identification of the limitations on how the monitoring can be implemented and what monitoring means should be applied. Theoretically, any structure can be instrumented at any point/location in order to understand its performance at its best. However, the number and the type of sensors chosen to be used for an efficient monitoring, is tied to the available financial resources, but also to the nature of the structure, the information that needs to be gathered and the importance of the building (Lorenzoni 2013).

Thus, during the design of the monitoring system of a historical structure the information that needs to be collected should be analytically studied. Initially, based on engineering observations the structural health issue should be defined. According to what the outcome is, the engineering team will define what parameters should be monitored, i.e. crack's deformation. Considering the following listed major requirements, the appropriate monitoring strategy will be defined by the engineering team.

1. Budget
2. Compatibility
3. Accuracy
4. Reliability
5. Flexibility
6. Reversibility
7. Minimum intervation
8. Non-invasiveness
9. Non-obstrusiveness
10. Presentation
11. Maintenance
12. Safety
13. Durability
14. Environmental conditions

2.2.3 Choice of monitoring means

Most heritage structures have been constructed by masonry or stone. Cracking is a common deterioration effect in historical structures and strain changes are made on the structural elements where the cracking occurs. These changes can be measured either by monitoring the cracks' displacement and deformation or the strain changes directly. The major limitation when monitoring a monumental structure is to avoid penetrating any of its structural members. According to table 2.1, for monitoring displacement and deformation or strain, sensors such as the crack-meter, the flat-jack, the tiltmeter and the extensometer require drilling or potential distortion of the monitored structural member. Digital image correlation (DIC) uses cameras which make non-contact measurements either of a small structural member or of an entire structure. The cameras do not require installation preparations so the method is easy to apply and ti does not either require knowledge of the exact cracks' locations. The captured images can be processed and produce displacement and strain profiles of the monitored object. Also, DIC is a monitoring method that can simultaneously measure 3-D dynamic displacements of several points of a vibrating or a stable structural.

Therefore, the digital image correlation (DIC) has been chosen as the monitoring method, which is able to detect both static and dynamic loading. Strain gauges, being a broadly and overused monitoring method, have also been employed as a comparison method to the DIC.

2.3 Monitoring Masonry

2.3.1 Overview

When a structure, or a structural element, or any type of element, is diagnosed with any type of issue, the responsible maintenance person, i.e. engineer, decides its restoration method. Prior step to any restoration work is the monitoring with the view of applying the most appropriate restoration technique. The choice of the appropriate monitoring strategy it is a critical step of the maintenance process. The monitoring strategy is comprised by two core components: the monitoring aim and the available cost. These two components interact all the way through the establishment of the monitoring strategy. There are series of parameters that influence the monitoring strategy. The choice of the monitored quantities based on the identification of the

desirable structural behaviour, the required monitoring duration, the selection of the monitoring method, its installation and maintenance, the collection of data, their management, their appropriate and critical representation, and in the case of monitoring disruptions or interruptions the application of appropriate pre-scheduled activities. In addition, some of these parameters may form sub-parameters. For example, the monitoring duration may be split to permanently (continuously) and periodically, the installation of the monitoring sensors may be embedded or direct, the application of multiple sensors may be feasible or not, the data may be collected remotely or on site, the monitoring conditions may be inappropriate i.e. weather, the covetable measured quantities i.e. linear and shear strains, deformed shapes, curvatures, displacements may require new technologies, the damage monitoring detection may be direct or indirect, the geometry of the monitored member may specify additional sub-parameters. All the described monitoring cases are important for the definition of the monitoring strategy and may be factored accordingly.

There are examples in the literature that show the monitoring strategy of model scale historical structures in the laboratory and of physical historical buildings in the field. These case studies have been used as examples for this research project where model scale specimens, as a scaled-down part of a historical structure, will be tested and monitored.

2.3.2 Case Studies

2.3.2.1 In the laboratory

Model scale applications which were built and tested in experimental laboratories are limited studies in the literature, due to needed expertise and cost.

Matteis *et. al.* (2010), studied the seismic behaviour of the Fossanoba Abbey (Priverno, Italy) church (fig. 2.1a) by carrying out model tests. The church was built in 1208 and it is a representative example of the pre-Gothic Cistercian architectural style. Its dimensions are 69.9m (length), 20.1m (height) and 23.2m (width) and the basic material of the church is a very compact sedimentary limestone. It is comprised of a nave, an apse, a transept and aisles which are all covered with vaults (fig. 2.1 b & c). Therefore, the dynamic response of the church was carried out by testing on the shaking table the central part of the church and three consecutive bays, all in a reduced scale of 1/5.5 (fig. 2.2a). The input acceleration value applied was 0.14g and the recorded frequency of the model, made by the installed accelerometers, was

2.5Hz. Two main cracks along the central arches of the model formed the main result of the test, and other minor cracks occurred as well all along the arches and the vaults of the model (fig. 2.2 b & c). The behaviour of this macro-element under dynamic loading may be assumed as a reference element characterising this kind of building typology, as it is repeated to Gothic style churches (Matteis *et. al.*, 2010).

Another example in the literature is published by Krstevska *et. al.* (2010). They have carried out an experimental investigation on a large scale model of the Mustafa Pasha Mosque (Skopje) (fig. 2.3a). The test was performed in the Laboratory of the Institute for Earthquake Engineering and Engineering Seismology (IZIIS) (fig. 2.4c). The Mosque, which is consisted of the main structure, a minaret and a portico, was built in 1492 and constructed by bricks in lime mortar. It is also consisted of vaulted elements and three domes, which all rest on hidden wooden belts (fig. 2.4 a & b) incorporated into the walls at several levels. The minaret has spiral staircases and its upper part is made of marble. The monument survived the 6.3(Mw) earthquake in 1963, but it was heavily damaged in several locations (fig. 2.3 b & c). The model (fig. 2.5a) was made with a scale of 1/6 and with only the two parts of the Mosque tested, the main structure and minaret, with an input acceleration value of 0.05-1.50g. In order to follow the dynamic response of the tested components, accelerometers were instrumented to both structures. The input data resulted to the fact that the main structure of the Mosque has a frequency of 12.8Hz and the minaret a frequency of 6.35Hz. Cracks were performed to the damaged tested model (fig. 2.5 b & c) (Krstevska *et. al.*, 2010).

(a)  ***(b)***  ***(c)*** 

Figure 2.1: *(a)* View of the main prospect of the Fossanova Church; *(b)* vaulted system of the church's nave; *(c)* ribbed vault in the transept zone (Matteis *et. al.*, 2010)

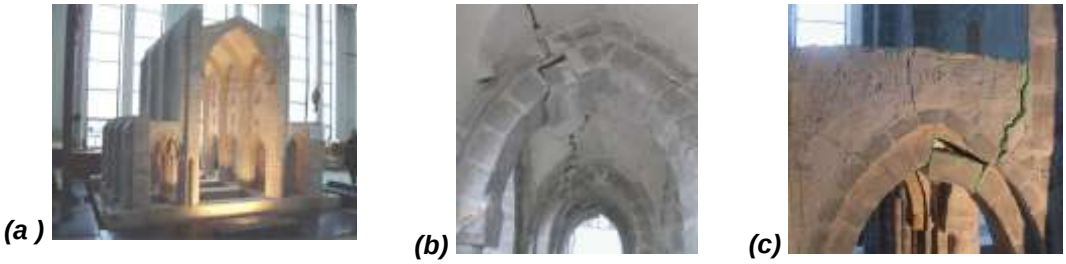

Figure 2.2: *(a)* View of the 1/5.5 scale model of the church; *(b)* & (c) damages locations of the model's vaults after test (Matteis *et. al.*, 2010)

Figure 2.3: *(a)* View of Mustafa Pasha Mosque in Skopje; *(b)* & *(c)* Views of the damaged monument due to the 1963 earthquake (Krstevska *et. al.*, 2010)

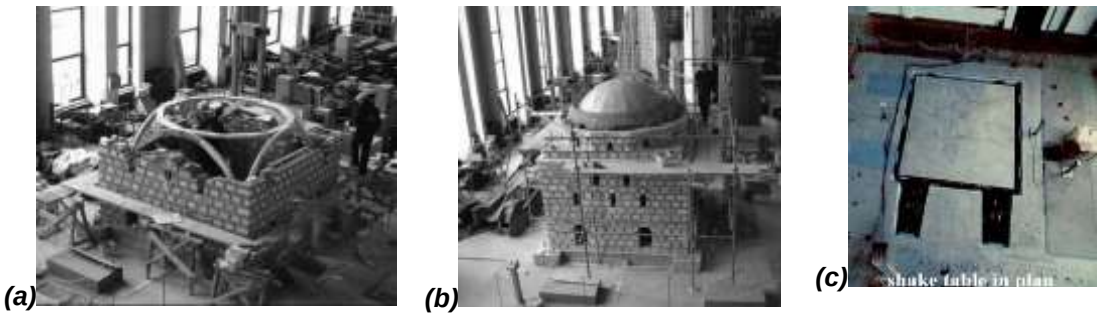

Figure 2.4: *(a)* & *(b)* Details on construction of Mustafa Pasha Mosque model; *(c)* Two component shaking table at the IZIIS' dynamic testing laboratory (in plain) (Krstevska *et. al.*, 2010)

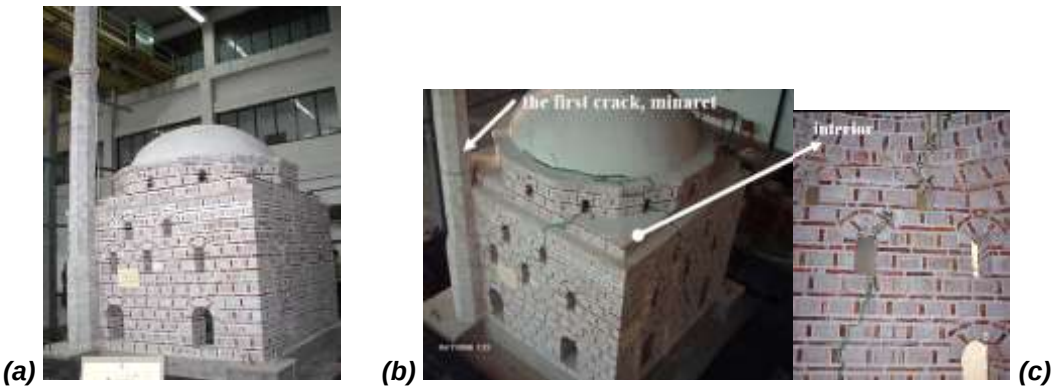

Figure 2.5: *(a)* The original large-scale model; *(b)* & *(c)* Damage to the minaret (horizontal crack) and the mosque after seismic testing (Krstevska *et. al.*, 2010)

2.3.2.2 In the Field

Field testing of historic structures is more common than laboratory experiments. The beginning of this research project was three on-site surveys to a historical masonry structure. Following two examples for the literature are presented.

Ottoni (2015) studied the monitoring of the Santa Maria del Quartiere's dome (Parma, Italy) (fig. 2.6a), built on the 17th century. It is a central plan church[2], surrounded by a hexagonal pavilion dome. Domes intent to open as they usually transfer both vertical and horizontal forces to their bearing structures, thus this forces' transfer generates structural changes and potential lack of stability over time. Therefore, domes' traditional method of monitoring, over the centuries, is the observation of their crack pattern. Santa Maria del Quartiere's dome seemed to have a suitable in-scale model of cracks' pattern and mechanical behaviour, as the passing and non-passing cracks were variously distributed on each of the dome's webs and edges. In particular, at the dome's abutment level six cracks are formed which rising up on the dome's edges for approximately two-thirds of the entire height and four cracks exist at the centre of webs I, II, IV and VI (fig. 2.6b). All these cracks form a crack pattern symmetry which is compatible with a typical domed structure collapse mechanism. Therefore, for investigating the cracks' behaviour over time with relation to both environmental and mechanical events, two different monitoring systems, one in March 2008 and the other one in March 2011, were installed to the church's dome. The first one was comprised of nine deformometers, manually operated, and the second one of ten

[2] A central plan church is the church which is comprised of a central space surrounded by symmetrical areas around each side.

automatically operated. The nine of the ten deformometers of the second monitoring system were installed at the same location of the first monitoring system. Both monitoring systems showed a good correlation of monitoring data and concluded to the same results, with a dropping of a global crack trend after the installation of the tie rod. In addition, all of the instruments showed a seasonal periodicity; cracks opening in winter and closing during summer, resulted by the thermal dilation of masonry phenomenon (Ottoni, 2015).

Squeglia *et. al.* (2015) studied the importance of structural monitoring through centuries. In particular, they looked at the leaning tower of Pisa, a historical construction built in the 12th century. The tower is one historical construction of the three of the Piazza dei Miracoli (Pisa, Italy). The other two are the Compo Santo and the Pisa Baptistery (fig. 2.7 b & a). A scientific conflicting debate was standing, since the beginning of the 19th century about the reason behind the tower's inclination. The argument was between two different opinions; the one was stating that the inclination was a construction characteristic of the tower and the other one that it was a construction accident. However, none of the two opinions proved to be right, as in the beginning of the 20th century the tower's inclination was concluded to be due to the nature of the subsoil. During the first construction phase (1173 – 1178) of the tower, a slight inclination northward was observed, which changed direction towards south in 1272. In 1278, the deduced inclination of the tower was 0.6° and in 1370 was 1.6°. In 1817, the first recorded measurement made using a plumb line and it was found that the inclination was approximately 4.9°. The excavation of the Pisa Baptistery followed and in 1859, the inclination was measured 5.0°. Since the beginning of the 20th century, the tower has been regularly monitored either by a geodetic survey or by the installation of a 35m long pendulum inside the structure. Over the years, the recorded inclination of the tower shows a larger increase than the foundation's rotation and in the early 1990s, the inclination was approximately 5.5°. As a conclusion, the stabilisation attempts of the monument, during the last decade of the 20th century, have been successful based on all the monitoring efforts (Squeglia *et. al.*, 2015).

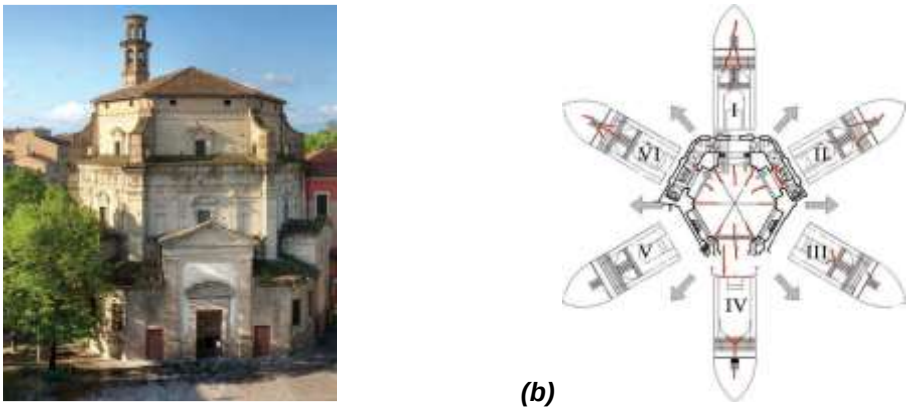

Figure 2.6: ***(a)*** Main view of Santa Maria del Quartiere; ***(b)*** Scheme of the dome crack pattern showing the six passing cracks on the edges and four major cracks on center of webs I, II, IV, and VI (webs numbering in clockwise direction, web I facing the choir) (Ottoni, 2015)

Figure 2.7: Piazza dei Miracoli; ***(a)*** Pisa Baptistery, ***(b)*** Compo Santo, ***(c)*** Tower (Squeglia *et. al.*, 2015)

2.3.3 Summary

The appropriate structural intervention of a historical structure, and in particular of a masonry one, originates from the extended knowledge of its structural behaviour. The determination of the structure's pathology is based on the application of monitoring systems. Moreover, the two major steps for setting up a suitable retrofitting intervention, which could be recalibrated, or even removed and changed, is the in-scale testing of existing monuments and their in-field survey, through monitoring. The percentage of effective efficiency of the applied and finally chosen monitoring systems is the key step prior to the strengthening interventions especially to heritage structures.

2.4 Monitoring Strategy

2.4.1 Overview

The following section, describes two monitoring methods; the close range digital photogrammetry (CRDP) and the strain gauges. These two methods are employed in order to monitor the vibrated specimens.

2.4.2 Close Range Digital Photogrammetry

2.4.2.1 Overview

Photogrammetry is the science, and art, of determining the position, size and shape of objects as a consequence of analysing images recorded on film or electronic media, instead of measuring them directly. This is carried out by the application of the laws of mathematics and physics. The name “photogrammetry” comes from a combination of Greek words that can be loosely translated as “measuring lines produced by light”. Photogrammetry is classified into two types: Long Range Photogrammetry, applied with the use of camera distance settings in the field of Aerial or Satellite Photogrammetry, which is broadly used for map creation; and Close Range Photogrammetry, applied with the use of camera distance settings in the field of Terrestrial Photogrammetry, which is broadly used in the measurement of engineering structures, with the cameras based very close to the object.

The concept of a camera’s perspective and central projection may be traced back to 1500s. However, in 1850, Frenchman Aimé Laussebat constructed a map of Paris based on geometric information that he extracted from his photographs taken from a balloon flying over the rooftops in the city. For this reason he is known as the father of photogrammetry. There are four eras of photogrammetry; plane table photogrammetry (1850-1900), analogue (1900-1960), analytical (1960-1985) and digital (1985 – present). The last era, Close Range Digital Photogrammetry (CRDP) is characterised by the development of Charge Coupled Device (CCD) or Complementary Metal-Oxide-Semiconductor (CMOS) sensors on the digital photogrammetric system. The first stereo CCD based system appeared in 1986, and in the same year the first multi-camera CCD based system was developed. Technological devices may come and go, but for the scientist working in photogrammetry, success will only be achieved from a thorough understanding of spatial relationships, camera geometry, angles of

intersection in three dimensions, the propagation of light rays through lenses and mathematical modelling of the sizes and shapes of objects; in other words simple geometry as it was introduced by Euclid (Atkinson, 1996).

2.4.2.2 Terminology

Photogrammetry is exploiting a series of images from several camera positions. By making measurements of features in these images and a knowledge of the 3D image geometry we can calculate the 3D coordinates of the features that change over time and the uncertainty of those coordinates as they change. For the purpose of this technique images or videos are employed and it is used for structural health monitoring purposes, when the extent of the measured object is usually less than 100 metres and the cameras are positioned close to the structure. It is an accurate, cost and time effective technique for collecting the field measurements of a real object – large or small – directly from images (Atkinson, 1996).

Following a few major terms related to photogrammetry, are briefly described.

The ***image size*** is the area of the image measured in pixels; its width multiplied by its height.

The ***focal length*** of a camera is a value that classifies how strong the lens is for diverging or converging the light ray. Both the focal length and the image size provide the angle of the view of the camera (fig. 2.8).

Image scale number or magnification (m) is the ratio of the object distance (h) to the principal distance (c) or the ratio of a distance in object space (X) to the corresponding distance in image space (x'); $m = h/c = X/x'$ (fig. 2.8).

Targets are used to signal the points of interest on the measured object, or to calibrate the camera/s, by providing a reference to a known object. They usually have a circular shape and they are categorised into passive and active, with the passive ones having a white or a yellow colour on a black or dark background and the active ones being made by retro-reflecting sheeting which are capable in responding to a camera's flash or ring-light and can be placed on any background.

The perspective axis POp is orthogonal to the projection plane which intersects at point p, the ***principal point***; in other words it is the point on the image plane where a light ray, following the optical axis, hits the image plane (fig. 2.9).

The ***principal distance*** (Op) is the perpendicular distance from the perspective centre of the lens system to the image plane (fig. 2.9).

The ***orientation*** is the determination of the position of the camera's attitude. ***Photo orientation*** data for the cameras can come from either a relative and absolute image orientation or from resections based on ground control targets.

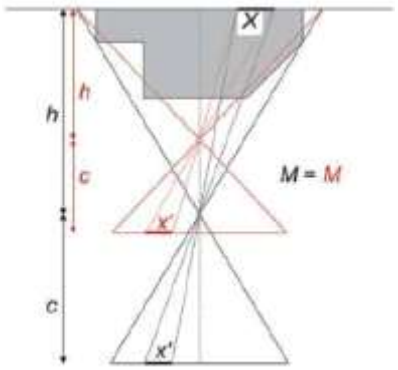

Figure 2.8: Dependency of image scale on image format, focal length and object distance (Luhmann et. al., 2013)

2.4.2.3 Background Theory

Geometry

In photogrammetry the position of a point in space is commonly defined by three dimensional cartesian co-ordinates in a relevant system, whose origin, scale and orientation can be defined.

For a ***two camera geometry*** (fig. 2.10) set up, when the orientation of both cameras is known and the perspective centres at O_1 and O_2 are, also known, the object space co-ordinates (X_A, Y_A, Z_A) of a target A can be determined. The same principle is followed for a ***multistation convergent geometry*** (fig. 2.11), also rederres to as multi-view stereo (MVS).

Target image size is 5-10 pixels[3], on average, and the diameter (d) of the target in the image is equal the diameter (D) of the target in the object space multiplied with the ratio of the principal distance of the camera (pd) over the camera to target array[4]

[3] Pixel is considered to be a single point on an image.

[4] Array is when any element is being displayed on a systematic order, i.e. columns or rows.

distance (R); $d = D \times (pd/R)$. Targets being less than 5 pixels cause deterioration in the accuracy, targets more than 10 pixels usually interfere with the background or with other targets and targets more than 15 pixels can cause systematic errors affecting negatively the measurements' accuracy (Atkinson, 1996).

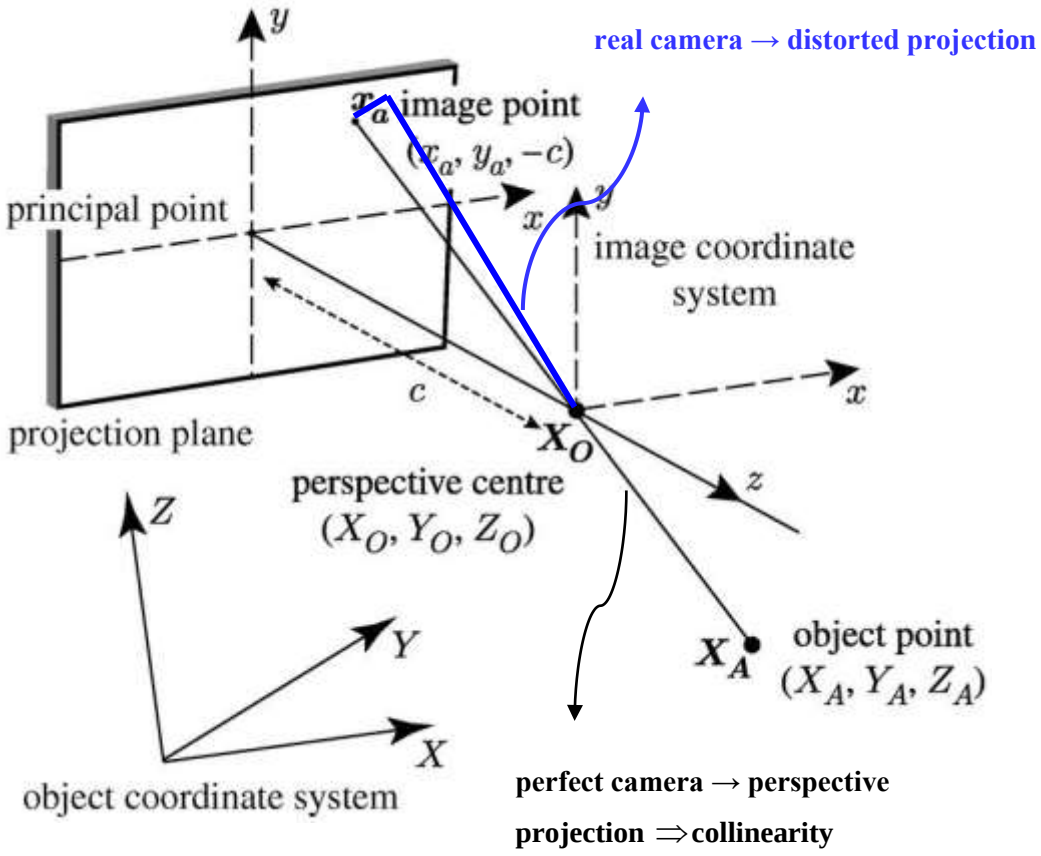

Figure 2.9: Central perspective projection (Atkinson, 1996)

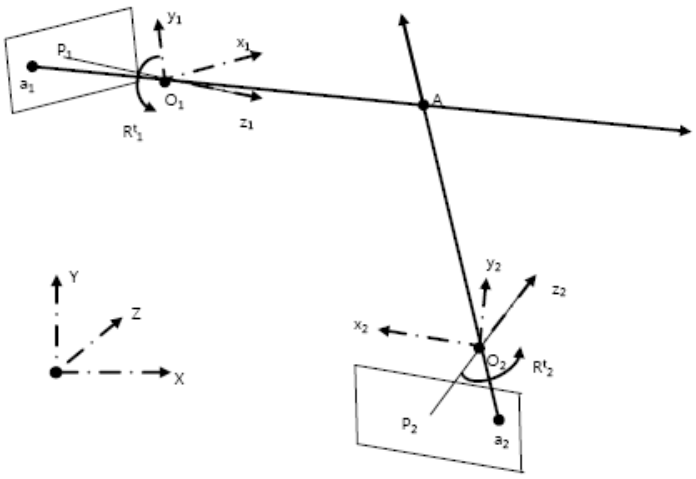

Figure 2.10: Intersection (Atkinson, 1996)

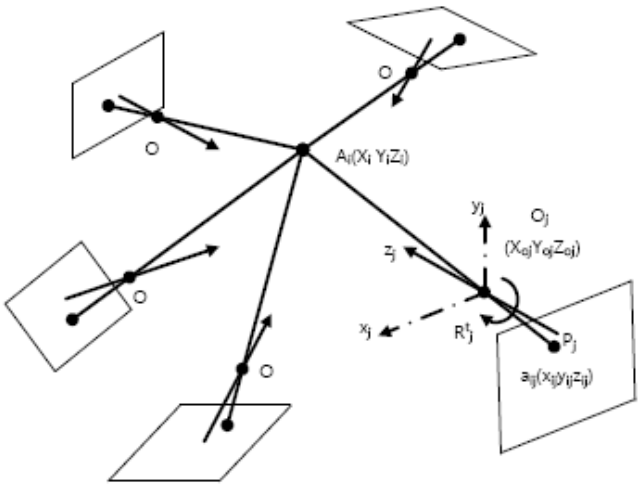

Figure 2.11: Multistation convergent configuration (Atkinson, 1996)

Functional Model

The relationship between the object and the image can be explained by the principle of ***collinearity***. A three dimensional Cartesian co-ordinate system is introduced in order to derive the functional relationship between the position of object point A and the position of a – the projection of A. The primary co-ordinate system (XYZ) is located arbitrarily in the object space. In this system the coordinates of the perspective centre O are (X_O, Y_O, Z_O) and the coordinates of the object point A in space are (X_A, Y_A, Z_A). The projection of point A through O in the image plane is expressed on the secondary co-ordinate system (xyz), which gives the coordinates of point a which are (x_a, y_a, z_a) or $(x_a, y_a, -c)$ since all image points are on the image plane a distanced c from the secondary's system origin. Figure 2.11 shows the collinearity of points A, O and a (Atkinson, 1996).

- When the vectors are written relative to the primary co-ordinate system, the X coordinate of the object point A is given by the following equation:

$$X_A = X_O + S \tag{2.2}$$

where

- S is the position vector of the object point A relative to the perspective centre O (fig. 2.14)

- When the vectors are written relative to the primary co-ordinate system, the X coordinate of the object point A, relative to its projection collinear point a, is given by the following equation:

$$X_A = X_O - \mu\ R^t\ x_a \tag{2.3}$$

where

- μ, is a scalar quantity greater than zero;
- R^t, is the transpose rotation matrix consisting of the rotation elements r_{ij} (fig. 2.17)

- The reverse transformation of eq. 2.3 is given by the following equation:

$$x_a = \mu^{-1}\ R\ \left(X_O - X_A\right) \tag{2.4}$$

- which in matrix notation is given by the following equation:

$$\begin{bmatrix} x_a \\ y_a \\ -c \end{bmatrix} = \mu^{-1} \begin{bmatrix} r_{11} & r_{12} & r_{13} \\ r_{21} & r_{22} & r_{23} \\ r_{31} & r_{32} & r_{33} \end{bmatrix} \begin{bmatrix} X_A - X_O \\ Y_A - Y_O \\ Z_A - Z_O \end{bmatrix} \tag{2.5}$$

- since the third equation of the reserve transform above can be written explicitly in terms of the scaling μ and substituted in the order two equations. The collinearity equations are given below:

$$x_a = \frac{-c\left[r_{11}\left(X_O - X_A\right) + r_{12}\left(Y_O - Y_A\right) + r_{13}\left(Z_O - Z_A\right)\right]}{\left[r_{31}\left(X_O - X_A\right) + r_{32}\left(Y_O - Y_A\right) + r_{33}\left(Z_O - Z_A\right)\right]} \tag{2.6}$$

$$y_a = \frac{-c\left[r_{21}\left(X_O - X_A\right) + r_{22}\left(Y_O - Y_A\right) + r_{23}\left(Z_O - Z_A\right)\right]}{\left[r_{31}\left(X_O - X_A\right) + r_{32}\left(Y_O - Y_A\right) + r_{33}\left(Z_O - Z_A\right)\right]} \tag{2.7}$$

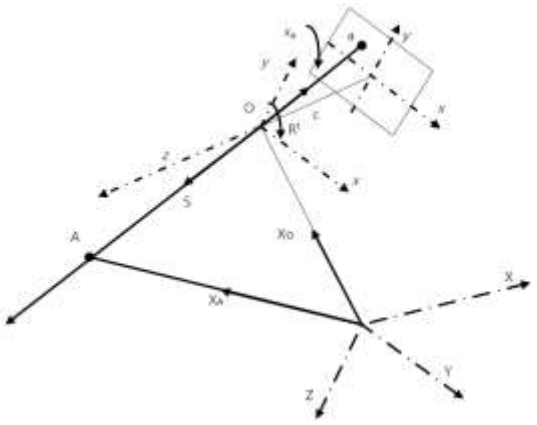

Figure 2.12: Collinearity condition (Atkinson, 1996)

Lens distortion (fig. 2.14) appears in the captured images because a geometric image aberration occurs. It is categorised into two kinds: the radial distortion and the tangential one. Both of these categories cause systematic displacement of the images, which will produce systematic errors during any photogrammetric measurement. To prevent lens distortion, all camera systems should be carefully calibrated before use and the image measurements rectified accordingly.

Radial lens distortion

Radial lens distortion is observed when the image of an off-axis point is displaced radially either closer to or away from the principal point. It is calculated from the principal point during the bundle adjacent process.

Tangential distortion

Tangential distortion is due to imperfect centring of the lens components and other manufacturing defects in a compound lens, which causes the geometric displacement of images vertically to the radial distance (fig. 2.15).

Affinity

The differences in length and width of the pixels in the image caused by synchronization and can be taken into account as ***affinity***.

Accuracy estimation

The accuracy of a photogrammetric measurement is computed with reference to an independent external standard and the precision can be estimated approximately with the help of figure 2.13. Therefore, the image measuring accuracy may be calculated using eq. 2.8.

$$dX = m \times dx' \rightarrow s_X = m \times s_{x'} \Rightarrow s_{x'} = s_x / m \tag{2.8}$$

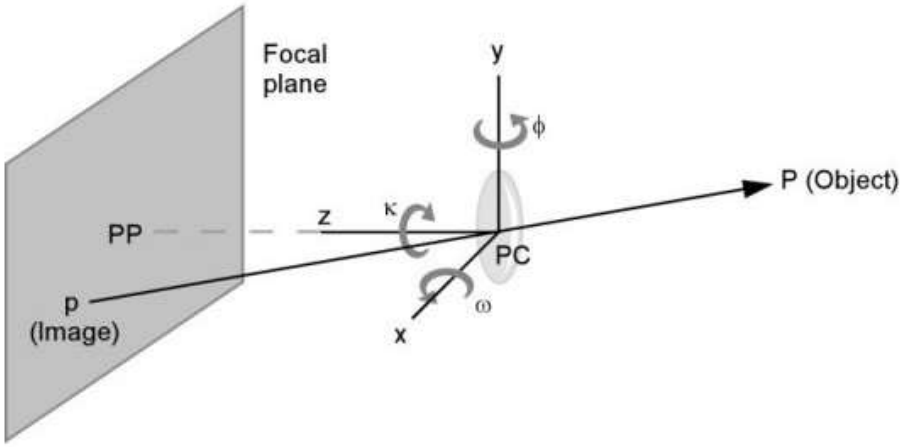

Figure 2.13: The relationship between the image, the coordinate system and the rotations for close-range (horizontal looking) photography (Luhmann et. al., 2013)

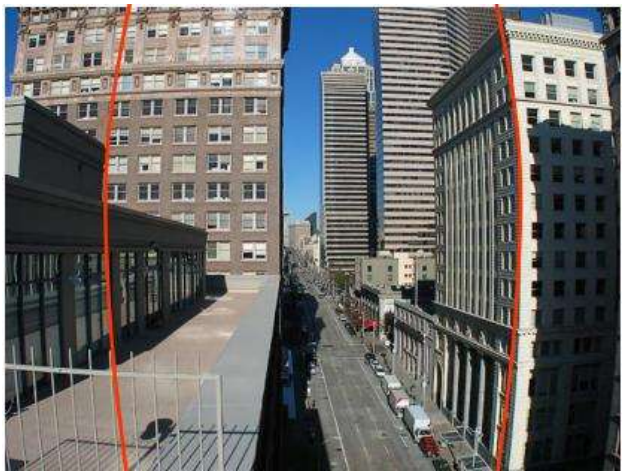

Figure 2.14: Lens Distortion (Luhmann et. al., 2013)

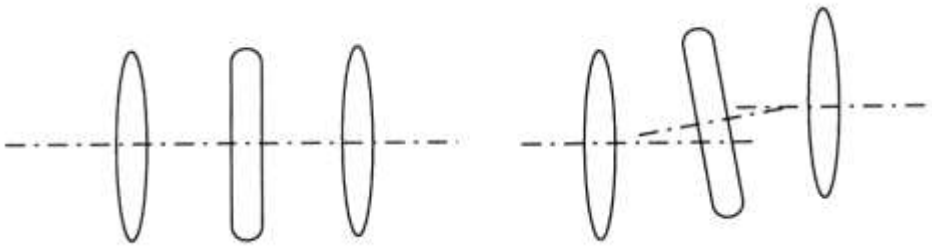

Figure 2.15: Cause of Tangential Distortion (Luhmann et. al., 2013)

Stochastic Model

The stochastic model is suitable for presenting the error and the uncertainty of the photogrammetric measurements.

The geometry of the camera and lens combination used to capture the image is identified through the ***camera's calibration***. This technique identifies how much the geometry of the image information in a real camera differs from the geometry of the central perspective centre's projection and it provides any analytical software with information such as the camera's focal length, the position of the principal point, the image size and the lens distortion.

The ***camera calibration parameters*** are described in the table 2.2. All parameters must be specified in the units of millimetres (or pixels) (VMS Manual).

Number	Parameter	Description
1	PPx	X image coordinate of the principal point
2	PPy	Y image coordinate of the principal point
3	PD	principal distance of the camera (separation between the lens perspective centre and the focal plane)
4	k3	3rd power term of radial lens distortion
5	k5	5th power term of radial lens distortion
6	k7	7th power term of radial lens distortion
7	p1	first term of descending (tangential) lens distortion
8	p2	second term of descending (tangential) lens distortion
9	a1	orthogonality of the image coordinate system
10	a2	affinity of the image coordinate system

Table 2.2: Camera Calibration Parameters (VMS Manual)

Radial lens distortion is computed using the following formula:

$$dR = \left(k_3 \times r^3\right) + \left(k_5 \times r^5\right) + \left(k_7 \times r^7\right) \tag{2.9}$$

The components of decentring (tangential) distortion are computed using:

$$dDx = \left[\left(p_1\right) \times \left(r^2 + 2x\right)\right] + \left(2 \times p_2 \times x \times y\right) \tag{2.10}$$

$$dDy = \left(2 \times p_1 \times x \times y\right) + \left[\left(p_2\right) \times \left(r^2 + 2y\right)\right] \tag{2.11}$$

The actual image location relative to the ideal location is given by:

$$x = x + \left(x/r\right)dR + dDx + \left(a_1 \times y\right) + \left(a_2 \times x\right) \tag{2.12}$$

$$y = y + \left(y/r\right)dR + dDy \tag{2.13}$$

where

$r =$ radial distance from the principal point $= \sqrt{\left(x^2 + y^2\right)}$

$x, y =$ coordinates of the image relative to the principal point

Image Residual (μm)

The magnitudes of the mean image residuals are normally determined by the size of the pixels from the CCD sensor (digital images) and the image measurement method. The use of centroids of high contrast target image should normally realise an RMS value of equal to or better than 1/10 of a pixel. If the RMS value is significantly higher or smaller to 1/10, it is likely that there are systematic or even gross errors in the measurements.

Least Square Estimation (LSE) is a systematic method for determining a unique set of coordinate values in close range photogrammetry, among other applications, based on a large number of measurements of different kinds and weights. It is also flexible as it allows elements to be treated as unknowns or as constants depending on the circumstances; the algorithm within an LSE process can be devised to suit particular measurement task. The general form of the linear equation of the Observation equations is as follows (Atkinson, 1996 / Kowk et. al., 2001):

$$Ax = l \tag{2.14}$$

where A is a coefficient matrix, x is the unknown and l is the vector set. For example, three equations with three unknowns can be expressed as:

$$\left.\begin{array}{l} 5x + 8y = 25 \\ 15x - 3y + 4z = -5 \\ x + 8y - 7z = 42 \end{array}\right\} \Rightarrow \begin{bmatrix} 5 & 8 & 0 \\ 15 & -3 & 4 \\ 1 & 8 & -7 \end{bmatrix} \begin{bmatrix} x \\ y \\ z \end{bmatrix} = \begin{bmatrix} 25 \\ -5 \\ 42 \end{bmatrix} \tag{2.15}$$

To calculate all of the unknowns, it is necessary to write the equation with respect to x:

$$x = A^{-1}l \tag{2.16}$$

To solve eq. 2.16, it is reformed by adding the vector v:

$$Ax = l + v \tag{2.17}$$

This subsequently leads to the Least Squares Solution which is expressed as:

$$\hat{x} = \left(A^t A\right)^{-1} A^t l \tag{2.18}$$

where t means the transpose form of the matrix. This produces the solution to the least squares best estimation. However, in order to obtain a solution that is closer to reality, a Weight (W) matrix has to be applied.

$$W = \begin{pmatrix} w_1 & 0 & 0 & 0 & 0 \\ 0 & w_2 & 0 & 0 & 0 \\ 0 & 0 & w_3 & 0 & 0 \\ 0 & 0 & 0 & \ddots & 0 \\ 0 & 0 & 0 & 0 & w_n \end{pmatrix} \tag{2.19}$$

This is a diagonal matrix and it is expressed with the variance function as:

$$w_i = 1/\sigma_i^2 \tag{2.20}$$

which is populated as:

$$w = (1/0.5)^2 \tag{2.21}$$

and finally it produces a standard deviation

$$\hat{x} = \left[A^t W \hat{x}\right]^{-1} \times \left(A^t W b\right) \tag{2.22}$$

with the W providing the input of the measurement uncertainty.

Therefore, one gets a pair of observation equations for each imaged target, six unknowns for each image, which are its exterior orientation parameters Xo, Yo, Zo, ω, φ, κ, and three unknowns for each target.

Target Coordinate Precisions

The precisions of the target coordinates are dependent on many factors, including the geometry of the intersection, the focal length of the camera/s, the camera to target range and the number of the photographs on which one target appears. It is not appropriate to generalise on the target coordinate precision that can be achieved. However, a well designed target intersection should realise precisions which are predictable based on the following formula:

$$st = (R/pd) \times \left(s_i/\sqrt{n}\right) \tag{2.23}$$

where

$st =$ predicted precision of the target coordinates

$pd =$ principal distance of the camera

$R =$ camera to target array distance

$s_i =$ precision of the target image measurements

$n =$ average number of photographs on which each target is imaged.

Analytical Tools

Resection is the process of finalising the camera's position and orientation when a picture is taken. It is essential to have measured at least three points in the image, for which corresponding coordinates in the object space are known; at least eight points will be illustrated in the same image.

Image Orientation

The image orientation consists of a series of information related to the monitored object. These are the X , Y and Z coordinate locations, the phi (ϕ), the omega (ω) and kappa (κ). In particular, the rotations of the image coordinate system are according to the right hand screw rule. In other words, the rotation is counter-clockwise when looking toward the coordinate origin. The omega, phi and kappa rotations are about the X , Y and Z coordinate axes respectively. The image coordinate system is defined by:

1. origin at perspective centre of the lens
2. $X - Y$ plane parallel to the focal plane of the camera
3. X axis parallel to the horizontal lines of the CCD array
4. Z axis is parallel to the camera axis, but pointing towards the camera.

The intersection of the Z axis with the focal plane is known as the principal point and generally does not coincide with the centre point of the CCD array.

Intersection (fig. 2.10) is the computation of the 3D location of a point or a set of points common to two or more images.

Bundle adjustment is a photogrammetric technique for producing the exterior orientation of overlapping images and consequently the 3 dimensional reconstruction of a scene from multiple images. It is usually used to provide higher quality results; simultaneous adjustment of all pictures will provide the best result.

2.4.2.4 Example Applications in structural elements

Armesto (2008) tried to detect the structural damage on historic masonry structures and more specifically the behaviour of the Basílica da Ascensión, in the north-west of Spain. The eastern wall of the monument has a crack which was documented by photogrammetric survey on two dates at an interval of 3 years in order to evaluate the size and stability of the damage to the structure. Multi-station convergent systems were employed for both measurements. The measurement of the crack (fig. 2.16) at a given moment was made by the restitution of points over the edges of the ashlars that constitute the surroundings of the crack, the definition of the surface enclosed by the cloud of points and the calculation of the area of that surface (Armesto, 2008).

Thomas *et. al.* (2009) developed, at the Institute for Environmental Engineering of the University of Rostock (Germany), an automated laboratory bending apparatus (fig. 2.17) for large-scale testing of clay beams for studying the positive effects of geogrid reinforcements in mineral sealing layers exposed to bending stresses. Due to time-dependent progress of deformation in soils and the fact that even very small bending deformations will cause cracking failure in clays, a contact-free photogrammetric method was chosen for the measurements. Therefore, a grid pattern of 113 circular points was established directly on the mineral sealing material and markers were installed at the visible ends of the grid ribs (fig. 2.17). During the experiment, digital images were captured and their analysis was based on a photogrammetric single-capture measurement. Horizontal strains and vertical compressions of the tested beams were calculated (1 and 2 in fig. 2.17). Additionally, for reinforced specimens the geogrid strain was evaluated (3 in fig. 2.17). The object coordinates, gained from the failure crack geometry in the bent clay beams, were used to calculate the length and width of cracks (4 and 5 in fig. 2.17) and to analyse their progression (Thomas et al., 2009).

Dias-da-Costa *et al.* (2011) studied the experimental and numerical characterisation of the behaviour of structural interfaces between new-to-old concrete layers using CRDP. To experimentally assess the shear strength between the original concrete layer and the new concrete layer with added reinforcement crossing the interface, push-off tests were adopted. The geometry adopted for the push-off specimens is represented in figure 2.18(I). The push-off specimens are anti-symmetrical and composed by two identical “L” shape halves, both differently reinforced. The push-off test was performed on a 5000kN universal testing machine with displacement control. A load cell placed at the top of the specimen and two displacement transducers connected to a data logger were used to measure, respectively, the load applied and the deformation of the specimen. The specimen was loaded by imposing a

displacement at the lower plate of the machine at a rate of 0.015mm/s. The opposite side was hinged and therefore small rotations were allowed. The experiment was carried out in six different stages. Each stage of image acquisition led to an independent photogrammetric project containing at least four images, taken from distinct point of views, with a multistation network located at an average distance of 2.0m. All pictures were taken included all targets. Just before loading, a reference photogrammetric project, denoted stage 0, was built. During testing, at each stage relevant to monitoring, the loading machine was immobilised by keeping constant the vertical position of the load plate and the corresponding set of images was acquired. This is strictly related to the multistation network requiring the specimen to remain static during a complete set of pictures. Figure 2.18(II) shows the results of the testing under the final stage. Therefore, the understanding of the structural response of the structure until failure is achieved by obtaining the process of crack formation, the evaluation of crack orientation as well as its corresponding opening (Dias-da-Costa *et. al.*, 2011).

Lee *et. al.* (2006) built up in the laboratory, a two-dimensional model tunnel test using multi-sized aluminium rods. The test was performed using CRDP method and displacement and strain data were computed. The aim was to create an experimental apparatus which is approximate to the condition within a tunnel during construction by simulating its real controlled supports and deformations. However, it could not be simulated the excavation method. Due to the natural self weight of the rods, the model tunnel tests carried out without any surcharge load on the ground surface. The progressive loss of material around and ahead of the tunnel face was simulated in the two-dimensions by a controlled reduction in the tunnel support diameter.

The model tunnel tests were conducted within the steel chamber under normal gravitational acceleration. Therefore, the intension of these controlled laboratory tests was to identify deformations patterns and eventually the failure mechanisms that develop during the controlled collapse of a tunnel diameter. The model tunnel tests were carried out at different tunnel embedment depths (Z_o = 270, 420 and 470mm), ten independent images were taken at each reduction of the tunnel's diameter, 372 retro-reflected were installed and each of those was fixed to the centre part on the ends of the smaller size rods (fig. 2.19I). The measured $x - y$ coordinates of the target points from the VMS program were arranged into a triangulation mesh. Finally, the measurement of the locations of many nodal points within the aluminium rod material by the close range photogrammetry provided the displacement data, which conveniently presented data showing the distribution of strains throughout the test

material. The results at embedded depth Z_o = 270 are presented in figure 2.19III (Lee *et. al.*, 2006).

Tsakiri *et. al.* (2004) measured in the laboratory the deflections of a loaded wooden beam with dimensions 1.5m x 0.14m x 0.07m, using close range digital photogrammetry and by analysing the data with the photo-triangulation method (fig. 2.20). A static load experiment was carried out with a controlled loading applied to the timber beam, which was placed on an indoor hydraulic jack system. The beam was vertically supported close to its two ends while the loading jack was located at the centre of the beam. Measurements were taken at three load levels (8, 12 and 23 kN) with the use of a Sony DSC-F707 digital camera with a CCD array of 2560 x 1920 pixels. The maximum deflections detected were –6mm, –8mm and –17mm for increments of 8kN, 12kN and 23kN respectively (Tsakiri *et. al.*, 2004).

Location of the Basílica da Ascensión, Allariz (Orense), Galicia, Spain

Image of Basílica da Ascensión

Image of the crack in the eastern wall of the Basílica da Ascensión (front view)

3D triangulation model of the crack

Figure 2.16: CRDP method applied to a historical structure in Spain (Armesto, 2008)

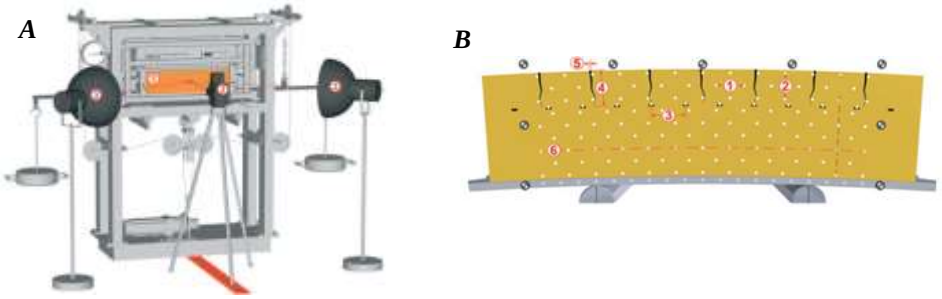

Figure 2.17: ***(A)*** Bending apparatus and instrumentation for experiments (schematic): (1) specimen with measuring field; (2) metric camera; (3) lamp. ***(B)*** Measurement plane with measured parameters (schematic): (1) horizontal strain; (2) vertical compression; (3) geogrid strain; (4) crack length; (5) crack width; (6) bending curvature (Thomas *et al.*, 2009)

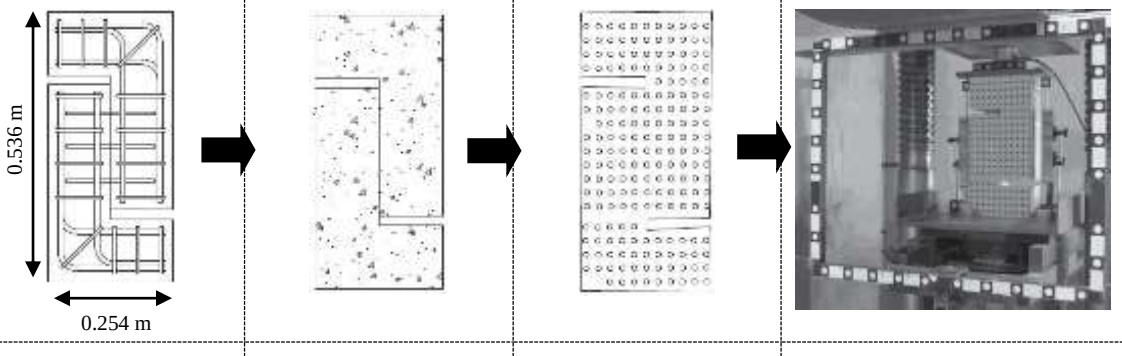

push-off specimen	push-off specimen with casting	scheme showing the targets of the specimen	final experimental set-up

Figure 2.18 (I): Different steps of production the experimental set-up (Dias-da-Costa *et al.*, 2011)

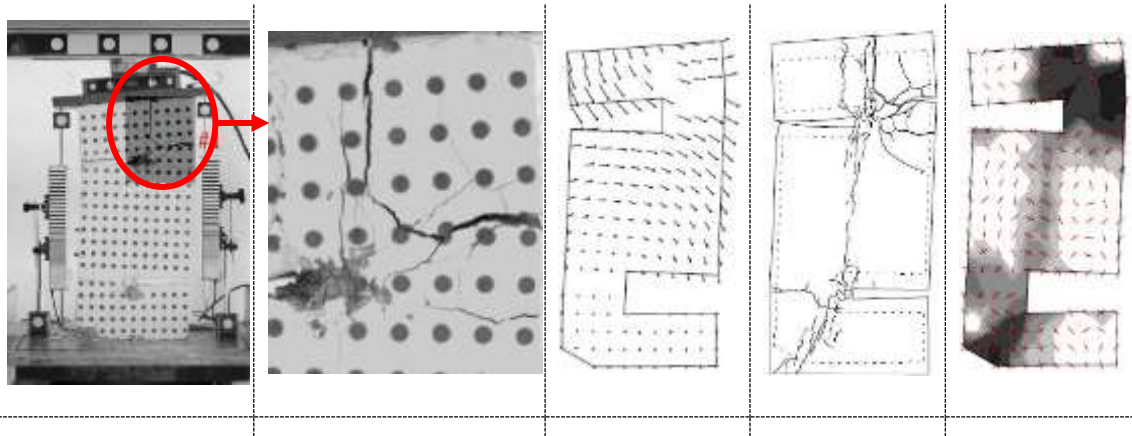

experimental test at final loading stage	detail of the specimen	displacement field of the target points	map of cracks	first principal strain

Figure 2.18 (II): Final obtained results of the specimen's loading testing (Dias-da-Costa *et al.*, 2011)

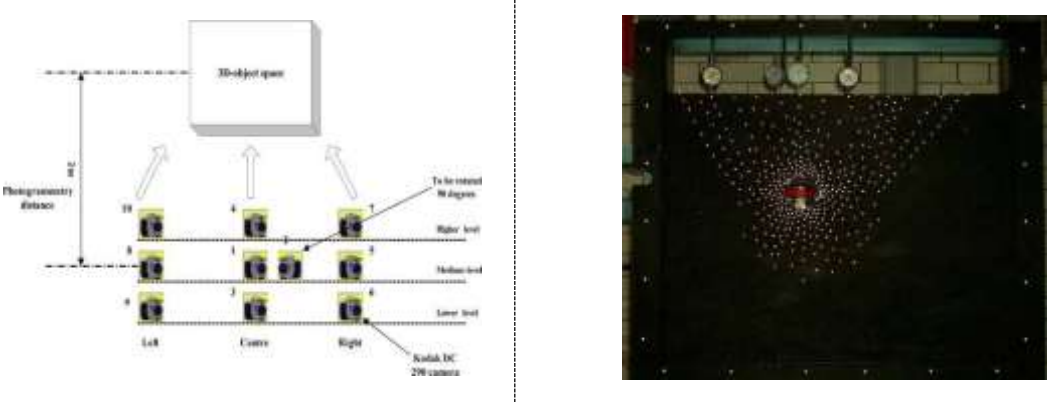

typical camera positions	experimental apparatus showing the 372 reflective targets

Figure 2.19 (I): Two first steps showing the testing procedure (Lee *et al.*, 2006)

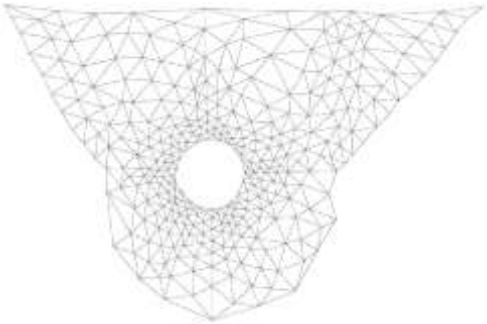

triangular mesh system

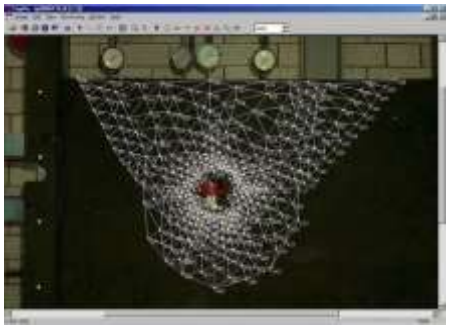

digital imaging process

Figure 2.19 (II): Two final steps showing the testing procedure (Lee *et al.*, 2006)

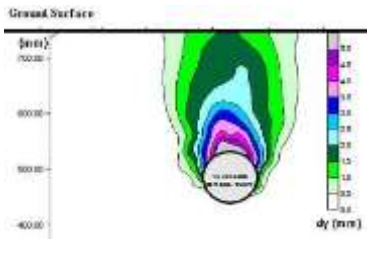

vertical displacement

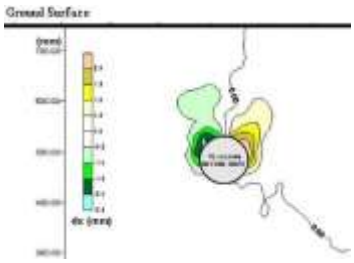

horizontal displacement

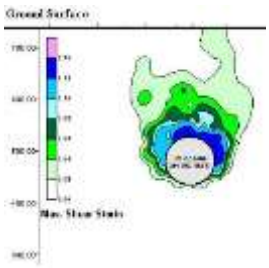

maximum shear strain

Figure 2.19 (III): results at Z_0 = 270mm (Lee *et al.*, 2006)

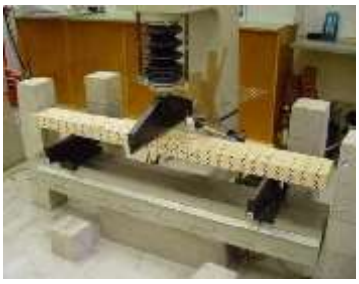

The timber beam positioned on the hydraulic jack system

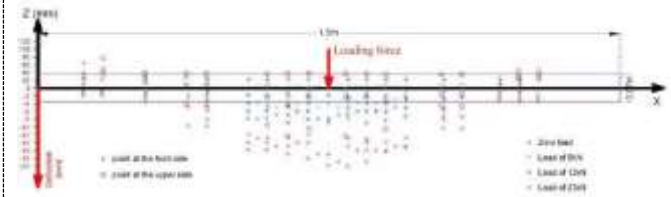

Photogrammetrically determined displacements

Figure 2.20: Load testing measurement & results of a wooden beam (Tsakiri *et. al.*, 2004)

2.4.2.5 Summary

The monitoring of crack propagation under static loading, with the use of close range digital photogrammetry (CRDP), has been successfully achieved. CRDP has also been successfully used for the detection of deformation patterns of vibrated structural

members. Wasil *et. al.* (1965) computed the displacements of a square plate free on all edges and vibrated in resonance, by measuring a pair of photographs during the plate's vibration (Wasil *et. al.*, 1965). Lee *et. al.* (2013) also performed a similar experiment by measuring the displacements of a vibrated cantilever beam which was fixed at its lower end and excited at 12Hz (Lee *et. al.*, 2013). Therefore, based on the examples described in the literature, CRDP is a structural monitoring technique that is able to provide the distribution of structural strains and potentially of shear ones.

2.4.3 Strain Gauges

2.4.3.1 Overview

Strain gauge is a device which forms different shapes and all are capable of measuring strain. It actually converts a displacement (strain) into an electrical signal, by connecting it in a bridge configuration. In 1938, Edward E. Simmons and Arthur C. Ruge invented the first strain gauge which was comprised of a small piece of filament bent in a zigzag pattern and glued on a carton base (Harris, 2002). The use of strain gauge is wide broadly, and such an example is the liquid strain gauge which is used in the hospitals for measuring fluctuations in blood pressure (Wilson, 2005).

2.4.3.2 Terminology

Piezoelectricity occurs when electricity is produced by pressure. Accordingly, any piezoelectric device measures and transforms the force into electrical signal (Harris, 2002).

Dissipation is the result of the energy's irreversible transformation from a form A to a form B (Harris, 2002).

Photochemical reaction is the chemical reaction resulted by the absorption of light either by the atoms or the molecules (Harris, 2002).

Wheatstone Bridge is a circuit which measures electrical resistances and these unknown values are compared with well-defined ones. All the strain and indicator recorders are operated with the use of a Wheatstone bridge (Harris, 2002).

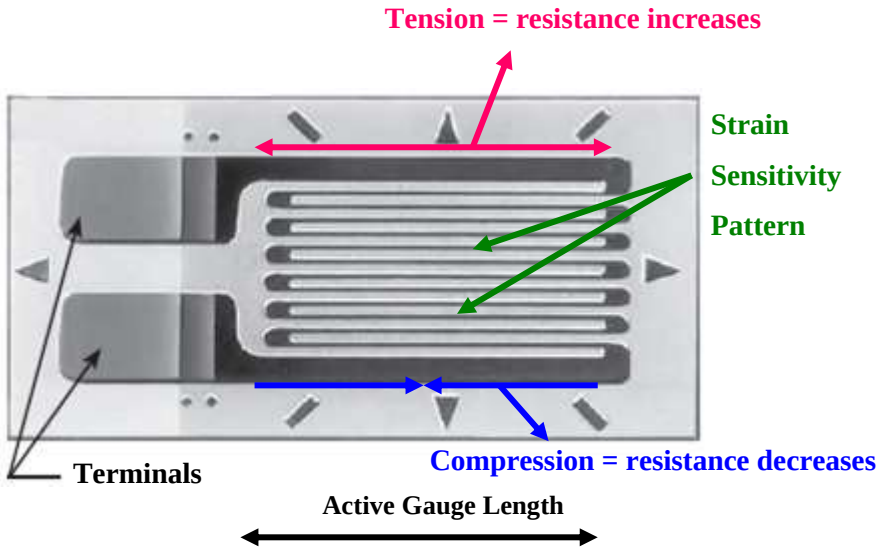

Figure 2.21: Foil Strain Gauge (Vishay Precision Group)

2.4.3.3 Technology

There are twenty different types of strain gauges, divided into numerous categories and sub-categories (table 2.3). The most used type of strain gauge is the etched foil one, which is produced from thin resistance foil by a photochemical etching process. It shows good bonding properties, heat dissipation rate, stabilisation under extreme temperature conditions and performance under prolonged loading, as it has a large ratio of surface area to cross-sectional area. The strain gauge is attached to the monitored object with a glue type according to the lifetime of the monitoring process. As the monitored object deforms (tensioned or compressed), the foil is deformed as well resulting to a change in its electrical resistance. This resistance change is related to the gauge factor (*GF*) and it is measured using a Wheatstone bridge. Therefore, when a force is acting to the strain gauge's wire (area=*A*, length=*L*, resistivity=ρ, resistance=*R*), will cause the wire to shorten or elongate, which potentially will cause the resistance to decrease or increase according to (Wilson, 2005 / Neubert, 1967):

$$R = \frac{\rho L}{A} \tag{2.24}$$

and

$$\frac{\Delta R}{R} = GF \frac{\Delta L}{L} \tag{2.25}$$

where *GF* is the gauge factor, which for foil gauges is around 2.

The simplest typical form of a Wheatstone bridge circuit (fig. 2.22) is consisted of four resistive arms (R_1, R_2, R_3, R_4) connected in a parallel series arrangement and four nodes with a voltage source (V_{in}). The two nodes which connect the bridge with the power supply are called the input corners and the other two nodes are called the output corners of the bridge, between which the differential output voltage (V_{out}) is measured. Other types of Wheatstone bridge are the two-wire quarter-bridge circuit and three-wire quarter-bridge circuit. A typical Wheatstone bridge is characterised as balanced when the output voltage is equal to zero, regardless of the V_{in}, as it is presented mathematically below (Vishay Precision Group):

$$V_{out} = \frac{R_1 R_3 - R_2 R_4}{(R_1 + R_2)(R_3 + R_4)} V_{in} \tag{2.26}$$

and

$$V_{out} = 0 \therefore R_1 R_3 = R_2 R_4 \tag{2.27}$$

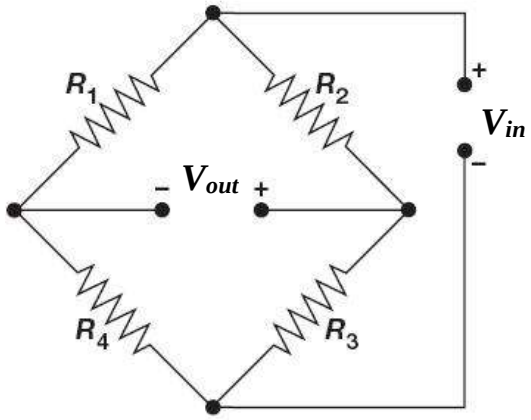

Figure 2.22: Typical Wheatstone bridge (Vishay Precision Group)

				Types of Strain Gauges	***Sub-category I***	***Sub-category II***	***Sub-category III***
I				Liquid			
II				Film			
III				Mechanical			
IV				Optical			
V				Pneumatic			
VI				Acoustic			
VII	A			Electrical	Inductance		
	B				Capacitance		
	C				Piezoelectric		
	D				Photoelectric		
	E	k	1		Resistance	Wire	Wrap-around
			2				Flat-grid
			3				Single-wire
			4				Woven
			5				Unbonded
			6				Etched-foil
		j	1			Semiconductor	Filament
			2				Gold Wire
			3				Lead Ribbon
			4				Backing

Table 2.3: Categories and sub-categories of strain gauges (Wilson, 2005 / Neubert, 1967)

2.4.3.4 Example Applications in structures

Xia *et al.* (2014) employed 400 strain gauges all installed at different heights along the 600m Canton Tower (Haizhu District, China) (fig. 2.23). The scope of the study was to calculate the horizontal displacement and the tilt angle of the building. The tower is a concrete-steel structure and it is consisted of an antennary mast and a main tower

which is a tube-in-tube structure, with the inner one having an oval shape. The performance of the tube structure will be monitored and checked, regarded as a cantilever beam. The longitudinal strain at different sections of a cantilever beam can present its deformation. If the number of the available recorded strain measuring points is *n*, consequently the cantilever beam is divided into *n* segments, with the length of the *i*-th segment, being h_i and the strain difference across the section, at point *i*, being De_i. Therefore, the strain difference distribution along the entire beam is illustrated in figure 2.24b, if it is assumed that the strain difference between the measurement points varies linearly. Subsequently, the results of the monitored points were calculated and presented having as initial reference value the strain at midnight (00:00). This assumption was based on the fact that actual position of the tower is unknown. Therefore, the strain variation of the four measured points during the 3rd of December 2008, at section 121.2m are illustrated in figure 2.24c. At 07:00, the strain at point 2 increased first, and then at 08:00, 12:00 and 14:00, the points 3, 4 and 1, increased as well (Xia *et al.*, 2014).

Marques *et. al.* (2012) in cooperation with the Portuguese railway administration carried out a fatigue assessment of the Trezói metallic railway bridge (Beira Alta, Portugal), by installing strain gauges at critical locations of the bridge. It is a 126m long bridge with two inverted warren trusses of 5.68m height and it opened in 1956 (fig. 2.25). The monitoring survey of the bridge was important due to different traffic conditions since its design. Fifteen strain gauge sensors were installed at the cross section of the bridge's bars, which experience higher tensile stress (fig. 2.26) and during the monitoring period 8 freight trains and 16 passenger trains crossed the bridge. The results of the survey showed that the measured strains are lower than the damage calculated ones computed using the Eurocode standards (fig. 2.27) (Marques *et. al.*, 2012).

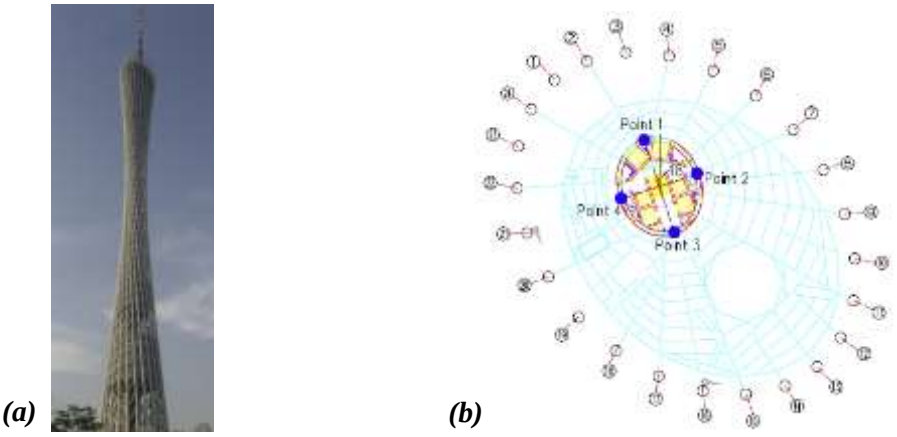

Figure 2.23: (a) Perspective view of Canton Tower; (b) Location of strain monitoring point at 121.2m section (Xia *et al.*, 2014)

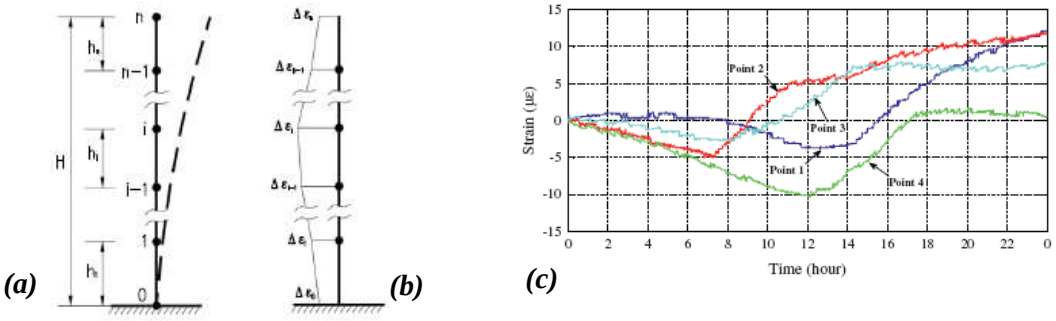

Figure 2.24: (a) Cantilever beam; (b) strain distribution element; (c) relative strain at section 121.2m on 3rd of December 2008 (Xia *et al.*, 2014)

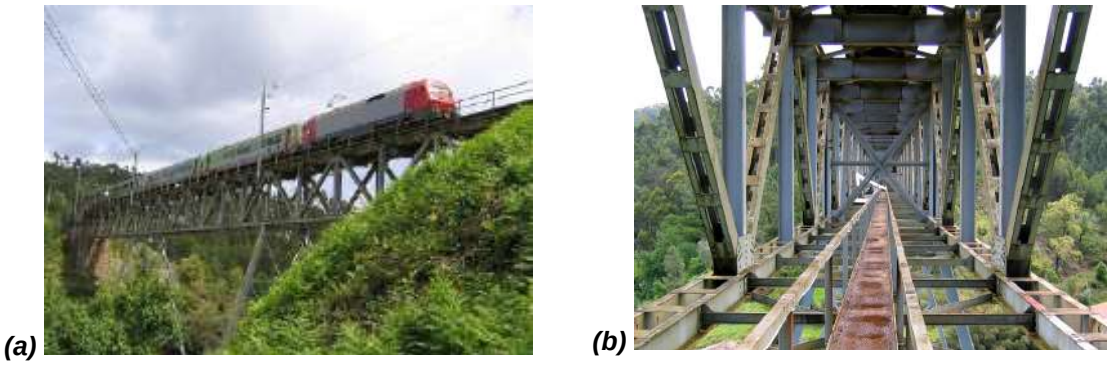

Figure 2.25: The Trozói Bridge: (a) global view; (b) view from the inside (Marques *et. al.*, 2012)

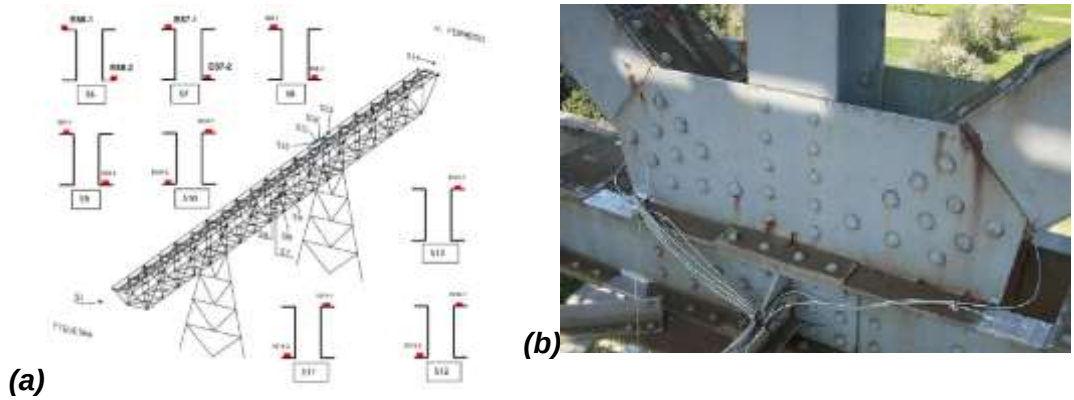

(a) (b)

Figure: 2.26: (a) Location of the 15 instrumented sections and corresponding distribution of the sensors; (b) Lower joint of the truss girder instrumented with strain sensors (Marques *et. al.*, 2012)

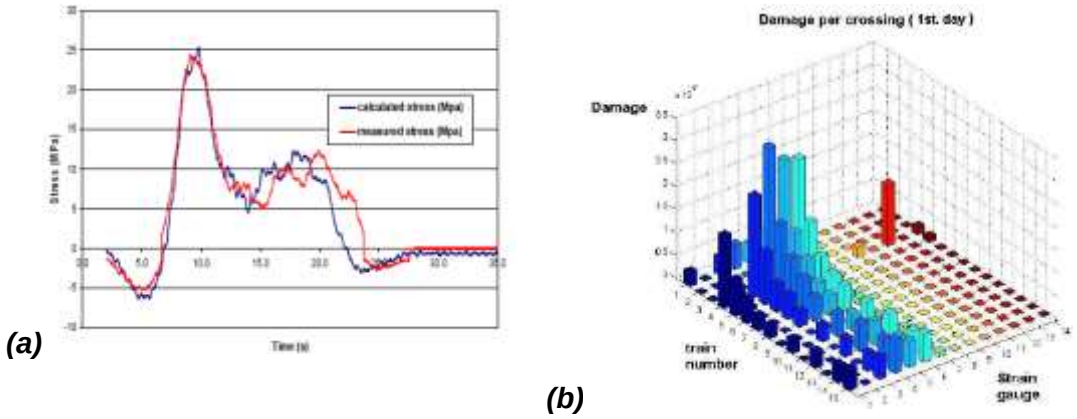

(a) (b)

Figure 2.27: a) comparison between measured and calculated stresses; b) damage calculated with the strain measured (Marques *et. al.*, 2012)

2.4.3.5 Summary

The long “life-time” of strain gauges and their broad use for the monitoring of different types of phenomena, proofs their adequacy as a cross-checking sensor. In the literature reviewed, it has been shown that they are also sufficient to monitor dynamic phenomena that any structure could experience. Their long and broad usage has also shown the importance of measuring strain, as it is a value capable of demonstrating satisfactory the condition of an element.

2.4.4 Concluding Remarks

The two monitoring methods presented are used for the experimental needs of this research. Terminology and glossary, along with background theory and example applications on structures for each technique demonstrate their efficiency and the potential to form a synchronised plan with the view to provide additional rehabilitation procedures.

2.5 Conclusion

The case study of Kapnikarea chapel has been the inaugural idea for defining a research gap on the structural health monitoring discipline and search and study in detail similar examples in the literature. This gap was specified on the cracking evolution problem, as it raises further questions.

Among the essential investigations, the analysis of potential damage and crack evolution is crucial to find any relationship between lack of stability and external damaging factors suffered by the building during time. Cracks and damages are only the manifestations of a building disease, and, as in medicine, a deep knowledge of its evolution is necessary to define the most efficient treatment. A crack that has shown a constant evolution in the past has a different importance than a crack that appeared during a traumatic event and then stabilized after a strengthening intervention. At present, the evolution of instability and cracking phenomena in a monument can be recorded by highly sophisticated systems, such as the electronic monitoring systems, which are capable of automatically detecting, with a certain periodicity or in continuous, even extremely small movements, far below the significance threshold for a building.

Hereafter, the offered monitoring strategy has proved its efficiency through the literature. The experimental background of the chosen monitoring means presented will be explained in thorough in Chapter 3. The reasoning behind each choice has been justified and discussed, as the correct design and proper use of monitoring systems is capable to control the evolution of pathological phenomena and provide a deep knowledge on the structural behaviour. The monitoring strategy is a core element as the diversity of structures' pathology, location, potential problems, or efficient strengthening intervention proposed programmes is relatively high.

CHAPTER 3

METHODOLOGY

3.1 Chapter Overview

This chapter gives a detailed overview of the methodologies and processes used in this thesis, encapsulated in a research framework. The Kapnikarea chapel located in Athens (Greece) is the main case study of this research project. The following sections present precise details and justifications of the approaches used.

3.2 Research Objective

This methodology aims to introduce a precise, cost efficient, non-destructive monitoring system, continuously applied to structural elements exposed to everyday vibrations, with the view to form an online data record, which in the future will be able to alter automatically an existing analytical structural model. The comparison and the synchronisation of monitoring means shows that monitoring arrangements may record and interpret potential differences during monitoring periods and present a robust conclusion for the current pathology of the monitored structural elements and/or structures. The definition and application of the appropriate timing and mitigation method is an added value for Building Information Modelling (BIM) and the retrofitting industry.

3.3 Experimental Development

3.3.1 Scaling Down

3.3.1.1 Background of the Approach

Small-scale models began to be used by builders and engineers for planning and structures' construction purposes. During the last decades, modelling of structures has been used to predict the deformations and strengths of the prototypes. The reliability of the results from a tested scaled model is a very important factor for the concluding results but it is very difficult to define. The factors affecting model accuracy include model material properties, fabrication accuracy, loading techniques, measurement methods, and the interpretation of the results (Harris & Sabnis, 1999). These factors need to be considered and analysed if the purpose of the experiment is to predict the performance of tested masonry specimens under dynamic loading. However, this project studies whether the applied precise monitoring techniques can provide us with information regarding the changes of shear strain, strain around the cracked areas and checks of the size effects[8] during monitoring. Therefore, two scaled-down size models are tested to check the two monitoring methods: five experiments of 1/17th size of a single-leaf masonry specimen and two of 1/5th size from the original wall of the chapel. The chosen scale of the specimens will be discussed in the following section.

3.3.1.2 Method Applied

The Chapel is comprised of three parts: the nave, the "oratory" and the exo-narthex (fig. App. I - 2). Based on the three surveys as will be discussed in chapter 3.4, the "oratory's" eastern side wall is chosen as the prototype wall to create the two sizes of the scaled-down models. Severe damp problems observed along the "oratory's" roof, which have been generated mainly by two cypresses, the existence of a well, a crack that has started propagating from the roof (fig. App. I - 10), the fact that the north door could not open during the underground construction period and the potential of the scaled-down dimensions of this wall to fit properly to both shaking tables (UCL's and University of Bristol's ones), have comprised the reasonings for choosing this wall (fig. 3.1).

[8] Size effect is a phenomenon related to the change usually an increase in strength when the specimen size is decreased (Harris & Sabnis, 1999).

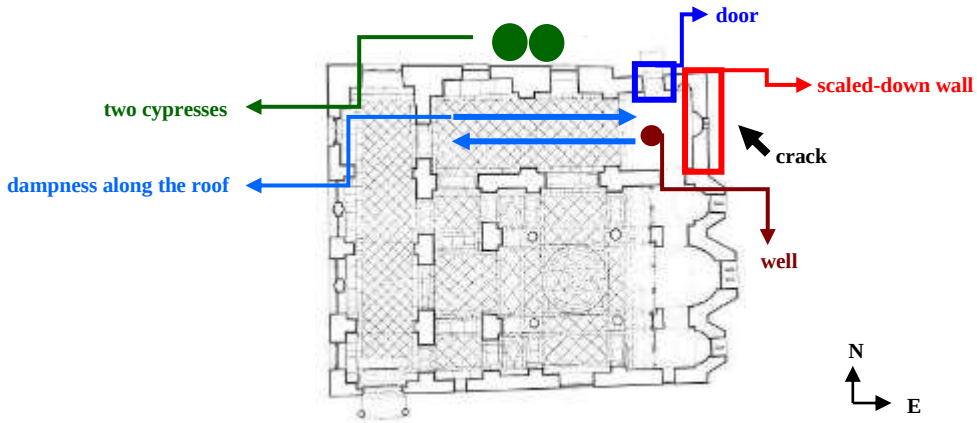

plan view of the entire chapel

scaled-down wall, door & **crack**

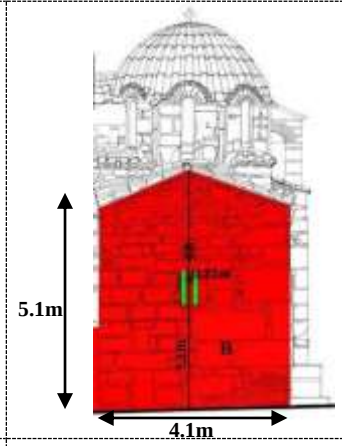

scaled-down wall (H:5.1m, W: 4.1m)

well

Figure 3.1: Representation of the reasonings for choosing this wall for the scaled-down purposes

The scale factors have resulted from the limitations of the dimensions of the small shaking table (254mm x 254mm), available within UCL, and the number of bricks available for the big scaled-down wall. Therefore, for keeping the resources manageable, the dimensions of the small specimen wall are 280mm high, 240mm long and 25mm deep (fig. 3.2 a), using a scaling factor of seventeen (17), and the big ones is 1044mm high, 856mm long and 208mm deep (fig. 3.2 b), using a scaling factor of 5 (≈ 4.7). Both model walls are built using the stretcher bond[9] brickwork for creating interlinking joints and at their end returns are added to concentrate the loading within the returns to avoid failure of the wall during shaking. Due to limitations posed by available methods for the experiments for the tested specimens, the depth for both scaled-down model walls has not followed the prototype's dimensions; just the depth of the bricks which have been used for building up the single-leaf walls. The point load

[9] A stretcher bond is the bond with all courses laid as stretchers and with the vertical joint of one course falling midway between the joints of the courses above and below.

of the roof is applied to the scaled-down wall using the suitable scaling factors (Krawinkler et al., 1978), as presented on the calculations in Appendix II. The prototype and both models are assumed to have the same material properties. Therefore, the uniformly distributed load applied to the small scaled-down wall is 11.2kg and to the big scale specimens the loading is 148kg (Appendix II). The loadings of the small wall are attached on a loading case made in UCL laboratories, which is glued at the top of the specimen. The loading on the big walls is placed to a similar stainless-steel loading case and with the use of additional steel robs the loading is fixed and secured. These rods are directly vertically drilled at the top of the wall and to the loading case, through the top bricks.

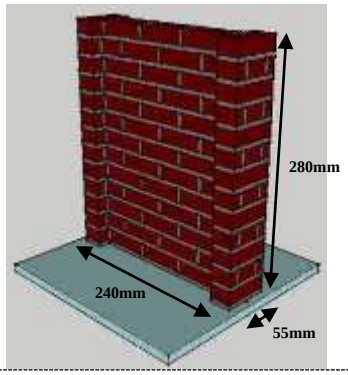

a | sketch of small specimen | small specimen

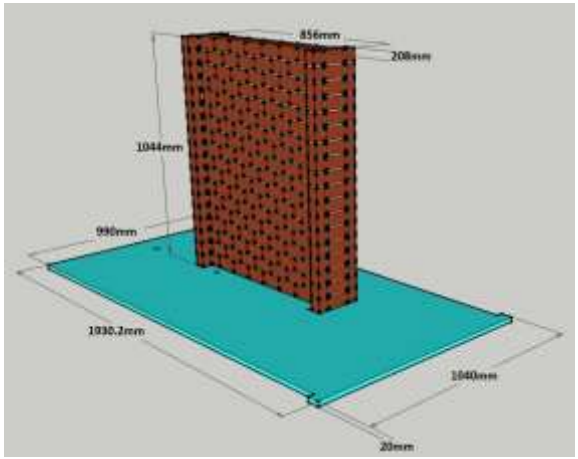

b | sketch of big specimen | big specimen

Figure 3.2: Tested small and big scaled-down walls

Therefore, eight experiments are carried out through the 12 months of the experimental period. Six experiments are performed at UCL's laboratories and two at the Earthquake and Large Structures Laboratory (EQUALS) at the University of Bristol. For the small scaled-down wall, two experiments are undertaken using brick type B (chapter 3.3.3.1) and mortar type I (chapter 3.3.3.1), actuated at X direction and

captured by the cameras positioned at zero (0°) degrees with respect to the specimen wall. For the purposes of the three tests on the small scaled-down wall the specimens are built using brick type A (chapter 3.3.3.1), mortar type I (chapter 3.3.3.1) and one of the two is plastered; one is actuated at the X direction and captured at zero (0°) degrees, the second one is actuated at the Z direction of motion and captured at zero (0°) degrees and the last one, from this group, is actuated at the X direction and captured at forty – five (45°) degrees, with respect to the specimen wall. The two tests performed on the large scaled-down wall are built with brick type C (chapter 3.3.3.1) and mortar type II (chapter 3.3.3.1), actuated at X direction and captured by the cameras at zero (0°) degrees with respect to the specimen walls. The last test (exp 2) is made using brick type C and mortar type II and it is tested to the concrete uniaxial compression machine for applying the static loading with the cameras capturing the specimen at zero (0°) degrees with respect to the specimen wall. Table 3.1 summarises the main characteristics of each of these experiments.

No. of Experiment	***Brick Type***	***Mortar Type***	***Direction of Motion***	***Degrees of Cameras capturing***	***Loading***	***Plastered***
1	A	I	X	0°	Dynamic	No
2	C	II	Y	0°	Static	No
3	B	I	X	0°	Dynamic	No
4	B	I	X	0°	Dynamic	No
5	A	I	X	45°	Dynamic	Yes
6	A	I	Z	0°	Dynamic	Yes
7	C	II	X	0°	Dynamic	No
8	C	II	X	0°	Dynamic	No

Table 3.1: Experimental schedule and their main characteristics

3.3.2 Monitoring

Two monitoring means are chosen for the continuous monitoring of a structural element, which are the method of close-range digital photogrammetry (CRDP) and the strain gauges.

3.3.2.1 Cameras

The photogrammetric monitoring method is applied to the model wall by taking pictures using four Redlake MASD, Inc. MegaPlus Camera, Model ES 1.0 cameras

(fig. 3.3 a) laboratory grade and two Nikon D700 (fig. 3.3 b) off the shelf professional / consumer grade Digital SLR cameras. All six cameras capture the wall's excitation on the shaking table. The pictures are processed and analysed using the Vision Measurement System (VMS). This method determines the movements of discrete targets points and the change in geometry between them to deliver 3D deflection and strain computations from discrete points.

The Redlake camera has a spatial resolution of one million pixels and an output channel data rate of 20 MHz, which gives a maximum frame rate of 30 frames per second (fps). The camera uses a global electronic shutter so that the complete image area is captured at the same instant rather than a rolling electronic shutter which would introduce motion artefacts. This electronic shutter is connected to a host computer through a dedicated digital interface card. The camera is capable of shutter speeds of 0.127 milliseconds. It operates continuously or on a triggered mode and it is suitable for both scientific and industrial imaging applications. The camera features a Charge Couple Device (CCD) sensor array, it has 1,008 (H) x 1,018 (V) light sensitive elements (pixels) and its active pixel area is 900 (microns) x 900 (microns).

The Nikon D700 camera is a single lens reflex digital camera (DSLR) that has 12.87 million pixels and it uses a colour sensor with a Bayer pattern (red, blue and green filters on adjacent pixels) from which a colour image is interpolated. The two cameras are synchronised with a Remote Shutter Release Cable.

VMS is an in-house software written in the Visual C++ language and operating under five functions:

1. The measurement of circular retro targets on multiple camera views that allow photogrammetric computations to calculate the positions and orientations of each camera and from those to estimate the 3D coordinates of unknown target locations at the instant the camera image is taken,
2. The photogrammetric adjustment of 2D measurements, which aims to target images on photographs, so that the most probable 3D object space coordinates of the targets can be determined,
3. The use of bundle adjustment to firstly calibrate the cameras during a setup process and subsequently to use the calibrated parameters to estimate the calibration of the cameras within the network,
4. By tracking the movement of targets (the 2D movements of imaged targets), image sequences of digital stills or AVI format video files can be processed,
5. Incorporate measured distances for scaling photogrammetric networks; and

6. The automatic process of calibration and measured networks.

a

b

Figure 3.3: (***a***) Redlake MASD, Inc. MegaPlus Camera, Model ES 1.0 camera and (***b***) Nikon D700

3.3.2.2 Strain Gauges

Vishay strain gauges are also installed on all the wall specimens to use a traditional method of strain change monitoring and their length is 50mm.

The Model P3 Strain Indicator and Recorder (fig. 3.4 a & b) is a portable, battery powered instrument used for recording strain gauge readings. It can record up to four gauges simultaneously and the data are streamed to a PC using the on-board USB interface.

The collected data will be plotted in Microsoft Excel 2016.

(***a***)

(b)

Figure 3.4: Model P3 Strain Indicator and Recorder

3.3.3 Experimental Set Up

3.3.3.1 Specimens

Three different types of bricks (fig. 3.5), Type A, B and C, are used for the undertaken experiments. Type A bricks are used for experiments 1, 5 and 6. These mini bricks are cleaned and re-used from an older project. Type B mini bricks are used for experiments 3 and 4. Type C large bricks are used for experiments 2, 7 and 8.

Two types of mortar are mixed and two types of targets and loading cases are installed on the model walls (Appendix III). The small model wall specimens have been built at University College London, the mortar is comprised of one part of cement, one part of lime and six parts of sand. This is the 1:1:6 mortar mix and it is a well-filled one with extra adhesion; it has a flexibility given by the lime and is balanced by the strength of the cement (BS EN 998-2). The mortar mix that is used for the big model wall specimens, which have been built at the University of Bristol, is a ready mixed brick laying mortar (by Wickes) created by just adding up water.

Both the three-different brick and two-different mortar types have no relationship to the original wall of the church which is used as the prototype pattern. The north-eastern wall of the church is defined as the prototype wall to present the background and the origin of the research idea.

Type A: 55.4x25.6x17mm	Type B: 51.83x25.31x16.76mm	Type C: 100x100x50mm

Figure 3.5: Three different types of bricks used

3.3.3.2 Acquisition

Both specimens, the small and large model walls, are tested on a small and a large shaking table, respectively. The small tests are undertaken at the University College London and the large ones at the University of Bristol. The small shaking table (fig. 3.7 a) is connected to an amplifier (fig. 3.7 b) and to a function/signal generator (fig. 3.7 c). A sine signal shaking motion (fig. 3.6) will be transferred from the generator to the amplifier and then to the small shaking table.

The small shaking table (254x254mm) (fig. 3.7 a) is an electrodynamic shaker, designed for exciting and studying the dynamic response characteristics of structures in the seismic frequency range. Its design has been optimised specifically for driving structures at their natural resonance frequencies, delivering maximum power to such resonant loads, with minimum total shaker weight and drive power. Its frequency range is 0-200Hz, the force rating for <0.1Hz is 133N peak and for 0.1-20Hz is 186N peak, the maximum stroke is 158mm pk-pk and the velocity is 762mm/s (Shaking Table Laboratory Manual).

The power amplifier (fig. 3.7 b) is designed to provide drive power to shakers. The particular model used consists of two heat sink mounted power modules, a circuit board containing input amplifiers, a current monitor amplifier and an output short-to-ground detector and relay (Shaking Table Laboratory Manual).

The TTi generator (fig. 3.7 c) can generate high quality sine, square and pulse waveforms between 0.1mHz and 10MHz. Triangle and ramp waveforms and multi-level square-waves can also be generated but with limitations as to the maximum useable frequencies (Shaking Table Laboratory Manual).

The large shaking table (3m x 3m) (fig. 3.8) can carry up to 15 tonnes and reach acceleration levels of up to about 5g with peak displacements of ±150mm, depending on the loading (Shaking Table Laboratory Manual).

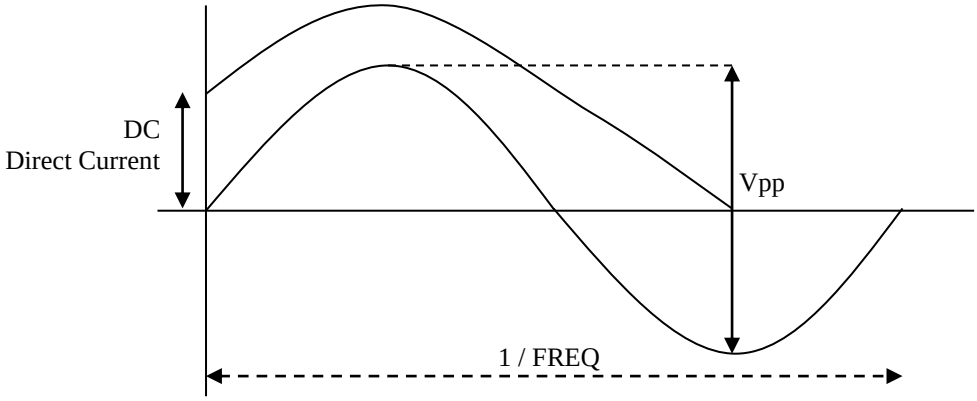

Figure 3.6: Shaking signal from the generator (Shaking Table Laboratory Manual)

(***a***) (***b***) (***c***)

Figure 3.7: (***a***) Small Shaking Table; (***b***) Amplifier; (***c***) Function/Signal Generator (Shaking Table Laboratory Manual)

Figure 3.8: Large Shaking Table (University of Bristol web page)

3.3.3.3 Set up

The experimental set up, for both the EQUALS (University of Bristol) and the Advanced Structures Laboratories (University College London – UCL), comprises of thirty-three pieces (table 3.2). Two shaking tables are used, on which the small and large model wall specimens are placed for testing. For both laboratories, two computers are used which are connected to four Redlake cameras and synchronised with a trigger (fig. 3.9 a). Two additional Nikon D700 cameras are synchronised with a shutter (fig. 3.9 b). Additionally, four headlights are turned on to provide extra light to the cameras. Lastly, one additional laptop is used connected to the data logger of the strain gauges, which was also displaying the timing above the tested specimens.

- UCL's laboratory

A tripod is placed opposite the tested specimens, where all six cameras are capturing the tested specimen. Each of the three legs of the tripod sits on anti-vibration pads (fig. 3.9 c). A Π – shape wooden frame (fig. 3.10) is attached to UCL's laboratory wall, where 28 control retro-reflected targets[10] are installed. Detailed pictures of all the apparatus pieces used in the UCL's laboratory are shown in figures 3.11 and 3.12.

Prior to the experimental phase, four accelerometers are installed at four different locations to check their performance; the first is at the top of the wooden frame (fig. 3.13), the second is at the bottom of the wooden frame (fig. 3.14), the third is on the floor (fig. 3.15), and the forth is on the anti-vibration pad (fig. 3.16) where the tripod sits on. The purpose of the installation of these four accelerometers was to perform a test for checking if the vibrations generated from the shaking table could affect the stability of the wooden frame attached to the wall, where the control reflected-targets were installed, and also to check if the tripod where the redlake and nikon cameras were installed could receive vibrations during the excitation of the shaking table. In case both acquisition, tripod and wooden frame, could receive vibration during the excitation of the shaking table, then these would affect the reliability of the collected pictures (data) and subsequently their analysis and the photogrammetric results. Therefore, the test ran for sixty seconds (60secs = 60000milliseconds), with an input excitation value to the shaking table of 7Vpp [Freq = 5Hz, EMF = 7Vpp (50Ω), DC = + 0.00mV, SYM = 50%]. The top band chart of figures 3.13-3.16 has double-checked the input excitation to the shaking table, the second one is the acceleration, which was recorded on the x axis, the third one on the y axis and the bottom one on the z axis. The test for the accelerometers installed at the top (fig. 3.13) and the bottom (fig.

[10] Photogrammetric control points are spaced around the project area to create a network of known points.

3.14) of the wooden frame consists of four steps. For each of these four steps, the author knocked the floor, the table and the wall using her hand and a materials' sieve (a random piece of equipment in UCL's laboratory). Therefore, 10 knocks made with the sieve on the floor (brown), 10 knocks with the sieve on the wall (blue), 10 knocks with the sieve on the table (pink) and 10 knocks on the wall by hand (purple). The knocks with the sieve on the floor (brown) show significant peaks for both accelerometers installed at the top (fig. 3.13) and the bottom (fig. 3.14) of the wooden frame, along all the axes, X, Y and Z. Similarly, high peaks, with slightly smaller ones along the Y axis only for the accelerometer installed at the top of the wooden frame, show the knocks made with the sieve on the table (pink) along X, Y and Z axes. However, the 10 knocks with the sieve on the wall (blue) and the 10 knocks on the wall by hand (purple) show very small values in all axes for both accelerometers, installed at the top and bottom of the wooden frame (fig. 3.13 & 3.14). Figures 3.15 and 3.16 show the test results of the accelerometers installed on the floor and on the anti-vibration pad, respectively. Comparing figure 3.15 with figure 3.16, there is a 0.14Vpp (= 0.2Vpp – 0.06Vpp) difference on X axis of the recorded acceleration, which means that the anti-vibration pad is a good tool for minimising the amount of vibration absorbed by the tripod when the vibration is travelling from the shaking table to the tripod through the floor. This is the reason why is decided to carry out all the experiments in the basement of UCL's laboratories rather than on the ground floor.

- EQUALS laboratory (University of Bristol)

Two tripods with three cameras attached to each other (fig. 3.17 – 3.19), are placed right opposite the tested specimen in the EQUALS laboratory. Each of the three legs of the tripods sits on anti-vibration pads (fig. 3.9 c). 50 control retro-reflected targets are installed at the back wall of the laboratory behind the tested specimens and on the protected rails around the shaking table. Detailed pictures of all the apparatus pieces used in the EQUALS's laboratory are shown in figures 3.17 – 3.19.


(***a***)

(***b***)

(***c***)

Figure 3.9: (***a***) Trigger; (***b***) Shutter; (***c***) Anti-Vibration Pad

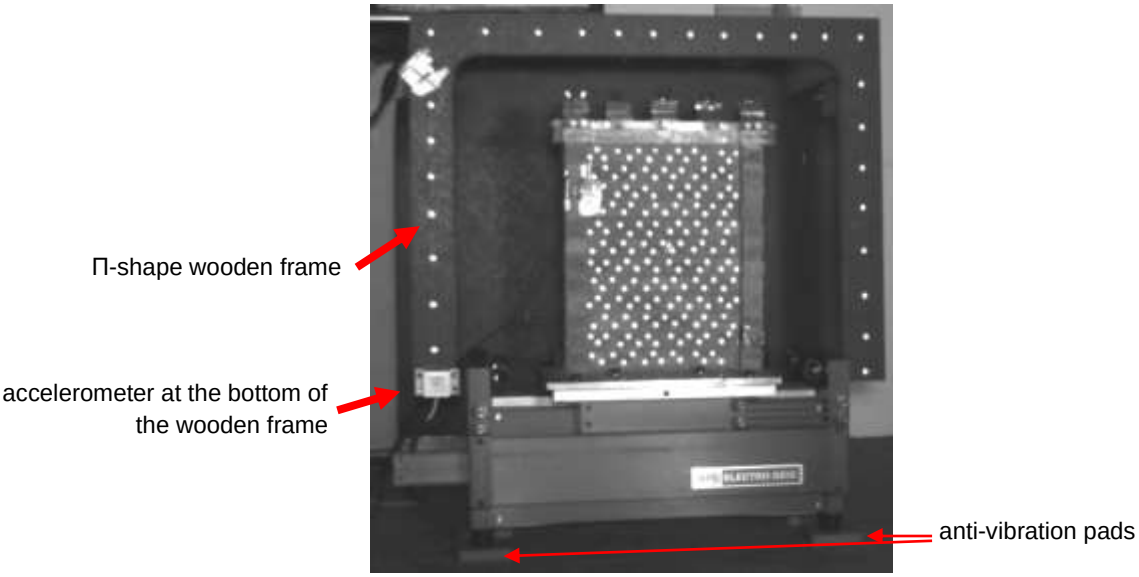

Figure 3.10: Π-shape wooden frame with 28 reflected targets installed, small shaking-table & small-scale wall specimen

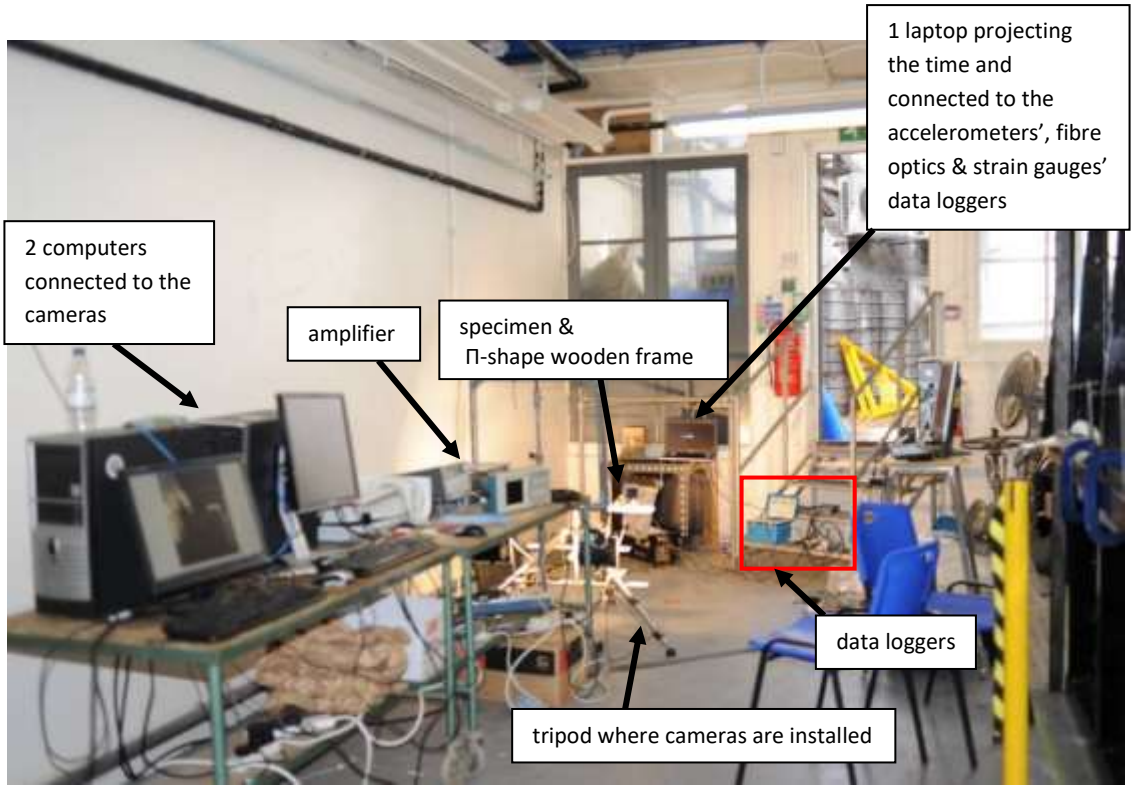

Figure 3.11: Equipment apparatus for the UCL based experiments

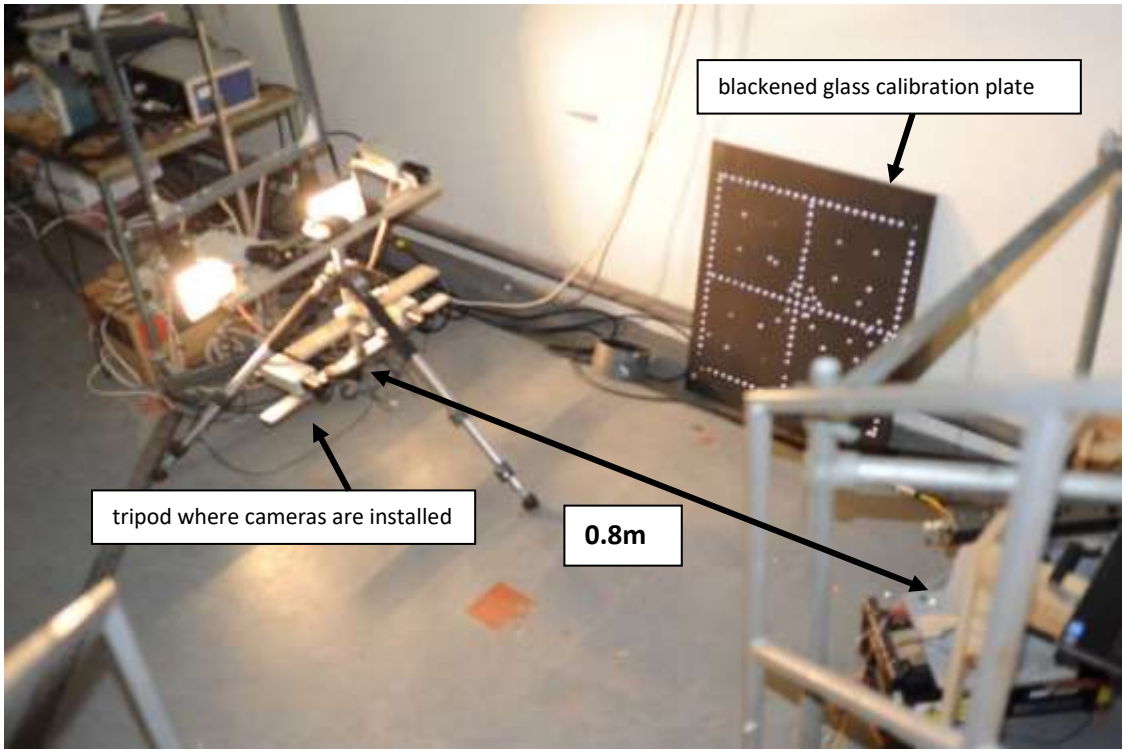

Figure 3.12: Headlights, 4 RedLake cameras and the blackened glass calibration plate

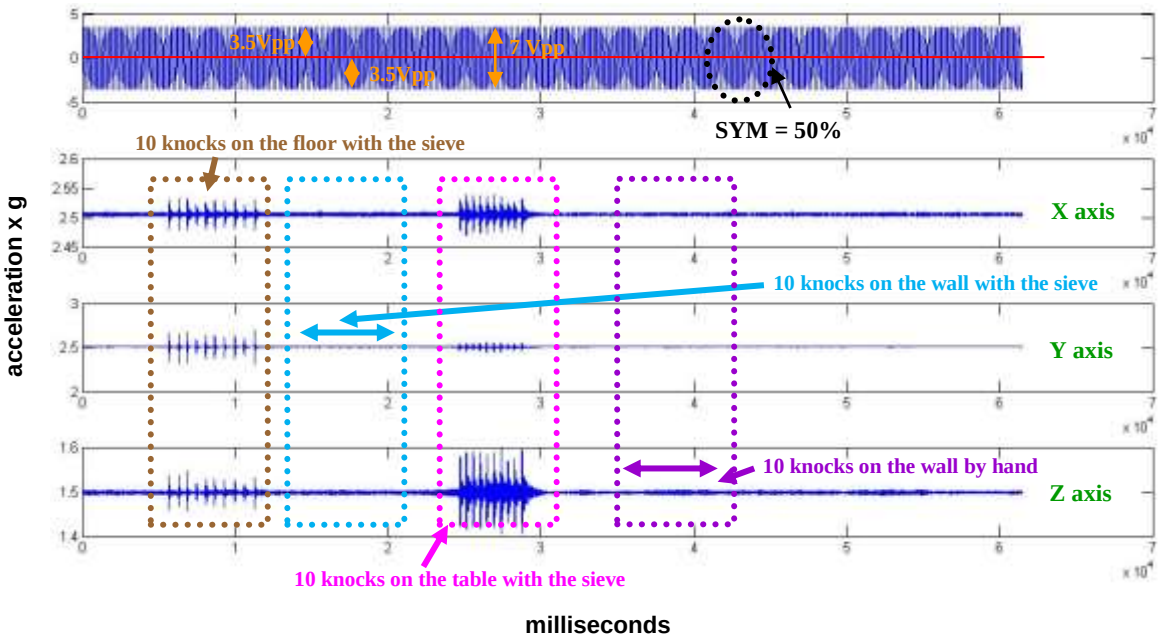

Figure 3.13: Accelerometer placed at the top of the wooden frame

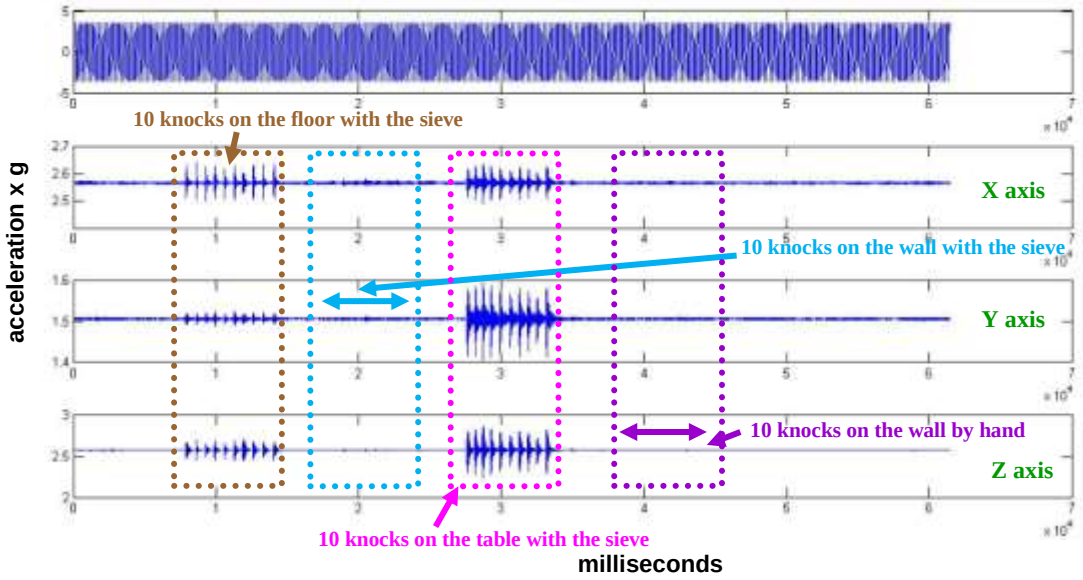

Figure 3.14: Accelerometer placed at the bottom of the wooden frame

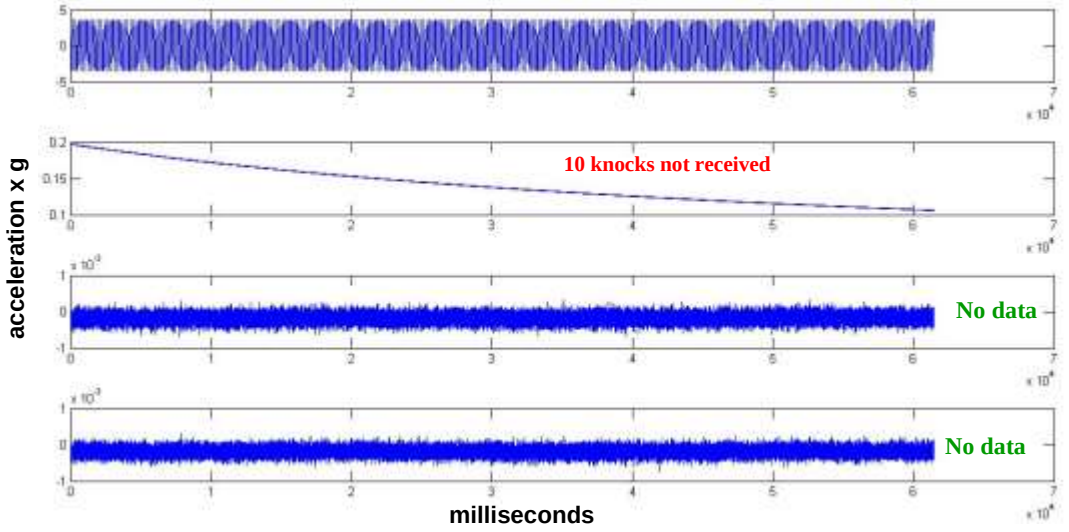

Figure 3.15: Accelerometer placed on the floor

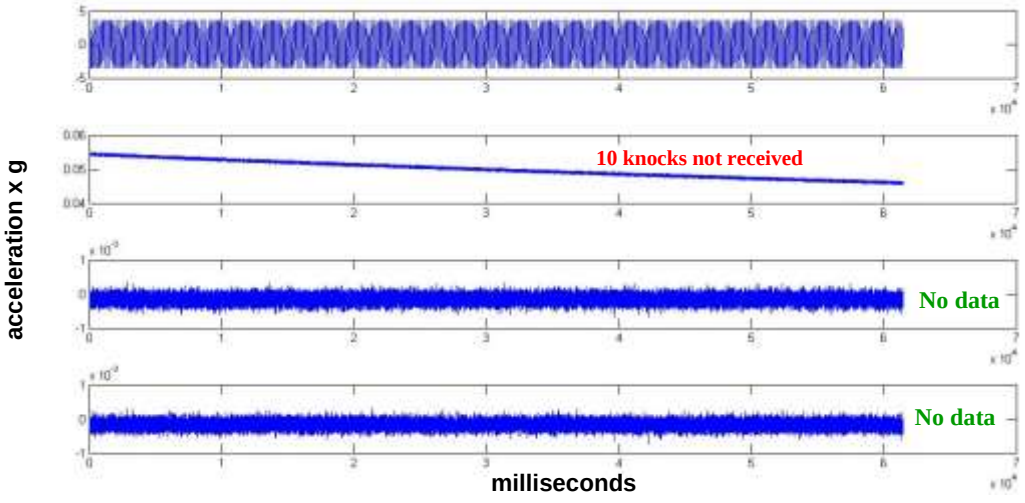

Figure 3.16: Accelerometer placed on the anti-vibration pad

		Number of pieces (adding up)	***Acquisition***
U C L		1	small shaking table
		2	amplifier
		3	function/signal generator
		4	Π – shape wooden frame
		6	2 accelerometers on the wooden frame
		8	2 accelerometers' Power Supply Interface
	B R I S T O L	9	1 tripod
		12	3 pieces of anti-vibration pad
		14	2 headlights
		16	2 Nikon cameras
		17	1 shutter
		21	4 redlake cameras
		23	2 computers for the redlake cameras
		24	1 trigger
		25	strain gauges
		26	strain Indicator and Recorder
		27	1 laptop
		28	1 tripod
		31	3 pieces of anti-vibration pad
		32	1 projector
		33	big shaking table

Table 3.2: List of all the acquisition

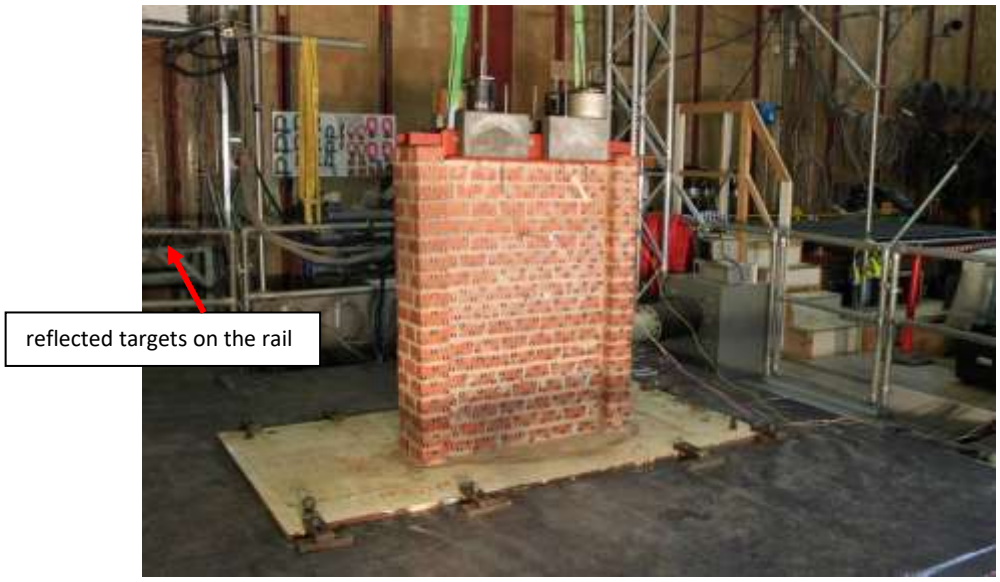

Figure 3.17: Large-wall specimen positioned on the large shaking table along with the loadings fixed at the top of the large wall with the use of the stainless-steel loading case and the appropriate steel rods, at the University of Bristol

Figure 3.18: Large-wall specimen positioned on the large shaking table along with the loadings; headlights, cameras and computers placed on a desk opposite to the shaking table, at the University of Bristol

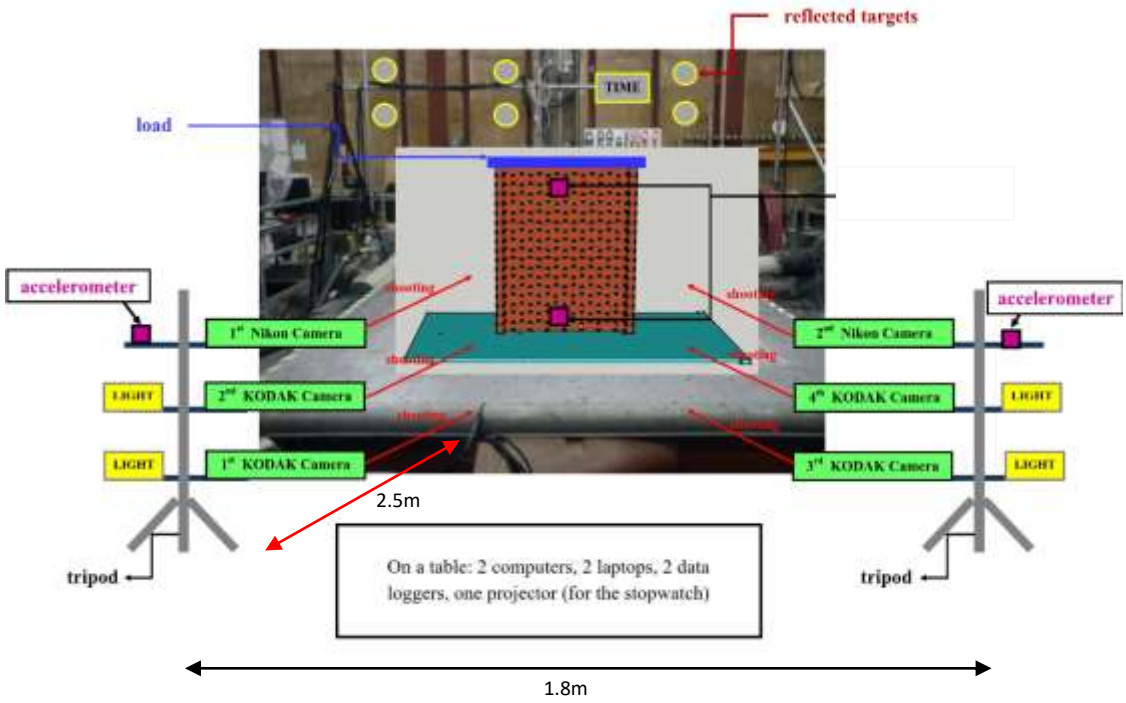

Figure 3.19: Sketch-up of the large-wall specimen positioned on the shaking table along with all the experimental pieces at the University of Bristol

3.3.4 Experimental Framework

3.3.4.1 Running an experiment

The experiment had a pre – and a post – experimental phase. During the pre – phase, the cameras are calibrated, by creating two projects in the VMS software a network one and an initial calibration one. To create the network project, ten images are taken using the Nikon D700 camera, capturing a blackened glass calibration plate (fig. 3.20) with 167 targets on it. Distances between these targets are measured with a vernier caliper, and these measurements are used to define scale during the processing of the network project[11]. The network project allows the calibration of the cameras by using target image measurements made from multiple views of the rigid calibration plate. Having provided the internal camera geometry for each camera, calibration parameters are estimated and can be used as starting values for all subsequent photogrammetric experimental tests (chapter 2.4.2.3). For the small-scale tests, calibrations were undertaken, using the 28 control points which are installed on the wooden frame (fig. 3.10) attached to the wall.

The glass plate (fig. 3.20) is also positioned in the space to provide more points and to ensure that the coordinates of the frame control points are consistent with the plate data. For these networks 8 convergent images are taken with each camera at different angles; at 0°, 90°, 180°, 270°, 30° turned both left and right and at 60° similarly turned both left and right (fig. 3.20). These data are processed in a bundle adjustment, the output of which provides an estimate of the control point coordinates and the internal calibration parameters for each camera. Cameras are then positioned at stable points to achieve a convergent network of the control frame and sample ready to be shaken for providing a sequence of images during the test. The pose of each camera could be readily computed from either the resection or from a network adjustment using coordinates of the frame control points as reference.

Once the network and the initial calibration file had been satisfactorily created, all the acquisition pieces are activated; the timing and the accelerometers recording through the laptop, the headlights, the four redlake cameras all synchronised through the tower pc and the trigger box and finally the shaking table through the amplifier. Prior to the run of each experiment, targets have been installed on the wall surface, and on

[11] Network project is a project created prior to the photogrammetric analysis of the collected pictures, where a network of control points along with their exact location/orientation/coordinates in space have been defined and act as reference line to the monitoring targets installed to the objects as illustrated on the collected images.

the bricks, following a triangle pattern, which is helpful during the stage of the displacements' and strains' computations as it will be discussed in the chapter 3.3.4.4.

During the experimental phase, the shaking table followed a sine (DC = +0 mV), symmetric (SYM = 50%) function of motion (fig. 3.6) and both the maximum amplitude and the frequency values inserted, started with the minimum shake and tuned up progressively until the point at which the shaking caused damage to the wall.

Once the shaking of the specimen has been completed, the post – phase starts running. During this phase, the raw image from the cameras and the collected data from the strain gauge/s are secured in the appropriate folders. Once all the phases are completed, additional pictures are taken of the tested specimens to provide a record of the tested specimens. Four software, including Microsoft Excel, are used for the computation and presentation of the data.

- VMS: Vision Measurement System software where pictures or videos can be analysed to obtain distance measurements of the installed targets on the shown objects.
- EngVis: Engineering Visualisation is a software which acts along with VMS, where the project files created in VMS, may be inserted in EngVis and by enabling the voronoi diagrams and the delaunay triagulations (Fortune S., 1995), the targets' triagulation system can be drawn. From these triangles, the strain computation can be obtained.
- Surfer: It is a visulisation software where results/data can be drawn using either grid or a map. In this research, for presenting the shear strain results, the contour map option has been enabled.

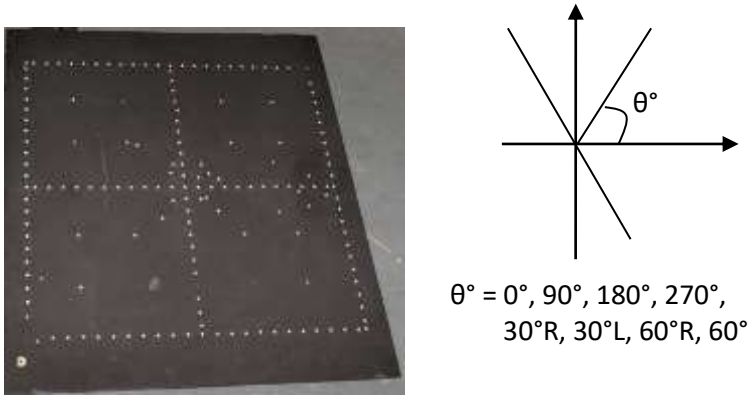

Figure 3.20: Glass plate and a network of images of it captured from different angles by one RedLake camera. These data provide a baseline calibration for each of the cameras and a quantification of the target image measurement capability.

3.3.4.2 Cameras' Calibrations (exp 1-8)

Prior to specimens' excitation, the photogrammetric system was calibrated to determine the geometrical optical properties of the cameras and their alignment to each other. To calibrate the cameras a set of images of a reference object is acquired. The reference object (fig. 3.20) used is a glass plate with 28 control points for the seven small-scale experiments and 186 control points for the large-scale experiment. During the calibration procedure, a network of images is acquired, target images are measured, and the data are processed in a self-calibrating bundle adjustment.

Another parameter is the variance factor (σ_0). This factor indicates if the magnitude of the error in the network agrees with the assumptions made for the control target coordinates and target image measurements. Therefore, it provides a measure of the overall parameters' quality of the network. When a factor of 1 is obtained, initial assumptions made about the precisions of the image measurements and the control targets agree with the network. Table 3.3 summarises the variance factor results from all the experiments. All the results are within acceptable ranges.

Of importance to the structural engineer using such a system is that the cameras are physically stable over long periods of time. To check the stability of the cameras of the stereo system over a period, calibrations are conducted at the start of every laboratory test prior to the specimens' excitation.

Experiment no.	***Unit weight estimate (sigma zero, σ_0)***
exp 1	1.00
exp 2	1.00
exp 3	1.00
exp 4	1.00
exp 5	1.00
exp 6	1.00
exp 7 & 8	0.97

Table 3.3: Calibration files sigma zero results

3.3.4.3 Data Processing

From the sets of the synchronised Redlake and Nikon cameras, the pictures which show the maximum movements are chosen and are classified to groups called “epochs”, based on the timing synchronisation. These pictures of the maximum movements are the pictures where the crack propagations occur. Thus, this is the reason for choosing them and based on this choice each experiment is comprised of different number of “epochs”. Processing the images requires the setting up of five files in the VMS software: the target file (.tar), the camera calibration file (.cal), the photo orientation file (.pho), the image measurement file (.sur) and the image file, before starting the analysis of the images.

The photo orientation and image files are created automatically while setting up the project file in the VMS software. The target file contains the coordinates, standard deviations and the identification of the control targets. The control targets define the datum and they are denoted by a flag of 7 in the target file. Their ID numbers for the UCL based projects are 1000 to 1028. All other reflective targets are located on the specimen or moving parts of the experimental structure and are flagged with a 0 to denote unknown points and numbered from 100 to 950, with intervals. For the Bristol based projects, the control targets are numbered from 1000 to 1050 and similarly flagged to 7, and the reflected targets on the wall are flagged with a 0 and they are numbered from 100 to 860, similarly with intervals. The survey measurement (.sur) file contains precisely measured distances between the control points made with vernier calipers. These data improve the control point precision and to provide traceability to the metre; the spacing between all the control points is approximately 45mm.

3.3.4.4 Data Analysis

Once all the required files have been processed in the VMS environment, initial orientations for all the photographs in each “epoch” are computed. An updated orientation is followed with the use of resection and, consequently, intersection and bundle adjustment are processed. The sigma zero is within an acceptable range (<=1), once the targets’ colour is green, which translates to good quality measurements. During the analysis, some of the targets can be yellow, which means that the measurement quality is ok, some can be white which is the colour for the unknown targets; and red is the colour for the rejected ones. The coordinate differences between estimated 3D target coordinates from one epoch to the next allow the computation and display of movement vectors and ultimately the computation of

strain. A check on the validity of the computed vectors can be made by verifying the level of movement observed between physically stable control points. Once the described process, has been successfully completed, a sequence file is created with the anticipated data. These data have detected the movement of the targets and are inserted into the EngVis environment. This software combines all the measurements from different “epochs” and can display the target movement in any stage of the experiment. However, the reason for using EngVis is to generate the triangulation system (fig. 3.22), which allows the centroid of any three reflected targets to be determined.

The images which capture the shaking of the model wall are selected and the $x-y$ coordinates of their reflective targets are measured by applying the standard photogrammetric technique of bundle adjustment (chapter 2.4.2.3). From the measured displacements, the strains are calculated based on the basic strain theory developed by Bassett (Lee *et. al.*, 2006) (chapter 2.4.2.4). The reason for choosing this method is the successful outcome of the computed shear strains in Lee *et. al.*’s project.

A procedure for analysing the coordinated system for the targets of the wall from a “before” and “after” epoch is used which was developed by Kwok *et al.*, 2001. Epochs are created based on the number of images used for the analytical process. All measurements within VMS software are in centimetres. Within the EngVis software and once the triangulation file (fig. 3.22) has been created, calculations are carried out on each triangle to compute the strains. The corners of each triangle are defined as points 1, 2 and 3. The triangles 123 are distorted to triangles 1’2’3’, with the lines moving from 12 to 1’2’, 23 to 2’3’ and 31 to 3’1’, respectively (fig. 3.21). To compute the strains of the lines ε_{12}, ε_{23} and ε_{31}, the Mohr circle method is used (Appendix IV).

By combining the triangulation system generated from EngVis along with the spatial measurements from VMS and the equations derived from the Mohr Circle (Appendix IV), the shear strain of the cracked locations is determined.

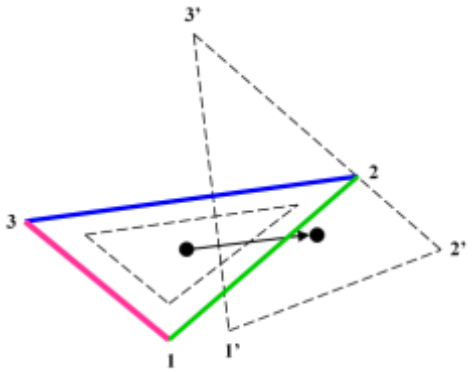

Figure 3.21: distorted triangles

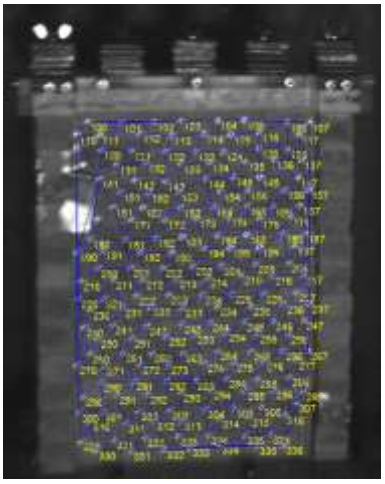

Figure 3.22: triangulation system of exp 1

Therefore, the strain is defined as the ratio of the change in length over the original length in the direction of the applied force. In this study, the strain computed from one epoch to the next one, for each point, is defined by equation 3.1. Similar strains are the recorded ones by the strain gauges. Additional step of the photogrammetric results is the computation of shear strains (eq. 3.2), with the use of the Mohr circle.

$\varepsilon = l_{12} - l_{1'2'} / l_{12}$ where 1 is the first point and 2 is the second point (3.1)

$\varepsilon_v = \varepsilon_1 + \varepsilon_3 / 2$ where ε_1 and ε_3 are the shear strain along the x axis of the circle (3.2)

Consequently, the photogrammetric workflow for all the experiments is outlined on the following points.

Setup

1. selection of camera positions and distances from object, camera focus, retro-target illumination and image quality
2. camera calibration and establishment of control points using calibration object and a VMS network project
3. creation of initial target [.tar], photo orientation [.pho], inter-target distance [.sur] and camera calibration [.cal] files, using resection and intersection based on nominal camera calibration [pixel count, pixel size and lens focal length]

4. bundle adjustment to give least squares best estimates of the above and to check that the photogrammetric data are OK [target coordinate precisions, residuals on inter target distances, variance factor and calibration stability]

Processing an image sequence

1. Capturing synchronised image sequences, using the above retro-target image settings
2. Creation of a VMS sequence project using the output .tar, .pho, .sur and .cal files from the setup process
3. Estimations of the camera pose in the experiments using resection from the control points
4. Computation of the initial XYZ target coordinates on the specimen using interactive target image identification with target centroiding image measurement followed by intersection from the first image set in the sequence which gives output the .tar, .pho, .obs and log files for the first image set
5. Checking the computation, particularly image measurement residuals displayed graphically to check that the solution is OK and does not have target mis-identification or measurement errors [some targets are partially hidden, or next to highly reflective strain gauge surfaces]
6. Stepping forward through the image sequence repeating the above two steps to produce output files for each set of synchronised frames in the sequence.

Visualising results

1. Loading the VMS sequence project into EngVis
2. Create the triangulation within the EngVis environment
3. Having created the triangles, the .evs file needs to be exported where all the displacement and plane strain values have been saved
4. Use of calculations (App. IV) along with the triangulation file for the shear strain computations.

3.3.5 Concluding Remarks

The monitoring of the tested specimens will be carried out by applying the methods of close range digital photogrammetry (CRDP) and strain gauges. Deformation which is caused by yield and not by a chemical reaction, is primarily measured by displacement, as most of the parameters i.e. shear stress, strain. Displacement will be used to monitor the masonry specimens that will be cracked or potentially cracked. The running of the eight experiments will prove the efficiency of the proposed monitoring strategy and the importance of cross-checking the performance of the monitoring methods with each other.

3.4 Surveys to the Chapel

3.4.1 Overview

Three onsite surveys of the chapel were carried out by the author, one in July 2008, the second one in November 2009 and the last one in September 2011. Their purpose was to address and highlight reasoning for the importance of continuous, simple and cost-effective monitoring.

3.4.2 2008

The monitoring purposes of this survey were to create a new set of records for the site plan of the chapel and the measurement of a crack's in plane dimensions using photogrammetry. It was carried out by the author. The surface levelling points around the chapel were monitored using a total station machine, TOPCON 700, a prism and a GPS and with the use of TECS – a software provided by TOPCON Corporation – and AutoCAD 2002, the new site plan was produced (fig. App. I – 6). This new site plan can be used as a reference sketch.

Cracks might change shape i.e. by water which is turned to ice during winter and stagnates in their cavity. Therefore, the purpose was to monitor cracks and record their length (Y direction) and width (X direction). A simple digital camera, CASIO Z50, was also used. Four major cracks were detected from the survey of the chapel (fig. App. I – 7 – 10). However, due to technical issues only Crack 2 (fig. App. I – 8) was measured. Coordinates (fig. App. I – 11) all along Crack 2 were measured and

determined using the non-commercial VMS 7.6 (2003) software[12]. The length of the crack was determined to be 0.3526m, and its width is 0.0072m (Metheniti, 2008). Most of the cracks on the inner walls of the chapel should also be detected and monitored for mitigating the paintings inside the chapel.

3.4.3 2009

The structural assessment of the chapel was set as an important activity for two main reasons: the definition of the weak points of the structure and their performance under dynamic loading scenarios and the identification of the structure's fundamental frequencies at the ground and at the dome, generated mainly by the passing tube trains.

Therefore, the field survey was carried out by the author and the Seismological Laboratory, Department of Geophysics – Geothermics, Faculty of Geology & Geoenvironment, National & Kapodistrian University of Athens. The acquisition equipment was comprised by a digital data-logger of REFTEK-72A[13] type, connected to 3 component Lennartz sensors of 1Hz, GPS for timing and a pc. Measurements were performed simultaneously in the vertical direction at 3 or 4 levels, ground (yard and interior), windows, roof and domes, to obtain common noise conditions, which would be efficiently removed when applying ratios between levels. A total of 87 measurements (fig. App. I – 12) were performed on ground and on structure. Data were processed by applying HVSR[14] method (Nakamura, 1989, 1999), using the GEOPSY[15] software. The peak frequencies (f_n) were calculated for each measurement point. The predominant frequencies range between 3-11 Hz (Metheniti *et al.*, 2010).

[12] VMS is the Vision Measurement System software where pictures or videos can be analysed to obtain distance measurements of the installed targets on the shown objects.

[13] The REF TEK is a portable seismic recorder consisted of three units, the data acquisition system (DAS), the hard disk recording subsystem (DAS) and the GPS.

[14] The method used for the numerical simulation of the recorded microtremor is the Horizontal to Vertical Spectral Ratio (HVSR) method, which is able to compute the fundamental frequency of the recorded position.

[15] GEOPSY software has tools for processing ambient vibration recordings.

3.4.4 2011

Based on the previous surveys, the purpose of this one, was to create a 3D model of the chapel as close as possible to reality, with the best rendering fit of the i.e. domes, vaults and other complex architectural elements of the structure, in order to simulate a real scenario in a structural analysis software environment; the prediction of the current pathology of the structure exposed to the everyday vibrations generated by the passing tube trains and the effects that the 10mm vertical settlement might had resulted to the structure.

Therefore, for creating a detailed 3D model and the geometrical documentation of the Kapnikarea Chapel, the laser scanning of the monument was conducted by the author and the Laboratory of Photogrammetry, Department of Photography, School of Rural & Surveying Engineering, National Technical University of Athens. For the collection of the raw data, the acquisition used was a Leica Scanstation2 terrestrial laser scanner, a TOPCON GPT 3003 series total station and a Canon DS M III (DSLR) camera with a calibrated 24mm lens. Cyclone v.7.0 by Leica, Geomagic Studio v.10.0 and Image Master by Topcon software were used for elaborating the raw data and produce the 3D model of the Kapnikarea Chapel (fig. App. I – 13). This model may be used as a reference point, as it is the first one being created for this structure. Finally, a 3D model of the monument in structural analysis software was created but not analysed, due to the narrowing down of the research question and time constraints (Metheniti *et al.*, 2011).

3.4.5 Concluding Remarks

The measure of displacements is critical for numerical and experimental studies in structural dynamics, especially for the displacement-based approach used for the seismic design of structures. Apart from the traditional sensors, i.e. accelerometers, cameras can track the dynamic displacement of selected points on the structures. A large-scale experiment has been undertaken which was monitored with nine infrared (NIR) cameras at the ENEA Casaccia Research Centre (fig. App. I – 14) under the PERPETUATE project. The test was undertaken on a masonry wall reinforced with external bonded composites (Lagomarsino, 2010). A similar approach is thought to have been followed in the Kapnikarea chapel to measure the recurrence of a potential settlement, by creating a system of cameras which either surrounding the monument or using the CCTV in the area. However, by following this approach, the research had to overcome three core limitations: the preparation of such a system in the laboratory

needed a larger team; there were timing constraints; and additional funding was needed. This research framework could only follow the path of narrowing down the initial question; therefore, having made conclusions based on the three surveys of, 2008, 2009 and 2011, the author produced the outlined research framework for assessing the cracked parts of a structure in similar conditions to those of the Kapnikarea chapel.

3.5 Conclusions

This chapter described the origin of the proposed research framework and the proposed experimental set up. Both the theoretical and the applied research objectives were defined based on the three site surveys of the monumental structure; the Kapnikarea church. Chapter 4 is the diagnostical procedure by presenting all the experimental and analytical tools applied to the two preliminary experiments.

CHAPTER 4

DIAGNOSIS

4.1 Chapter Overview

This chapter gives results and discussion of the two preliminary experiments which form the future experiments sequence based on the diagnosis of the first two ones. Experiment 1 is carried out on a small-scale single-leaf masonry wall tested under dynamic loading on a small shaking table and Experiment 2 is carried out on a small piece created along with the large-scale wall specimens using large-scale bricks, tested under uniaxial loading, using the laboratory's compression machine.

4.2 Preliminary Experiments

4.2.1 Overview

Tables 4.1 summarises the properties of the masonry specimens used for the purposes of experiment 1 and 2, their experimental assumptions, inputs and outputs. Experiments 1 and 2 cannot be compared due to their input differences, however, will be used as a reference line for the research purposes of this project.

	duration (sec)	*type of shaking table / compressor*	*no. of cameras*	*no. of targets*	*no. of images / camera*
exp 1	7.623	small shaking table	3	180 (small ones)	200
exp 2	148	compressor	2	167 (small ones) 30 (large ones)	20
	SG's location			*brick type*	*mortar type*
exp 1	N/A			A	I
exp 2	2nd horizontal mortar joint			C	II
	Vpp	*Hz*	*applied load/pressure*	*direction of excitation*	*direction of failure*
exp 1	15	5	11.2kg	X axis	in plane
exp 2	N/A	N/A	429MPa	Y axis	horizontal & vertical

Table 4.1: exp 1 & 2 → characteristics, assumptions, inputs & outputs

4.2.2 Dynamic Experiment (exp 1)

The purpose of this test, which adopts only the physical characteristics of the church's North-eastern wall, is to monitor the initiation and propagation of a potential crack with the use of non-destructive monitoring means.

During the experimental phase, the amplifier is set to 15 Volt and 5 Hz resulting to actuation of the connected shaking table. The shaking follows a sine (DC = +0 mV), symmetric (SYM = 50%) function of motion (fig. 3.6), which starts with the minimum value and it is tuned up (frequency) progressively until the point at which the shaking causes damage to the wall. It is an interactively outcome, by gradually increasing the frequency till damage is created to the wall. The tuned-up method is applied, as the initial low frequency actuations are not able to create damage to the single-leaf masonry specimen. The purpose of the specimen's monitoring during the test is to check the behaviour of the wall, which is loaded with 11.2kg (App. II) at its top. The monitoring is carried out with two sets (four) of synchronised Redlake cameras activated for 7.284 seconds (200 pictures/camera; 1000ms $\rightarrow$ 10frames/sec).

Once the experiment has been completed, the post test phase starts running. During this phase, the image data from the cameras are secured in the appropriate folders. However, the limited capturing of the cameras' – i.e. limited frames – is not able to monitor the tested damaged wall specimen.

On the first experiment four Redlake cameras are used, positioned at a 0.85m distance from the measured mini wall. Three of the four cameras remained synchronised during the test, collecting two hundred images per camera. The analysis of the photogrammetric results is comprised of fifteen images, five from each camera. These fifteen images, one from each camera of the three synchronised cameras, are sorted into individual timestamps each termed an "epoch" within the VMS software, based on the timing synchronisation. Therefore, the five stages of the experiment (fig. 4.1) comprised of five "epochs".

These five epochs were chosen on the basis that the wall damaged after the moment that the cameras were shooting. The computers' memory disc limited the amount of the collected photogrammetric data. Therefore, the wall cracked and then fell of the shaking table without being recorded by the cameras. The cameras stopped shooting 1-2 seconds prior to the damage and progressively to the failure of the wall-specimen. Diagram 4.1 presents the sequence in accordance to the time, that the wall followed during experiment 1. The cameras started recording at 17:47:16.417 (hr:min:sec:millisecond) and stopped at 17:47:23.701, having collected 200 pictures per

camera. Therefore, it was decided to choose 4 timings (diagram 4.1 & fig. 4.1) before the end of recording and 1 sec prior to the 4 timings, which will act as the reference timing, where no damage will be shown on the plotted graphs of the computed shear strains as obtained by the monitored tested wall-specimen. Also, the 4 timings were chosen on the basis that on these timings the reflected targets are well visible by the monitoring cameras. Clear reflected targets on the pictures help through their analysis in the VMS environment. Similar background thinking has been followed for choosing the epochs to the rest experiments. On figure 4.1a is illustrated the specimen in epoch 1 as captured at 17:47:22.101. On figure 4.1b is illustrated the specimen in epoch 2 as captured at 17:47:23.385. On figure 4.1c is illustrated the specimen in epoch 3 as captured at 17:47:23.497. On figure 4.1d is illustrated the specimen in epoch 4 as captured at 17:47:23.583. And lastly, on figure 4.1e is illustrated the specimen in epoch 5 as captured at 17:47:23.664.

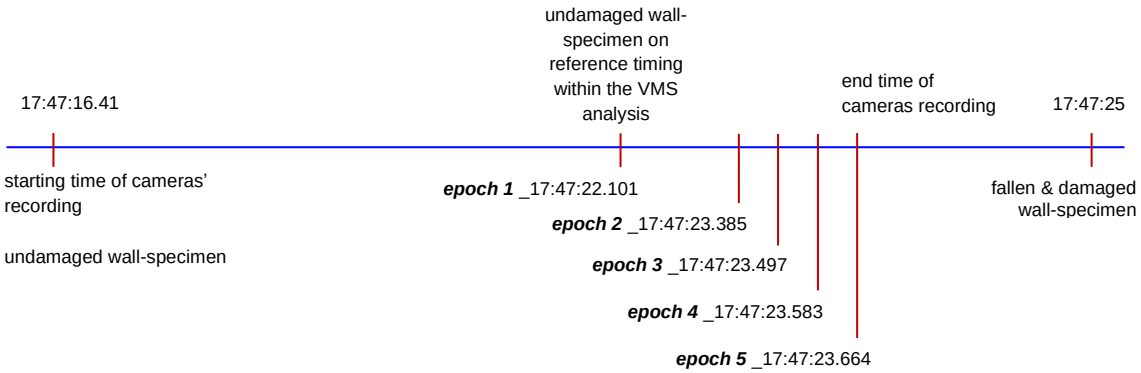

Diagram 4.1: cameras' recording timings for experiment 1

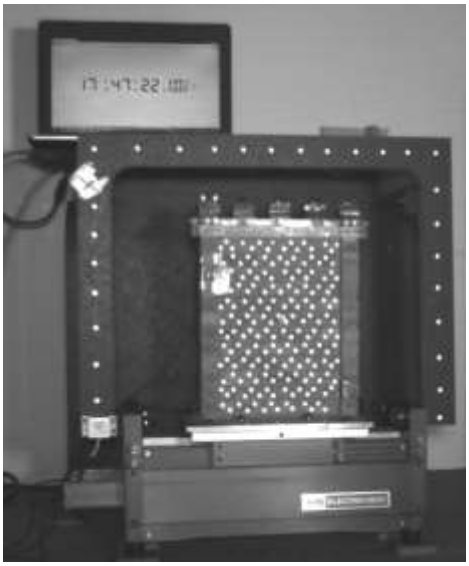

a

17:47:22.101 (epoch 1)

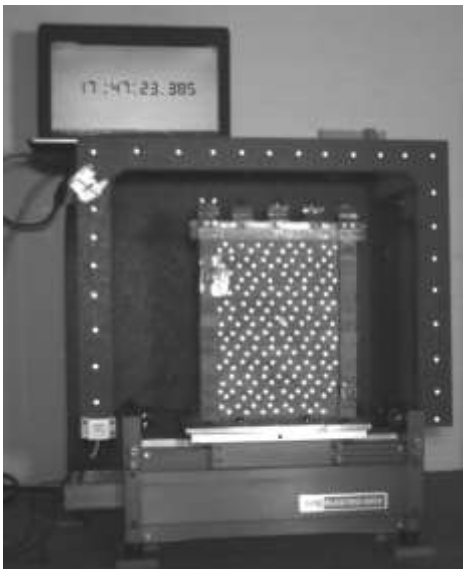

b

17:47:23.385 (epoch 2)

c

17:47:23.497 (epoch 3)

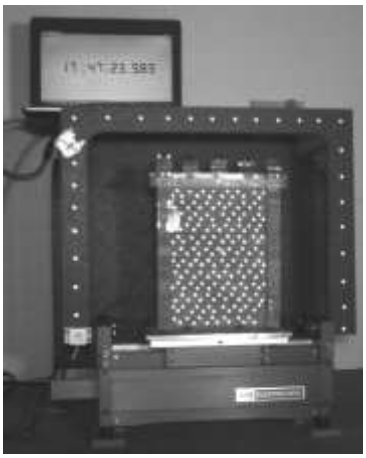

d

17:47:23.583 (epoch 4)

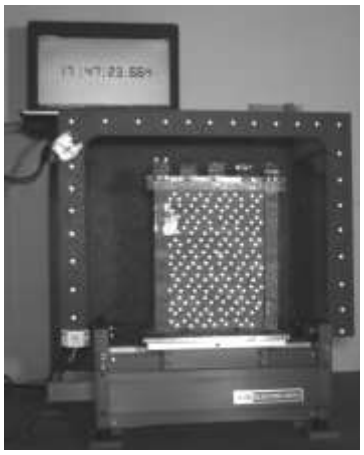

e

17:47:23.664 (epoch 5)

Figure 4.1: images' sequences capturing the actuated tested wall – exp 1

Twenty-eight control points are installed on the Π-shape frame attached to the wall and one-hundred eighty reflected targets on the face of the specimen which look the three cameras (fig. 4.1). Once the project has been set up on the VMS software and the targets have been inserted, observations are created for both the control and the free targets (fig. 4.2). Once the required files have been processed in the VMS environment, data showing the movement of the targets are produced which are inserted further into the EngVis software. This software combines all the measurements from different "epochs" and can display the target movement in any stage of the experiment. As mentioned previously, the reason for using EngVis is to generate the triangulation system (fig. 3.22), which allows the centroid of any three retro-reflected targets to be determined.

From the fifteen images, which captured the shaking of the model wall, the $x - y - z$ coordinates of the retro-reflective targets are measured. The standard photogrammetric technique of bundle adjustment is employed. The internal geometry (i.e. focal length, principal distance, etc.) of each camera is not considered during the analysis, and the coordinates are measured by assuming the use of unknown cameras. From the measured displacements, the strains are calculated based on the basic strain theory (Lee *et. al.*, 2006). All the displacements are measured in centimetres within the VMS environment, and these triangles are used as the basis for the strain computation.

Figure 4.2a shows the numbered reflected targets (targets ID) on the specimen (green numbers) and on the wooden frame attached to the wall (blue numbers – control points) and the three cameras (green cones). Figure 4.2b is the same as figure 4.2a along with the observations from the cameras. Figure 4.2c is similarly the same as figure 4.2a, but on 3D space. Figure 4.2d shows the three pictures of the specimen as captured by the three cameras in the VMS software.

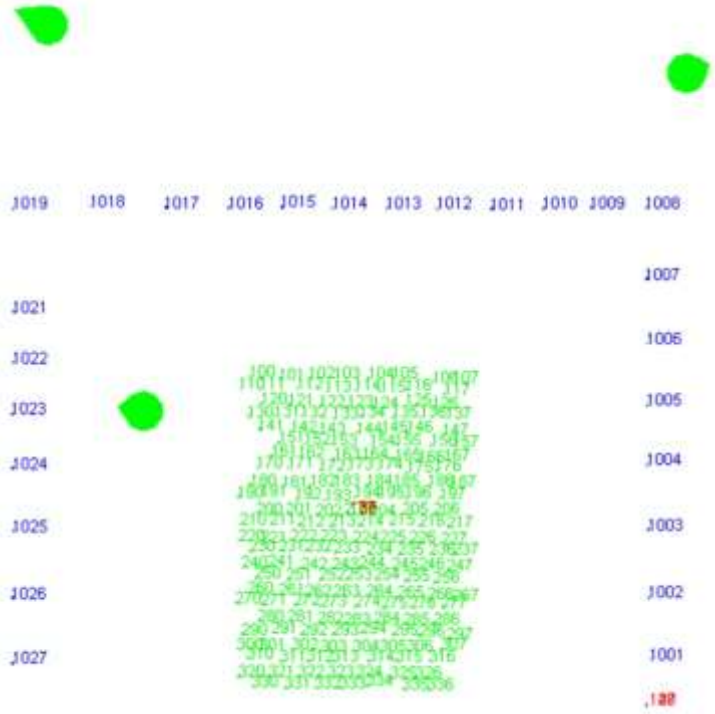

a

object view with target IDs and cameras in 2D

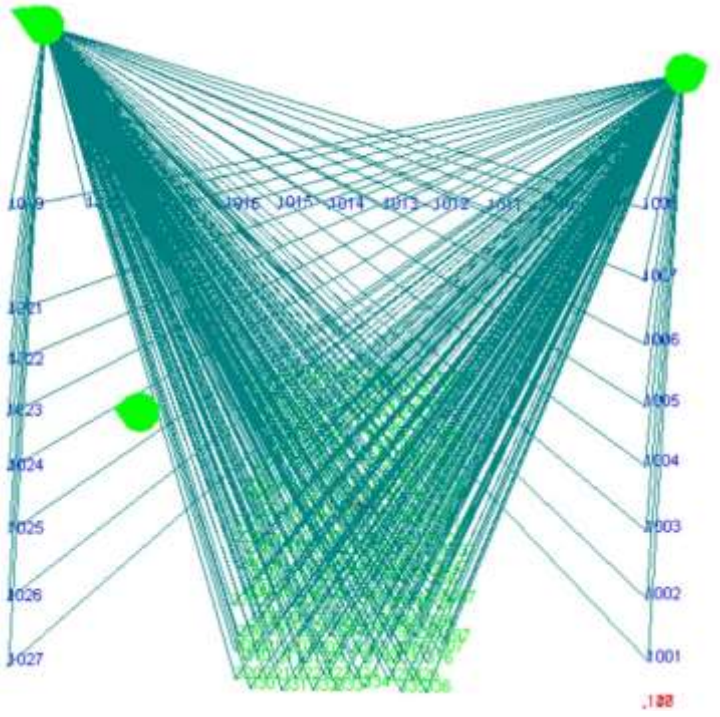

b

object view with observations

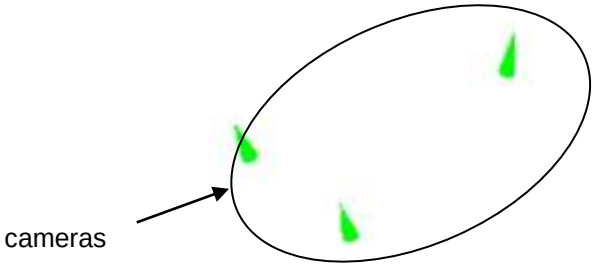

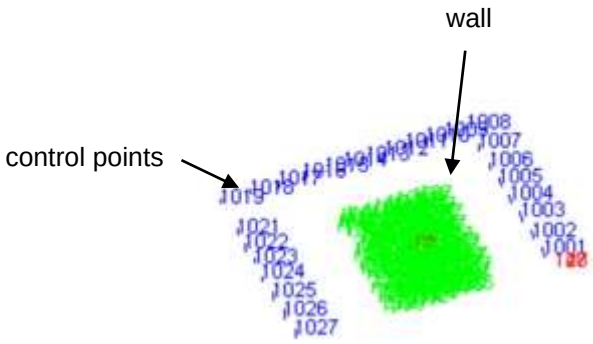

c

object view with target IDs and cameras in 3D

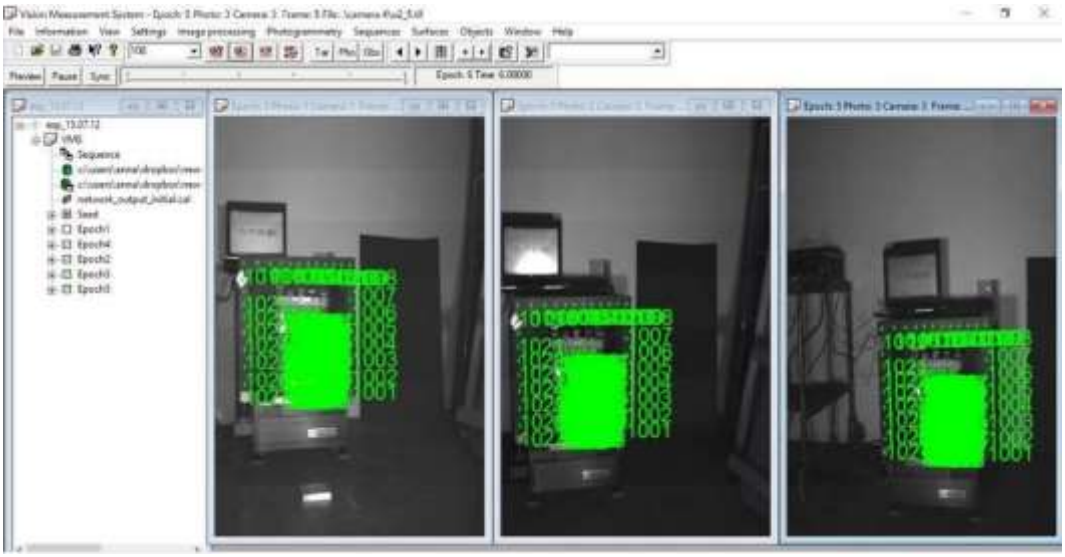

d

VMS analysis photos

Figure 4.2: object view of the mini-wall specimen in VMS environment – exp 1

Figure 4.3 presents the tested uncracked small scaled brick wall prior to the experimental phase with the red triangles showing two examples of the triangles that will be formed during the triangulation process. Figure 4.4 shows the specimen during the post-experimental phase, with the specimen being damaged along the red dotted line. The cameras' monitoring period did not capture the initiation and propagation of the crack, because it occurred after the frame count was completed. Due to this incident, the output frame per second was increased, after the completion of this experiment.

Figure 4.5 presents the computed maximum shear strain of the measured targets, using for plotting the $x-y$ $-z$ centroid coordinates of each triangle, which is created using the Surfer software. On the contour map, the x-axis represents the length of the tested specimen, the y-axis the height, and the contours the maximum shear strain as they are scaled on the right-hand side label. This plot shows that the wall started undergoing a small amount of damage in an area where the path of the crack has been formed. On the wireframe, the x-axis similarly represents the length of the tested specimen, the y-axis its height, and the z-axis presents the cracking which is caused by the out of plane failure. The wireframe plot shows better presentation of the specimen's failure, as shown in figure 4.4.

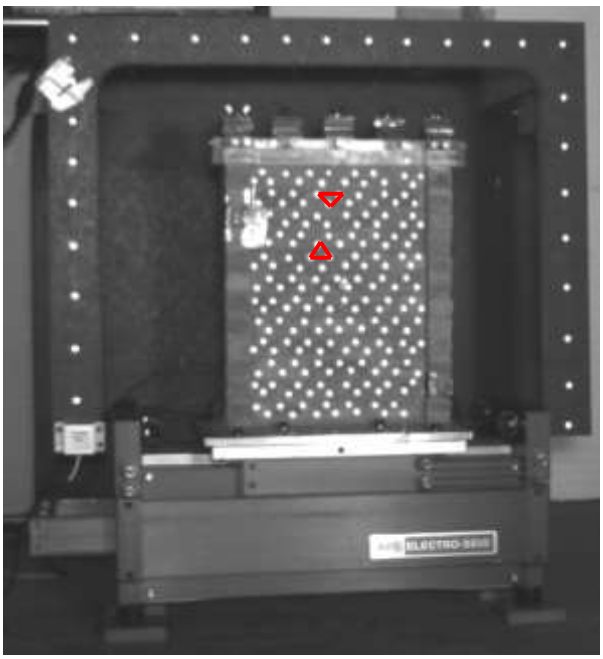

Figure 4.3: uncracked mini-wall; red triangles indicate the measured triangles for strain computation – exp 1

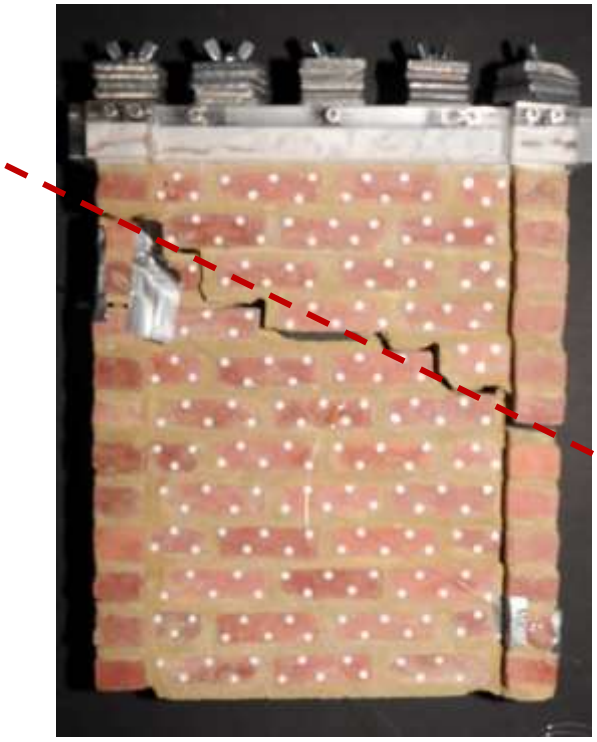

Figure 4.4: post-experimental phase of the tested wall – exp 1

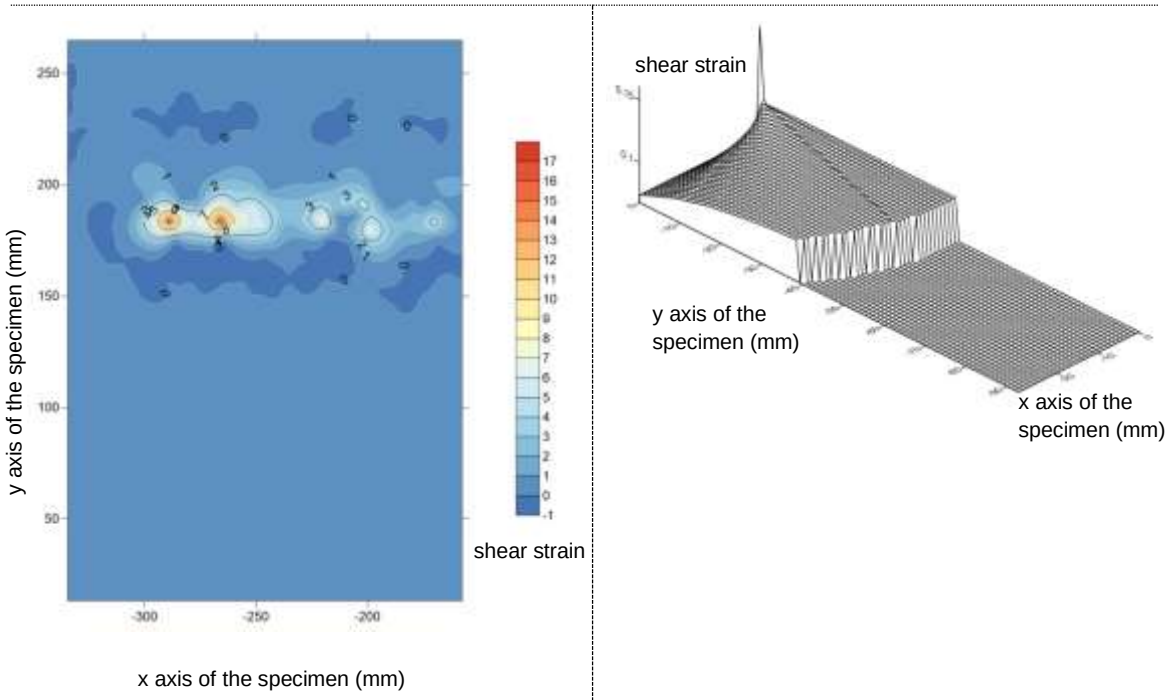

contour map (2D) wireframe (3D)

Figure 4.5: maximum shear strain (epochs 4-5) – exp 1

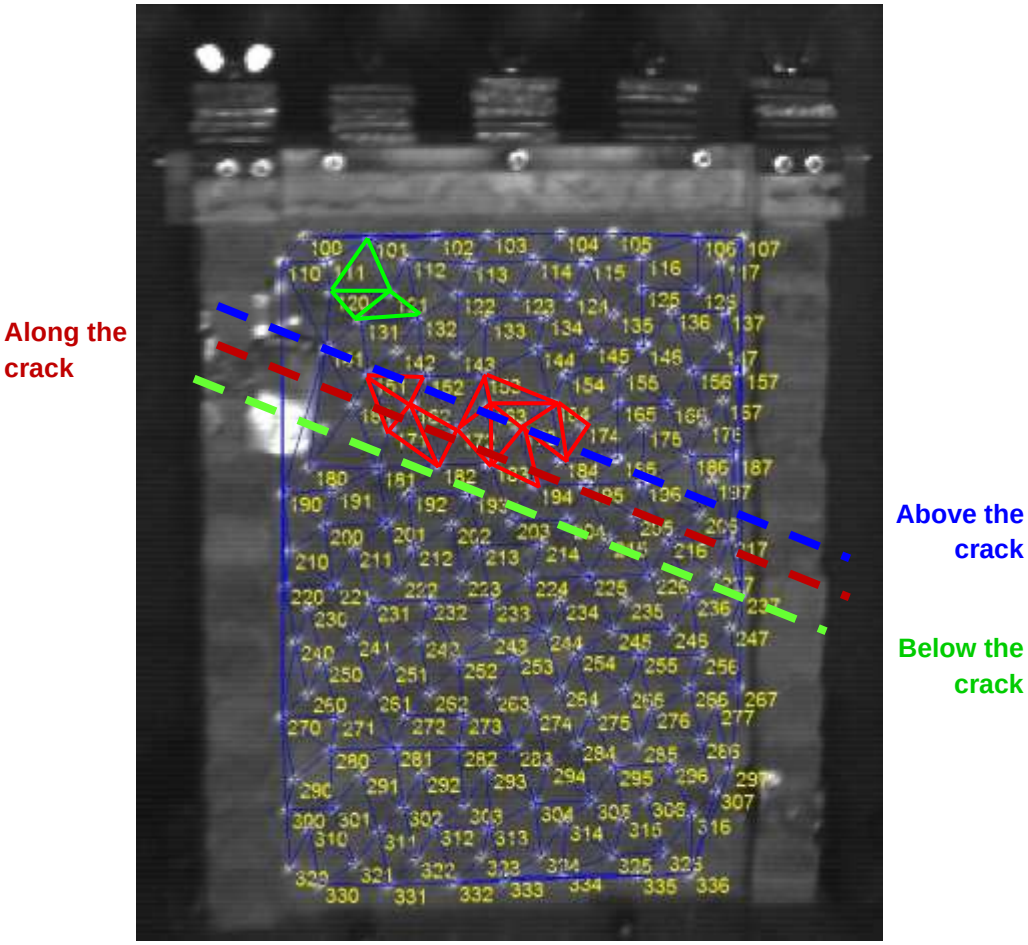

Figure 4.6: triangulation computed in EngVis (the **red** and **green** colours of the above triangles do not correspond with the graphs; they are chosen to make the triangles visually distinguished) – exp 1

After the completion of the experiment and having observed the crack path (fig. 4.4), three groups of triangles are decided to be analysed and discussed additionally for their displacement results. These are presented in graphs in relation to the specimen's length. The first group consists of twenty-one triangles showing the displacement range of the triangles' centroids located above the crack (blue line – fig. 4.6), as it is observed and monitored during the experimental phase. For example, in figure 4.6, above the red dotted line such triangles are i.e. 131-132-142, 132-142-152, etc. The second group is consisted of thirty triangles along the same crack (red line – fig. 4.6) and the third group of thirteen triangles below the crack (green line – fig. 4.6).

Figures 4.7- 4.10 present the displacement range of the triangles' centroids of these three groups in relation to the specimen's length (x axis) between the five different epochs. It does not start at zero on the x axis as the first measurement is the centroid of the first triangle, which is at 12.5mm on the axis of the graph (fig. 4.7). Figure 4.7 shows a displacement range of 1-2.2mm for the group of triangles above, along and below the crack from epoch 1 to epoch 2, illustrating the specimen's distortion during

the first 1284 milliseconds of its monitored motion. Within this time-frame only two triangles, located above the crack and approximately within the zone area where figure 4.5 presents the localisation of the specimen's shearing, showed a larger displacement of 4.5mm. Figure 4.8 shows the triangles' centroids displacement from epoch 2 to 3 for the same groups of triangles, mostly ranging between 0-1mm, apart from the same pair of triangles above the crack, which are displaced by 5.4mm. Figure 4.8 is a mirror of figure 4.7, which possibly explains that as the specimen is moving in time from epoch 1 to epoch 2 and then to epoch 3, the materials' particles of the mini-wall have behaved the same on the x axis of the motion. The triangles' displacement extent is relatively small for the time intervals between epoch 1 and 2 and 2 and 3 and turns slightly larger for the times between epochs 3 and 4 and 4 and 5. However, a different result is presented in figures 4.9 and 4.10: a displacement of 2-4mm for the triangles groups above and below the crack. The displacement results for the triangle groups along the crack show random results between the 40mm to 160mm of the specimen's length on the x axis, which proves the fact that this movement progressively led to the crack after epoch 4. It is worth mentioning that in both figures 4.9 and 4.10, after the 115mm of the specimen's length on the x axis, a significant drop of the readings has been recorded for the group of triangles above the crack. Table 4.2 shows eleven high peaks (red triangles – table 4.2) of figures 4.9 and 4.10 along with the targets where these readings have been recorded. These eleven triangles (table 4.2), which represent the 3.23% of the overall 341 triangles, define a small structural component of the mini-wall, proving the capability of the monitoring technique (CRDP) to capture the failure and with the use of the appropriate computation means (Mohr circle) to translate this failure to displacement and shear strain. Similar behaviour is presented in figures 4.10-4.14, which show the displacement of the same group of triangles along y axis with larger values. Even larger values are presented in figures 4.15-4.18, which show the triangles' displacements for these three groups on the z axis. The very big values computed on the z axis may be used as a prognosticate element for the shear failure occurred and the formation of the crack, as shown in figure 4.4. Similar results are presented in table 4.2 which shows the increasing displacement values on the x axis to the y axis and then to z axis for these 14 triangles. Triangles no. 5 and 7 present the largest values (table 4.2).

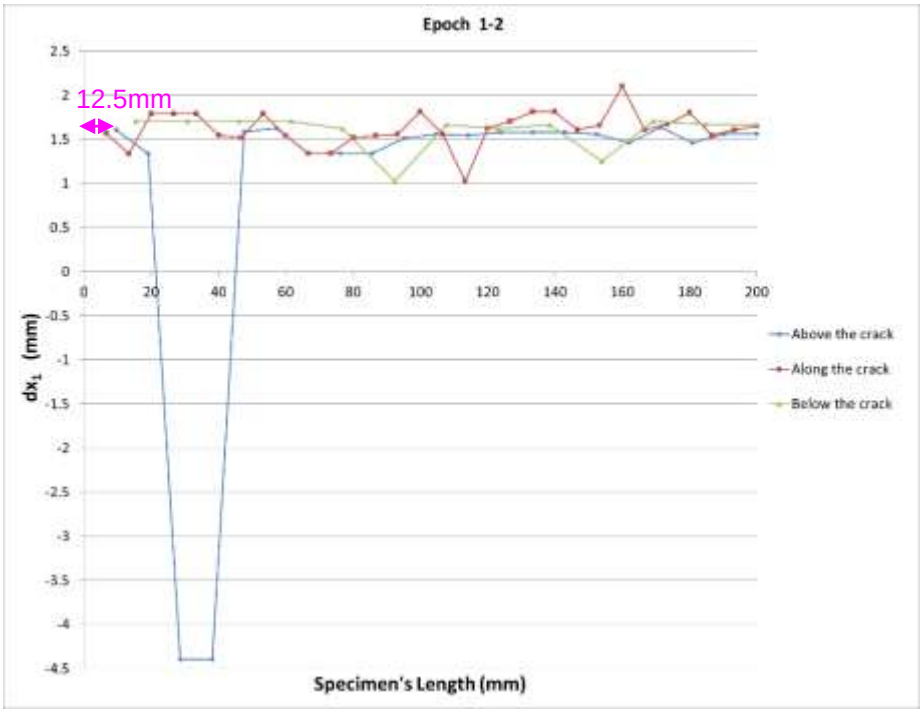

Figure 4.7: epoch 1-2 (dx_1 – exp 1)

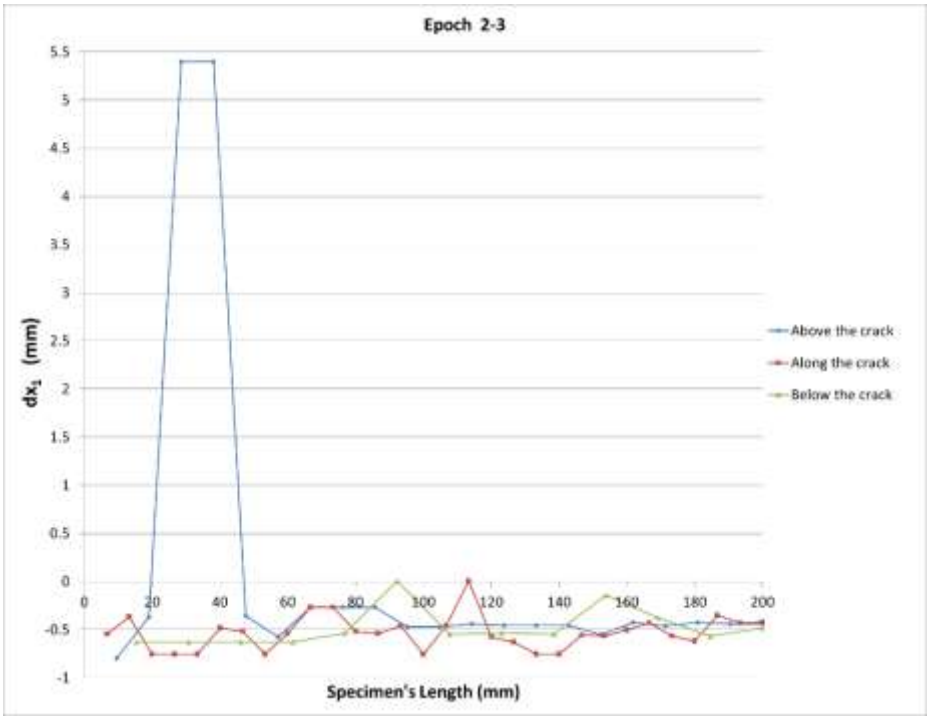

Figure 4.8: epoch 2-3 (dx_1 – exp 1)

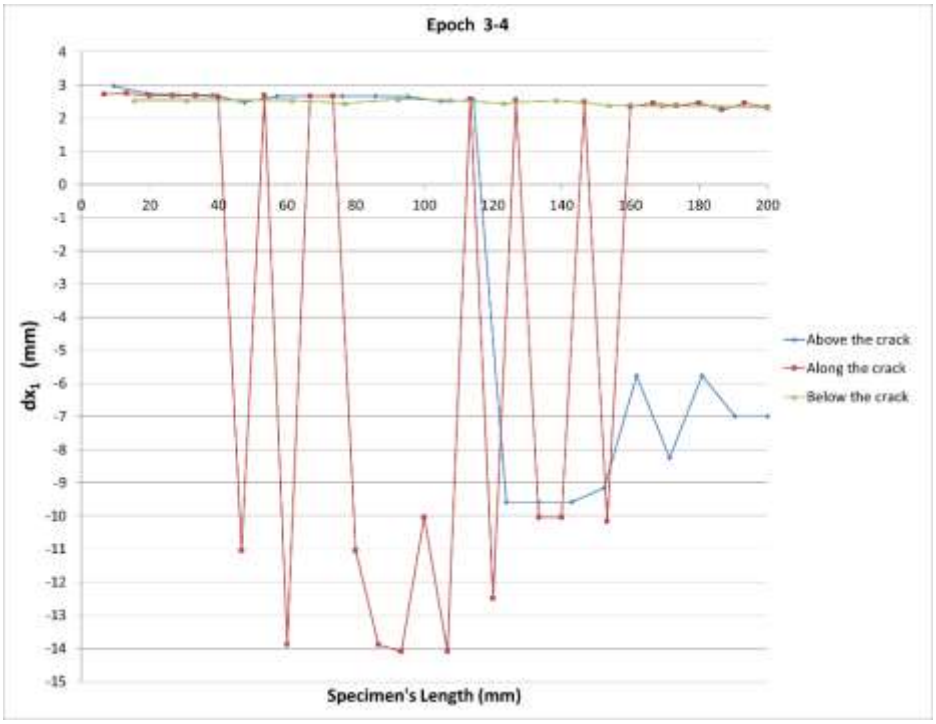

Figure 4.9: epoch 3-4 (dx_1 – exp 1)

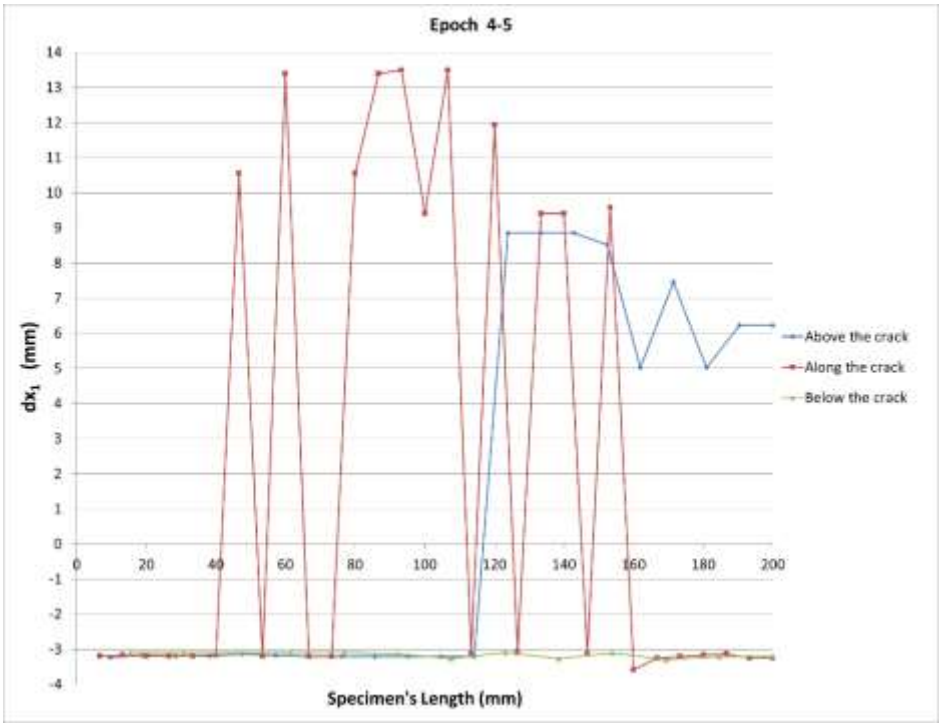

Figure 4.10: epoch 4-5 (dx_1 – exp 1)

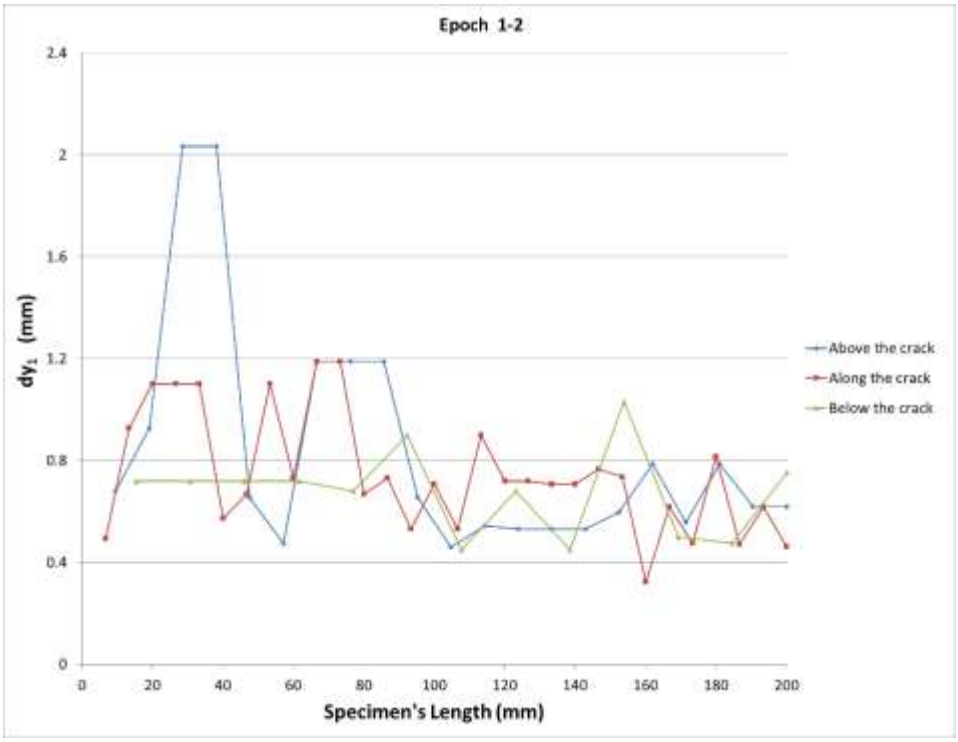

Figure 4.11: epoch 1-2 (dy_1 – exp 1)

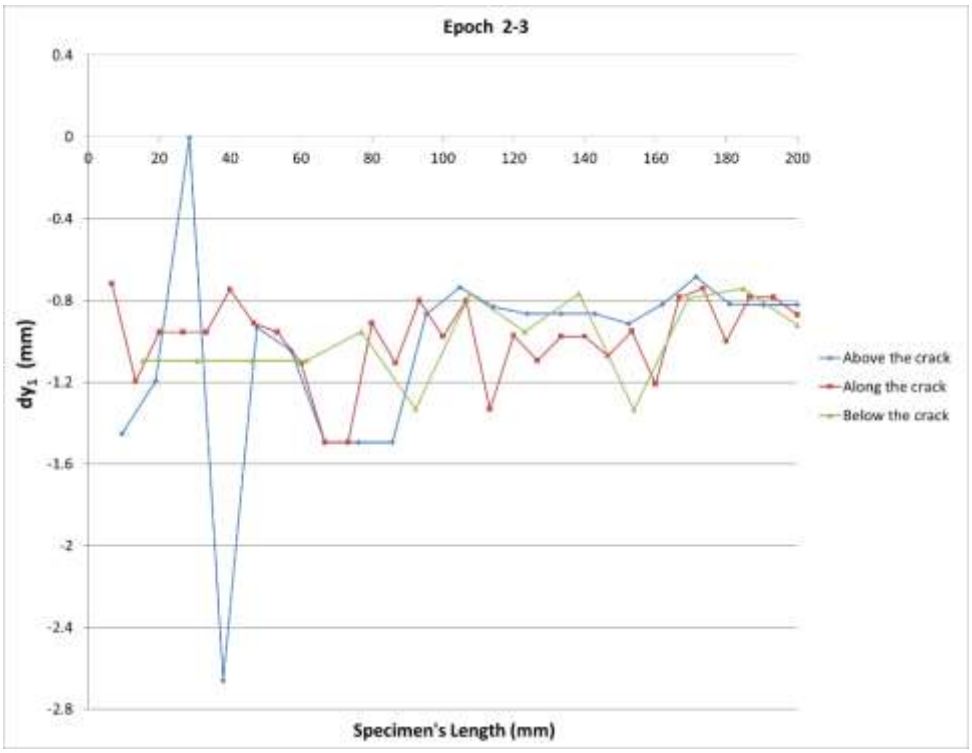

Figure 4.12: epoch 2-3 (dy_1 – exp 1)

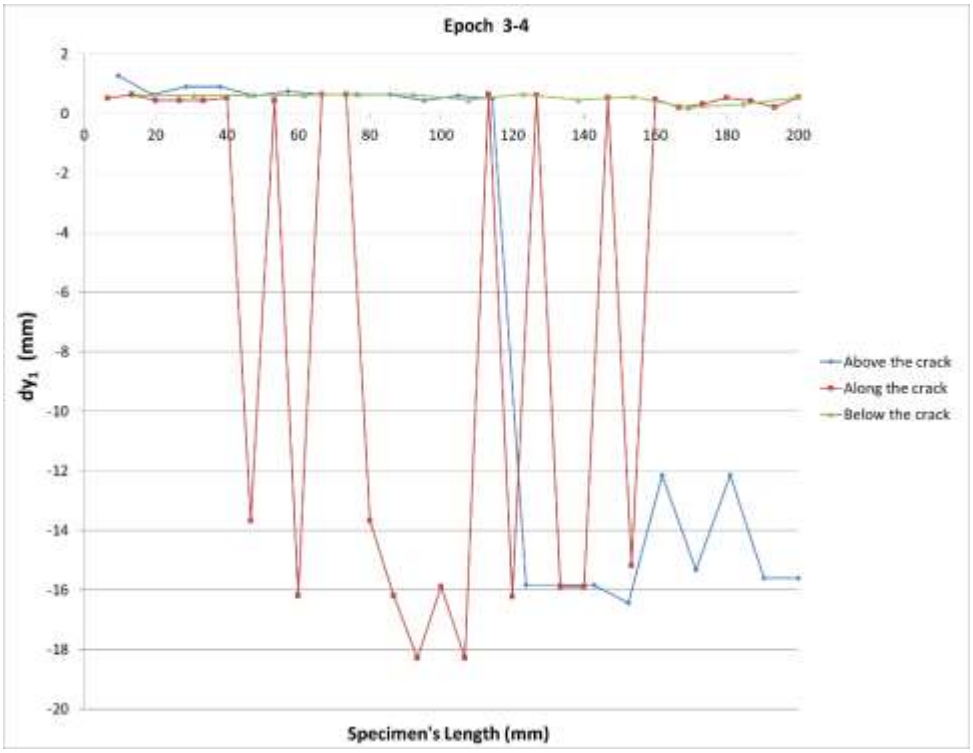

Figure 4.13: epoch 3-4 (dy_1 – exp 1)

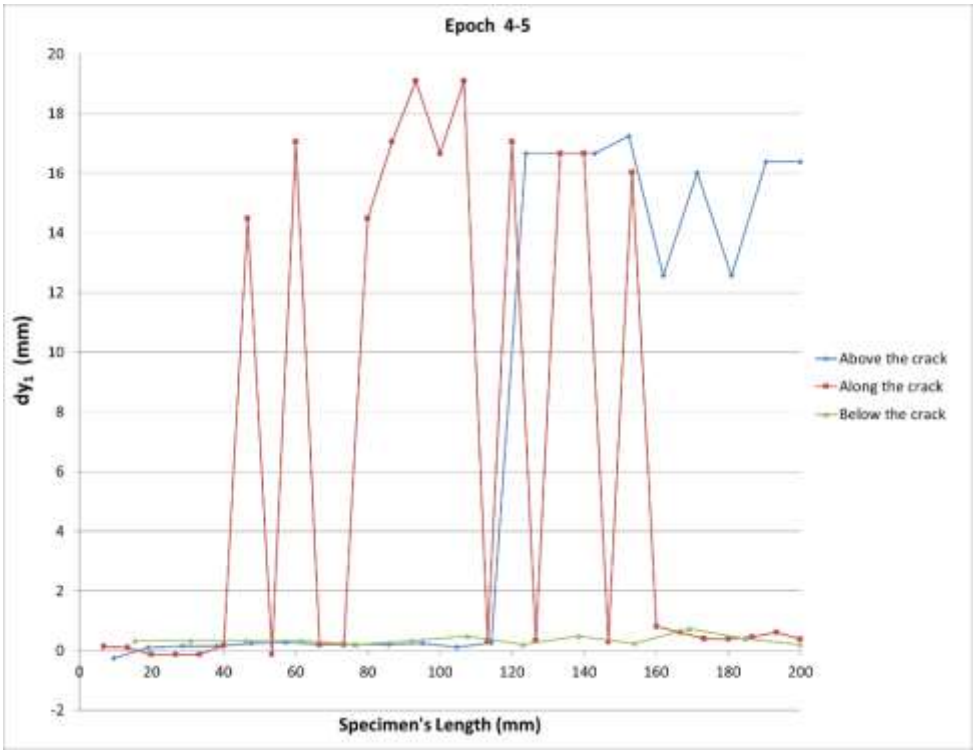

Figure 4.14: epoch 4-5 (dy_1 – exp 1)

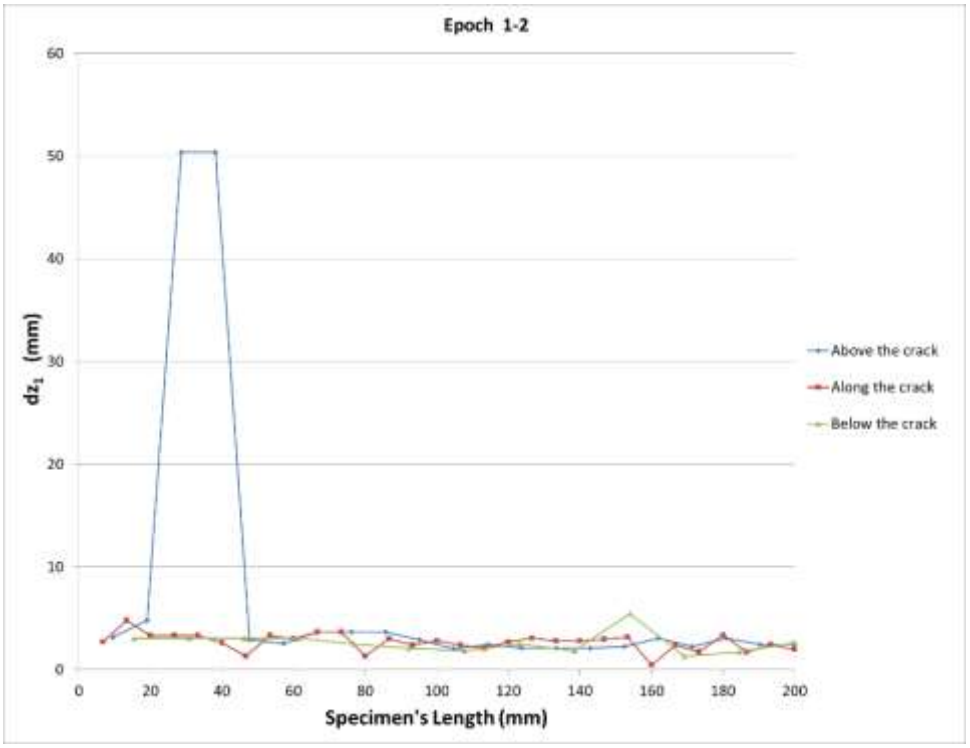

Figure 4.15: epoch 1-2 (dz_1 – exp 1)

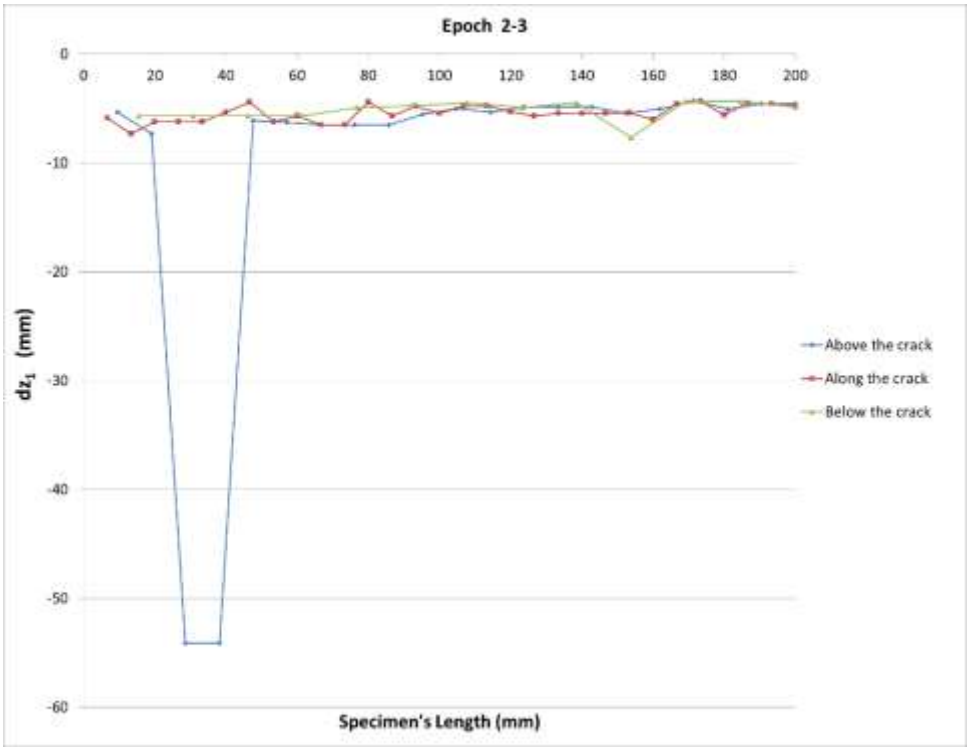

Figure 4.16: epoch 2-3 (dz_1 – exp 1)

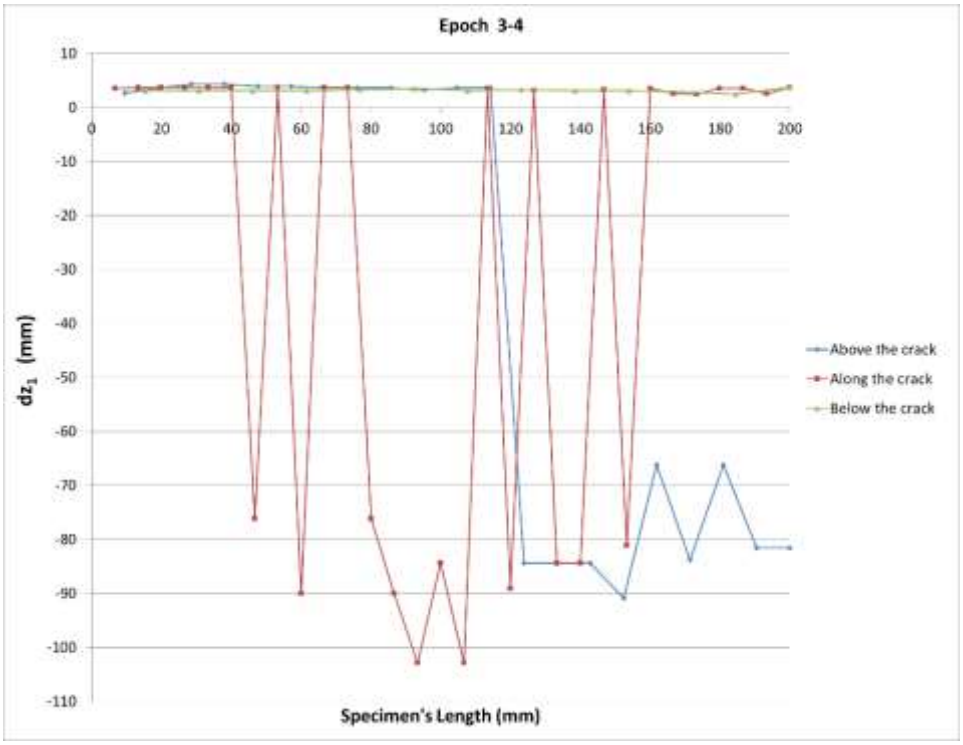

Figure 4.17: epoch 3-4 (dz_1 – exp 1)

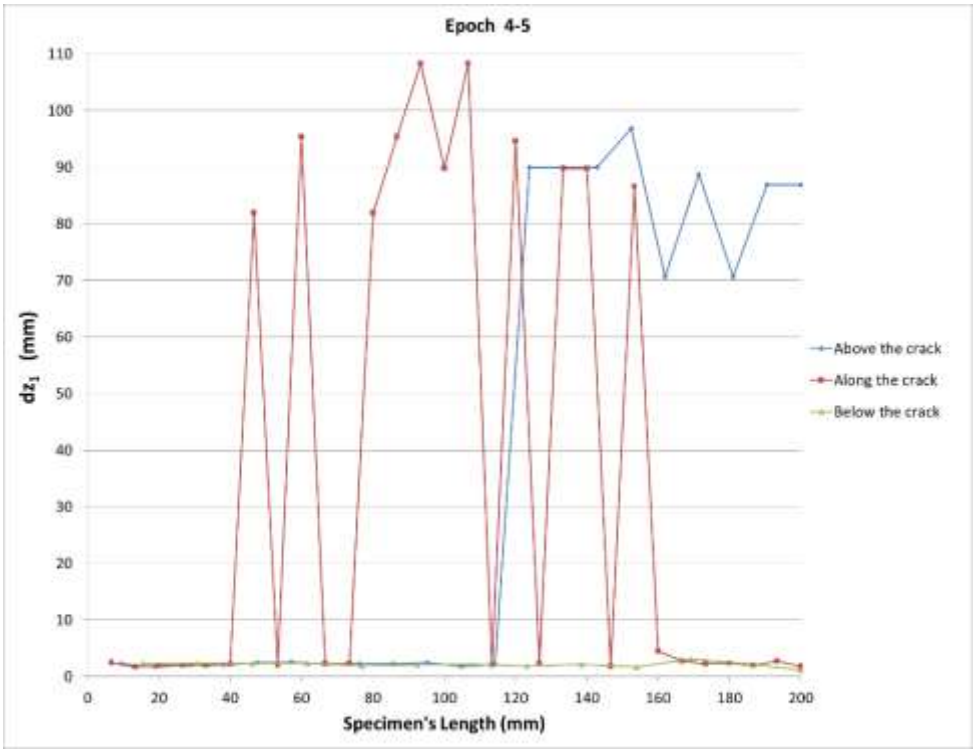

Figure 4.18: epoch 4-5 (dz_1 – exp 1)

	No. of targets Triangles			dx_1 (mm)		dy_1 (mm)		dz_1 (mm)	
	along the crack			epoch 3-4	epoch 4-5	epoch 3-4	epoch 4-5	epoch 3-4	epoch 4-5
1	162	152	151	-11.052	10.555	-13.679	14.481	-76.150	81.988
2	161	171	151	-13.890	13.388	-16.186	17.058	-89.990	95.386
3	162	182	172	-11.052	10.555	-13.679	14.481	-76.150	81.988
4	171	182	162	-13.890	13.388	-16.186	17.058	-89.990	95.386
5	172	163	153	-14.102	13.495	-18.281	19.090	-102.900	108.383
6	153	163	164	-10.050	9.403	-15.895	16.661	-84.390	89.748
7	163	173	164	-14.102	13.500	-18.281	19.090	-102.900	108.383
8	172	183	163	-12.488	11.933	-16.235	17.049	-89.160	94.642
9	164	184	174	-10.050	9.403	-15.895	16.661	-84.390	89.748
10	164	173	184	-10.050	9.403	-15.895	16.661	-84.390	89.748
11	183	194	173	-10.163	9.575	-15.190	16.029	-81.110	86.572
	above the crack			epoch 1-2	epoch 2-3	epoch 1-2	epoch 2-3	epoch 1-2	epoch 2-3
12	120	121	101	-4.391	5.398	2.033	-0.005	50.385	-54.128
13	121	120	131	-4.391	5.398	2.033	-2.662	50.385	-54.128
14	121	131	132	1.587	-0.358	0.653	-0.934	2.9028	-6.133
				shear strain					
	above the crack			epoch 1-2	epoch 2-3				
12	120	121	101	0.301	0.468				
13	121	120	131	0.470	0.519				
14	121	131	132	0.603	0.592				

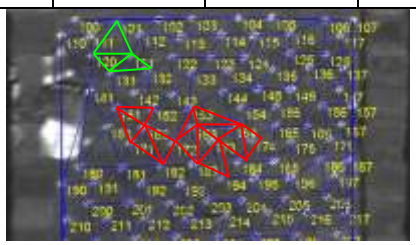

Table 4.2: High-peaks recorded during the test – exp 1

Figure 4.19 shows the same results as figures 4.7-4.10, but on a different format by presenting the deformation of targets from epoch 1 to epoch 5. Dots correspond to the monitored targets and figure 4.19 verifies figure 4.1. Epoch 1 shows the targets on their initial position, epoch 2 presents the initiation of a slight differentiation between the top three layers of the specimen and the rest bottom ones. On figure 4.19, for epochs 3, 4 and 5, is showing again the same differentiation between the three top layers of the specimen, to the rest bottom ones, presenting a larger intensity on the targets' movement, which explains that as the specimen was vibrating on the x axis, it was close to shearing. The colour coded[1] epoch by epoch movement show the targets' movement for all the epochs and it is also presented in epochs 1-5 deformation figure.

[1] The targets of each epoch are coded with different colours for distinguishing purposes.

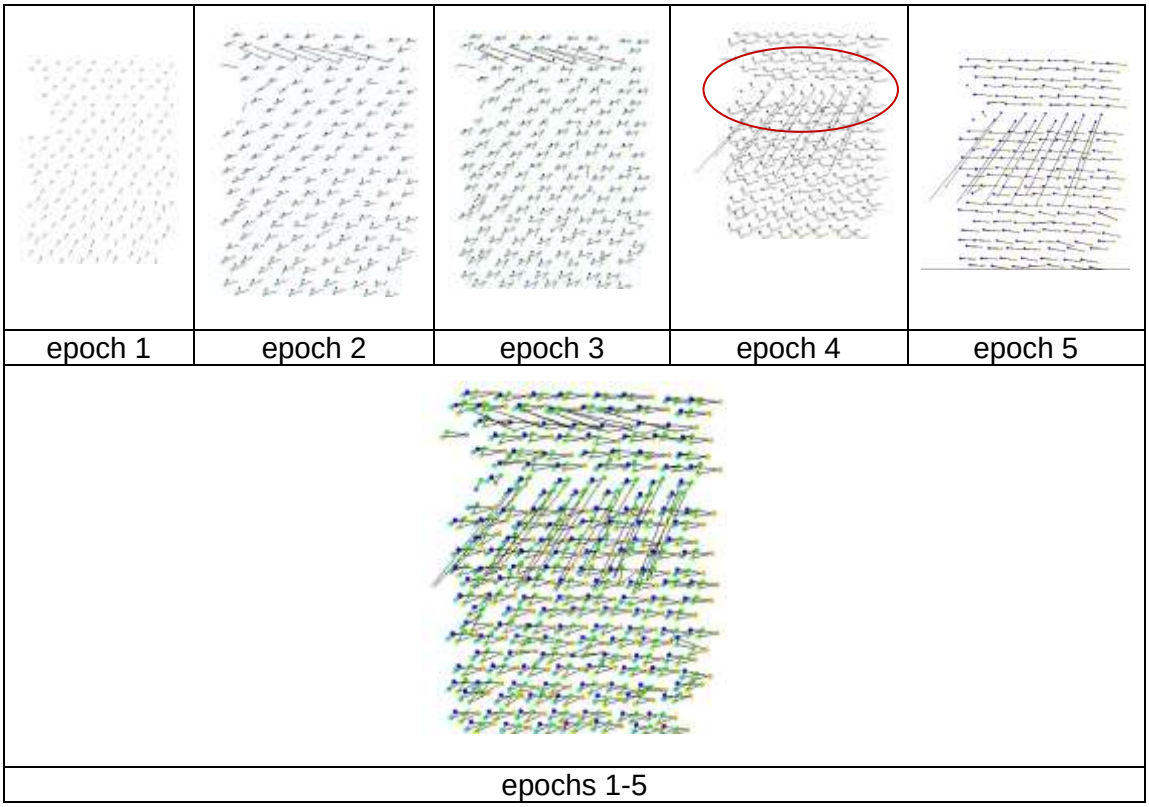

Figure 4.19: Epoch to epoch movement of specimen's triangles – exp 1

Figures 4.20 – 4.23 show the shear strain results along the specimen's face, using a contour map. The maximum shear strain is the tangent of the angle, due to the deformation of a body, and it is equal to the length of deformation at its maximum stage divided by the perpendicular length at the direction of the applied force. Figures 4.20 and 4.21 show the effect of the loading applied at the top of the mini-wall and the resulting shearing through the specimen's movement during the first 1701 milliseconds (epochs 1-3) of its monitored motion. Figure 4.22 shows the targeting area where shear will occur due to the input dynamic loading. Lastly, figure 4.23 shows the location where the crack started to propagate and not captured by the cameras. The maximum recorded shear strain is 17; this large value explains that there was a sliding at the crack's location. Figure 4.23 is significant as the contour map shows the location where cracking will occur without capturing the crack by the cameras. This means that cracking can be predicted with the use of the cameras as monitoring means and the method of CRDP (close range digital photogrammetry).

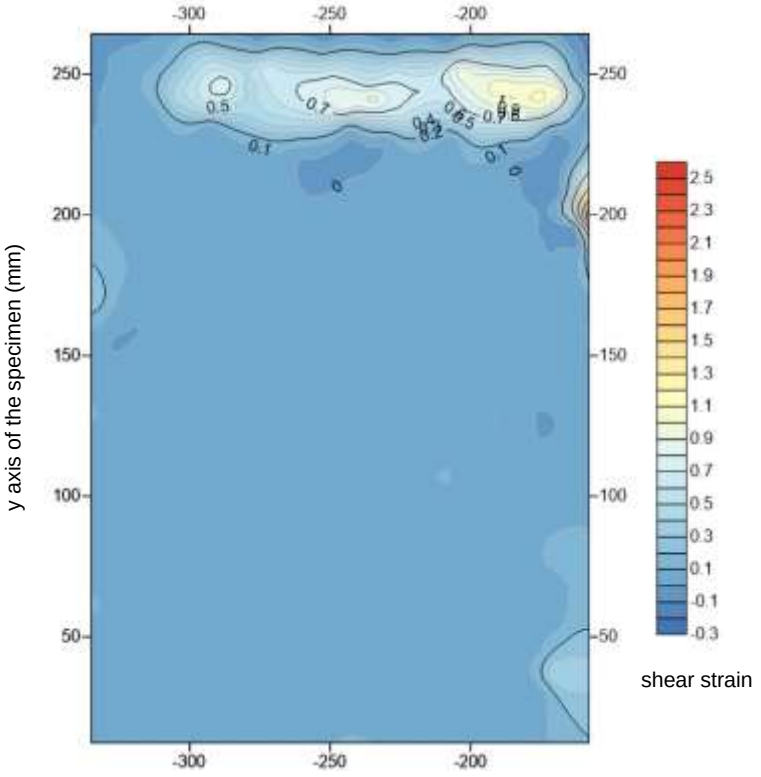

Figure 4.20: epoch 1-2 (shear ε – exp 1)

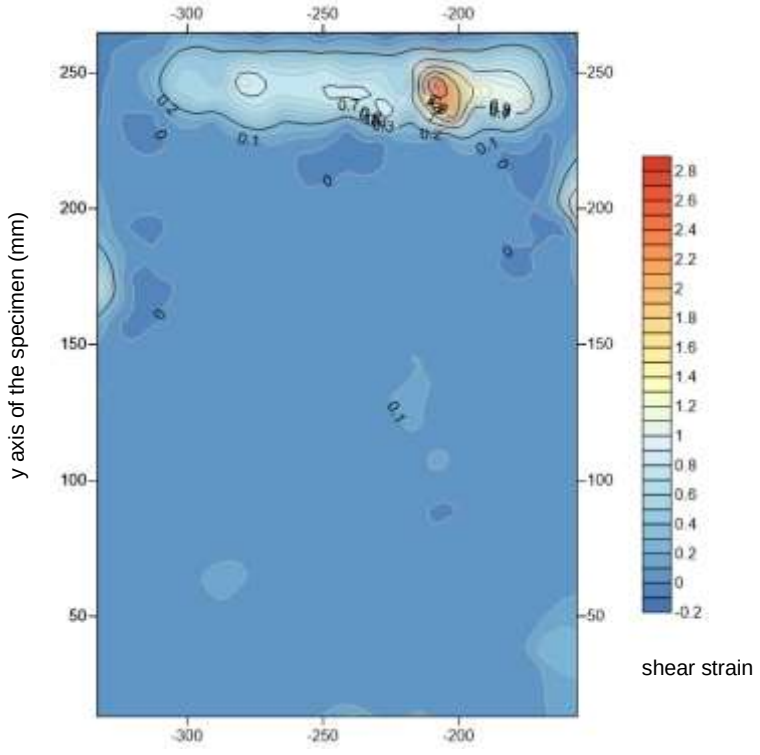

Figure 4.21: epoch 2-3 (shear ε – exp 1)

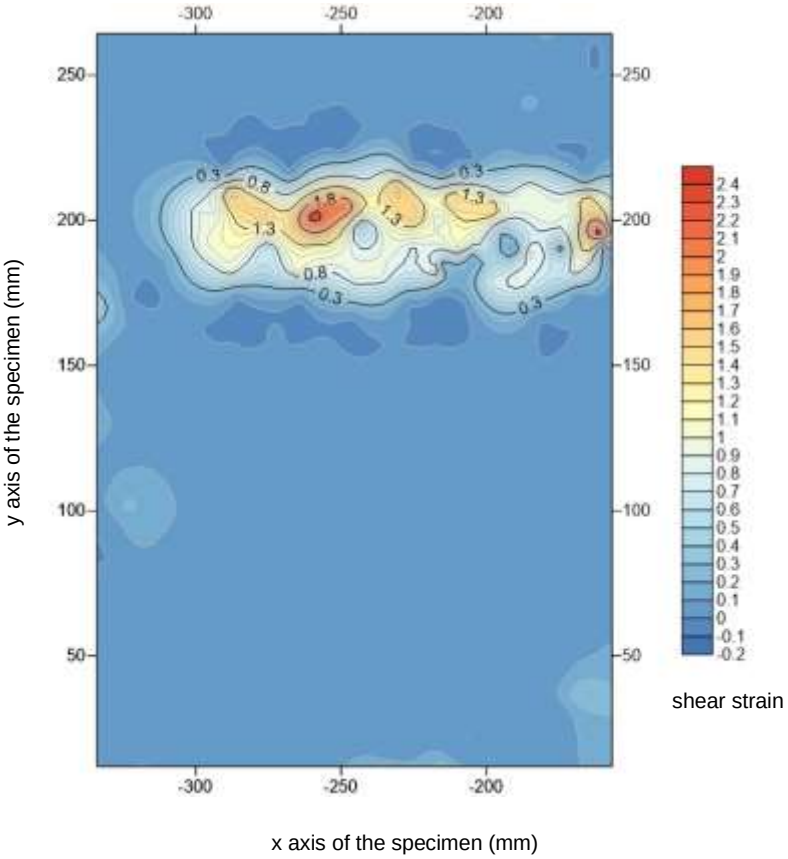

Figure 4.22: epoch 3-4 (shear ε – exp 1)

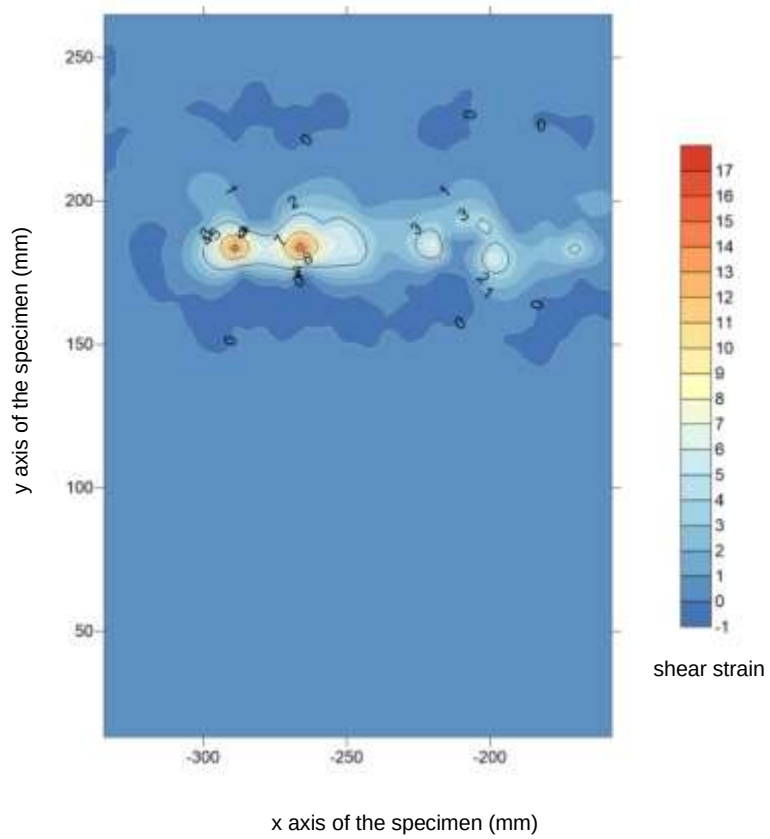

Figure 4.23: epoch 4-5 (fig. 4.5) (shear ε – exp 1)

4.2.3 Static Experiment (exp 2)

This section presents the results computed by the second experiment, which was carried out in the Concrete Technology Laboratory (C.E.G.E., U.C.L.). The purpose of this test is to identify the performance of a masonry specimen loaded under uniaxial pressure, the necessary synchronisation steps for the chosen monitoring methods – strain gauges and photogrammetry – and the comparison of their results.

The preliminary experiment is built using model bricks of type C (100x100x50mm) and a ready-mix brick laying mortar, by Wickeys, which is created by adding up water. This ready mix is used to accelerate the building up of the large-scale wall specimen, as there were time and cost constraints during the laboratory period spent at the University of Bristol. A strain gauge (fig. 4.30) is also installed on the masonry specimen, alongside with the mortars' joints. The strain gauge was installed on the 2nd horizontal mortar joint, from the top of the specimen. 198 targets are set up on two of the four specimen's faces (A and B) (fig. 4.29) and two D700 Nikon cameras are positioned opposite to the specimen for the photogrammetric monitoring purposes. The loading is applied on the y axis of the specimen, using the laboratory's compression machine (fig. 4.24), by reaching the stress value of 429.7 MPa (fig. 4.25), under which failure started occurring to the specimen. During the experiment, the compression frame's window remained open to create similar experimental conditions with the dynamic test. Initially, the strain gauge data logger started recording, secondly the two cameras started shooting synchronised and finally the compression machine started applying the pre-set pressure to the specimen. The test lasted for 153.4 seconds.

Figure 4.24: Compression Frame – Laboratory equipment

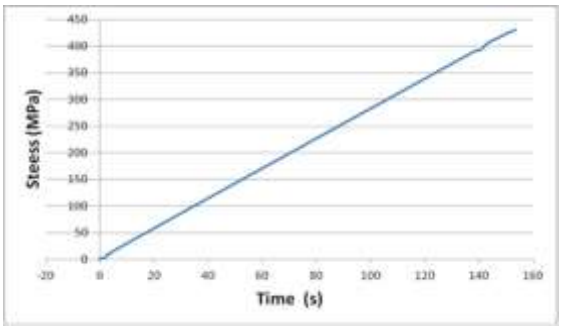

Figure 4.25: Applied pressure – exp 2

4.2.3.1 Close Range Digital Photogrammetry (CRDP)

Figure 4.26 shows the specimen during the 4 chosen epochs. The first chosen epoch was epoch 2, where the crack started being propagated (fig. 4.26b). Figure 4.26a shows the undamaged wall specimen and figures 4.26 c and 4.26d shows the formed crack on the specimen being further propagated. 31 control points have been installed for the purposes of this experiment (fig. 4.27), such locations are the corners around the compression machine's window. Once the project has been set up on the VMS software and the targets have been inserted, observations are created for both the control and the free targets (fig. 4.28). As for the previous shaking table test (exp 1), once the required files have been processed in the VMS environment, data showing the movement of the targets has been produced which are inserted further into the EngVis software. This software combines all the measurements from different "epochs" and can display the target movement in any stage of the experiment. The reason for using EngVis is to generate the triangulation system, which allows the centroid of any three reflected targets to be determined. Diagram 4.2 presents the sequence in accordance to the time. The cameras started recording at 16:50:10 and stopped at 16:52:38, having collected 20 images per camera, 40 images in total.

a

epoch 1__16:50:58

b

epoch 2__16:51:46

c

epoch 3__16:51:52

d

epoch 4__16:52:02 (fig. 4.12)

Figure 4.26: Images' sequences capturing the compressed tested of the masonry specimen – exp 2

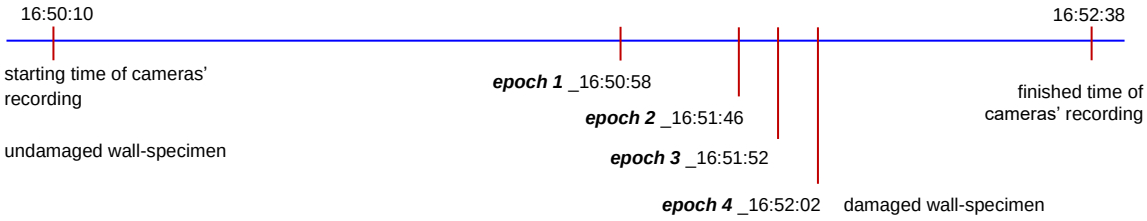

Diagram 4.2: cameras' recording timings for experiment 2

Figure 4.27: Control points as measured in the network file – exp 2

Figure 4.28a shows the numbered reflected targets (targets ID) on the specimen (green numbers) and the two cameras (green cones). Figure 4.28b is the same as figure 4.28a along with the observations from the cameras. Figure 4.28c is similarly the same as figure 4.28a, along with the control points. Figure 4.2d shows the two pictures of the specimen as captured by the two cameras in the VMS software.

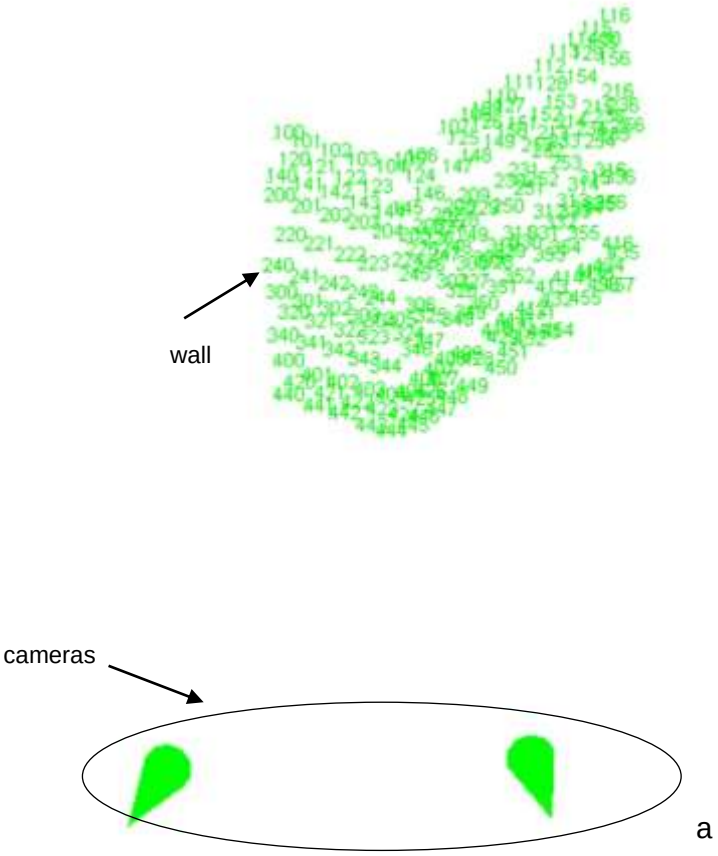

object view with target IDs and cameras in 3D

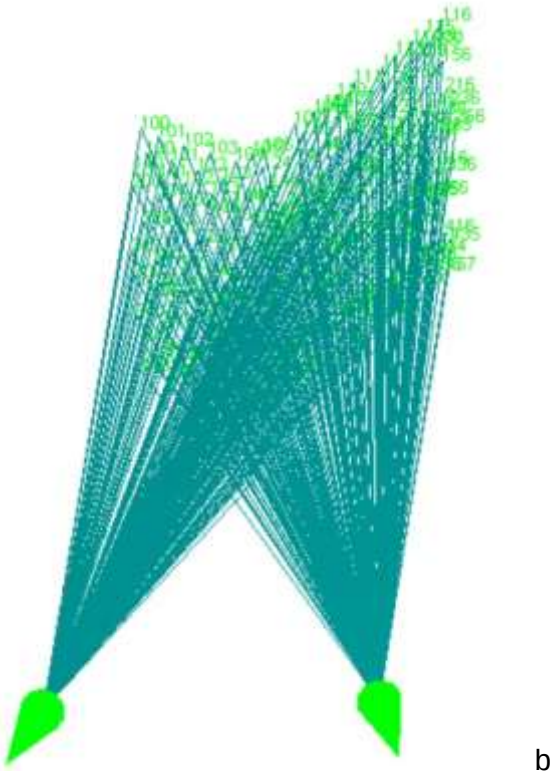

object view with observations

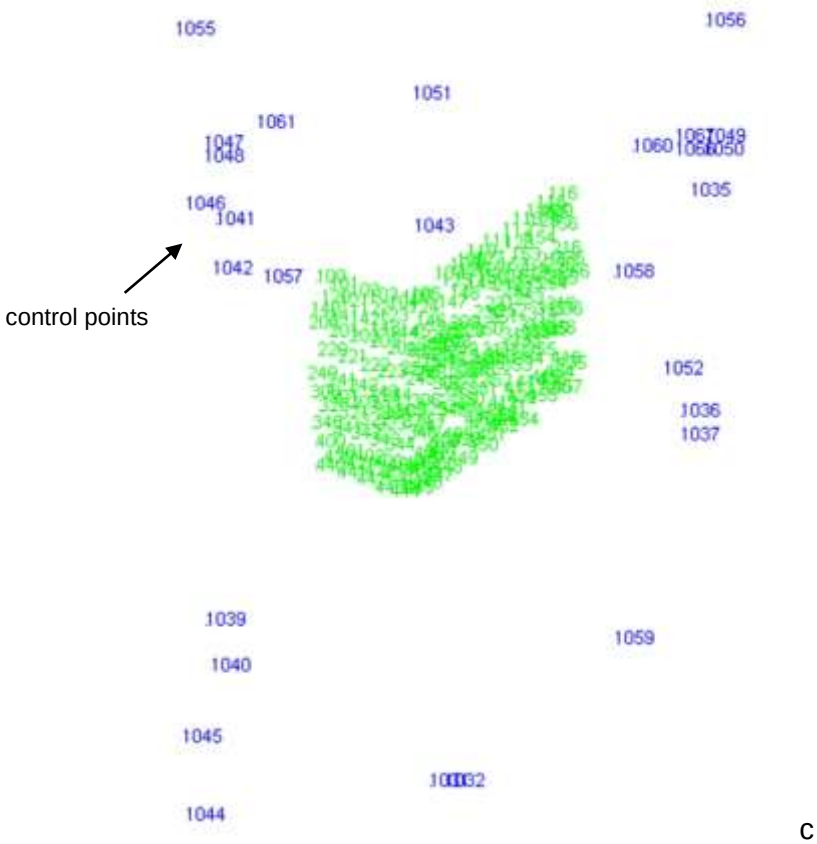

c

3D object view with target IDs (**green** points) and control targets (**blue** points) corresponding to features in the laboratory that were assumed static during the testing

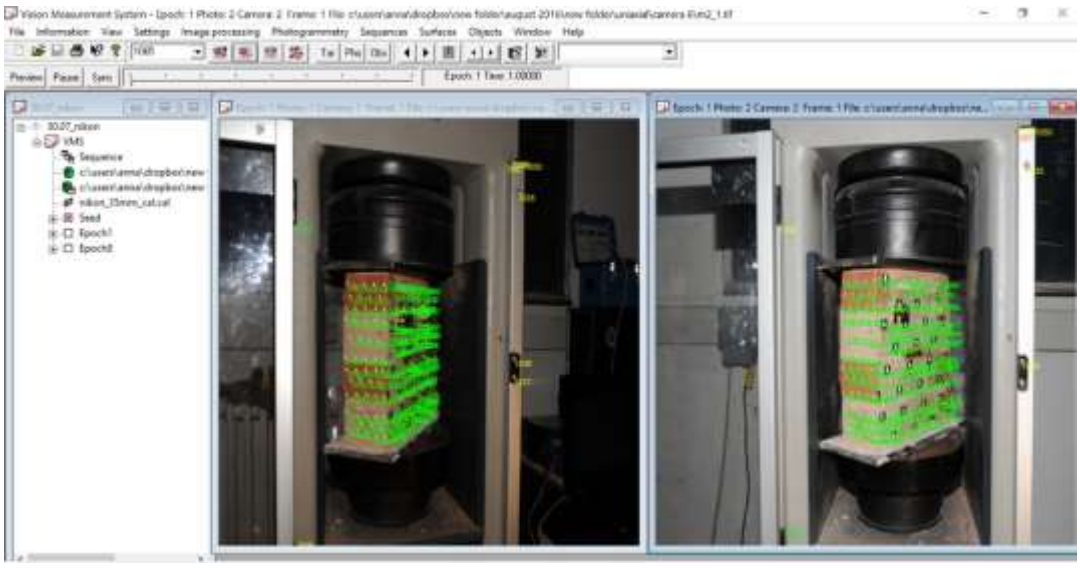

d

VMS analysis photos

Figure 4.28: object view of the mini-wall specimen in VMS environment – exp 2

Figure 4.30 presents the tested uncracked small scaled brick wall prior to the experimental phase and figure 4.29 shows the same specimen during the post-experimental phase. The cameras' monitoring captured the initiation and propagation of the two cracks. The brown ellipse in figure 4.29 shows the vertical crack on face B and the red ellipse shows the horizontal crack along both faces A and B.

Figure 4.31 presents the computed maximum shear strain of the measured targets, using for plotting the $x-y$ – z centroid coordinates of each triangle, which is created using the Surfer software. The x-axis represents the length of the tested specimen for both faces A and B (fig. 4.29), the y-axis the height, and the contours the maximum shear strain as they are scaled on the right-hand side label. This plot does show the damage on faces A and B, and the effect due to loading at the top of the specimen. In this example, the effect of loading was constant at the top as this was the location where the loading was acting. Figure 4.32 shows the triangulation system as it was created on EngVis environment. The pictures collected from Nikon cameras were automatically rotated once inserted to the software. However, the triangulation system is based on the non-rotated picture, showing the distortion along both the horizontal and the vertical cracks.

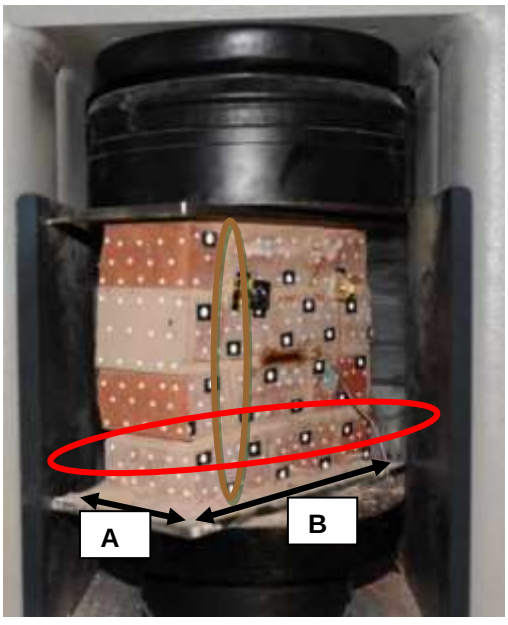

Figure 4.29: Damaged specimen once the test completed, with the **red** ellipse showing the horizontal crack on both faces A and B and the **brown** ellipse showing the vertical crack on face B – exp 2

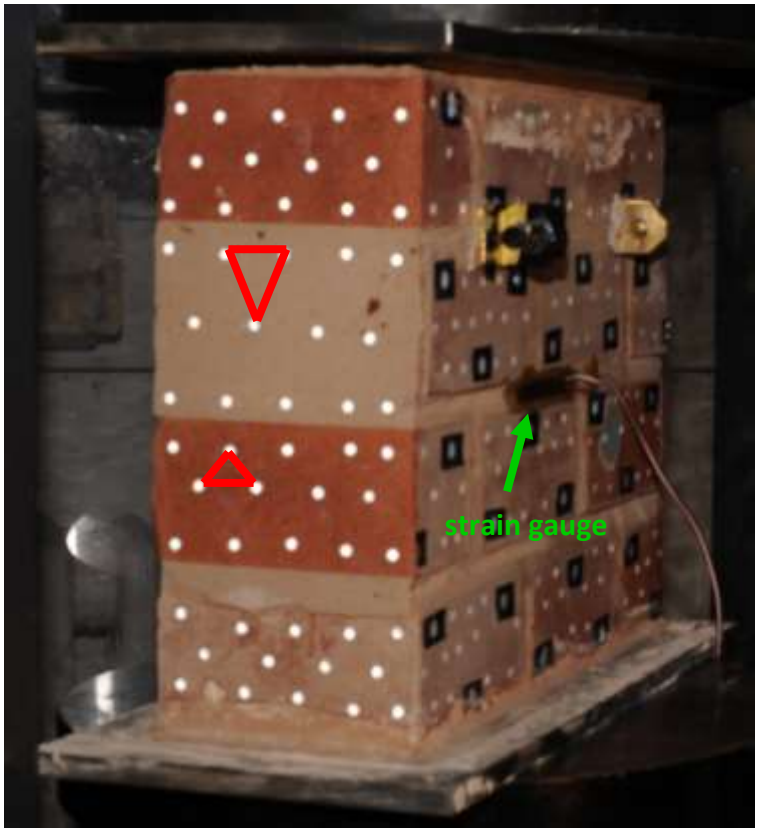

Figure 4.30: uncracked specimen – exp 2

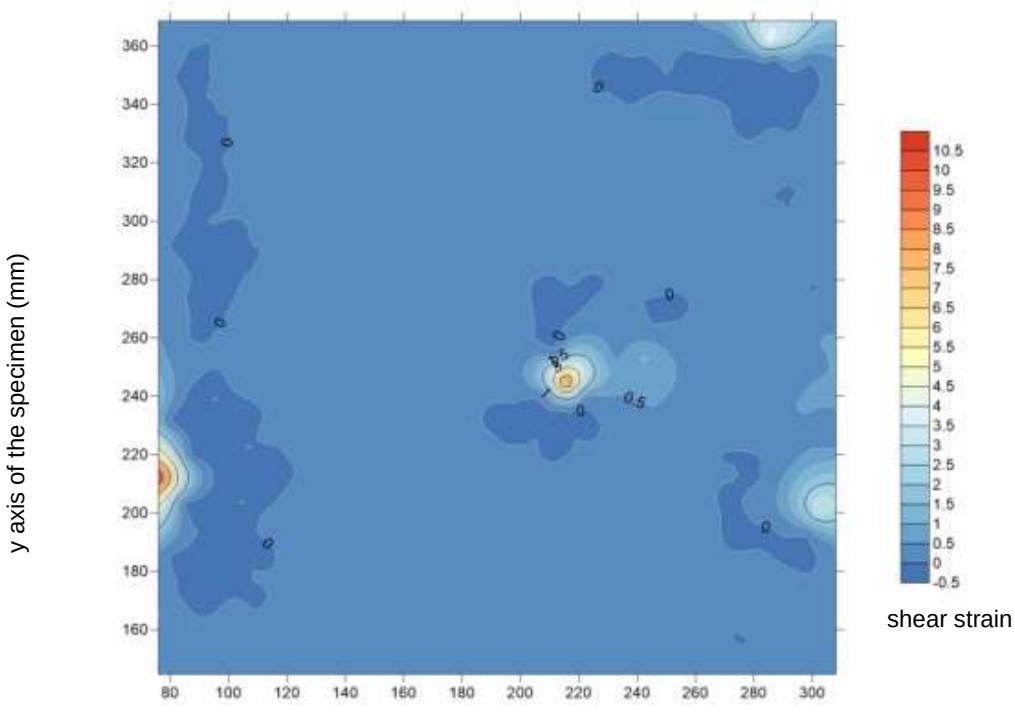

Figure 4.31: maximum shear strain (epochs 3-4) – exp 2

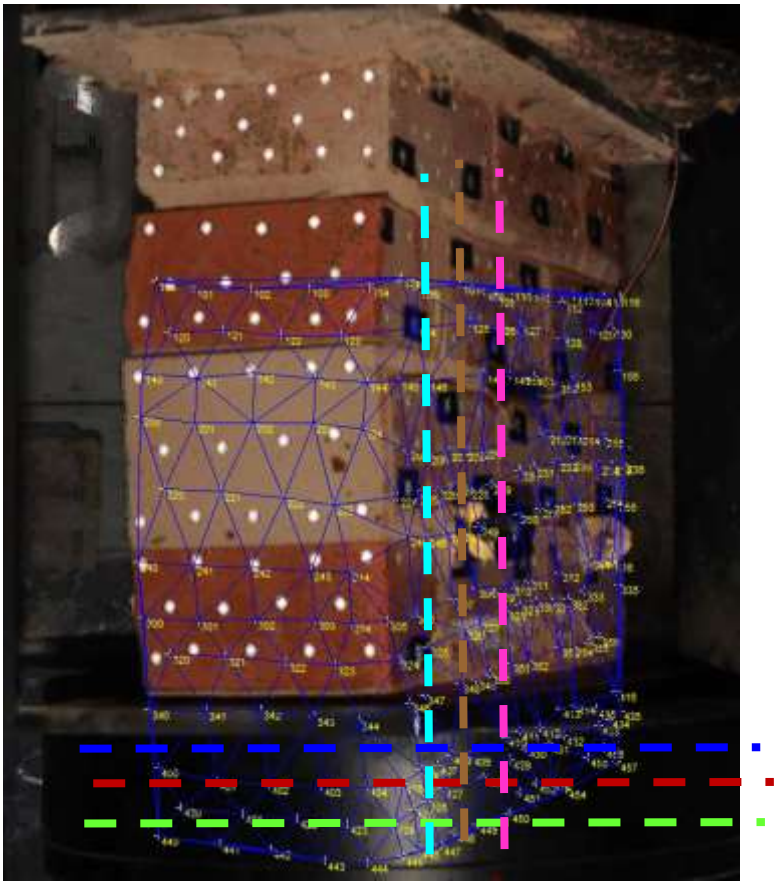

Figure 4.32: triangulation computed in EngVis – exp 2

Three groups of triangles are created to present their displacement in relation to the specimen's length. The first group consists of thirty triangles showing the displacement range of the triangles' centroids located above (blue line – fig. 4.32) the **horizontal** crack, as it is observed and monitored during the experimental phase. The second group consisted of twenty-five triangles along (red line – fig. 4.32) the **horizontal** crack and the third group of twenty-nine below the **horizontal** crack (green line – fig. 4.32). Additionally, three more groups of triangles are created to present their displacement in relation to the specimen's height. The first group consists of nine triangles showing the displacement range of the triangles' centroids located left (cyan line – fig. 4.32) of the **vertical** crack, as it is observed and monitored during the experimental phase. The second group is consisted of fifteen triangles along (brown line – fig. 4.32) the **vertical** crack and the third group is consisted of eight triangles right (pink line – fig. 4. 32) of the **vertical** crack.

Figures 4.33 – 4.35 present the displacement range on the x axis of the triangles' centroids of three groups, below the **horizontal** crack, along and above, all in relation to the specimen's length (x axis), with faces A and B combined both in one axis, between the four different epochs. Figure 4.33 shows a displacement range of 0-

3.5mm, for the group of triangles above, along and below the crack from epoch 1 to epoch 2, providing a figure of the specimen's distortion during the first 48 seconds of its monitored motion. Figure 4.34 shows the triangles' centroids displacement from epoch 2 to 3 for the same groups of triangles, mostly ranging between -0.8 – 1.3mm and between epoch 3 to 4 they were mostly ranging between 0.6 – (-)2.1mm. Figure 4.35 is a mirror of figure 4.33, which explains that as the specimen was distorted in time from epoch 1 to epoch 2 and then to epoch 3, the materials' particles of the specimen behaved the same on the y axis of the loading. Figures 4.33 – 4.35 have a common point. The readings of the first 100mm, which correspond to face A (fig. 4.29) of the specimen, have a small range and after this point show significantly larger peaks. This explains that the main failure occurred on face B (fig. 4.29) and the opening of the crack was larger compared to the opening occurred on face A on the x axis. Figures 4.36 – 4.38 present the displacement range on the x axis of the triangles' centroids of three groups, left of the **vertical** crack, along and right, all in relation to the specimen's length (x axis) between the four different epochs. All readings through the epochs show a very small range of 0.3 – (-)1.8mm.

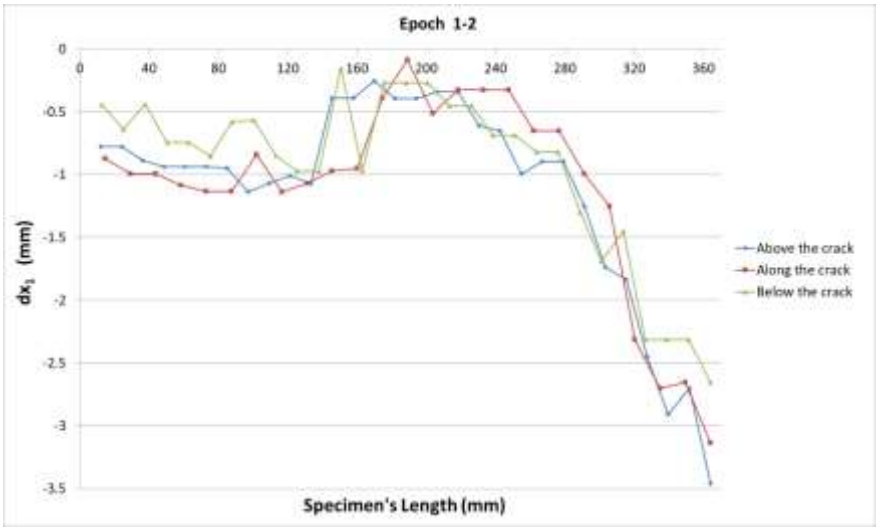

Figure 4.33: epoch 1-2 – horizontal crack (dx_1 – exp 2)

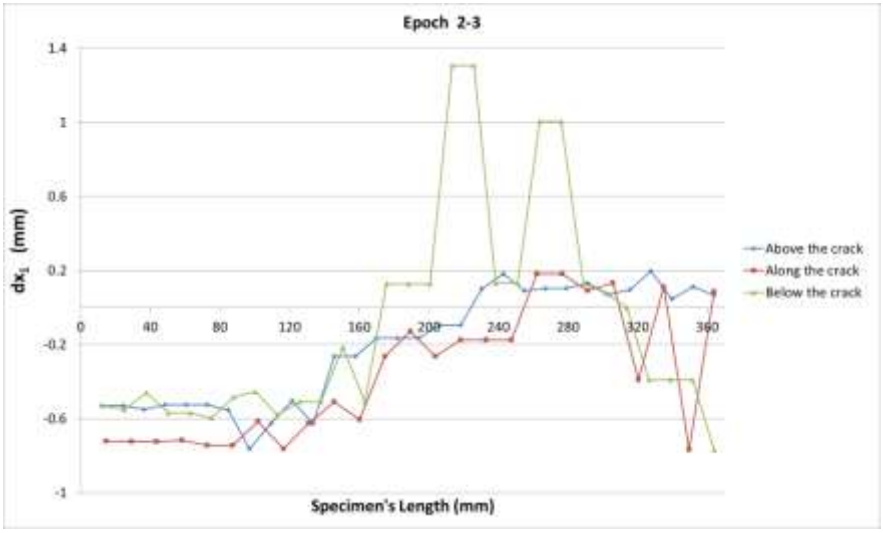

Figure 4.34: epoch 2-3 – horizontal crack (dx_1 – exp 2)

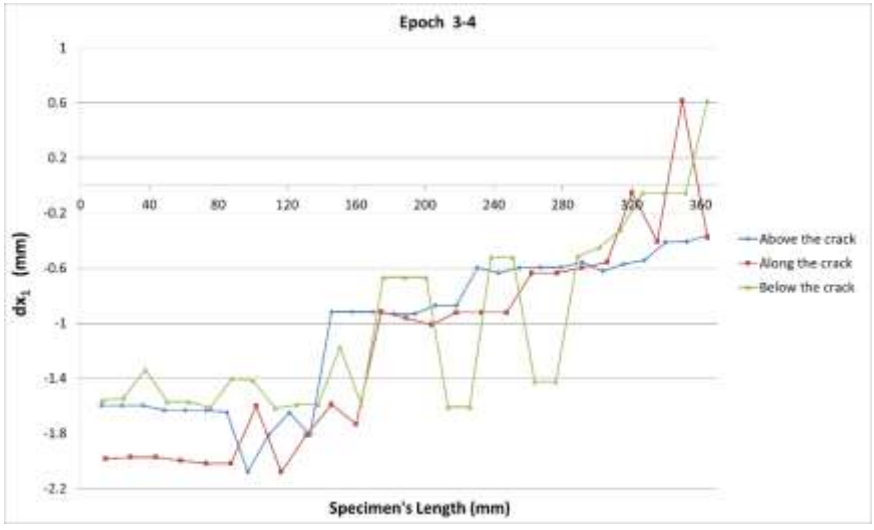

Figure 4.35: epoch 3-4 – horizontal crack (dx_1 – exp 2)

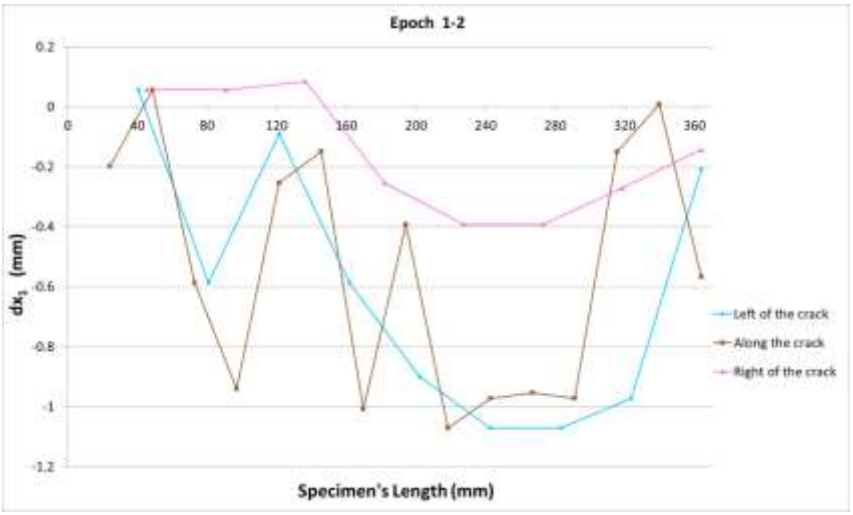

Figure 4.36: epoch 1-2 – vertical crack (dx_1 – exp 2)

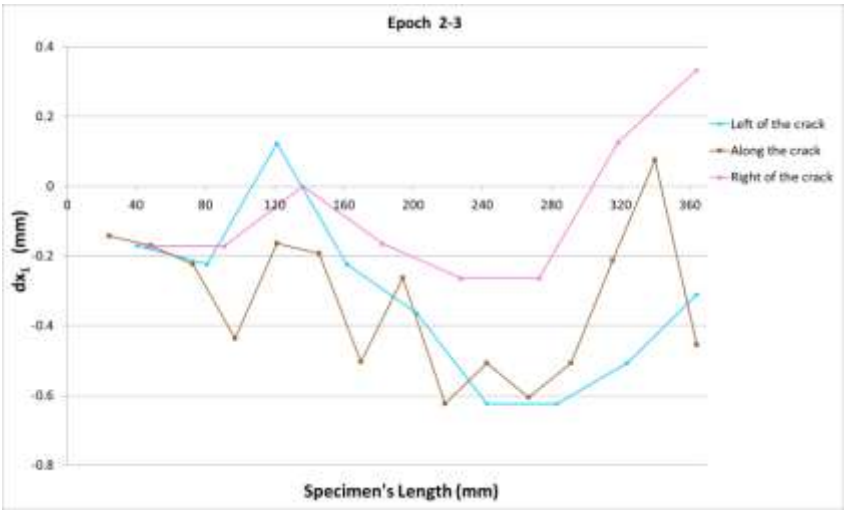

Figure 4.37: epoch 2-3 – vertical crack (dx_1 – exp 2)

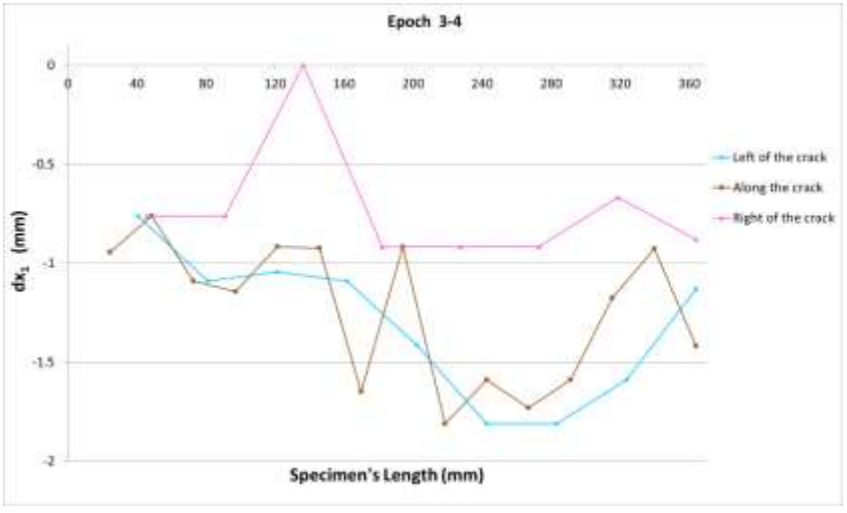

Figure 4.38: epoch 3-4 – vertical crack (dx_1 – exp 2)

Figure 4.39 shows the specimen's deformation of all the free reflected targets from epoch 1 to epoch 4, on a different format. The dots correspond to the monitored reflected targets and figure 4.39 verifies figure 4.26. Epoch 1 shows the targets on their initial position, epoch 2 presents the initiation of the vertical crack along face B. On epochs 3 and 4, the formation of both cracks is illustrated on both faces, A and B. The summary of the targets' movement for all the epochs, is also presented in epochs 1-4 deformation figure of figure 4.39.

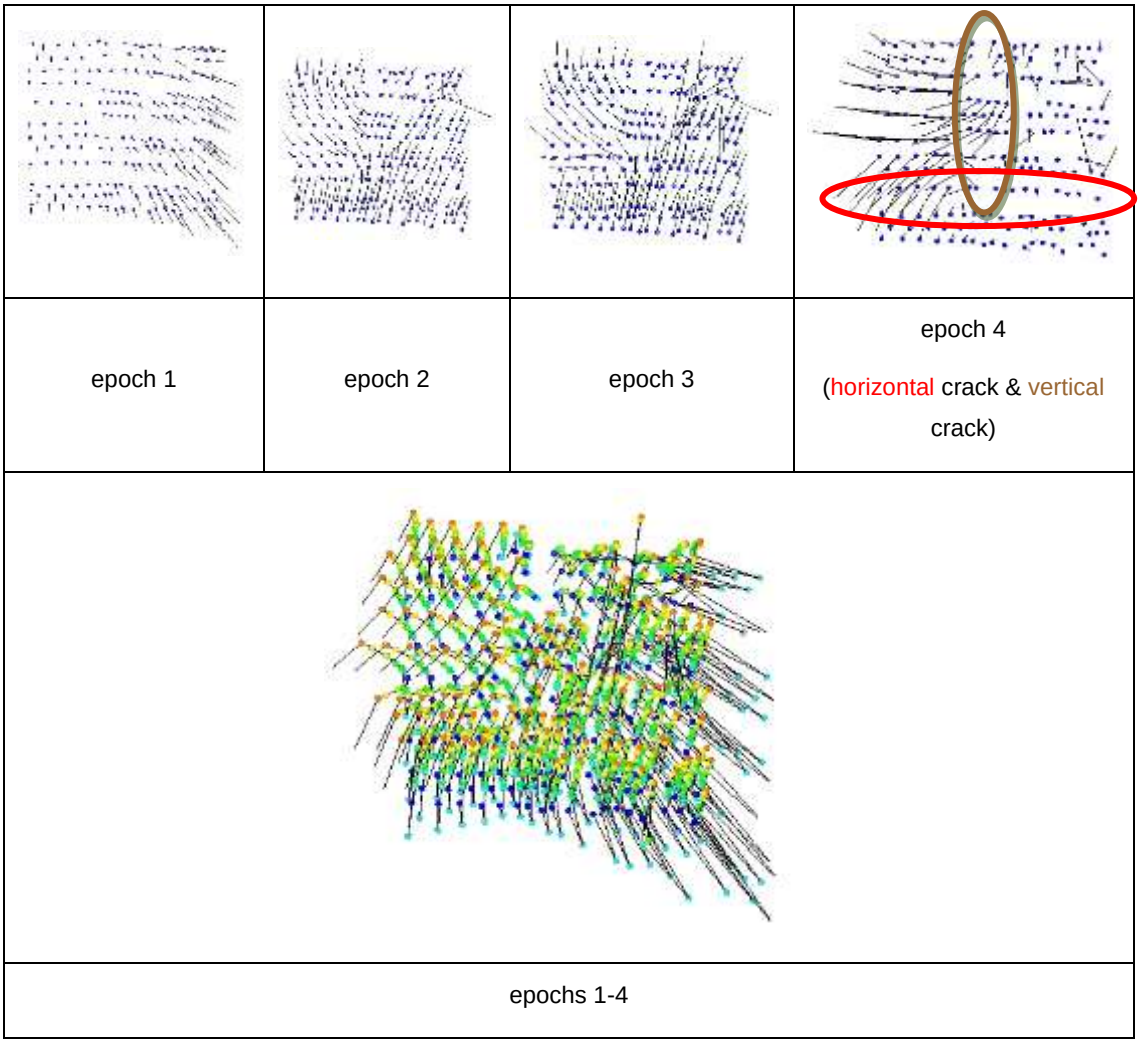

Figure 4.39: Deformation of specimen's triangles – exp 2

Figures 4.40-4.42 show the shear strain results along the specimen's face, using a contour map. Figures 4.40 shows the effect of the loading at the top, where the maximum values were recorded. Figures 4.41 and 4.42 show the targeting area A, where the horizontal crack is formed.

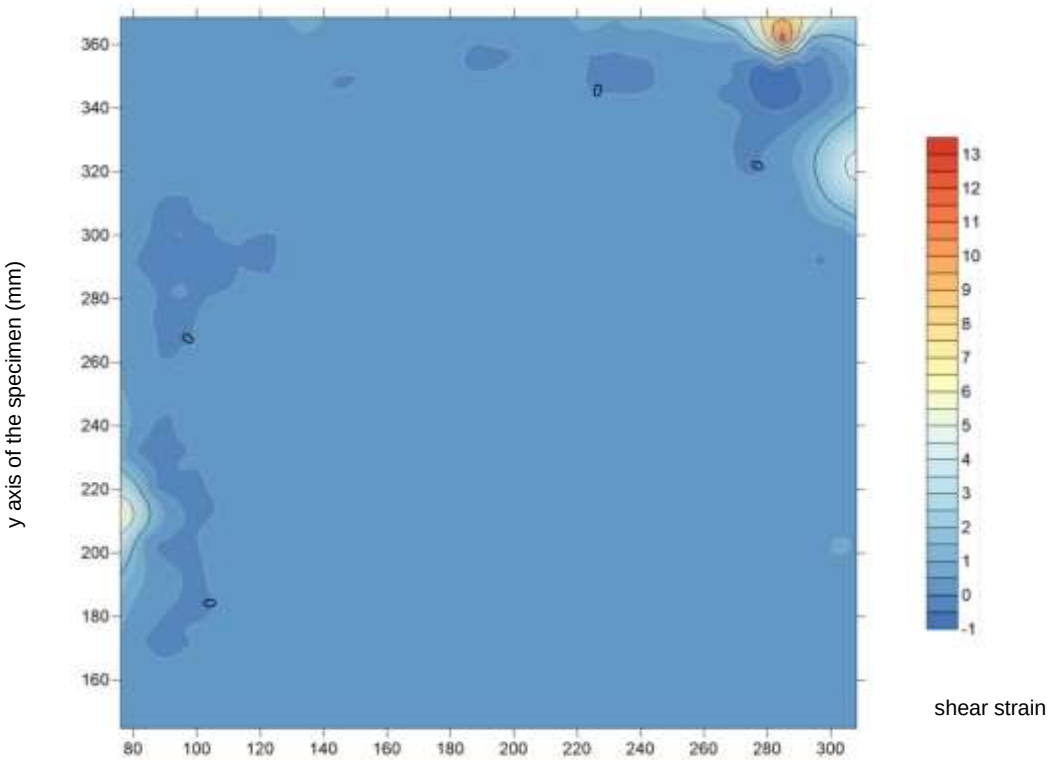

Figure 4.40: epoch 1-2 (shear ε – exp 2)

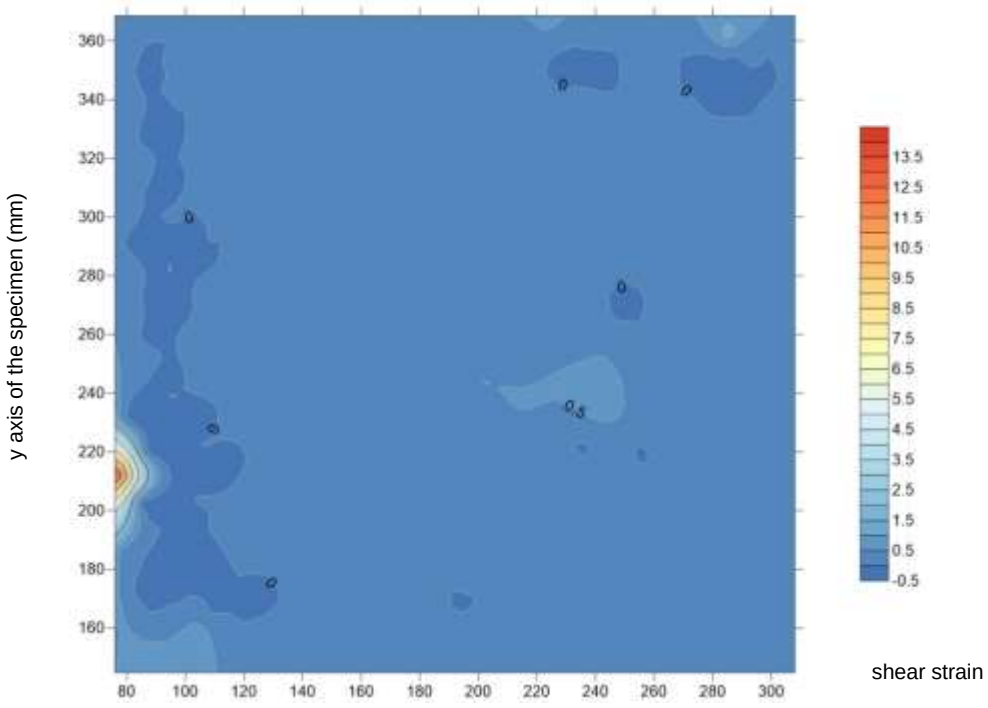

Figure 4.41: epoch 2-3 (shear ε – exp 2)

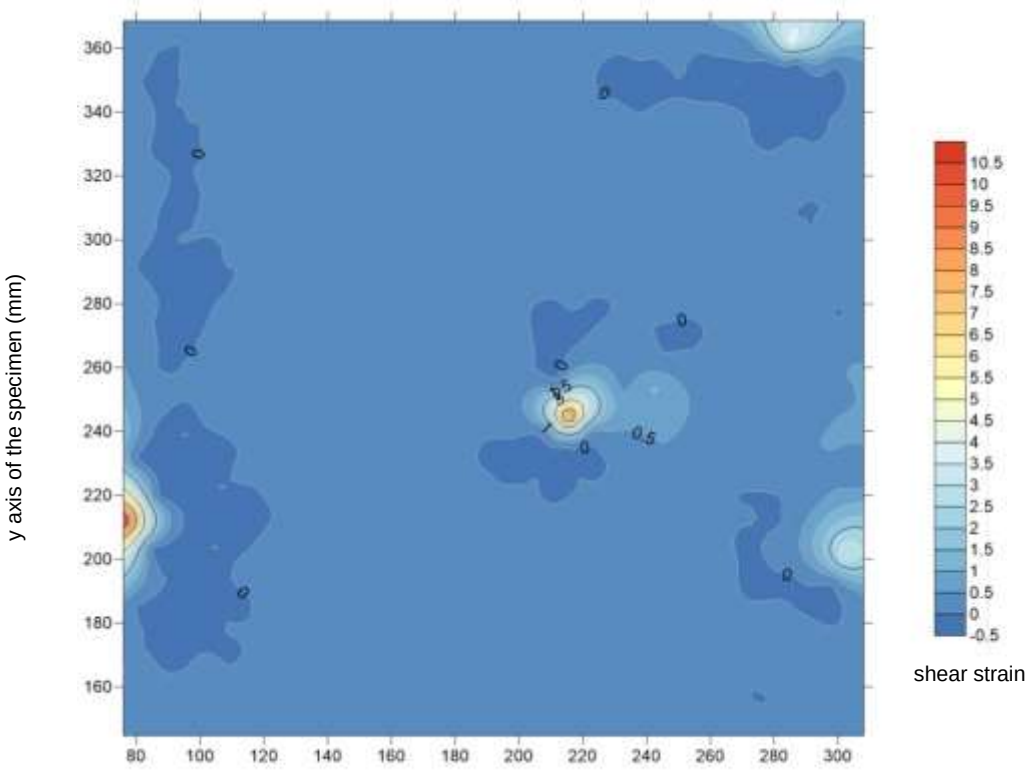

Figure 4.42: epoch 3-4 (shear ε – exp 2)

4.2.3.3 Strain Gauge

One strain gauge was installed horizontally at the middle of the wall specimen, on the 2nd horizontal mortar joint (fig. 4.30). It was installed directly on the specimen using glue. Figure 4.43 shows SG's results as recorded during the compression machine's motion resulted to the specimen's distortion. The maximum recorded strain is 0.01 and the two first peaks recorded at 16:51:42 and 16:52:06, as shown in figure 4.43, which are close to epoch 2 (16:51:46) and epoch 4 (16:52:02), respectively, as illustrated in figure 4.26. Figure 4.43 also shows that as the specimen was being compressed, the strain was giving maximum and zero values, consecutively.

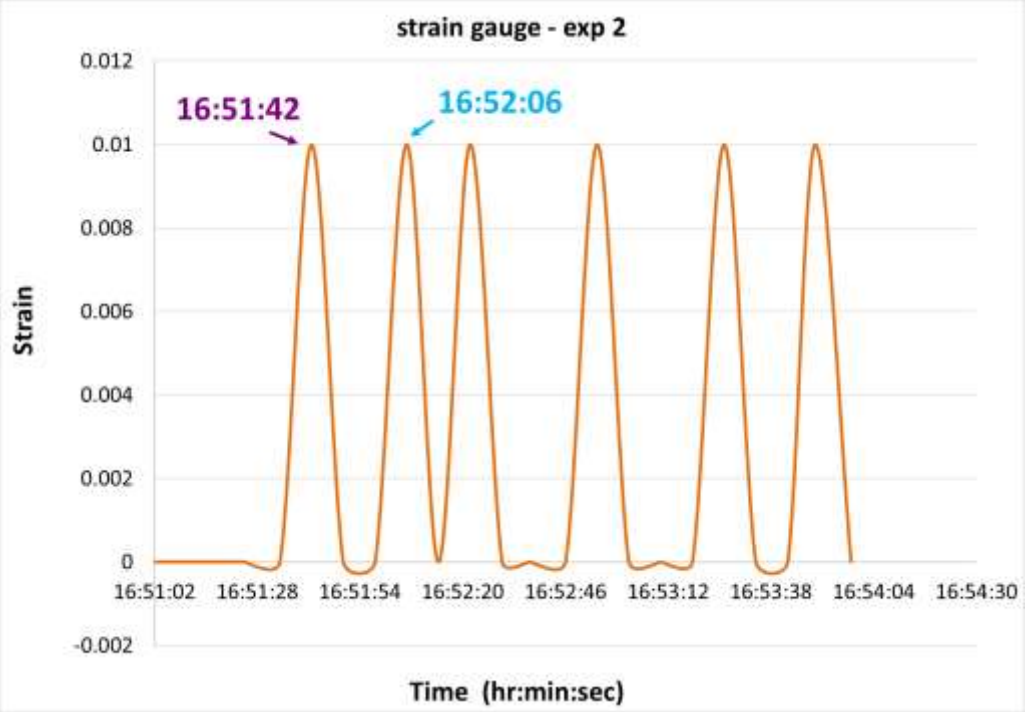

Figure 4.43: SG's results – strain over time (hour:minute:second) – exp 2

4.2.3.4 Comparisons

Figure 4.44 presents the triangulation picture from the experimental analysis, showing the triangles along the installed SG, with the view to select the corresponding triangles for the purposes of strain computation using the CRDP method. Each triangle computed one strain value using the CRDP method. The picture also shows the damage localisation as it was formed through the vertical and horizontal cracks.

Therefore, during the experimental analysis, four triangles were selected along the strain gauge (table 4.3). All the negative strain data, computed based on the CRDP method, converted to absolute values, they summed up and divided by the number of triangles. Hence, for experiment 2 the four epochs produced three strain values for each triangle using the CRDP method. These strain data are plotted and presented in figure 4.45. The maximum strain value computed between epochs 3 and 4, is 0.038 (table 4.3) recorded at 16:52:02 (diagram 4.3). Observing figure 4.43, the maximum strain recorded by the strain gauge is 0.01 at 16:52:06. Therefore, diagram 4.3 shows the time difference of 4 seconds of the recorded strains by the strain gauge and the CRDP along SG.

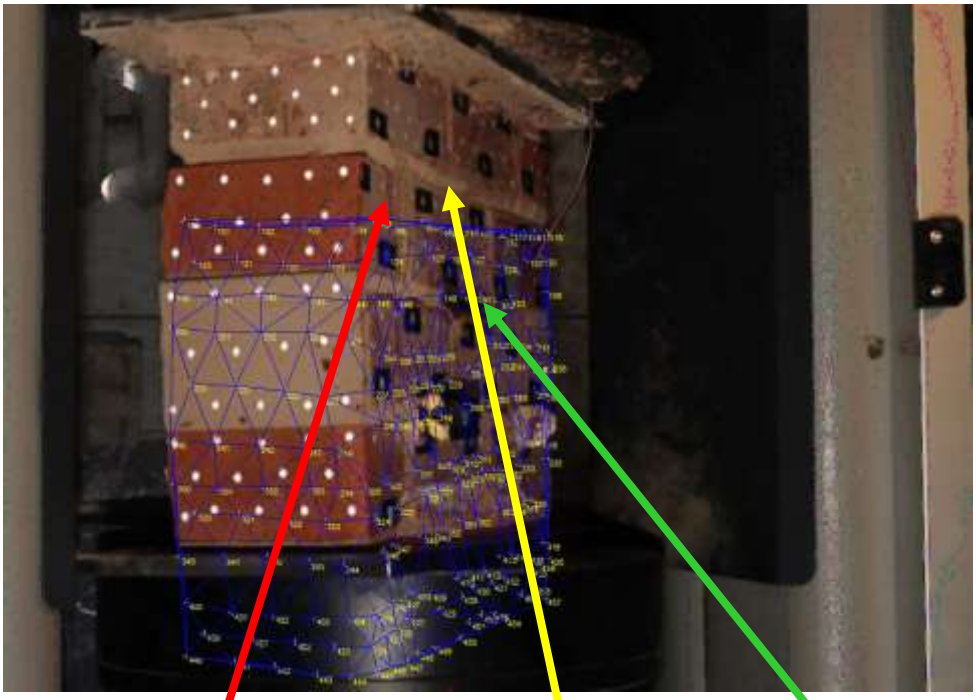

Figure 4.44: triangulation formation – exp 2

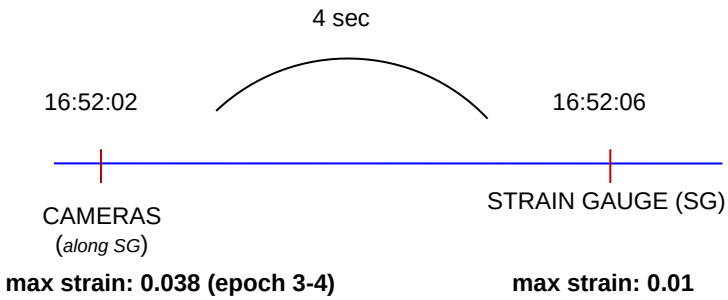

Diagram 4.3: monitoring methods recording sequence for experiment 2 along with their **max. strains**

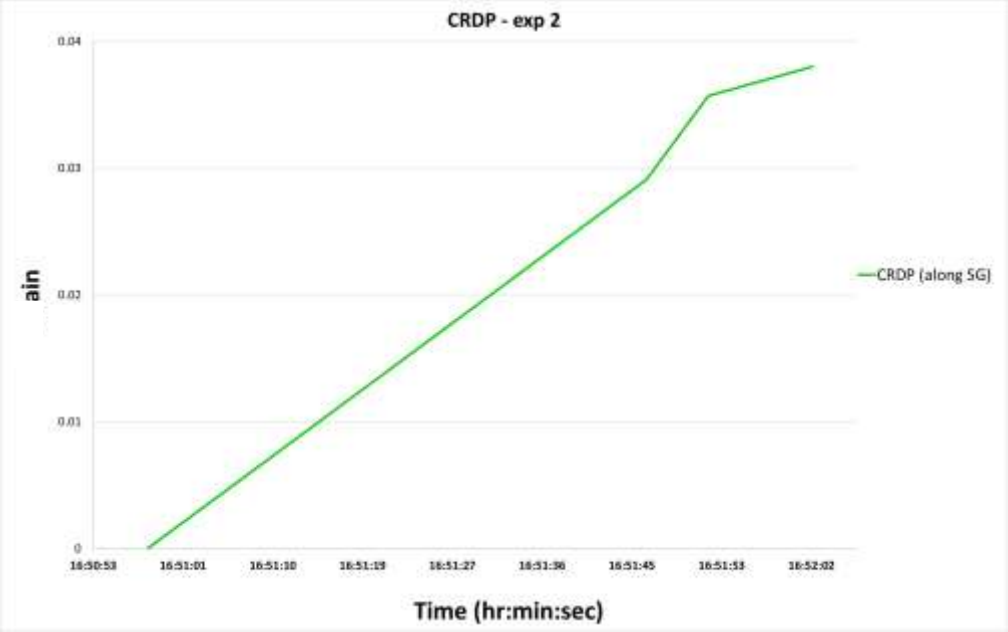

Figure 4.45: CRDP's readings along SG sensor – exp 2

					Strain - CRDP		
					Strain (1-2)	Strain (2-3)	Strain (3-4)
	triangles along SG						
1	249	309	310		0.009	0.035	-0.024
2	249	311	250		-0.020	0.047	-0.019
3	250	311	312		0.030	0.049	-0.074
4	251	312	252		-0.057	-0.012	0.035
					0.029	0.036	0.038

Table 4.3: strains using CRDP method along SG – exp 2

4.2.3.5 Summary

All monitored methods used showed sufficient deformation, displacement and strain results. Experiment 2 is the only static experiment carried out for the purposes of this research. The static set up is chosen to derive a reference experimental line for the performance, the synchronisation assumptions and the results of the monitoring means of the close-range digital photogrammetry and the strain gauge. The specimen's plasticity has been visually better presented on the deformation figures as computed from the EngVis software. However, strain gauge also showed the exact timing of the specimen's damage initiation and propagation.

4.3 Discussion

Both dynamic and static experiments carried out to single-leaf masonry specimens and have demonstrated satisfactory results for their shear strains. Figure 4.46 summarises the final deformation of the installed targets on the monitored faces and their maximum shear strains. Both graphs which present the deformation and the shear failure, for both experiments, dynamic and static, show very good correlation as they managed to capture the exact location of the damage occurred during the experiments, respectively. Therefore, the technique of close-range digital photogrammetry has been proven sufficient for capturing, monitoring and interpreting the shear failure of a masonry specimen tested under static and dynamic loading. There is a significant difference of the applied load on top of the specimens in the two experiments, as the loading under the static test was applied only at the top of the specimen. On the other case, the loading applied at the top of the specimen during the dynamic test was a simulation of the loading applied to the eastern wall of the church. There are no comparison points between the dynamic and the static loading experiments as the input loading has different characteristics. However, the static experiment is the baseline for monitoring the deformation and the shear failure of single-leaf masonry specimens and the dynamic experiment is similarly the reference line for monitoring the same parameters on experimental specimens under different set ups.

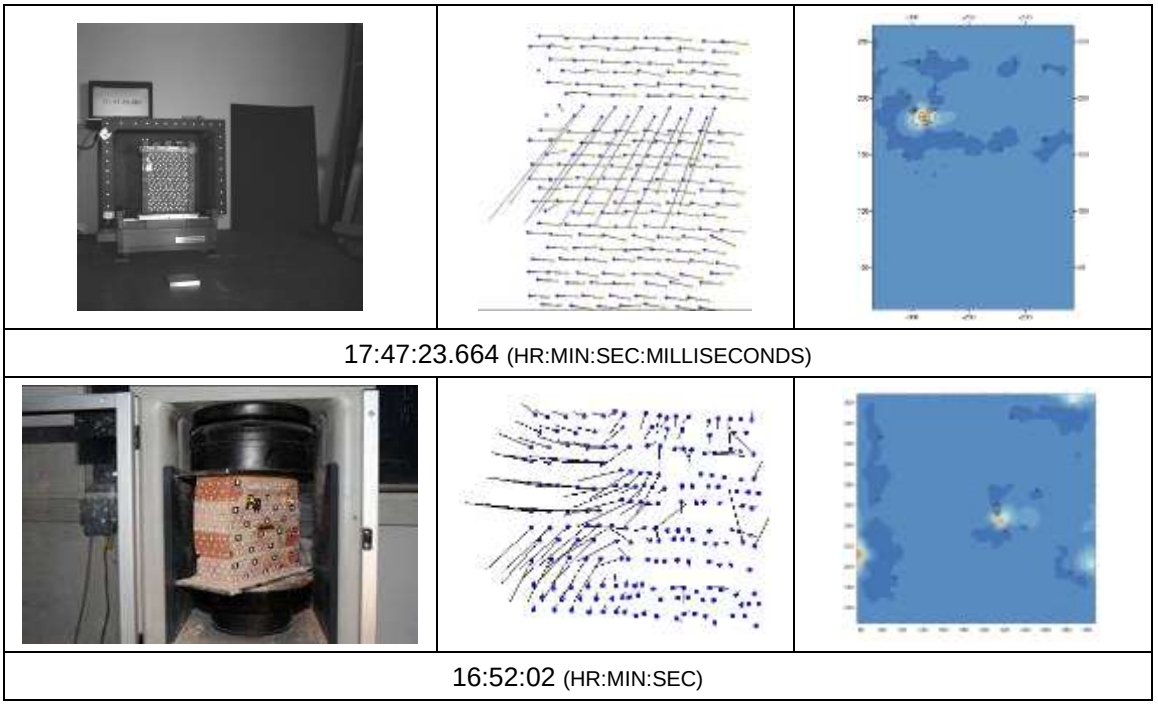

Figure 4.46: Summary of the specimens' final deformation and their maximum shear strains

There are also no comparison points between the static and dynamic base line experiments for the monitoring method of strain gauge. This technique has been proven adequate to capture and translate a difference in strain when the failure occurred on the single-leaf specimen under static loading test.

The main conclusions of experiment 1, is the necessity to increase the computers' memory and the cameras' capturing timing with the view to record the engineering specimens' damage when this will occur. Another conclusion is the importance of additional reflected targets to mini-wall's returns as crack patterns are usually formed on the connection areas between the wall's main body and their returns. The strain gauges installation with the use of an adhesive was proven sufficient to provide the readings during both experiments. Therefore, for the future experimental set ups it is decided to use this adhesive for the strain gauges.

Based on the above conclusions, regarding the static and dynamic baseline experiments, the future experimental plan is set up to show the results on an out of plane dynamic experiment, on a diagonal one – in relation to the cameras' location – and on a larger scale one.

4.4 Conclusion

The purpose of this chapter was to define the diagnostic purposes of this research through the applied experimental paths. The purpose has been accomplished, as both reference experiments, dynamic and static, have been proven adequate to provide deformation and shear failure representation of the tested single-leaf masonry specimens. Additional conclusion is the capability of the CRDP method to capture the failure and with the use of the appropriate computation means (Mohr circle) to translate this failure to displacement and strain. Therefore, for the purposes of the next steps of this research, the experimental and computational means used for the reference dynamic and static experiments, will be applied again to the remaining six experiments. Chapter 5 will present the four small scale experiments.

CHAPTER 5

SMALL SCALE EXPERIMENTS

5.1 Overview

This chapter presents and compares the results of four experiments carried out in the Advanced Structures Laboratory (UCL). Two monitoring techniques applied to the tested engineering specimens, close range digital photogrammetry and strain gauges. The experiments are categorised into two groups (Group A & B). Group A comprises of three experiments acting under an in-plane excitation and resulting to an in-plane crack propagation and collapse. However, Group B presents the out of plane crack propagation and collapse caused by out of plane excitation of the tested specimen.

The experimental work carried out and subsequently analyses are divided in two parts, one for the photogrammetric (CRDP) data and one for the strain gauge (SG) data. The SG started recording prior to the specimens' excitation. Once the shaking commenced, the cameras started shooting and recording the vibrated samples.

Group A consists of three experiments (exp 3, 4 & 5) which carried out in UCL, to the small-scale model by using model bricks of type A and B and mortar of type I. The applied excitation was on the x axis of the shaking table. The intensity of the vibration's input differed for each experiment (table 5.1). In addition, the loading to experiment 3, is double to experiment 4 and 5. However, the most important factor for this rerun is to triple-check the proposed monitoring strategy and to ensure the level of its reliability. Besides all, experiment 5 holds the same characteristics as the previous two ones with the difference that the shaking table was placed diagonally opposite to the cameras. Group B (table 5.1) consists of one experiment (exp 6) which was also carried out in UCL, to the small-scale model wall by using model bricks of type B and mortar of type I. The applied excitation was on the z axis of the shaking table. Therefore, table 5.1 summarises the characteristics of these four experiments, along with the location and number of the sensors installed. The applied load was installed at the top of each wall specimen and the excitation was applied with the purpose to produce damage to the specimen.

The applied excitation to all the experiments it is not a scaling down product, but the input amplitude (Vpp) and frequency (Hz) are the values that caused cracking to the vibrated specimens; it is a trial and error approach for all the experiments. The purpose of the different excitation inputs is to show the effect of different photogrammetric setups.

Experiment 3 has been split into two versions. Experiment 3i is comprised of 4 epochs and experiment 3ii is comprised of 5 epochs.

Similarly, experiment 4 has been split into two versions. Experiment 4i analyses the results collected by the redlake cameras and experiment 4ii analyses the results by the Nikon cameras.

	duration (sec)	*no. of cameras*	*no. of images / cameras*	*no. of epochs*	*type of shaking table*	*no. of targets*
exp 3i	117	4 redlake	300	4	small shaking table	256
exp 3ii				5		
exp 4i	15	3 redlake	300	4		
exp 4ii	92	2 nikon	20	2		
exp 5	129	4 redlake	300	4		
exp 6	129	3 redlake & 2 nikon	300 & 20	4		

	SG's location	*brick type*	*mortar type*
exp 3	horizontally along the 3rd mortar layer	B	I
exp 4	horizontally along 7th brick layer & vertically along 6th to 8th brick layer	B	I
exp 5	one diagonally along the 4th and 6th brick layer and one horizontally on the 9th mortar joint	A	I
exp 6	one horizontally along the 9th horizontal mortar joint	A	I

	Vpp	*Hz*	*applied load (kg)*	*direction of excitation*	*direction of failure*
exp 3	15	5	11.2	X axis	in plane
exp 4	20	30	5.6	X axis	in plane & out of plane
exp 5	20	25	5.6	X axis	in plane (direction of shaking)
exp 6	20	25	5.6	Z axis	in plane & out of plane

Table 5.1: Characteristics of exp 3, 4, 5 & 6

5.2 Experiment 3

Experiment 3 carried out on a small-scale masonry specimen excited on a small shaking table. The specimen was built with brick type B and mortar type I and its dimensions were 280mm in height, 240mm in length and 25mm in width. 28 control reflected targets were installed on the Π-shape frame attached to the laboratory's wall and 256 free reflected targets installed on the front face of the specimen facing the 4 redlake cameras installed at a 0.85m distance from the specimen. Each camera collected 300 images. The test ran for 117 seconds, with an input excitation value to the shaking table of 15Vpp in amplitude and of 5Hz in frequency. The input excitation applied on the x axis was a result of a trial and error with the scope to create cracking to the specimen. The imposed load applied at the top of the specimen was 11.2kg (App. II) and the strain gauge installed horizontally along the 3rd mortar layer (fig. 5.1.1).

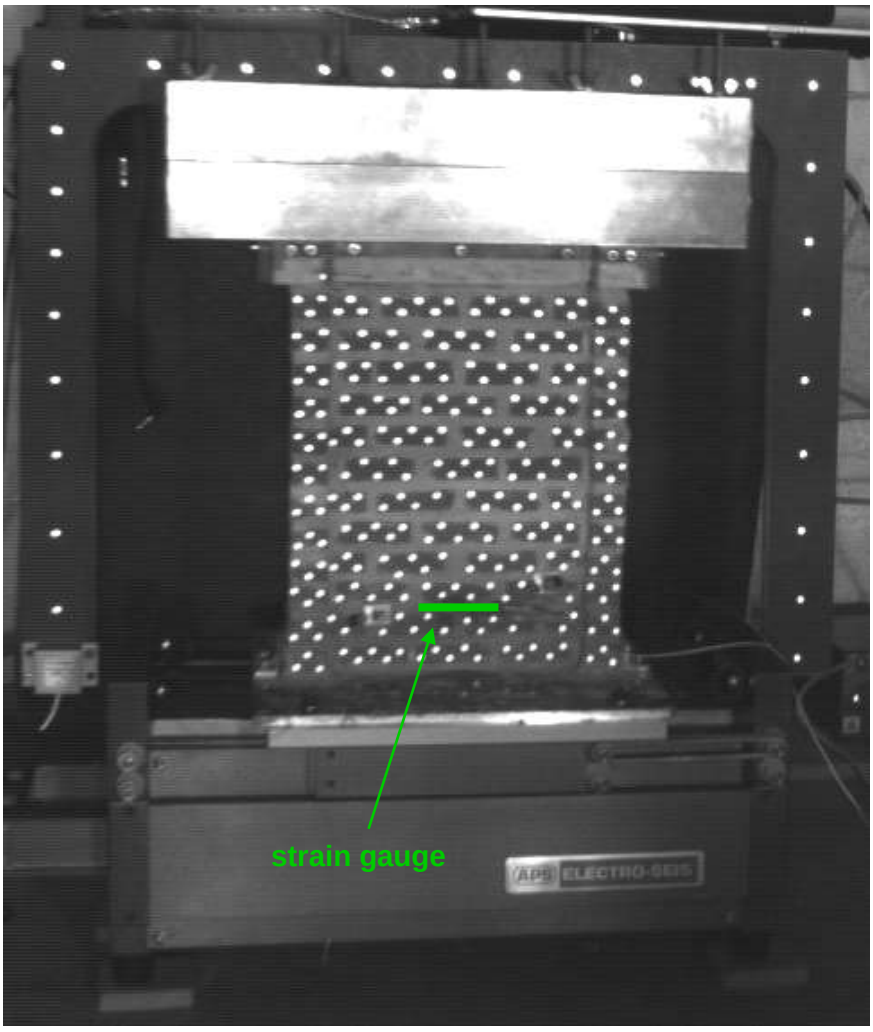

Figure 5.1.1: undamaged small-scale masonry specimen – exp 3

5.2.1 Close Range Digital Photogrammetry

For the purposes of experiment 3, two methods have been applied to analyse the images collected by the four redlake cameras. During the first method (exp 3i) sixteen images are analysed, four from each camera, which are classified into different sets of pictures called epochs. The first method is comprised of 4 epochs (diagram 5.1, fig. 5.1.2). The first epoch was chosen prior to the damage and epochs 2, 3 and 4 were chosen to show the damaged specimen during its in-plane failure. To be more specific epoch 2 was the first image that showed the cracking initiation to the specimen and based on that, the rest of the pictures were chosen and subsequently the epochs 1, 3 and 4 were defined. Epoch 1 shows the undamaged tested wall specimen, epoch 2 shows the initiation of the crack and epochs 3 and 4 the crack's propagation.

During the second method (exp 3ii) twenty images are analysed, five from each camera, comprising 5 epochs (diagram 5.1, fig. 5.1.3). This method is the same with the first one, with an extra epoch prior to the first epoch as presented in method one. The reason of this extra epoch, in method two, is to check if the prediction of the crack's initiation is feasible, under dynamic loading.

Figure 5.1.2a shows the undamaged wall-specimen in epoch 1. Figure 5.1.2b shows the slightly damaged wall-specimen in epoch 2. Figure 5.1.2c and figure 5.1.2d show the damaged wall-specimen in epochs 3 and 4, respectively. Figure 5.1.3 shows the undamaged wall-specimen in epoch -1.

Diagram 5.1 presents the timings when recording started and completed and the timings of the 5 epochs for both methods applied.

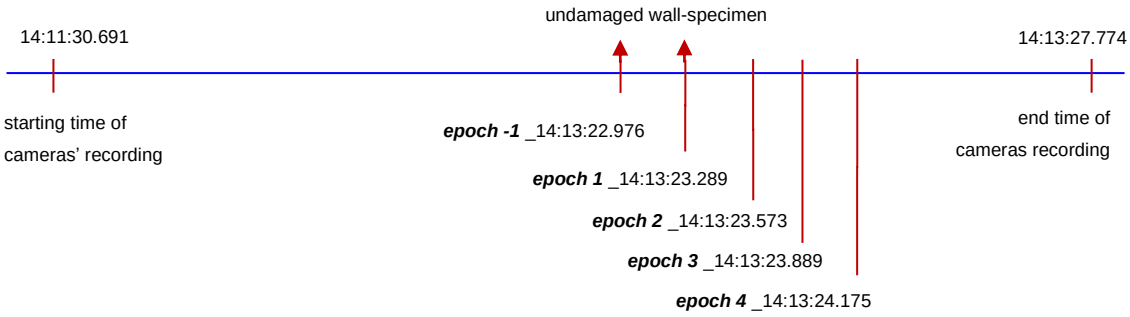

Diagram 5.1: cameras' recording timings for experiment 3 showing both methods (exp 3i & 3ii)

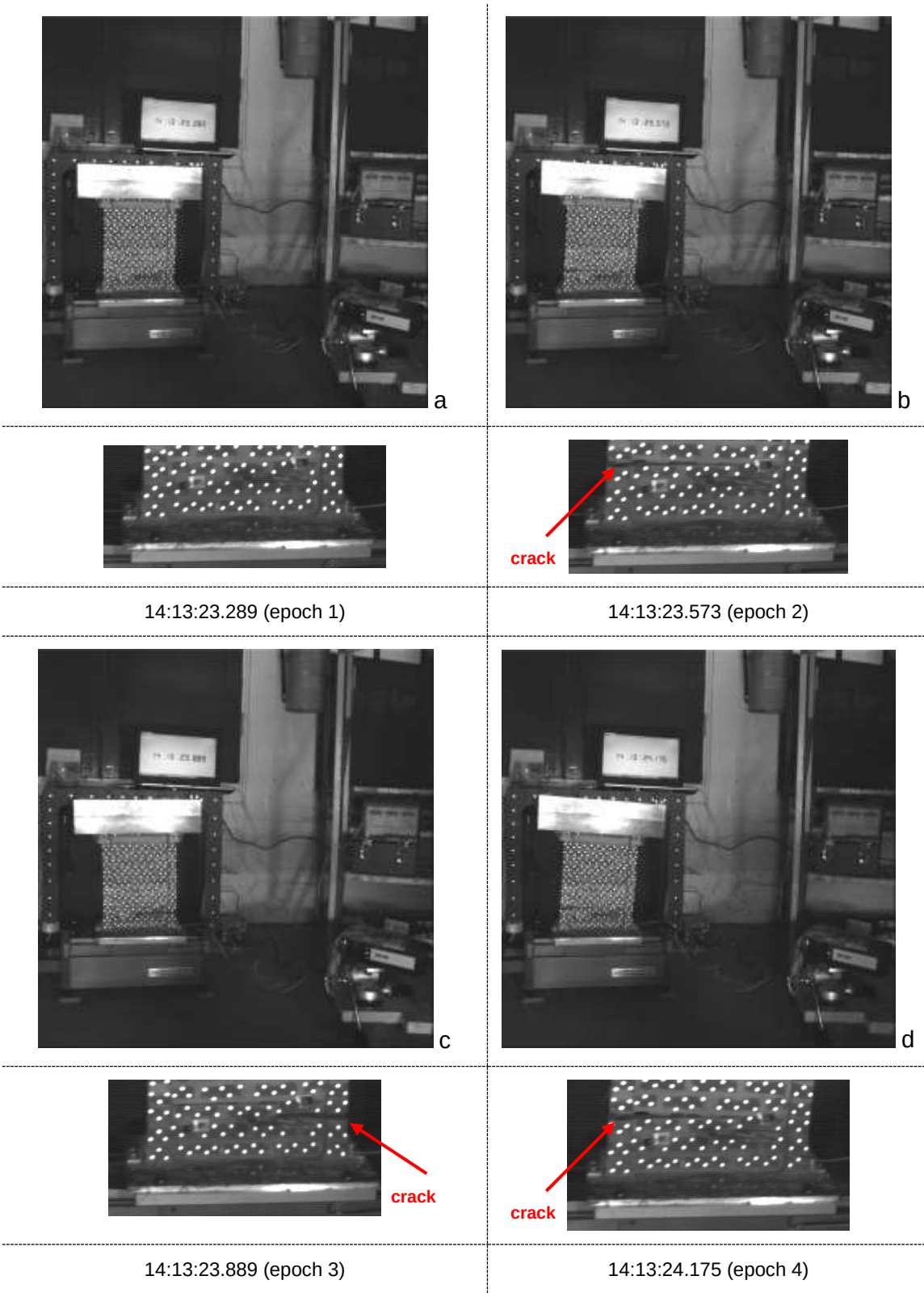

Figure 5.1.2: Images' sequences capturing the actuated tested wall – exp 3i

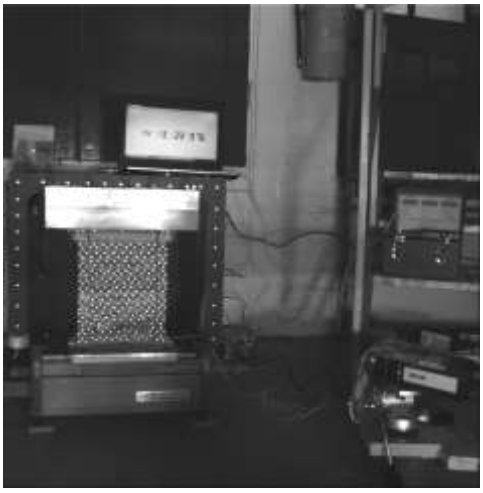

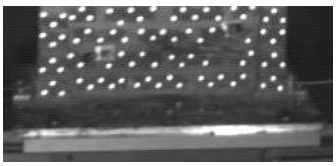

14:13:22.976 (epoch -1)

Rest epochs similar to Figure 5.1.2

Figure 5.1.3: Images' sequences capturing the actuated tested wall – exp 3ii

Once the project was set up on the VMS software and the targets were inserted, observations were created for both the control and the free targets (fig. 5.1.4). Once the required files were processed in the VMS environment, data showing the movement of the targets were produced which were inserted further into the EngVis software. This software combined all the measurements from different epochs and displayed the target movement during any stage of the experiment. The reason for using EngVis was to generate the triangulation system (fig. 5.1.8), which allowed the centroid of any three retro-reflected targets to be determined.

From the sixteen images for exp 3i and from the twenty images for exp 3ii, which captured the shaking of the model wall, the $x - y - z$ coordinates of the retro-reflective targets were measured. These images were chosen because they show the initiation and propagation of the crack. Therefore, the standard photogrammetric technique of bundle adjustment was used. From the measured displacements, the strains were calculated based on the basic strain theory (App. IV & Lee *et. al.*, 2006). All the displacements were measured in centimetres within the VMS environment, and these triangles were used as the basis for the strain computation.

Figure 5.1.4a shows the numbered reflected targets (targets ID) on the specimen (green numbers) and on the wooden frame attached to the wall (blue numbers – control points) and the four cameras (green cones). Figure 5.1.4b is the same as figure 5.1.4a along with the observations from the cameras. Figure 5.1.4c is similarly the same as figure 5.1.4a, but on 3D space. Figure 5.1.4d shows the four pictures of the specimen as captured by the three cameras in the VMS software. Figure 5.1.5 presents the additional epoch, creating 5 epochs in total for the second method, similarly in the VMS environment.

a

object view with target IDs and cameras in 2D

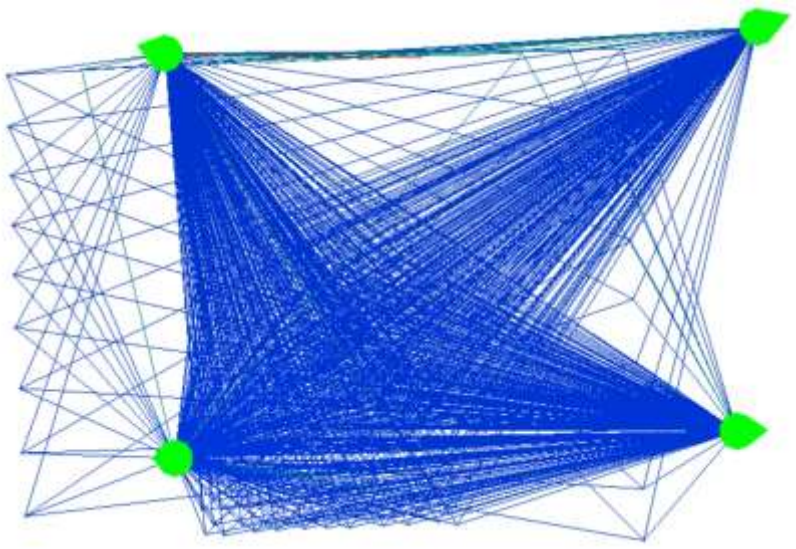

b

object view with observations

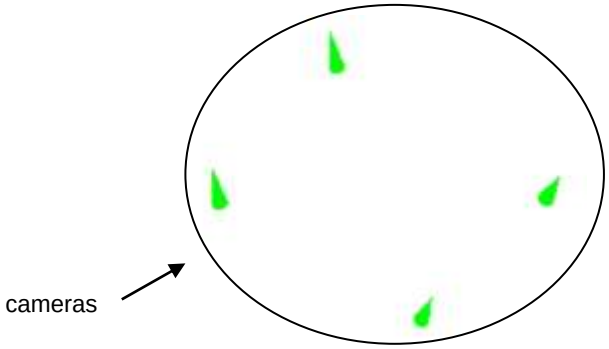

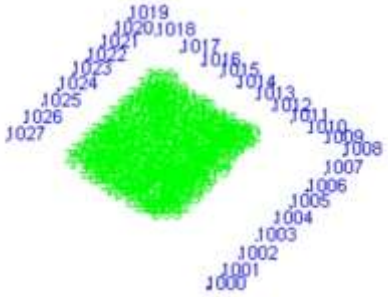

c

object view with target IDs and cameras in 3D

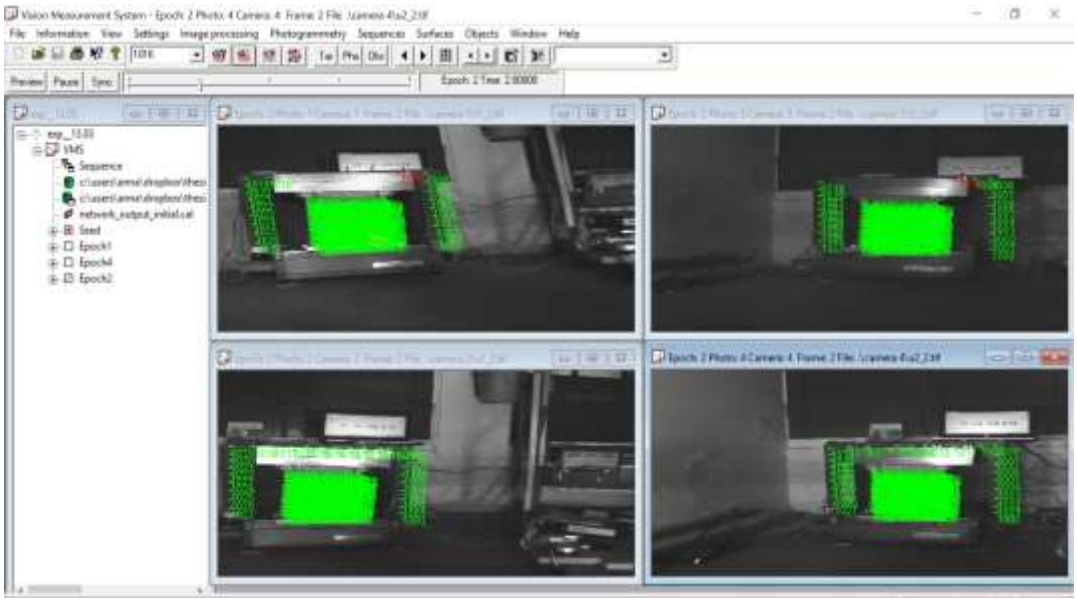

d

VMS analysis photos

Figure 5.1.4: object view of the mini-wall specimen in VMS environment – exp 3i

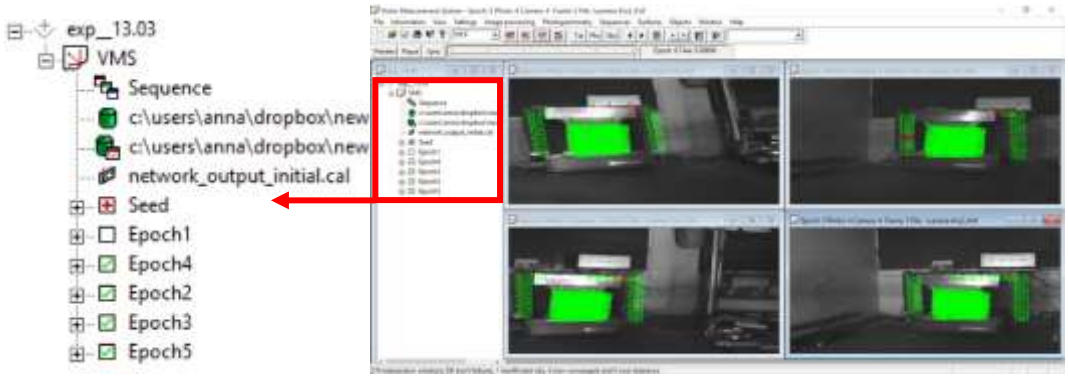

Figure 5.1.5: analysis photos of the mini-wall specimen in VMS environment – exp 3ii

Figure 5.1.6 shows the deformation of all the free reflected targets from epoch 1 to epoch 4 for experiment 3i. The dots correspond to the monitored reflected targets and figure 5.1.6 verifies figure 5.1.2. Epoch 1 shows the targets on their initial position, epoch 2 presents the initiation of a slight differentiation between the bottom three layers of the specimen and the rest top one, where the crack has been initiated according to figure 5.1.2. On figure 5.1.6, for both epochs 3 and 4, show again the same differentiation between the three bottom layers of the specimen, to the rest top ones, showing a larger intensity on the targets' movement, which explains that as the specimen was vibrating on the x axis, the opening of the crack was increasing. The summary of the targets' movement for all the epochs, is also presented in figure 5.1.6.

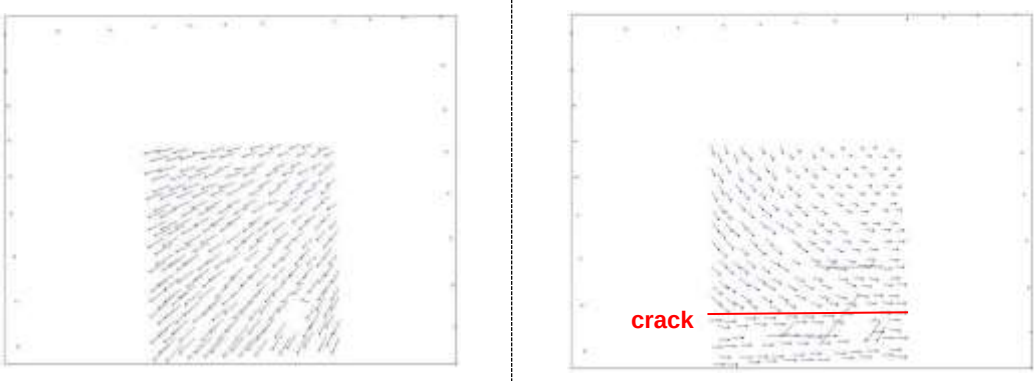

epoch 1 | epoch 2

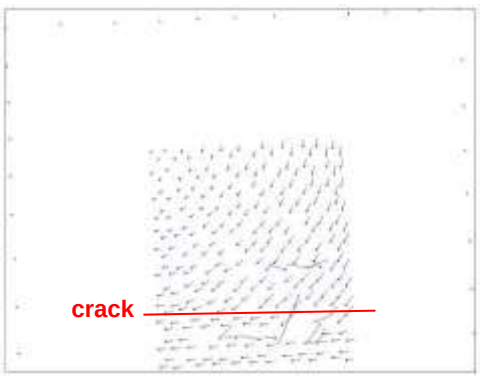

epoch 3

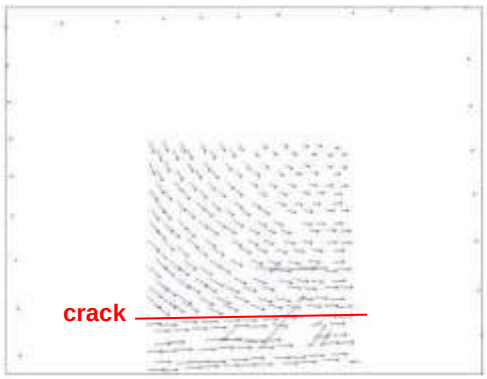

epoch 4

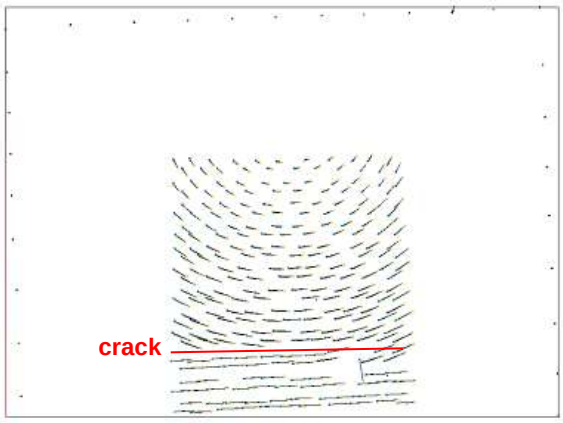

epoch 1-4

Figure 5.1.6: Deformation of specimen's triangles – exp 3i

Figure 5.1.7 shows the deformation of all the free reflected targets from epoch -1 to epoch 4 for experiment 3ii. The dots correspond to the monitored reflected targets and figure 5.1.7 verifies figure 5.1.3. Epoch -1 shows the targets on their initial position and epoch 1 presents their minor movement. Epoch 2 shows the differentiation between the bottom three layers of the specimen and the rest top ones, where the crack was initiated according to figure 5.1.2. Under this epoch, the top rows of the targets show a rapid circular movement, which reflects to a rapid motion of the specimen during this timing. On figure 5.1.7, the deformation pictures for both epochs 3 and 4, show again the same differentiation between the three bottom layers of the specimen, to the rest top ones, at a larger intensity on the targets' movement, which explains that as the specimen was vibrating on the x axis, the opening of the crack was increasing. The summary of the targets' movement for all the epochs, is also presented in figure 5.1.7.

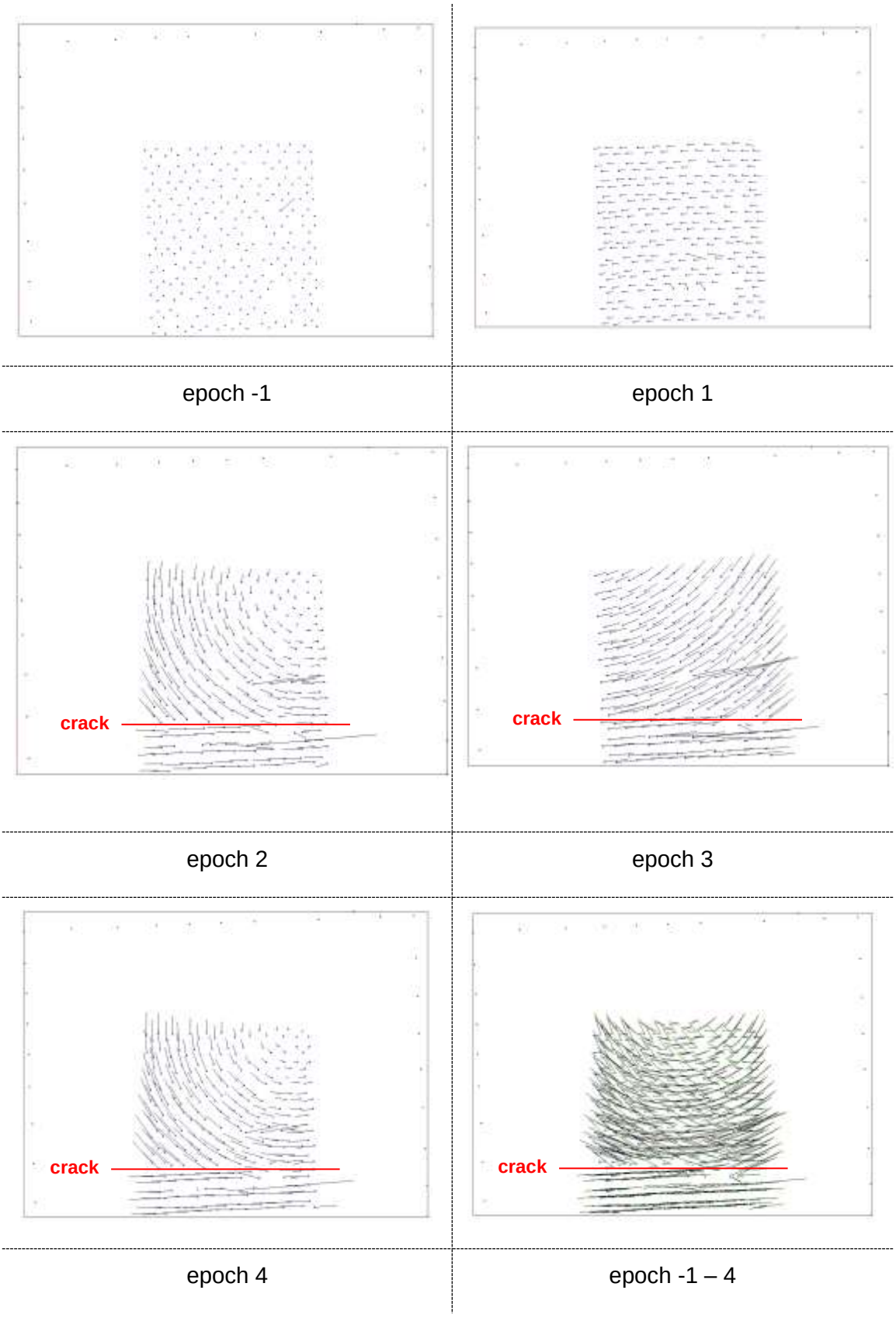

Figure 5.1.7: Deformation of specimen's triangle – exp 3ii

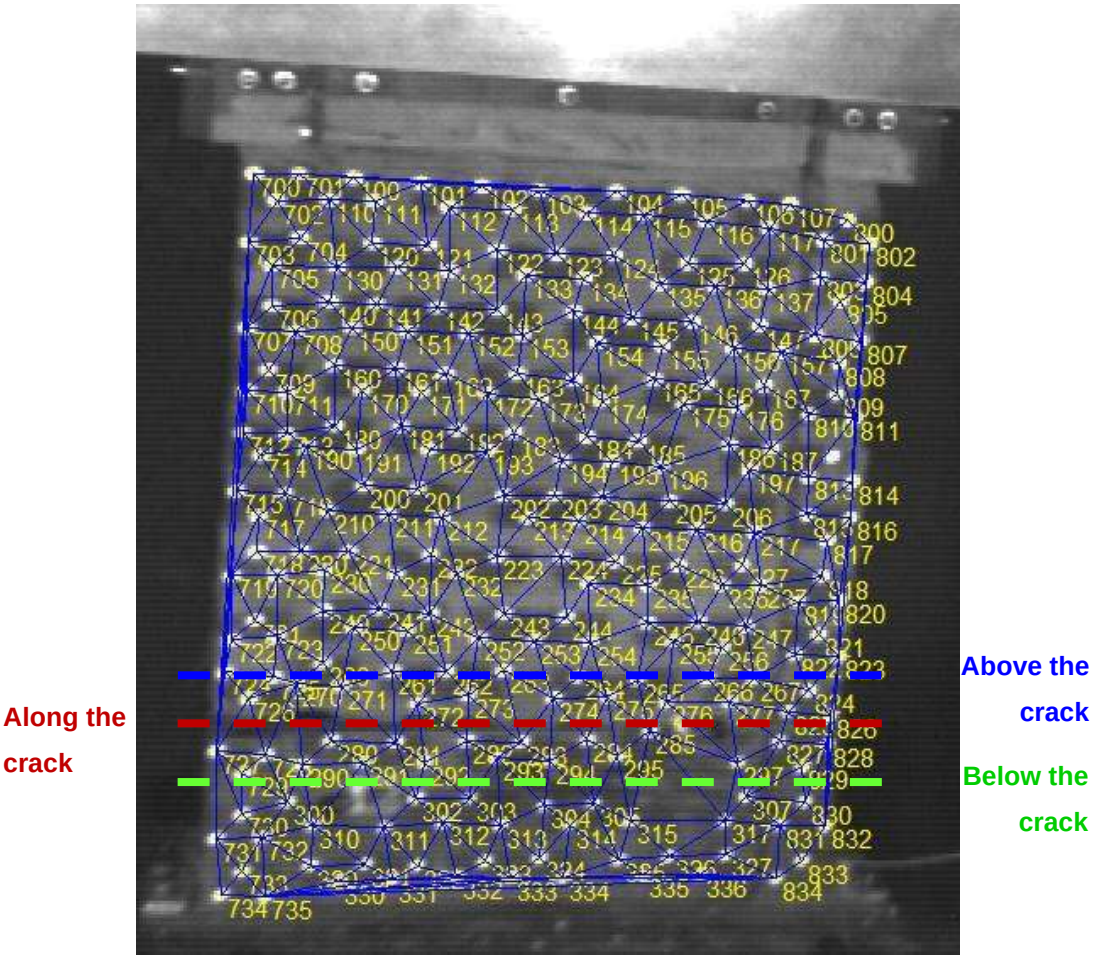

Figure 5.1.8: triangulation computed in EngVis – exp 3i

After the completion of the experiment and having observed the crack path, three groups (fig. 5.1.8) of triangles are decided to be analysed and discussed additionally for their displacement results. These are presented in graphs in relation to the specimen's length. The first group is consisted of twenty triangles showing the displacement range of the triangles' centroids located above the crack, as it is observed and monitored during the experimental phase. The second group is consisted of nineteen triangles along the same crack and the third group of seventeen below the crack.

Figures 5.1.9 – 5.1.11 present the displacement range of the triangles' centroids of these three groups in relation to the specimen's length (x axis) between the four different epochs. It does not start at zero on the x axis as the first measurement is the centroid of the first triangle, which is at 12.5mm on the axis of the graph (fig. 5.1.9). Figure 5.1.9 shows the triangles' centroids displacement from epoch 1 to epoch 2 with a range of 1.9-3.23mm for the group of triangles above, along and below the crack,

providing a figure of the specimen's distortion during the first 284 milliseconds (epochs 1-2) of its analysed motion. Within this timing (epochs 1-2) only four triangles, one located above the crack, one along the crack and two below the crack, which are located between the 100-140mm along the specimen's x axis show smaller peaks displaced from 0.47mm to 1mm. Figure 5.1.10 has the same form as figure 5.1.9 and shows the triangles' centroids displacement from epoch 2 to epoch 3, however the displacement range for the same group of triangles is significantly larger than the previous epoch, with a range of 13-18.9mm during the next 316 milliseconds (epochs 2-3) of the analysed motion. Again, within this timing (epochs 2-3) only four triangles, one located above the crack, one along the crack and two below the crack, which are located between the 100-140mm along specimen's x axis show smaller peaks displaced from 5mm to 8.3mm. Figure 5.1.11 is a mirror of figures 5.1.9 and 5.1.10, which possibly explains that as the specimen was moving in time from epoch 1 to epoch 3 and then to epoch 4, the materials' particles of the mini-wall behaved the same on the x axis of the motion. Figure 5.1.11 shows the triangles' centroids displacement from epoch 3 to epoch 4 with a range of 15-22mm for the group of triangles above, along and below the crack, providing a figure of the specimen's distortion during the last 286 milliseconds of its analysed motion. Within this timing only four triangles, one located above the crack, one along the crack and two below the crack, which are located between the 100-140mm along the specimen's x axis show larger peaks displaced from 5.6mm to 9.3mm. The very big values computed on the x axis may be used as a prognosticate element for the shear failure occurred and the formation of the crack, as shown in figure 5.1.2.

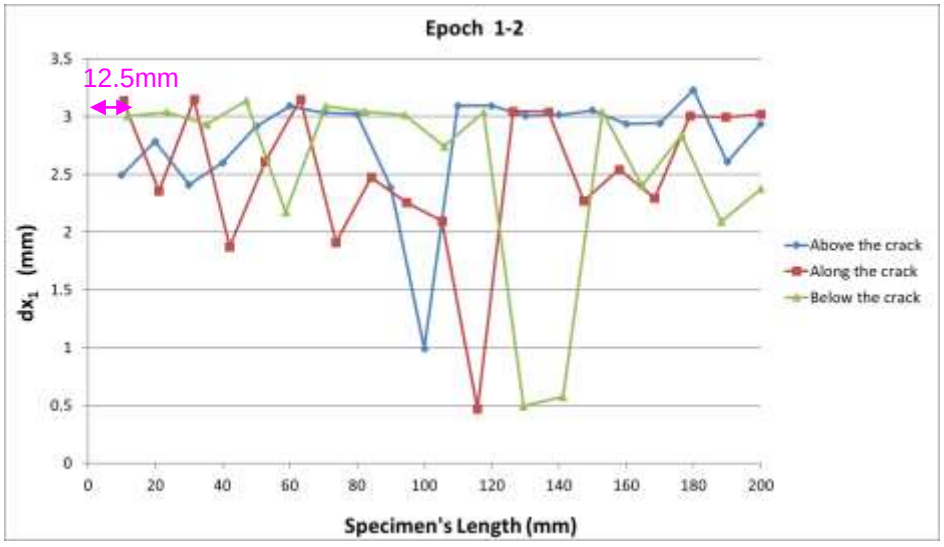

Figure 5.1.9[1]: epoch 1-2 (dx_1 – exp 3i)

[1] Figure 5.1.9 corresponds to experiment 3.

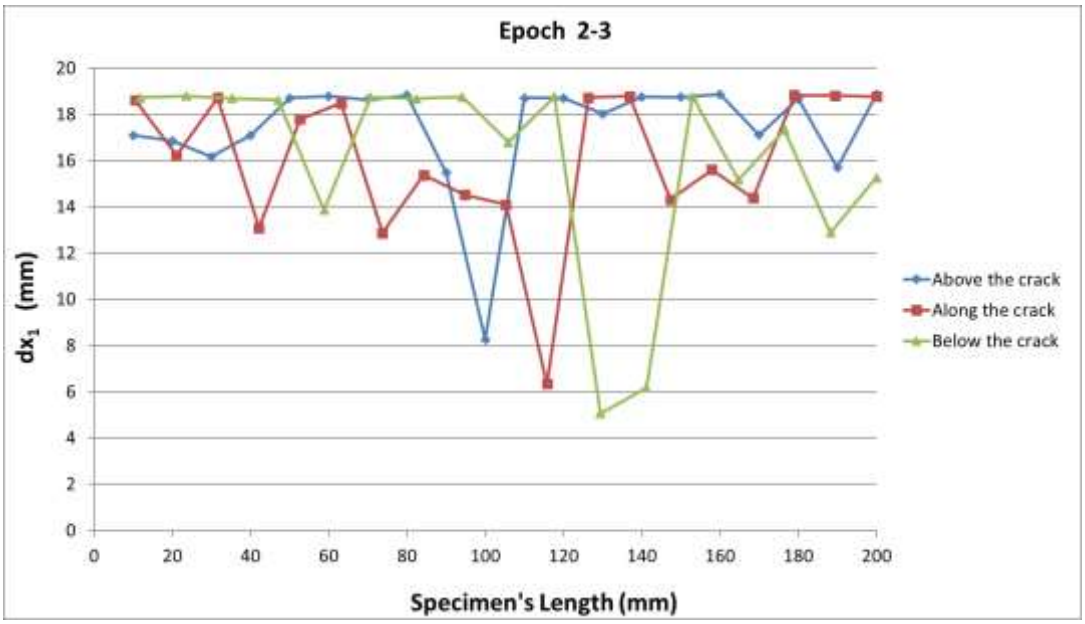

Figure 5.1.10: epoch 2-3 (dx_1 – exp 3i)

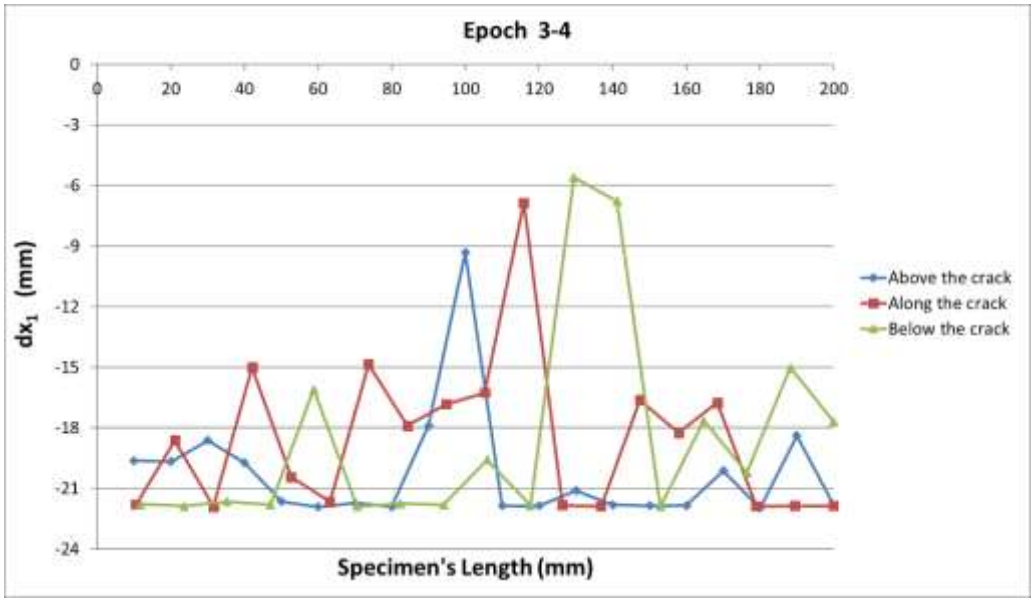

Figure 5.1.11: epoch 3-4 (dx_1 – exp 3i)

Figures 5.1.12 – 5.1.14 present the computed shear strain of the measured targets for experiment 3i, using the layout of a contour map. These contour maps use for plotting the $x-y$ – z centroid coordinates of each triangle, which is created using the Surfer software. The x-axis represents the length of the tested specimen, the y-axis the height, and the contours the shear strain. Figure 5.1.12 shows shear strain values up to 2.5 mainly at the bottom of the specimen between epochs 1 and 2. Figure 5.1.13

shows the shear strain values up to 8, between epochs 2 and 3, similarly at the bottom of the specimen. Figure 5.1.14 shows the shear strain values up to 18, between epochs 3 and 4. These big values show that the specimen was undergoing a crack opening at the bottom of the specimen.

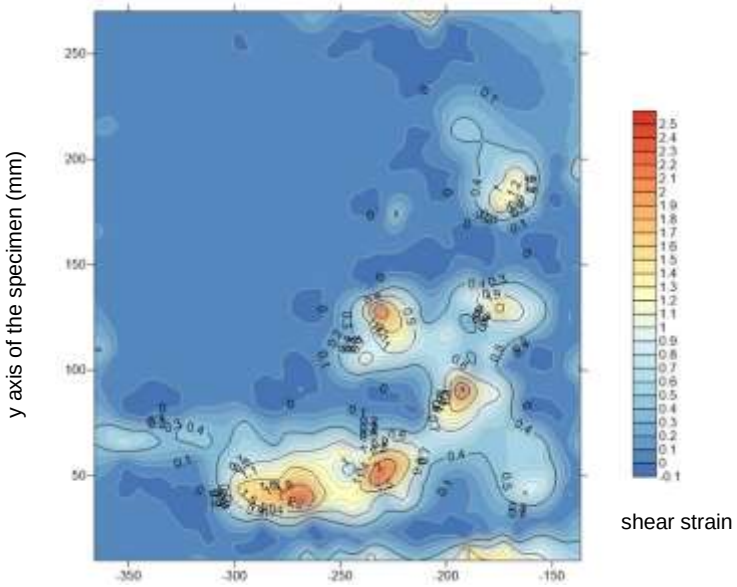

Figure 5.1.12: epoch 1-2 (shear ε – exp 3i)

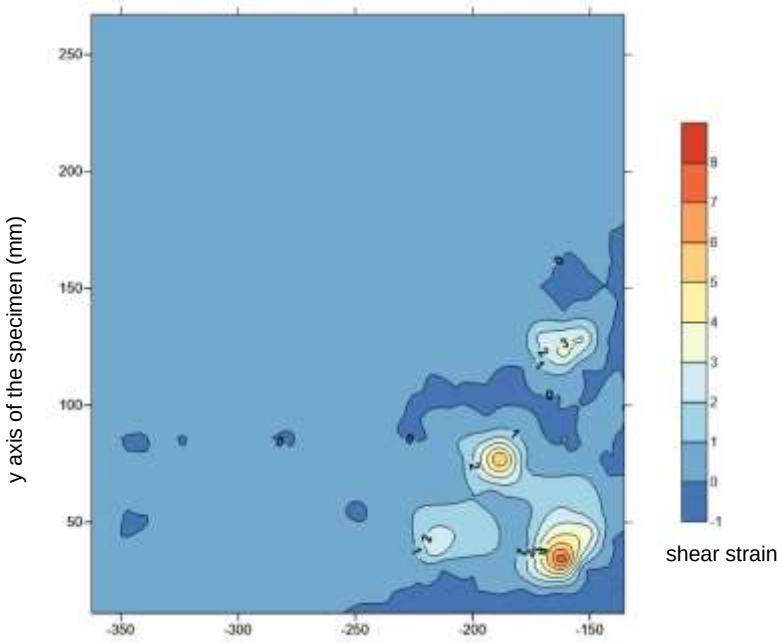

Figure 5.1.13: epoch 2-3 (shear ε – exp 3i)

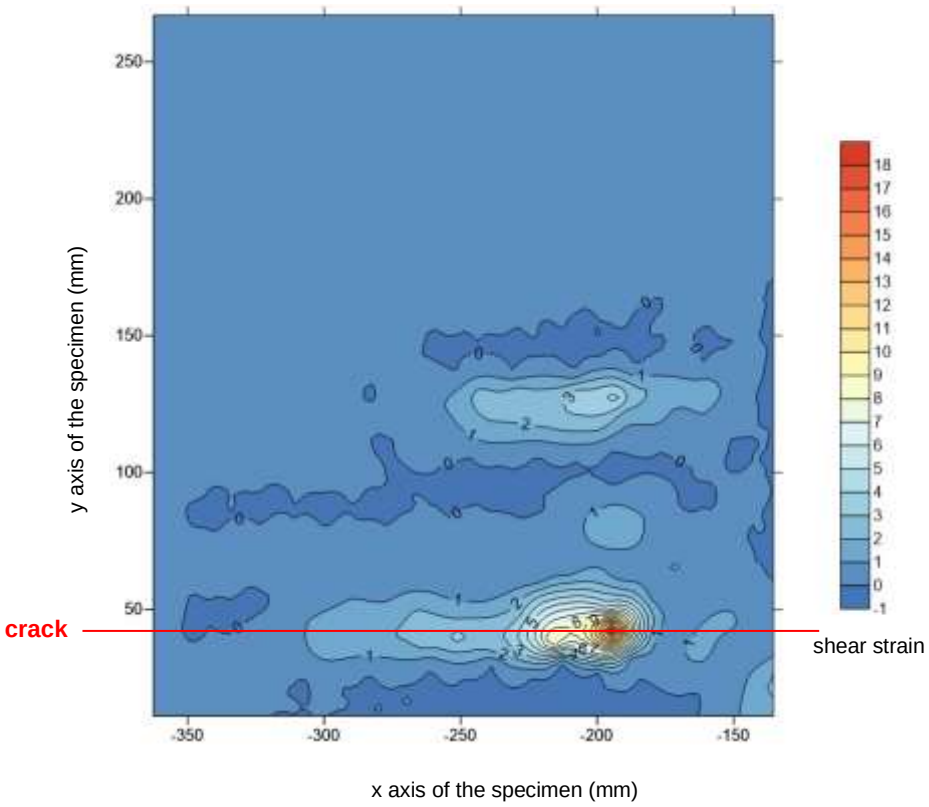

Figure 5.1.14: epochs 3-4 (shear ε – exp 3i)

Figures 5.1.15-5.1.18 present the shear strain results of the tested mini-wall for experiment 3ii using the layout of a contour map. These contour maps use for plotting the $x-y$ – z centroid coordinates of each triangle, which is created using the Surfer software. The x-axis represents the length of the tested specimen, the y-axis the height, and the contours the shear strain.

Figure 5.1.15 shows shear strain values up to 5.2 between epochs -1 and 1. These shear strain contours show the initiation of the crack before being captured by the cameras as shown in figure 5.1.3. Therefore, the monitoring method of close-range digital photogrammetry can detect the location of the shear failure of a crack before it is visible. This is of major importance for the monitoring method of CRDP, as it is proved that it can predict failure before it is captured.

Figure 5.1.16 shows shear strain values up to 2.5 mainly at the bottom of the specimen between epochs 1 and 2. Figure 5.1.17 shows the shear strain values up to 6, between epochs 2 and 3 and figure 5.1.18 shows the shear strain values up to 21, between epochs 3 and 4. These big values show that the specimen was undergoing a crack opening at the bottom of the specimen.

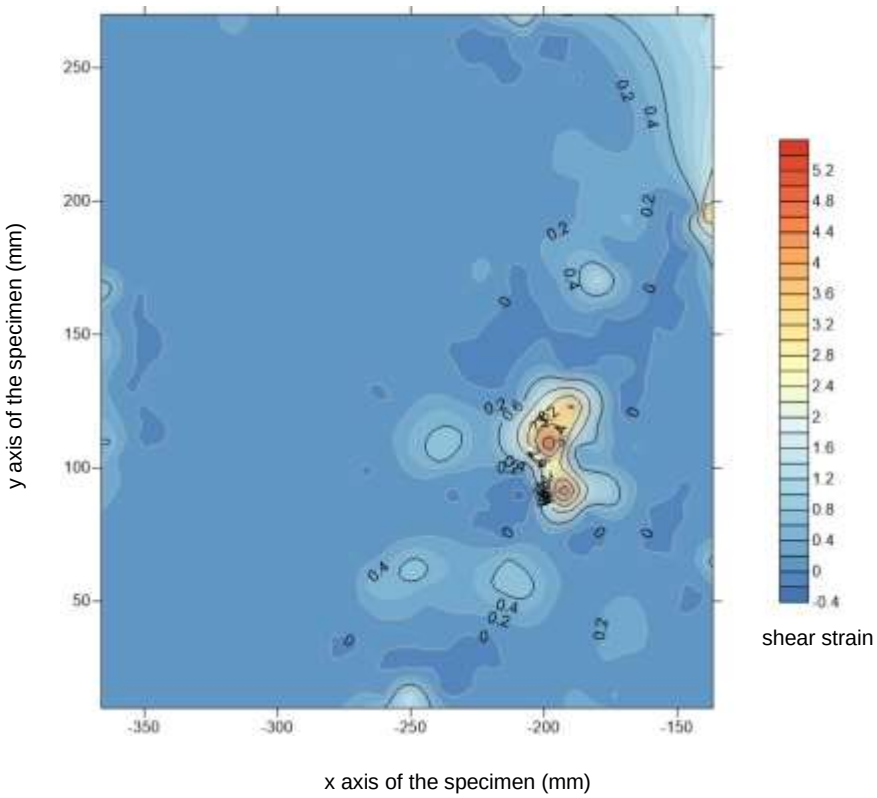

Figure 5.1.15: epoch -1 – 1 (shear ε – exp 3ii)

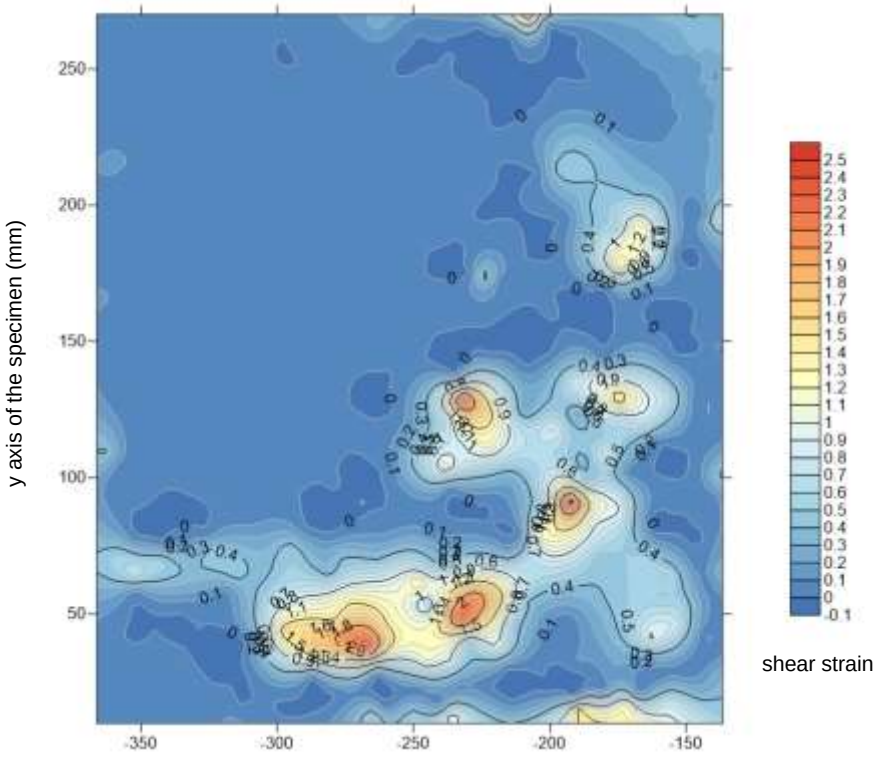

Figure 5.1.16: epoch 1-2 (shear ε – exp 3ii)

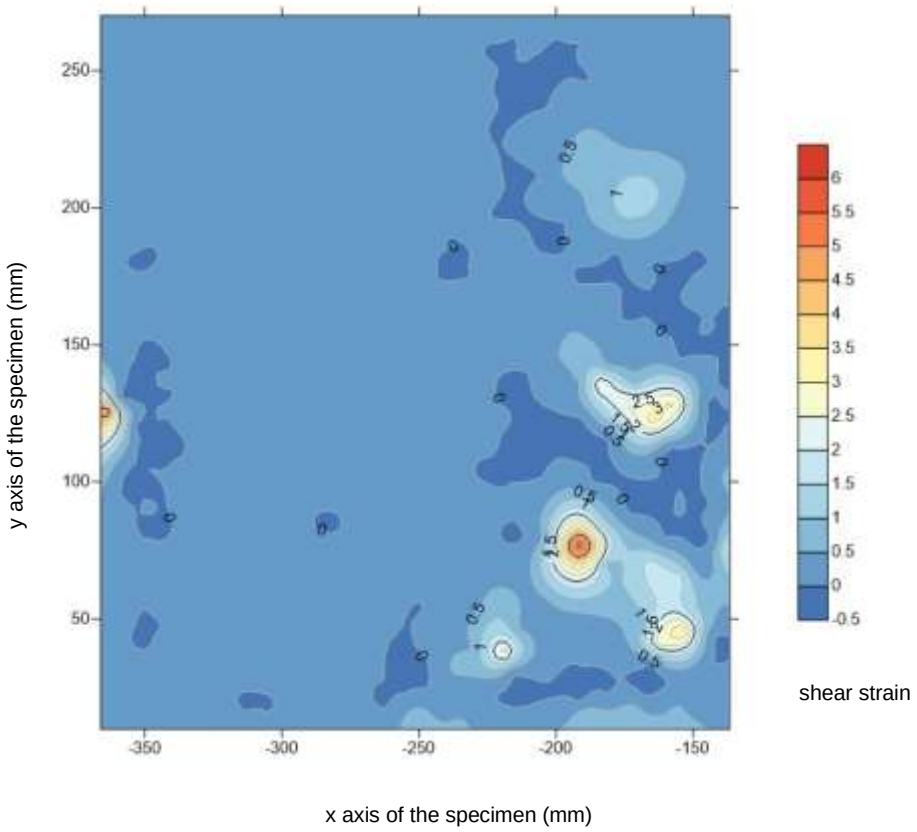

Figure 5.1.17: epoch 2-3 (shear ε – exp 3ii)

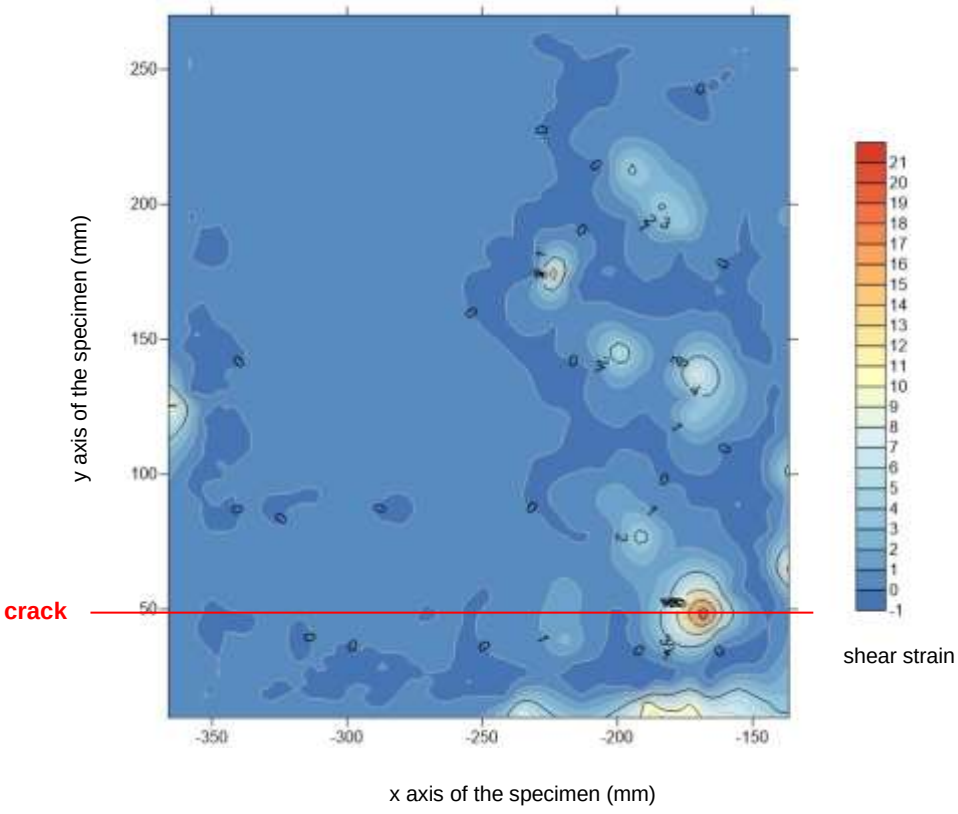

Figure 5.1.18: epoch 3-4 (shear ε – exp 3ii)

5.2.2 Strain Gauge

One strain gauge was installed at the bottom of the mini-wall, horizontally right above the second row of bricks at the bottom of the specimen, on the mortar's location. It was installed using the same method as described in chapter 4.2.3.3. Figure 5.1.19 shows the SG's results as recorded during the motion of the specimen. The graph shows that the crack started occurring after the 20-25 seconds of the monitored motion. As shown on figure 5.1.2, the crack started occurring at 14:13:23.289. At 14:13:23, it was also recorded the largest peak from the strain gauge showing a value of 0.057.

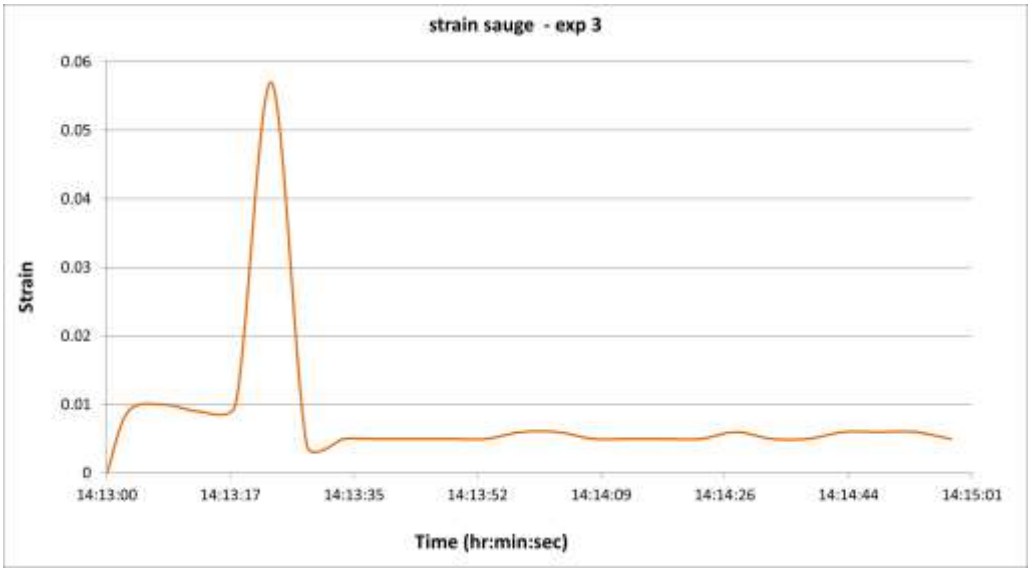

Figure 5.1.19: SG's results – strain over time (hour:minute:seconds) – exp 3

5.2.3 Comparisons

Figure 5.1.20 presents part of the triangulation picture from the experimental analysis. The triangulation picture is zoomed in, on the area of the installed strain gauge (SG) to select the corresponding triangles for the purposes of strain computation using the CRDP method. Each triangle computed one strain value using the CRDP method.

Therefore, during the experimental analysis, eleven triangles were selected along the strain gauge (table 5.2). All the negative strain data, computed based on the CRDP method, converted to absolute values, they summed up and divided by the number of triangles. Hence, the four epochs produced three strain values for each triangle using

the CRDP method (fig. 5.1.21). The strain value computed between epochs 3 and 4, is 0.016 (table 5.2) recorded at 14:13:24.175 (diagram 5.2). Observing figure 5.1.19, the maximum strain recorded by the strain gauge is 0.057 at 14:13:23. Therefore, diagram 5.2 shows the time difference of 1.175 seconds of the recorded strains by the strain gauge and the CRDP along SG.

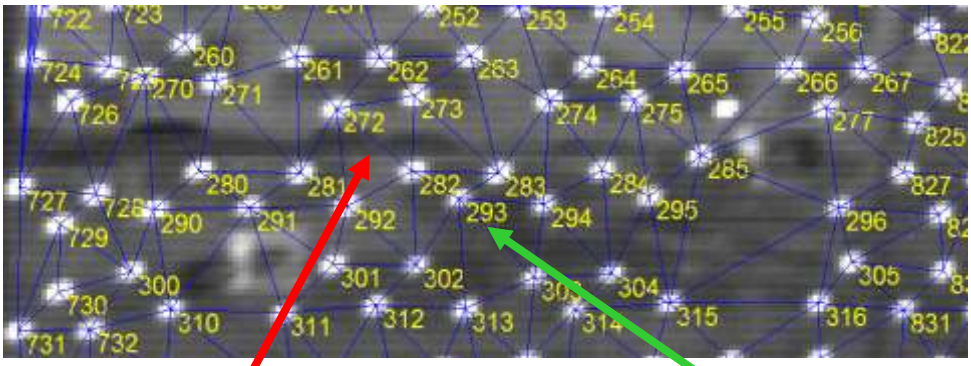

crack | strain gauge

Figure 5.1.20: zoomed area on the triangulation picture – exp 3

					Strain - CRDP		
					Strain (1-2)	Strain (2-3)	Strain (3-4)
	triangles along SG						
1	283	293	294		0.002	-0.005	0.003
2	302	303	292		-0.001	0.005	-0.004
3	303	293	292		0.001	-0.002	0.001
4	293	303	304		-0.002	-0.001	0.003
5	282	292	293		-0.001	0.010	-0.009
6	282	293	283		-0.010	-0.047	0.059
7	283	294	284		-0.004	0.005	-0.006
8	294	295	284		0.018	0.060	-0.077
9	294	293	304		-0.012	-0.002	-0.007
10	285	275	284		-0.010	0.006	0.004
11	285	284	295		0.001	-0.002	0.000
					0.006	0.013	0.016

time (hr:min:sec:millisec) – epochs	14:13:23.573	14:13:23.889	14:13:24.175

Table 5.2: strains using CRDP method along SG – exp 3

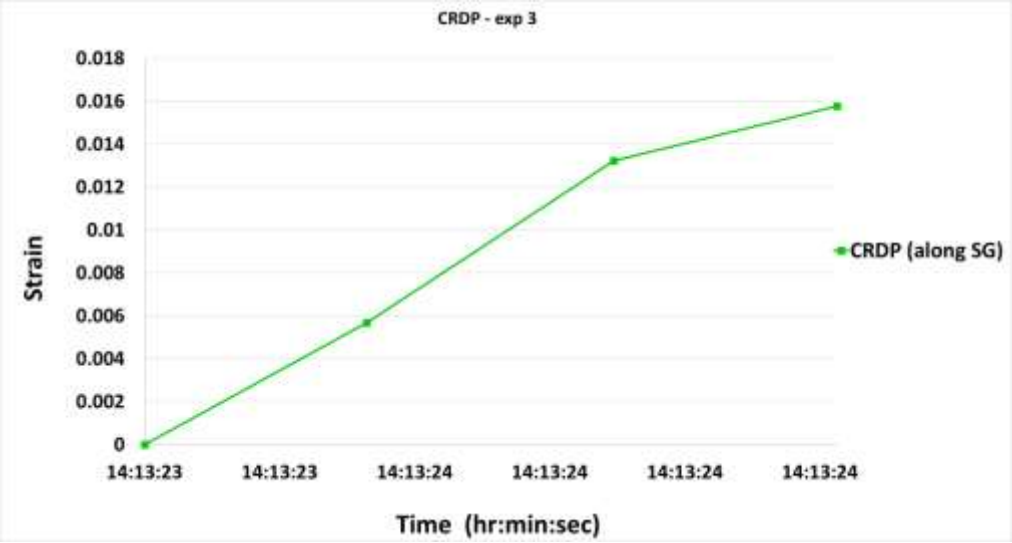

Figure 5.1.21: CRDP's readings along SG sensor – exp 3

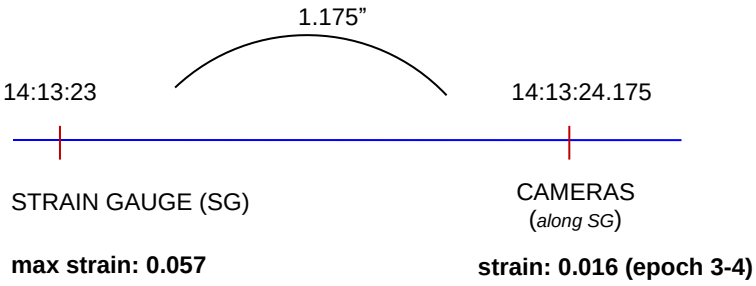

Diagram 5.2: strains along the monitoring methods for experiment 3

5.3 Experiment 4

Experiment 4 carried out on a small-scale masonry specimen excited on a small shaking table. The specimen was built with brick type B and mortar type I and its dimensions were 280mm in height, 240mm in length and 25mm in width. 28 control reflected targets were installed on the Π-shape frame attached to the laboratory's wall and 256 free reflected targets installed on the front face of the specimen facing the 3 redlake cameras and the two Nikon cameras installed at a 0.85m distance from the specimen. Each redlake camera collected 300 images and each Nikon camera collected 20 images. The test for the redlake cameras ran for 15 seconds and 92 seconds for the Nikon cameras, with an input excitation value to the shaking table of 20Vpp in amplitude and of 30Hz in frequency. The input excitation applied on the x axis was a result of a trial and error with the scope to create cracking to the specimen. For checking the specimen's distortion under different loading, an imposed load of

5.6kg was applied at its top. One strain gauge installed horizontally along the 7th brick layer and another one installed vertically along the 6th to the 8th brick layer (fig. 5.2.1).

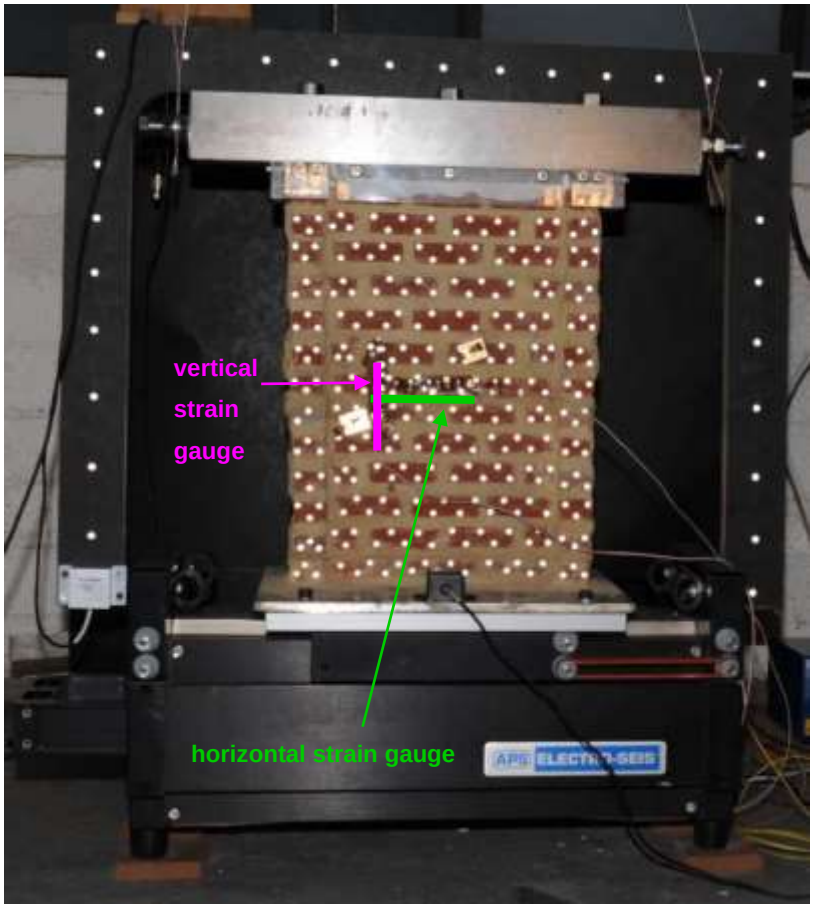

Figure 5.2.1: undamaged small-scale masonry specimen – exp 4

5.3.1 Close Range Digital Photogrammetry

For the purposes of experiment 4, two methods have been applied to analyse the images collected by the three redlake cameras and the two nikon cameras. During the first method (exp 4i), the three synchronised redlake cameras collected three hundred images per camera from which thirty-nine images were analysed, thirteen from each camera, and are classified into different sets of pictures called epochs. Due to minor changes between the thirteen epochs, the analysis was further narrowed down to four stages. Therefore, the first method is comprised of 4 epochs (diagram 5.3, fig. 5.2.2). The first epoch was chosen prior to the damage and epochs 2, 3 and 4 were chosen to show the damaged specimen during its in-plane failure. To be more specific epoch 2 was the first image that showed the cracking initiation and based on that, the rest of the epochs were created and subsequently the epochs 1, 3 and 4 were defined.

Epoch 1 shows the undamaged tested wall specimen, epoch 2 shows the initiation of the crack and epoch 3 and 4 the crack's propagation.

During the second method (exp 4ii), the two synchronised nikon cameras collected five images per camera, from which two from each camera are analysed, comprising 2 epochs (diagram 5.3, fig. 5.2.12). The reason of the second method is to check if the prediction of the crack's initiation is the same either using redlake or nikon cameras.

Diagram 5.3 presents the timings for both methods when recording started and completed and the timings of all the epochs for both methods applied. Figures 5.2.3 and 5.2.13 show the observations which are created for both the control and the free targets and their analysis in the VMS environment.

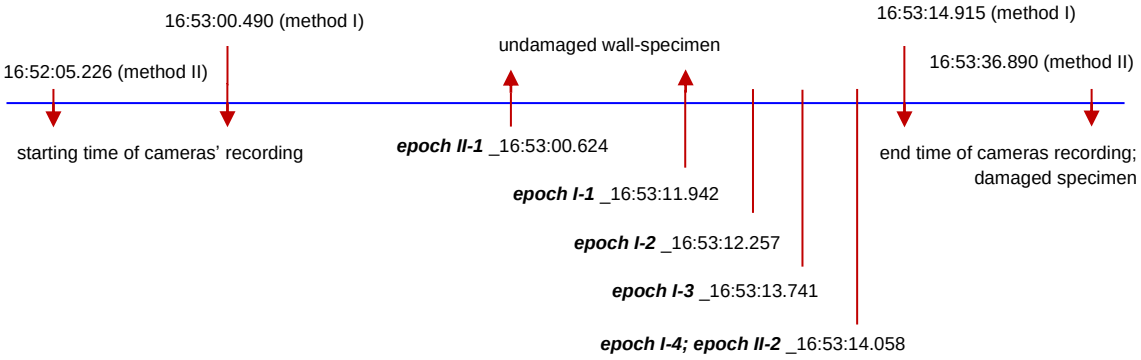

Diagram 5.3: cameras' recording timings for experiment 4 showing both methods (exp 4i & 4ii)

5.3.1.1 Experiment 4i

For the purposes of experiment 4i three redlake cameras were used for collecting the image data. The first epoch was chosen prior to the damage and epochs 2, 3 and 4 were chosen to show the damaged specimen during its in-plane failure as captured by the redlake cameras. Figure 5.2.2a shows the undamaged wall-specimen in epoch 1. Figure 5.2.2b shows the damaged wall-specimen in epoch 2. Figure 5.2.2c and figure 5.1.2d show the damaged wall-specimen in epochs 3 and 4, respectively.

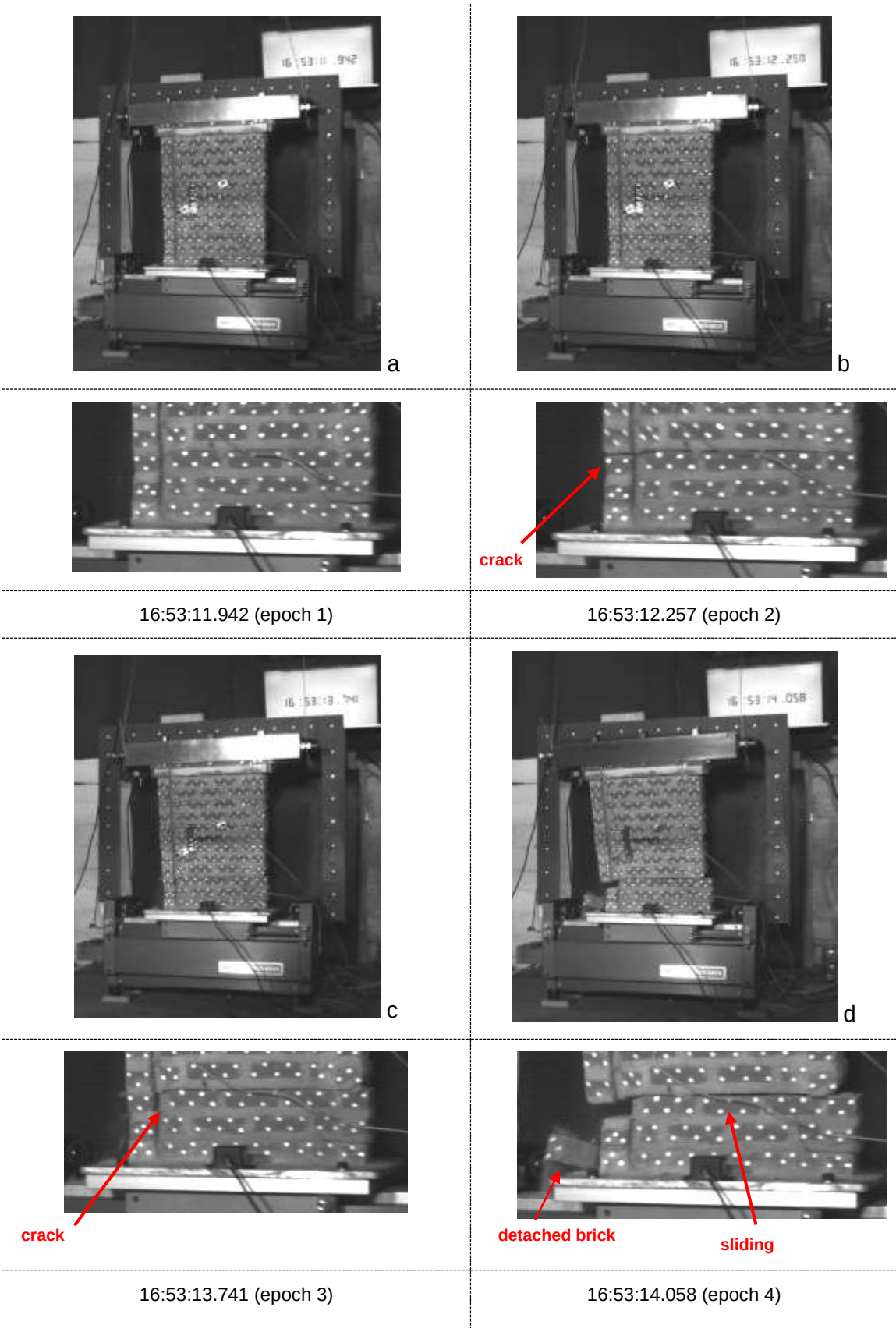

Figure 5.2.2: Images' sequences capturing the actuated tested wall – exp 4i

Once the project was set up on the VMS software and the targets were inserted, observations were created for both the control and the free targets (fig. 5.2.3). Once the required files were processed in the VMS environment, data showing the movement of the targets were produced which were inserted further into the EngVis software. This software combined all the measurements from different epochs and displayed the target movement in any stage of the experiment. The reason for using EngVis was to generate the triangulation system (fig. 5.2.4), which allowed the centroid of any three retro-reflected targets to be determined.

From the thirty-nine images, which captured the shaking of the model wall, the $x - y$ – z coordinates of the retro-reflective targets were measured. The standard photogrammetric technique of bundle adjustment was used. From the measured displacements, the strains were calculated based on the basic strain theory (App. IV & Lee *et. al.*, 2006). All the displacements were measured in centimetres within the VMS environment, and these triangles were used as the basis for the strain computation.

Figure 5.2.3a shows the numbered reflected targets (targets ID) on the specimen (green numbers) and on the wooden frame attached to the wall (blue numbers – control points) and the three cameras (green cones). Figure 5.2.3b is the same as figure 5.2.3a along with the observations from the cameras. Figure 5.2.3c is similarly the same as figure 5.2.3a, but on 3D space. Figure 5.2.3d shows the three pictures of the specimen as captured by the three cameras in the VMS software.

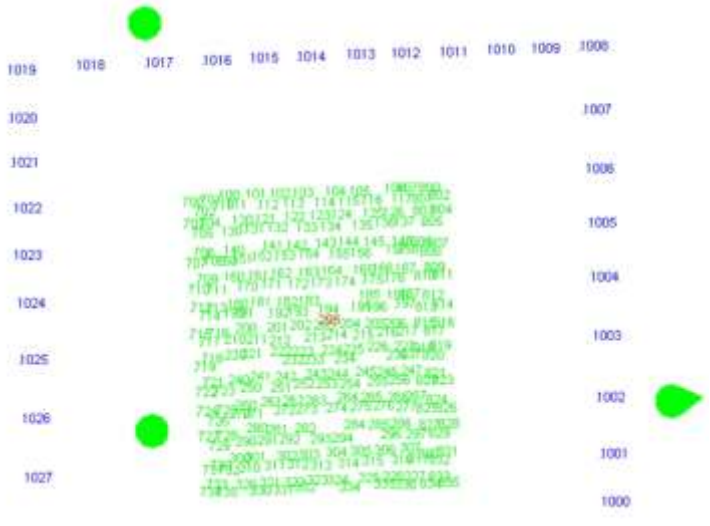

a

object view with target IDs and cameras in 2D

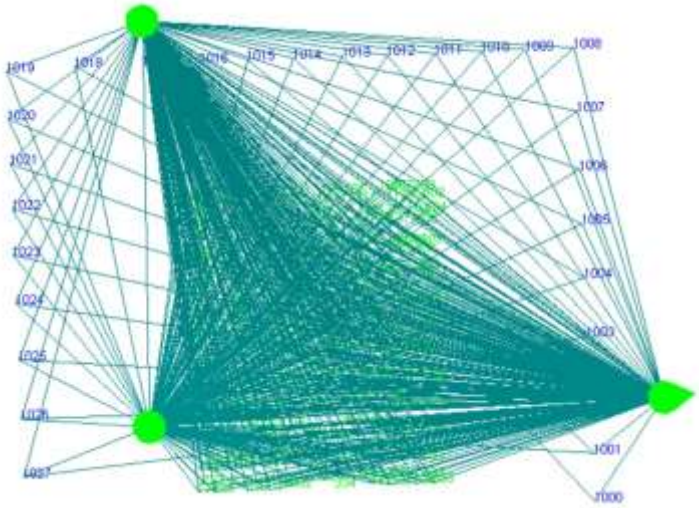

b

object view with observations

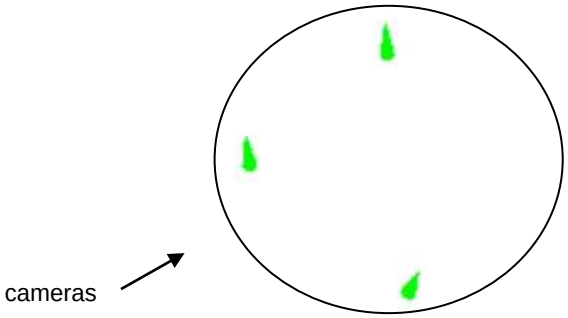

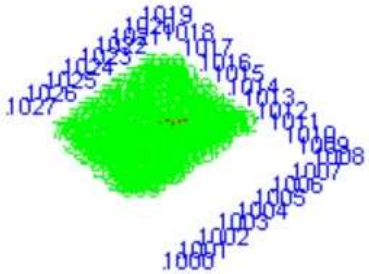

c

object view with target IDs and cameras in 3D

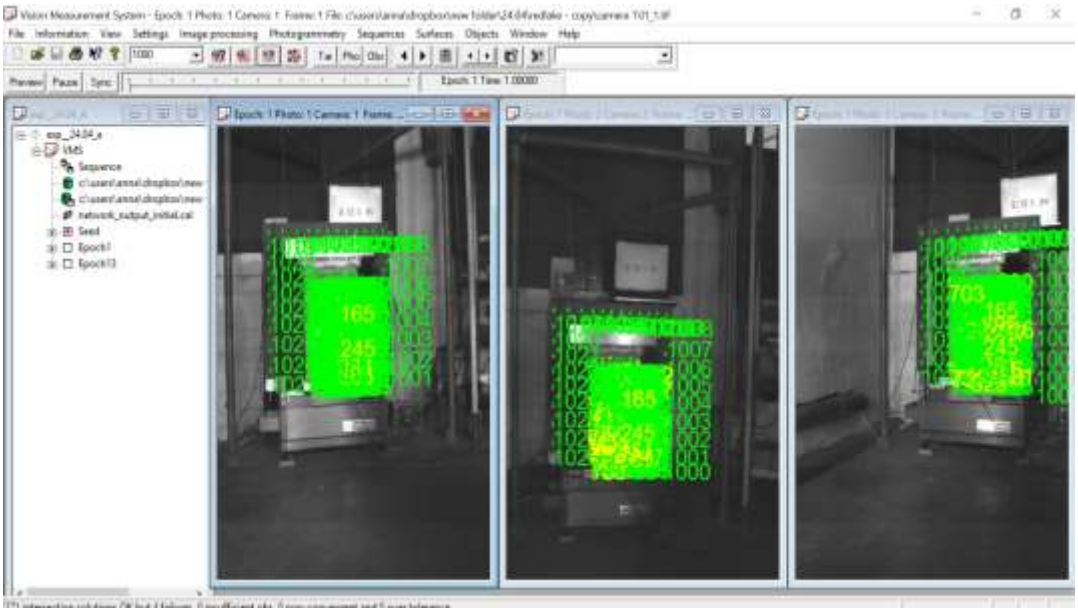

d

VMS analysis photos

Figure 5.2.3: object view of the mini-wall specimen in VMS environment – exp 4i

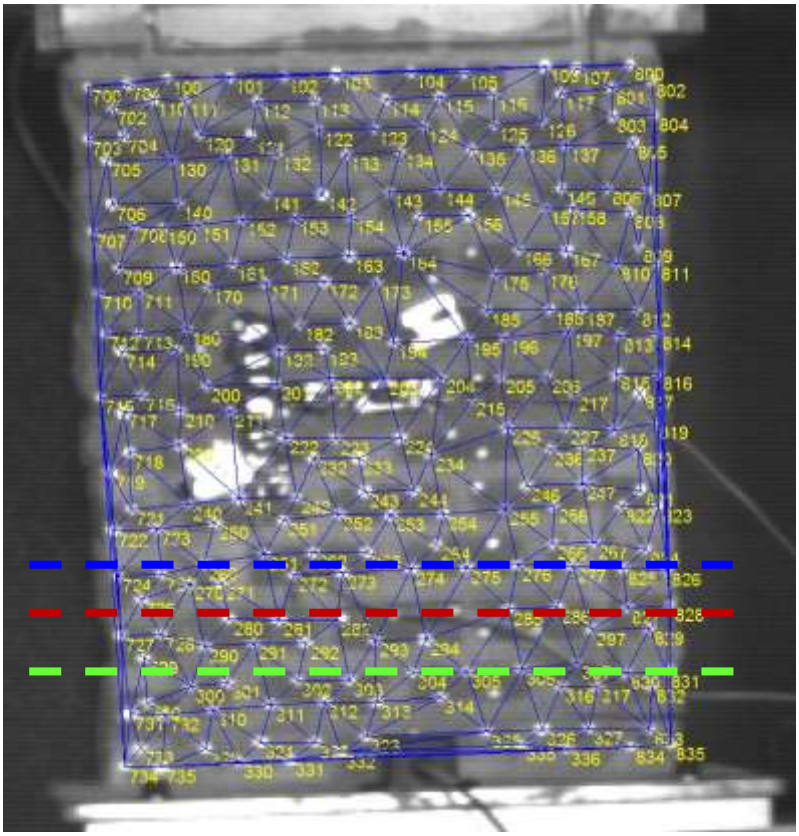

Figure 5.2.4: triangulation computed in EngVis – exp 4i

Figure 5.2.5 shows the deformation of all the free reflected targets from epoch 1 to epoch 4. The dots correspond to the monitored reflected targets and figure 5.2.5 verifies figure 5.2.2. Epoch 1 shows the targets on their initial position presenting a very small movement, epoch 2 presents the initiation of a slight differentiation between the bottom three layers of the specimen and the rest top one, where the crack was initiated according to figure 5.2.2. In figure 5.2.5, for both epochs 3 and 4, shows again the same differentiation between the three bottom layers of the specimen, to the rest top ones, showing a larger intensity on the targets' movement, which explains that as the specimen was vibrating on the x axis, the opening of the crack was increasing. During epoch 4, a small piece of brick was detached from the tested wall specimen as shown in figures 5.2.2 and 5.2.5. The summary of the targets' movement for all the epochs, is also presented in figure 5.2.5 in both 2D and 3D format. The brick which was detached of the specimen is illustrated in epoch 4 and in both 2D and 3D summary deformation figures. The 3D summary deformation figure also shows the small deformation on the y axis for the top part of the mini-wall leaning towards the cameras.

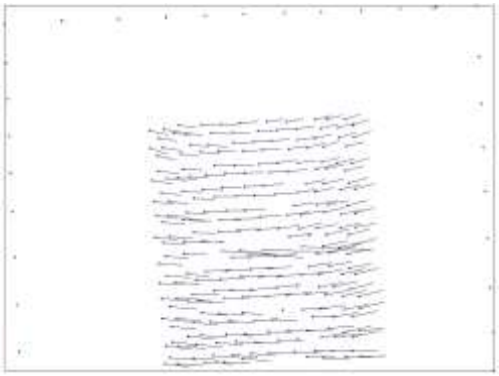

epoch 1

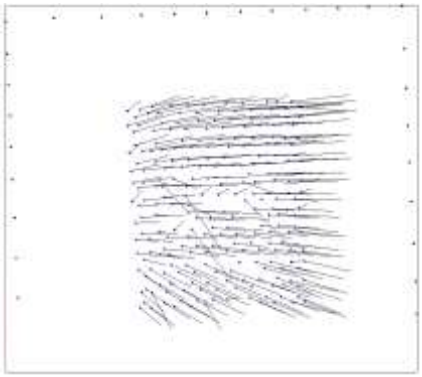

epoch 2

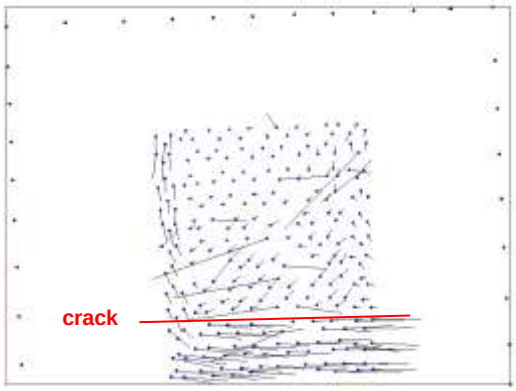

epoch 3

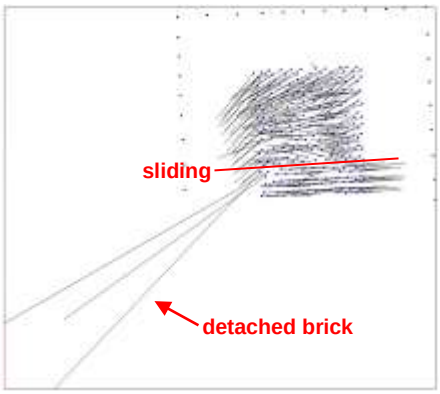

epoch 4

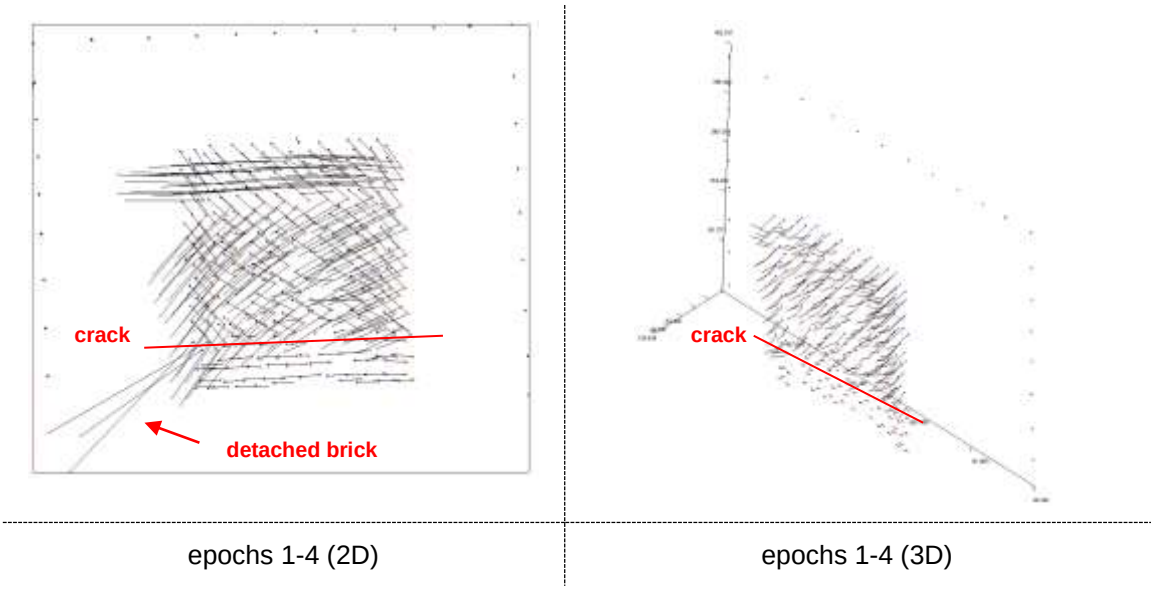

Figure 5.2.5: Deformation of specimen's triangles – exp 4i

After the completion of the experiment and having observed the crack path, three groups (fig. 5.2.4) of triangles were decided to be analysed and discussed additionally for their displacement results. These are presented in graphs in relation to the specimen's length. The first group is consisted by thirteen triangles showing the displacement range of the triangles' centroids located above the crack, as it was observed and monitored during the experimental phase. The second group was consisted of twenty-three triangles along the same crack and the third group of seventeen below the crack.

Figures 5.2.6-5.2.8 present the displacement range of the triangles' centroids of these three groups in relation to the specimen's length (x axis) between the four different epochs. It does not start at zero on the x axis as the first measurement is the centroid of the first triangle, which is at 12.5mm on the axis of the graph (fig. 5.2.6). Figure 5.2.6 shows the triangles' centroids displacement from epoch 1 to epoch 2 with a range of -4.7-6.7mm for the group of triangles above, along and below the crack, providing a figure of the specimen's distortion during the first 315 milliseconds (epochs 1-2) of its analysed motion. Within this timing the triangles' displacement results have an ascending track along the specimen's x axis. Figure 5.2.7 has the same form of figure 5.2.6 with significant larger displacement values towards all groups of triangles, with a range of 1.2-19.4. Figure 5.2.8 shows the displacement results between epochs 3 and 4, which predominately presents the damage of the mini-wall for the group of triangles along the crack. For the groups of triangles above and below the crack high peaks have been recorded after the 90mm of the specimen's x axis. These triangles' centroids displacement ranges from -7.6mm to 4mm.

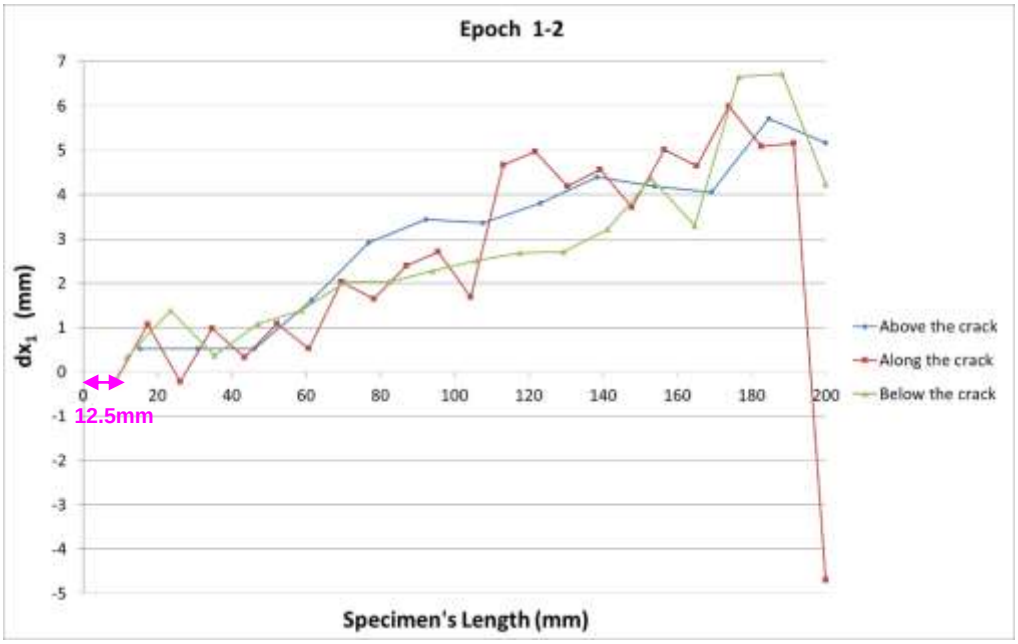

Figure 5.2.6: epoch 1-2 (dx_1 – exp 4i)

Figure 5.2.7: epoch 2-3 (dx_1 – exp 4i)

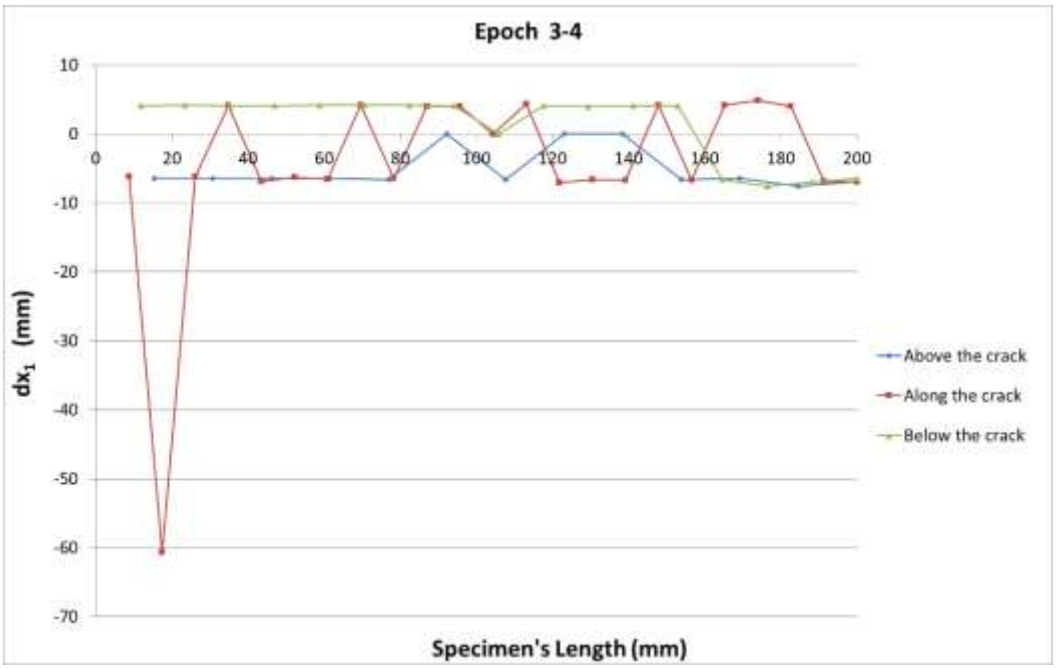

Figure 5.2.8: epoch 3-4 (dx_1 – exp 4i)

Figures 5.2.9 – 5.2.11 present the computed shear strain of the measured targets, using the layout of a contour map. These contour maps use for plotting the $x-y-z$ centroid coordinates of each triangle, which is created using the Surfer software. The x-axis represents the length of the tested specimen, the y-axis the height, and the contours the shear strain. Figure 5.2.9 shows shear strain values up to 2.4 between epochs 1 and 2. Figure 5.2.10 shows the shear strain values up to 2.2, between epochs 2 and 3 and figure 5.2.11 shows the shear strain values up to 5.2, between epochs 3 and 4. The big values of shear strain are shown in figures 5.2.9 and 5.2.11 at the bottom left of these contour maps where the detachment of the mini brick occurred during the specimen's excitation. These computed shear strains were made based on the remaining bricks of the specimen.

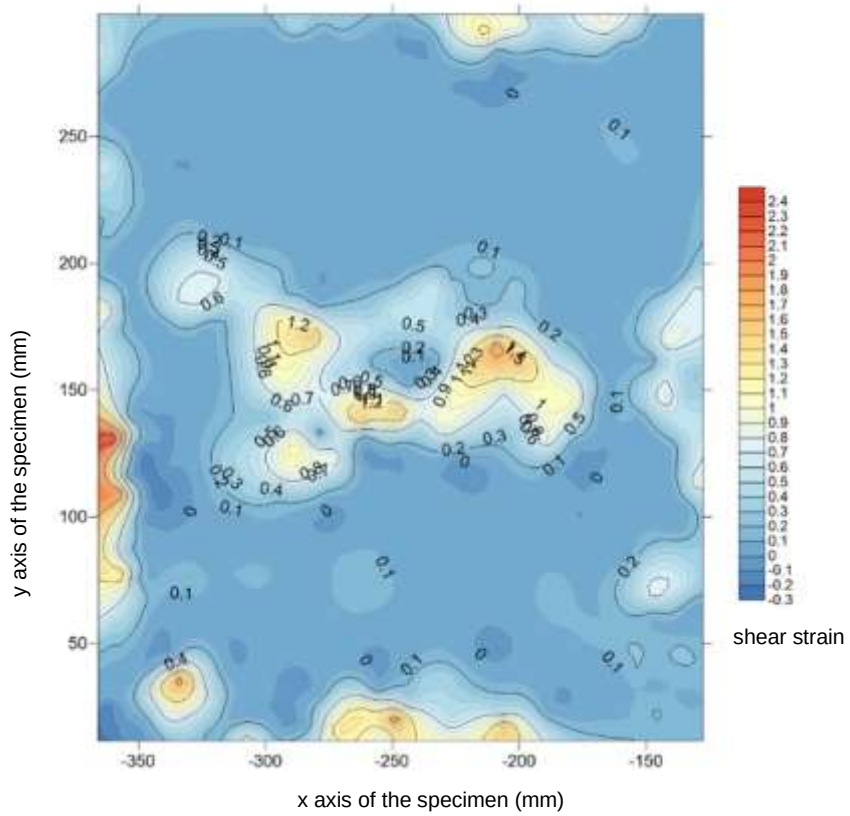

Figure 5.2.9: epoch 1-2 (shear ε – exp 4i)

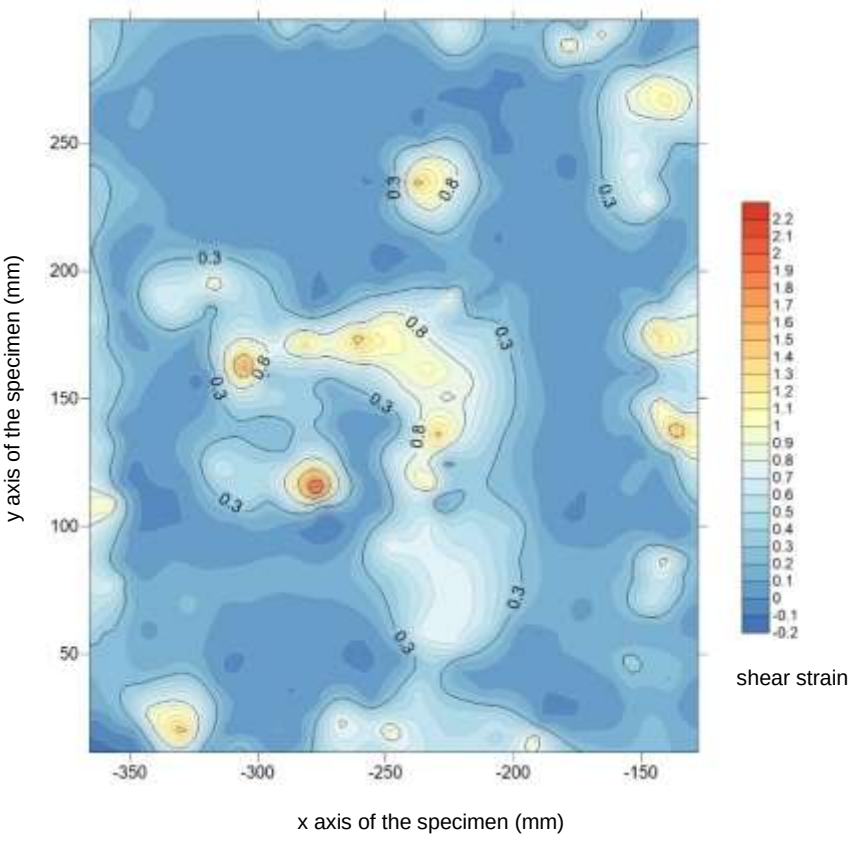

Figure 5.2.10: epoch 2-3 (shear ε – exp 4i)

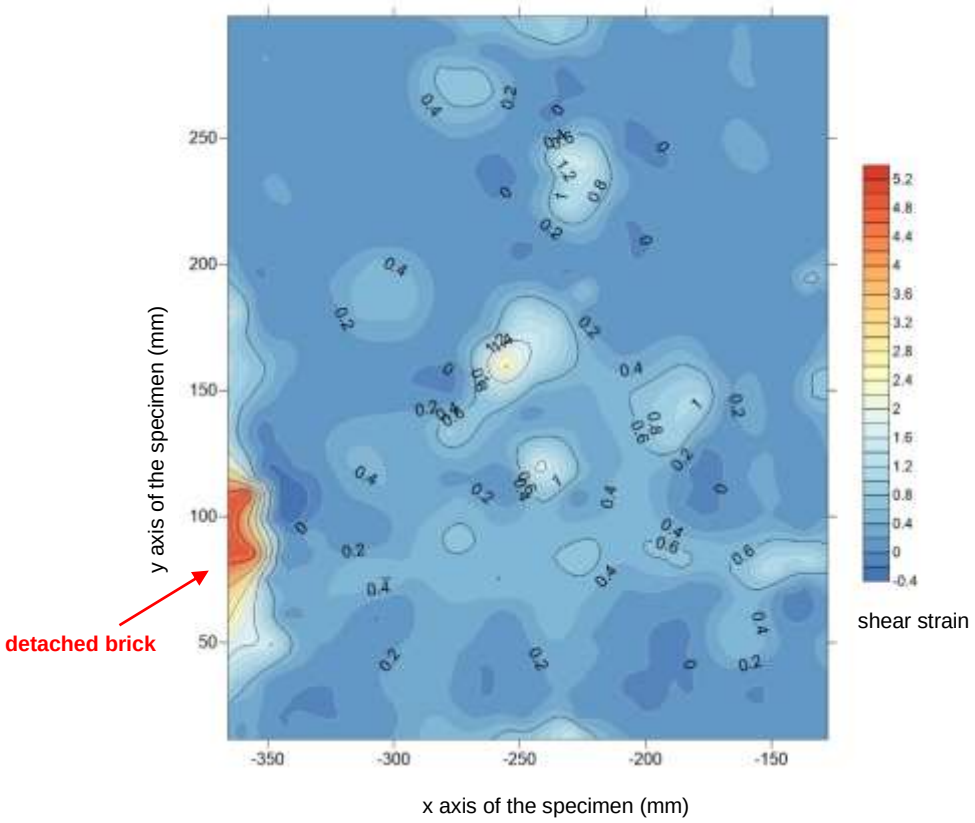

Figure 5.2.11: epoch 3-4 (shear ε – exp 4i)

5.3.1.2 Experiment 4ii

For the purposes of experiment 4ii, two Nikon cameras were used and two images per camera were analysed in the VMS environment (fig. 5.2.12). The first epoch was chosen prior to the damage and epoch 2 was chosen to show the damaged specimen during its in-plane failure as captured by the nikon cameras. Figure 5.2.12a shows the undamaged wall-specimen in epoch 1 and figure 5.2.12b shows the damaged wall-specimen in epoch 2.

Once the project was set up on the VMS software and the targets were inserted, observations were created for both the control and the free targets (fig. 5.2.13). Figure 5.2.13a shows the numbered reflected targets (targets ID) on the specimen (green numbers) and on the wooden frame attached to the wall (blue numbers – control points) and the two cameras (green cones). Figure 5.2.13b is the same as figure 5.2.13a along with the observations from the cameras. Figure 5.2.13c is similarly the same as figure 5.2.13a, but on 3D space. Figure 5.2.13d shows the two pictures of the specimen as captured by the two cameras in the VMS software.

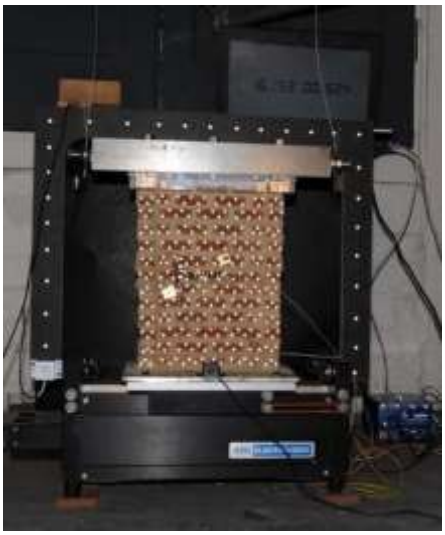

a

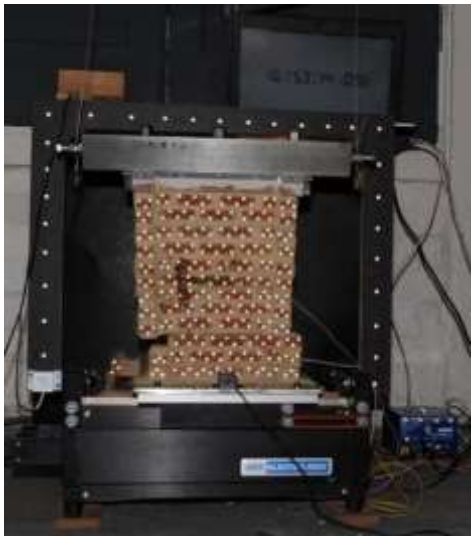

b

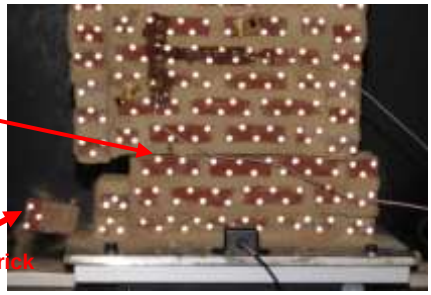

16:53:00.624 16:53:14.058

Figure 5.2.12: images' sequences capturing the actuated tested wall – exp 4ii

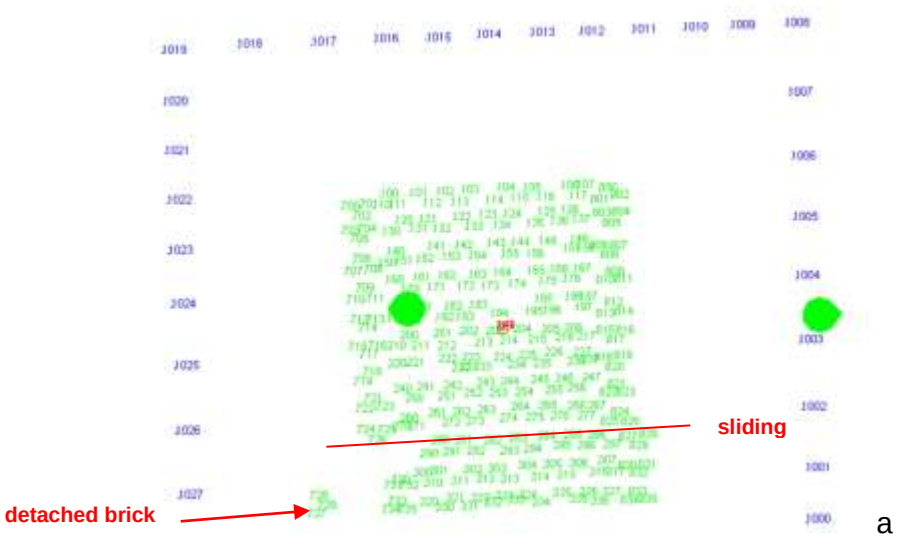

a

object view with target IDs and cameras in 2D

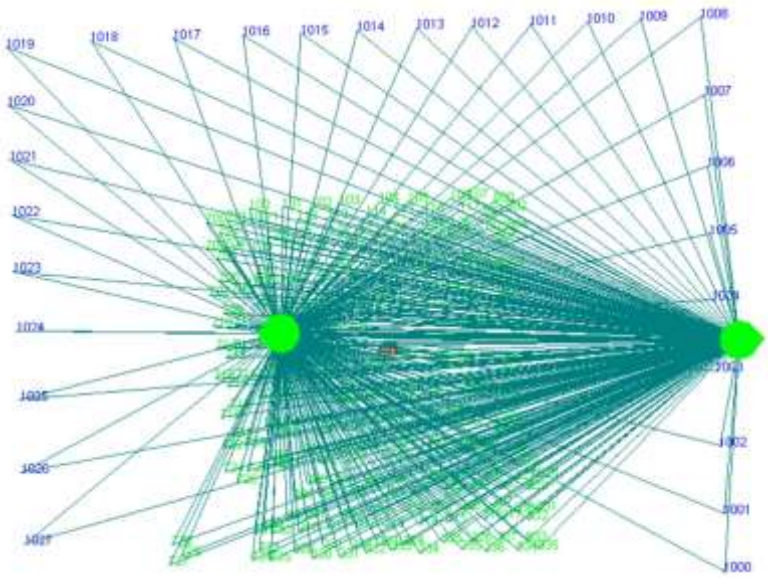

b

object view with observations

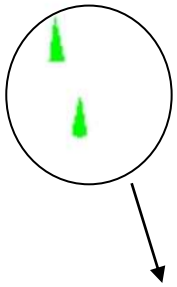

Nikon cameras

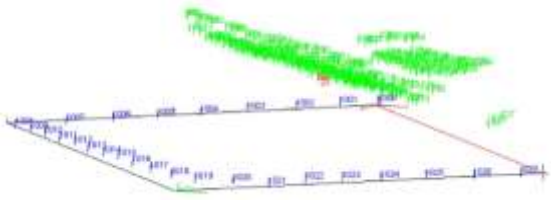

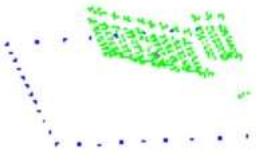

c

object view with target IDs and cameras in 3D

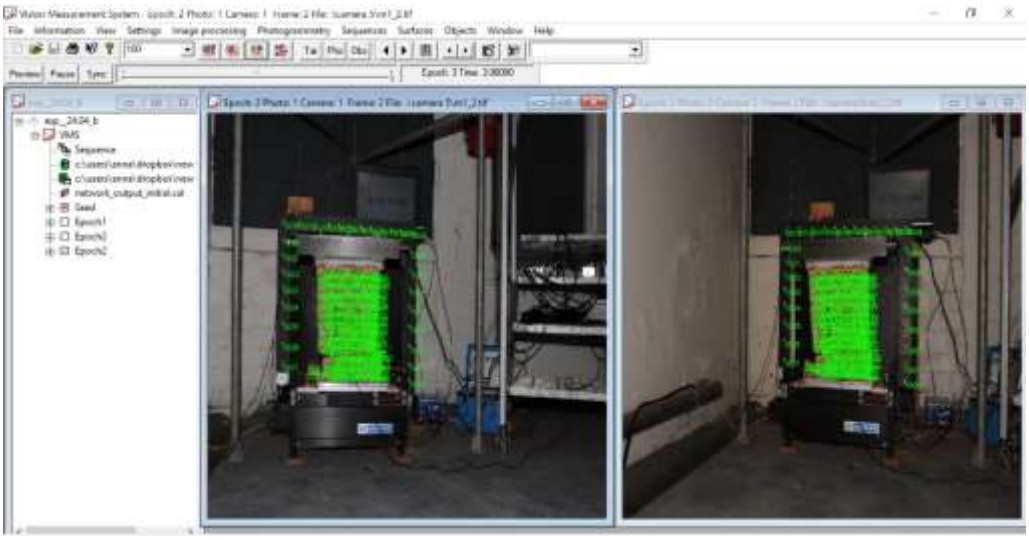

d

VMS analysis photos

Figure 5.2.13: object view of the mini-wall specimen in VMS environment – exp 4ii

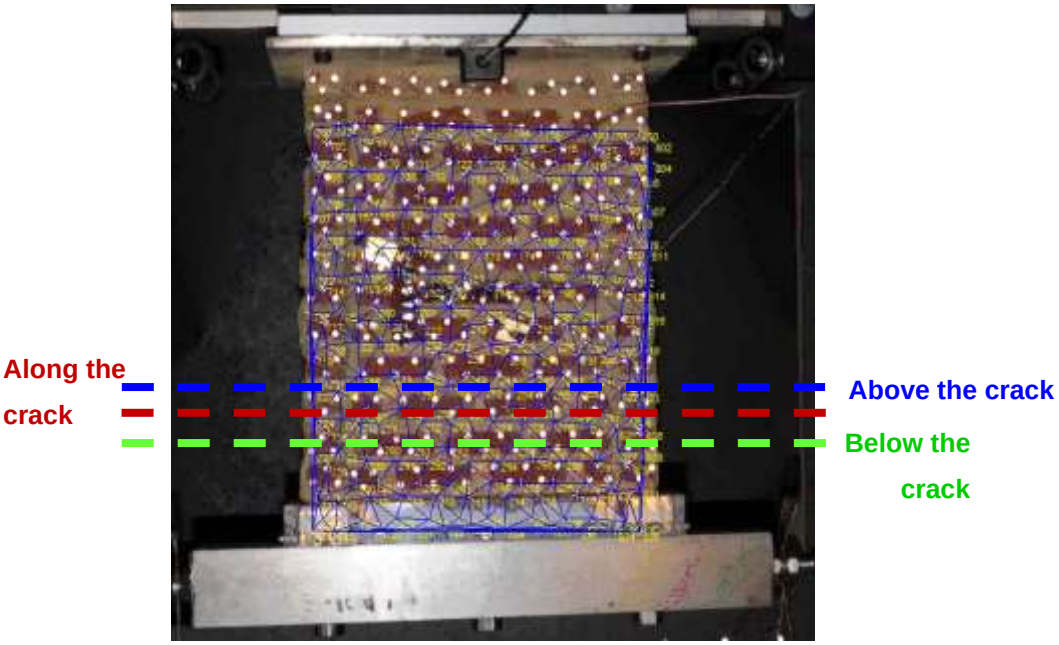

Figure 5.2.14: triangulation computed in EngVis – exp 4ii

Figure 5.2.14 shows the triangulation system which is rotated by 180°. The EngVis software, which is used for creating the triangulation files, rotates all the images collected by the nikon cameras. Figure 5.2.15 shows the deformation of all the free reflected targets from epoch 1 to epoch 2. The dots correspond to the monitored reflected targets and figure 5.2.15 verifies figure 5.2.12. Epoch 1 shows the targets on their initial position. Epoch 2 presents the differentiation between the three bottom

layers of the specimen, to the rest top ones, showing a larger intensity on the targets' movement, which explains that as the specimen was vibrating on the x axis, the opening of the crack was increasing. On the deformation figure for epochs 1-2, showing the x-y axes, the three lines on the left bottom corner represent the de-attached small brick. However, the same figure for epochs 1-2, showing the z-y axes, confirms the distortion on the z axis at the top of the specimen and its leaning towards the cameras.

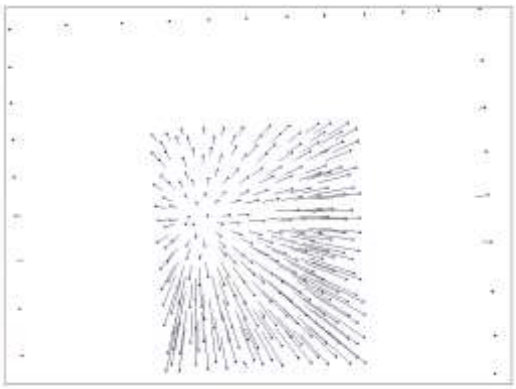

epoch 1 (x-y)

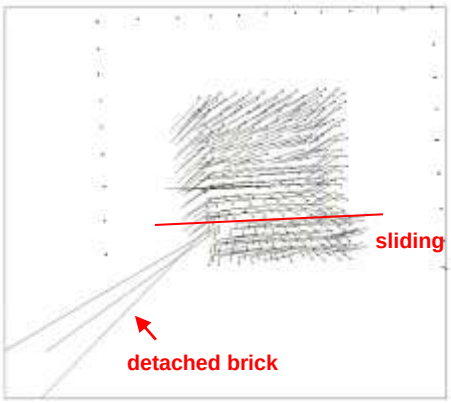

epochs 1-2 (x-y)

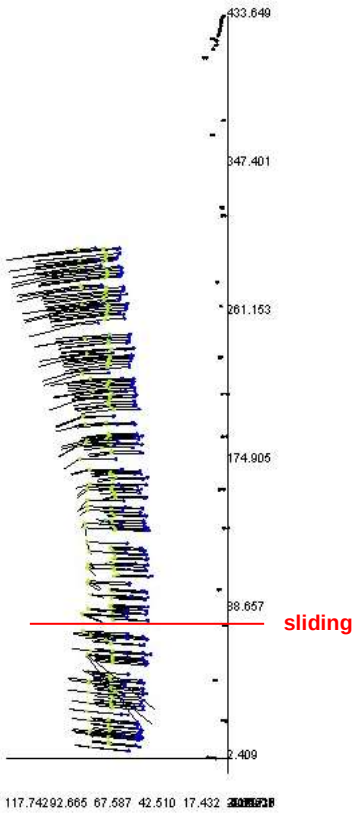

epochs 1-2 (z-y)

Figure 5.2.15: deformation of specimen's triangles – exp 4ii

After the completion of the experiment, three groups (fig. 5.2.14) of triangles are decided to be analysed and discussed for their displacement and strain results. These are presented in graphs in relation to the specimen's length. The first group is consisted of thirteen triangles showing the displacement range of the triangles' centroids located above the crack, as it was observed and monitored during the experimental phase. The second group is consisted of twenty-three triangles along the same crack and the third group of seventeen triangles below the crack.

Figure 5.2.16 presents the displacement range of the triangles' centroids of these three groups in relation to the specimen's length (x axis) between the two epochs. It does not start at zero on the x axis as the first measurement is the centroid of the first triangle, which is at 12.5mm on the axis of the graph (fig. 5.2.16). Figure 5.2.16 shows the triangles' centroids displacement from epoch 1 to epoch 2 with a range of -8.37 – 9.47mm for the group of triangles above, along and below the crack, providing a figure of the specimen's distortion during its monitored motion. Within this timing only six triangles, three located along the crack and the other three located below the crack, all located on the 40mm along the specimen's x axis, show significant large peaks displaced from -52.54mm to -66.7mm. These large displacements from the six triangles represent the detached small brick, as illustrated in figure 5.2.12.

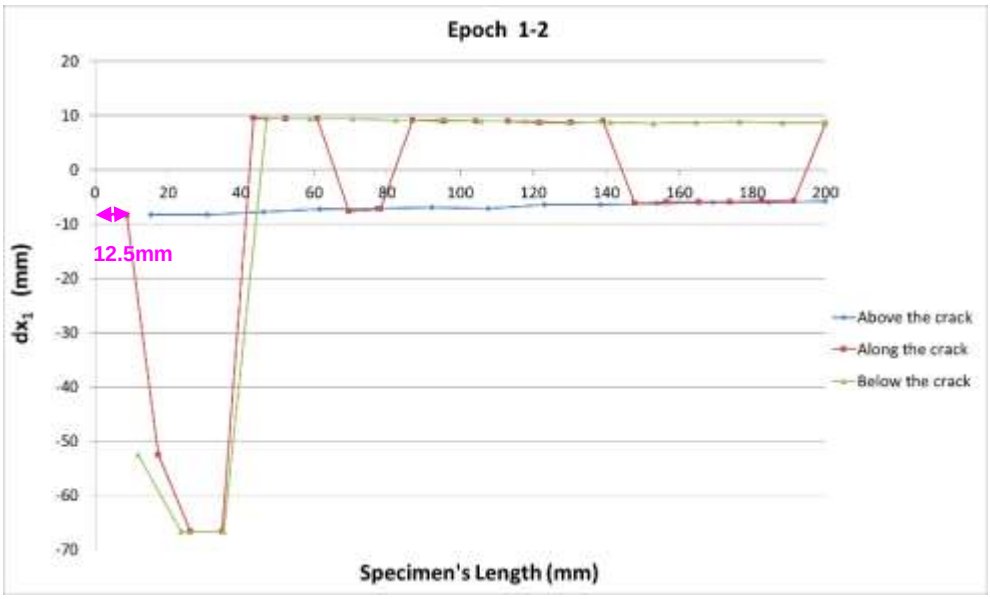

Figure 5.2.16: epoch 1-2 (dx_1 – exp 4ii)

Figure 5.2.17 presents the computed shear strain of the measured targets, using the layout of a contour map. This contour map uses for plotting the $x-y$ – z centroid coordinates of each triangle, which is created using the Surfer software. The x-axis represents the length of the tested specimen, the y-axis the height, and the contours the shear strain. Figure 5.2.17 shows shear strain values up to 4.8 mainly at the bottom left, where the detachment of the mini brick occurred.

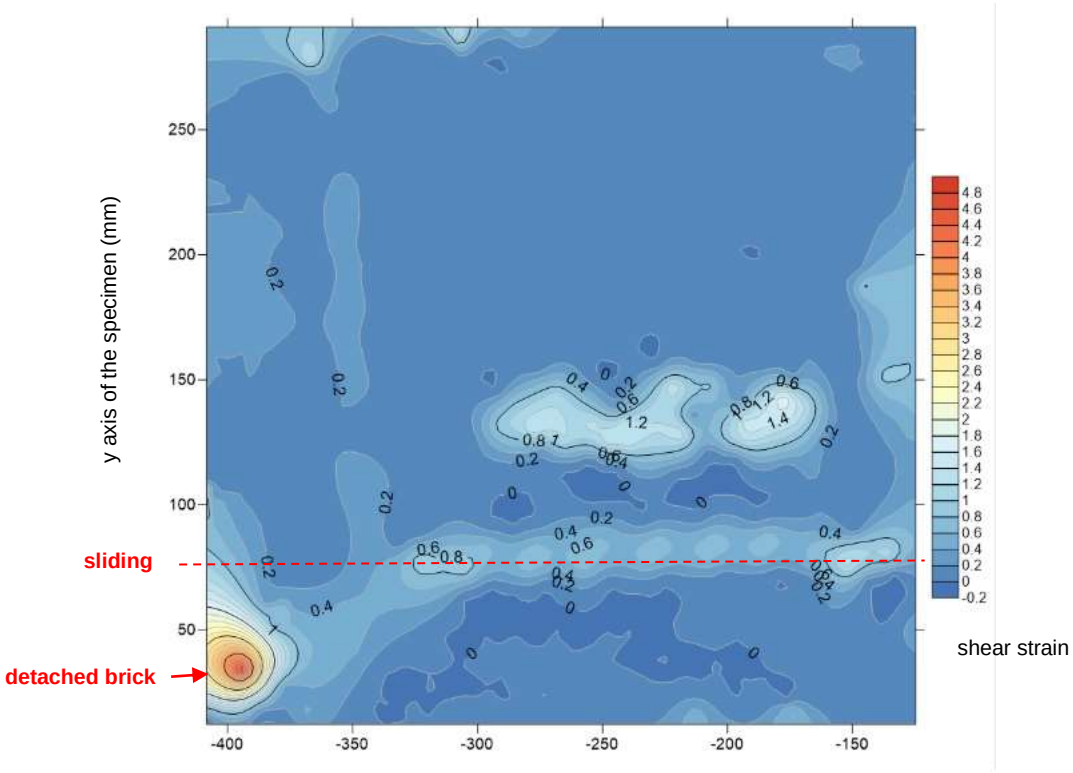

Figure 5.2.17: epoch 1-2 (shear ε – exp 4ii)

5.3.2 Strain Gauge

Two strain gauges were installed on the front face of the mini-wall, facing the cameras. The horizontal one was placed along bricks, at the centre of the 7th row of the specimen and the second one, vertically covering the right edge of the horizontal strain gauge and located along the 6th to the 8th row of the mini-wall. Both gauges were installed using the same method as described in chapter 4.2.3.3. Figure 5.2.18 shows the SGs' results as recorded during the motion of the specimen. The largest strain reading recorded by the horizontal strain gauge is 0.16 at 16:53:14 (hr:min:sec) and by the vertical strain gauge is 0.03, similarly at 16:53:14.

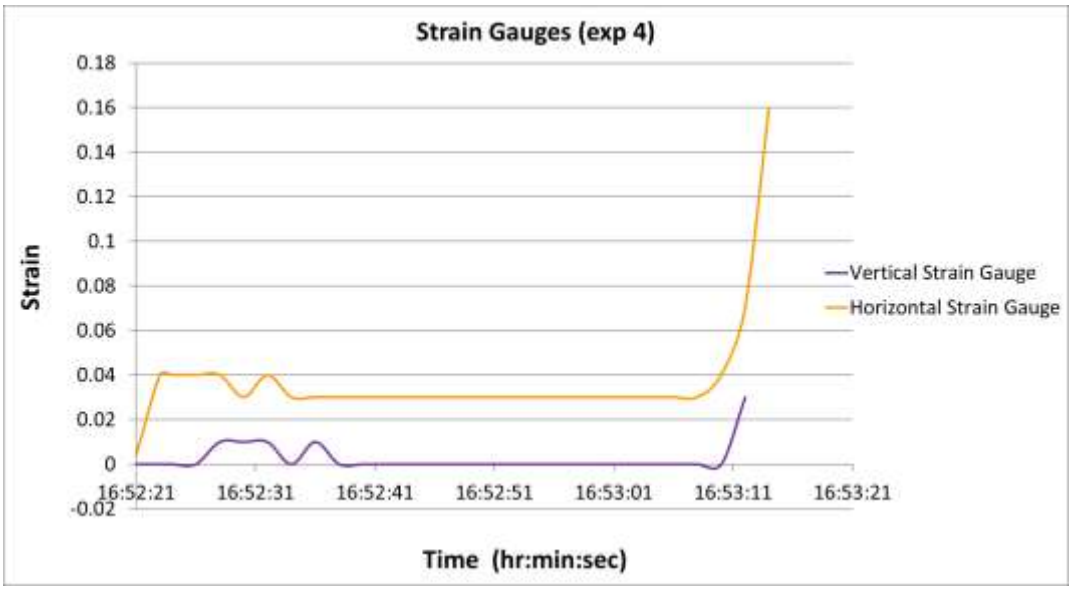

Figure 5.2.18: SG's results – strain over time (hour:minute:second) – exp 4

5.3.3 Comparisons

Figure 5.2.19 presents part of the triangulation pictures for the redlake experimental analysis. The triangulation picture is zoomed around the areas of the installed strain gauges to select the corresponding triangles for the purposes of strain computation using the CRDP method. Each triangle corresponds to one calculated strain value using the CRDP method.

Therefore, during the redlake experimental analysis, four triangles are selected along the vertical strain gauge and eight triangles along the horizontal strain gauge (table 5.3). All the negative strain data, computed based on the CRDP method, converted to absolute values, they summed up and divided by the number of triangles. Hence, the four epochs produced three strain values for each triangle using the CRDP method, as shown in figure 5.2.20. The computed strain value, along the horizontal strain gauge, between epochs 1 and 2, is 0.238 (table 5.3, fig. 5.2.20) recorded at 16:53:12.257 (diagram 5.3). Observing figure 5.2.18, the maximum strain recorded by the horizontal strain gauge is 0.16 at 16:53:14, which is close to the strain of epochs 1-2 as computed by the CRDP. Therefore, diagram 5.3 shows the time difference of 1.743 milliseconds of the recorded strains by the strain gauge and the close-range digital photogrammetry. The strain value, along the vertical strain gauge, computed between epochs 3 and 4, is 0.064 (table 5.3, fig. 5.2.20) recorded at 16:53:14.058 (diagram 5.4). Observing figure 5.2.18, the maximum strain recorded by the vertical strain gauge is 0.03 at 16:53:14, which is close to the strain of epochs 3-4 as computed by the

CRDP. Therefore, diagram 5.4 shows the time difference of 58 milliseconds of the recorded strains by the strain gauge and the close-range digital photogrammetry.

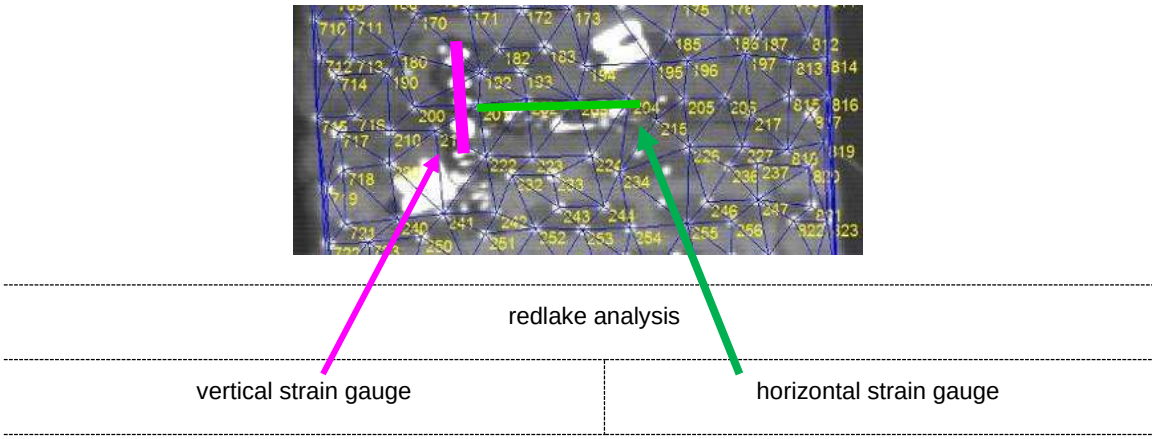

Figure 5.2.19: zoomed area on the triangulation picture – exp 4

					Strain - CRDP		
	triangles along horizontal SG				Strain (1-2)	Strain (2-3)	Strain (3-4)
1	200	211	201		0.011	0.262	0.006
2	202	223	203		-0.090	-0.253	-6.851
3	223	224	203		0.096	-0.579	0.256
4	203	204	194		0.332	0.594	-0.140
5	203	224	204		-0.036	0.667	-0.180
6	204	224	234		-1.142	-0.587	-0.353
7	204	234	215		0.182	0.486	0.582
8	192	201	202		0.013	-0.263	-0.007
					0.238	0.461	1.047
	triangles along vertical SG						
9	200	211	201		0.011	0.262	0.006
10	211	222	201		-0.076	0.176	-0.003
11	211	241	222		-0.079	-0.155	-0.217
12	222	241	242		0.337	0.017	0.028
					0.126	0.152	0.064

time (hr:min:sec:millisec) – epochs	16:53:12.257	16:53:13.741	16:53:14.058

Table 5.3: strains using CRDP method along SGs – exp 4i

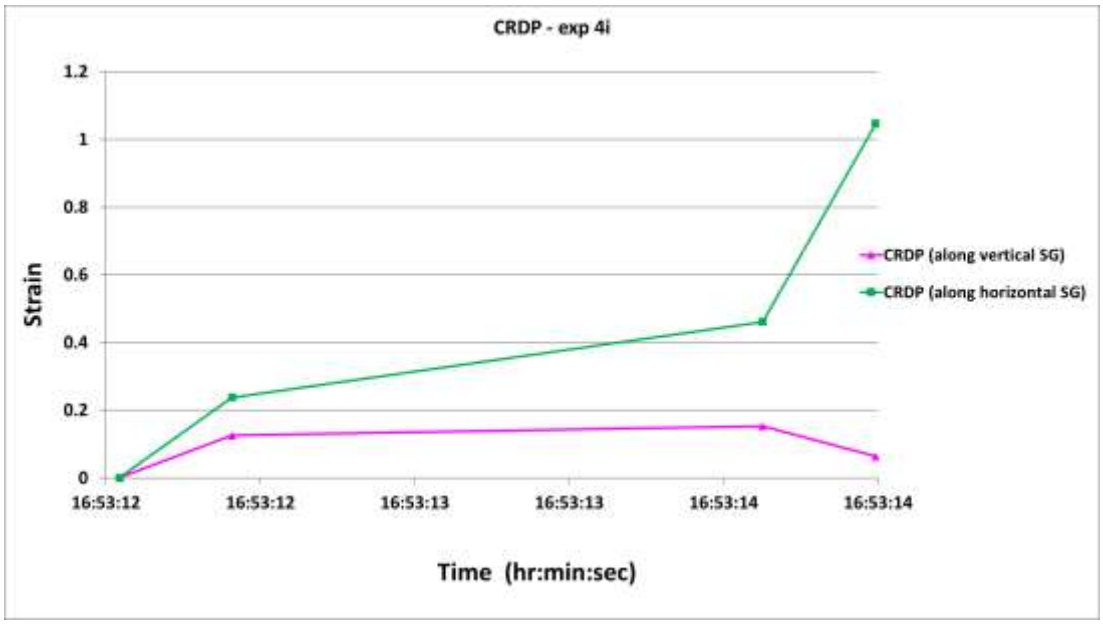

Figure 5.2.20: CRDP's readings along SG sensors – exp 4i

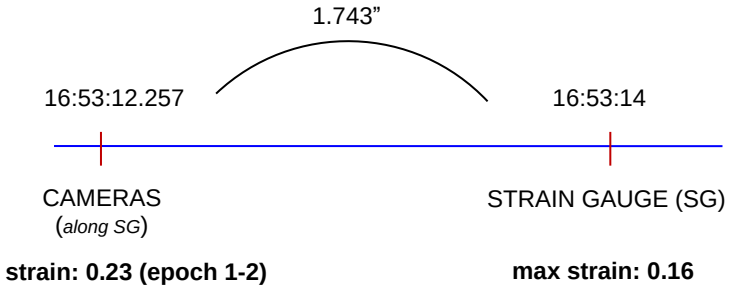

Diagram 5.3: strains along the monitoring methods for experiment 4i – horizontal

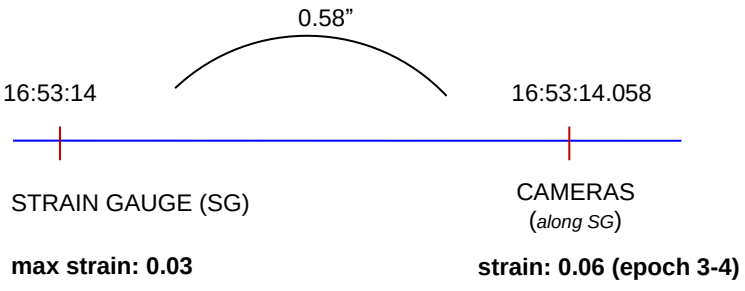

Diagram 5.4: strains along the monitoring methods for experiment 4i – vertical

5.4 Experiment 5

Experiment 5 carried out on a small-scale masonry specimen excited on a small shaking table. The specimen was built with brick type A and mortar type I and its dimensions were 280mm in height, 240mm in length and 25mm in width. The specimen covered with plaster in order to check if the crack's propagation can be detected by the cameras and it was also positioned at an angle of 45° in order to check if the application of the CRDP method is efficient when the cameras capture an object in an angle. 28 control reflected targets were installed on the Π-shape frame attached to the laboratory's wall and 256 free reflected targets installed on the front face of the specimen facing the four redlake cameras installed at a 0.85m distance from the specimen. Each redlake camera collected 300 images. The test ran for 129 seconds, with an input excitation value to the shaking table of 20Vpp in amplitude and of 25Hz in frequency. The input excitation applied on the x axis was a result of a trial and error with the scope to create cracking to the specimen. For checking the specimen's distortion under different loading, an imposed load of 5.6kg was applied at its top. One strain gauge installed diagonally along the 4th and 6th brick layer and one horizontally on the 9th mortar joint (fig. 5.3.1).

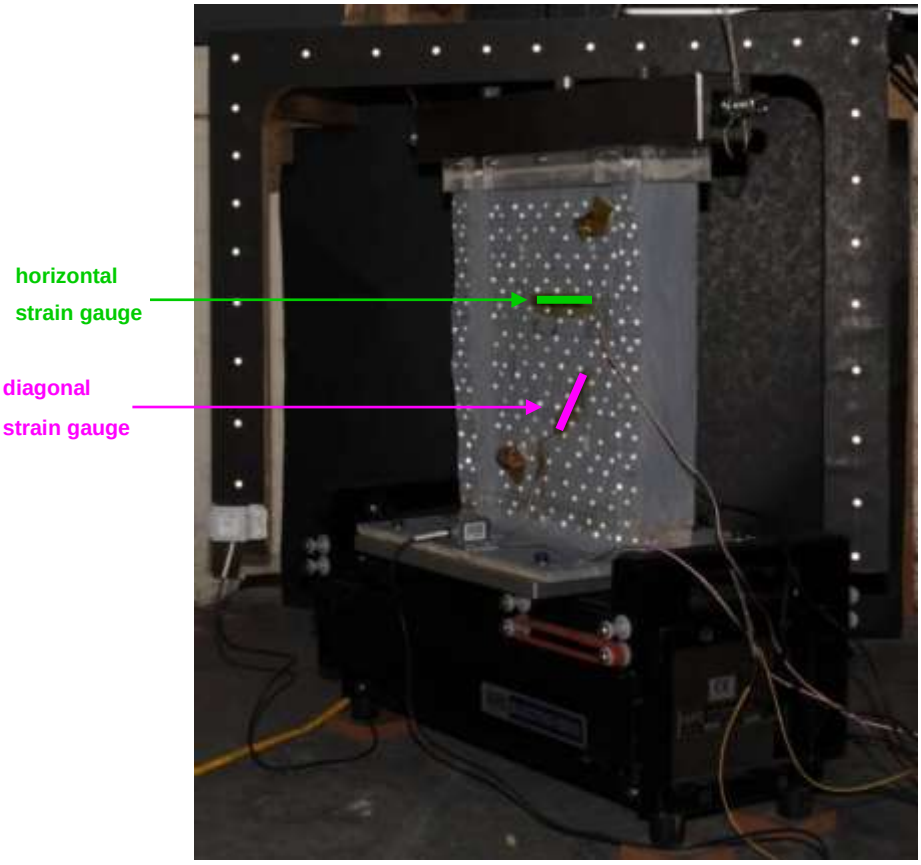

Figure 5.3.1: undamaged small-scale masonry specimen – exp 5

5.4.1 Close Range Digital Photogrammetry

For the purposes of this experiment four redlake cameras were used with the specimen positioned diagonally at 45° (fig. 5.3.2). The four synchronised redlake cameras collected three hundred images per camera. The analysis of the photogrammetric results is comprised only of sixteen images, four from each camera. These sixteen images, one from each camera, are classified into different sets of photographs called epochs. In total, four epochs were set up. Therefore, the four stages of the experiment (fig. 5.3.2) comprised of four epochs (diagram 5.5). Epoch 2 was the first epoch capturing the crack's initiation and epoch 1 was chosen to show the specimen prior to the damage. Epochs 3 and 4 were chosen to show the crack at the bottom of the specimen. Figure 5.3.2a shows the undamaged wall-specimen in epoch 1. Figure 5.3.2b shows the damaged wall-specimen in epoch 2. Figure 5.3.2c and figure 5.3.2d show the damaged wall-specimen in epochs 3 and 4, respectively. Figure 5.3.3 shows the tested specimen after its cracking propagation. The cameras' monitoring period successfully captured the initiation and propagation of the crack.

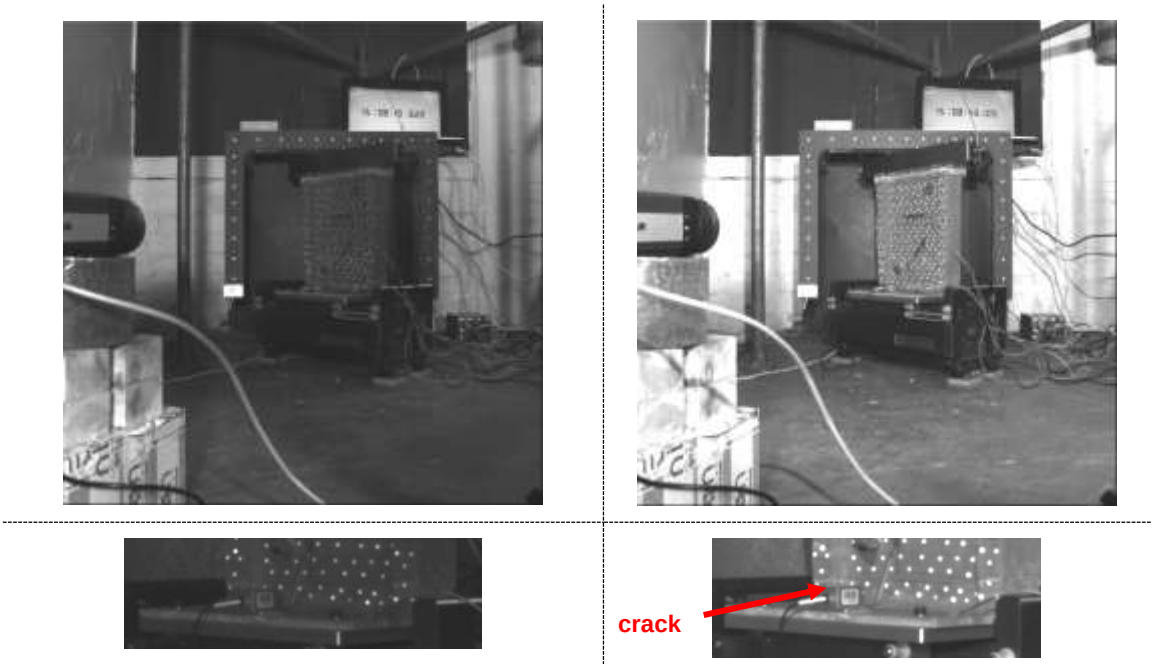

15:08:19.622 (epoch 1) 15:08:43.105 (epoch 2)

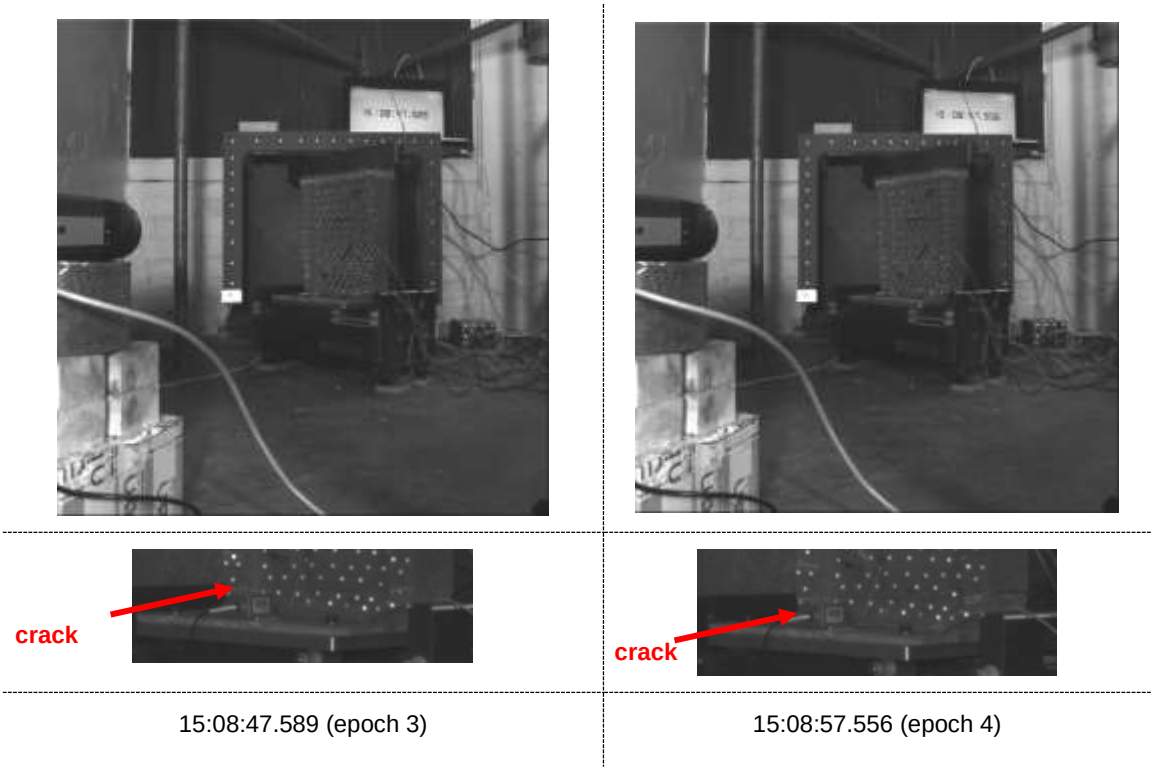

Figure 5.3.2: Images' sequences capturing the actuated tested wall – exp 5

Figure 5.3.3: propagation of the crack – exp 5

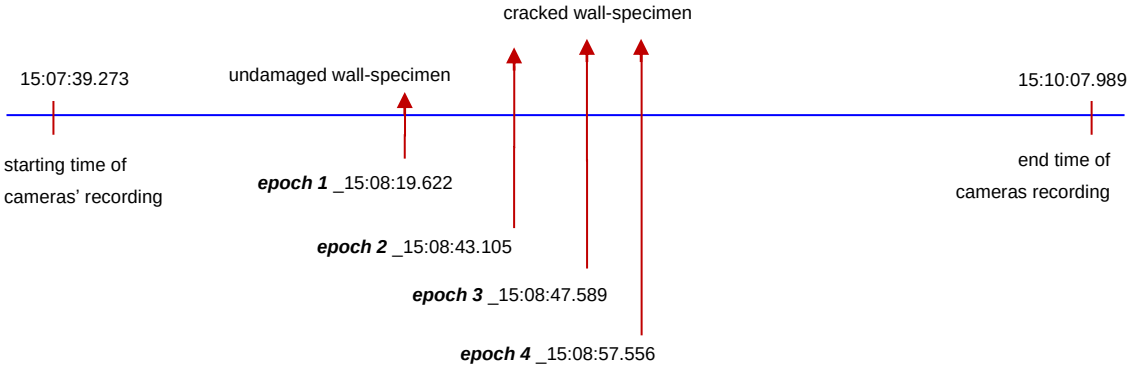

Diagram 5.5: cameras' recording timings for experiment 5 showing both methods (exp 5)

Once the project has been set up on the VMS software and the targets have been inserted, observations are created for both the control and the free targets (fig. 5.3.4). Once the required files have been processed in the VMS environment, data showing the movement of the targets are produced which are inserted further into the EngVis software. This software combines all the measurements from different epochs and can display the target movement in any stage of the experiment. The reason for using EngVis is to generate the triangulation system (fig. 5.3.6), which allows the centroid of any three retro-reflected targets to be determined.

From the sixteen images, which captured the shaking of the model wall, the $x - y - z$ coordinates of the retro-reflective targets were measured. The standard photogrammetric technique of bundle adjustment was used. From the measured displacements, the strains were calculated based on the basic strain theory (App. IV & Lee *et. al.*, 2006). All the displacements were measured in centimetres within the VMS environment, and these triangles were used as the basis for the strain computation.

Figure 5.3.4a shows the numbered reflected targets (targets ID) on the specimen (green numbers) and on the wooden frame attached to the wall (blue numbers – control points) and the four cameras (green cones). Figure 5.3.4b is the same as figure 5.3.4a along with the observations from the cameras. Figure 5.3.4c is similarly the same as figure 5.3.4a, but on 3D space.

a

object view with target IDs and cameras in 2D

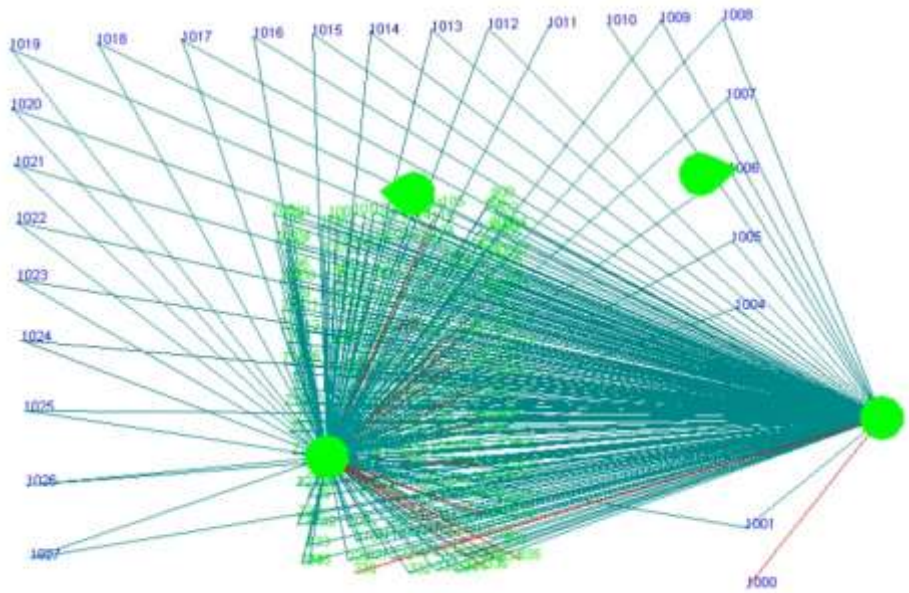

b

object view with observations

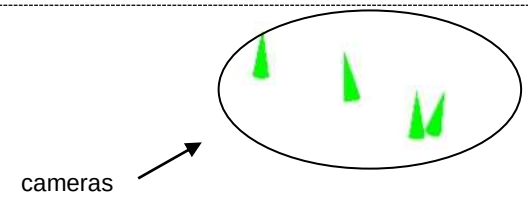

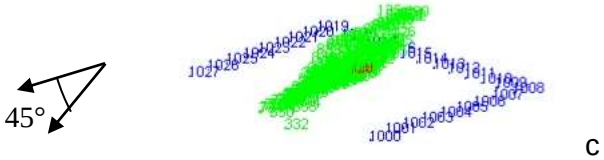

c

object view with target IDs and cameras in 3D

Figure 5.3.4: object view of the mini-wall specimen in VMS environment – exp 5

Figure 5.3.5 shows the deformation of all the free reflected targets from epoch 1 to epoch 4. The dots correspond to the monitored reflected targets and figure 5.3.5 verifies figure 5.3.2. Epochs 1 and 2 show very small movement of all the monitored

targets. However, epochs 3 and 4 show larger displacements at the bottom of the specimen, where the crack occurred during the mini-wall's motion.

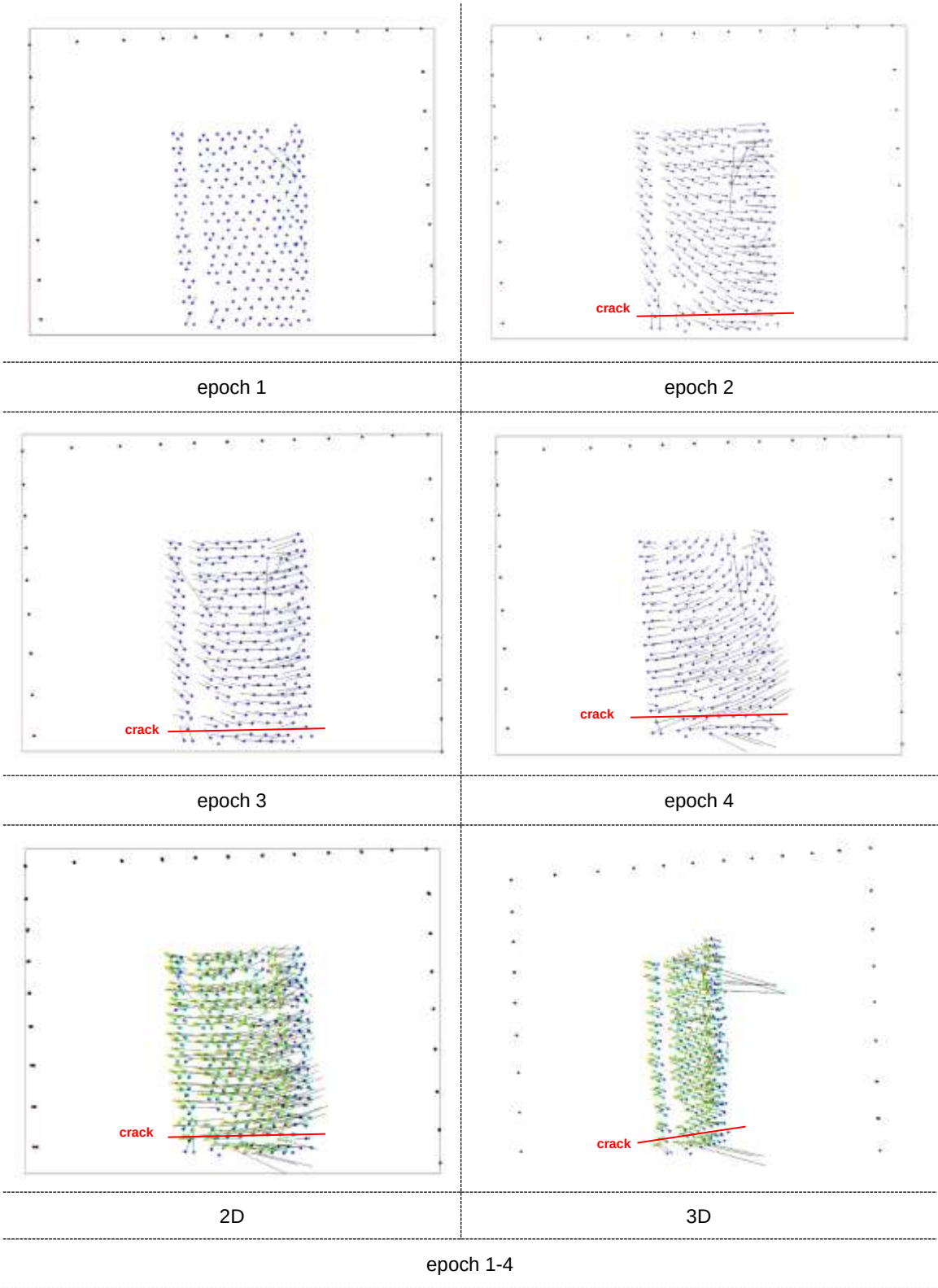

epoch 1 | epoch 2

epoch 3 | epoch 4

2D | 3D

epoch 1-4

Figure 5.3.5: Deformation of specimen's triangles – exp 5

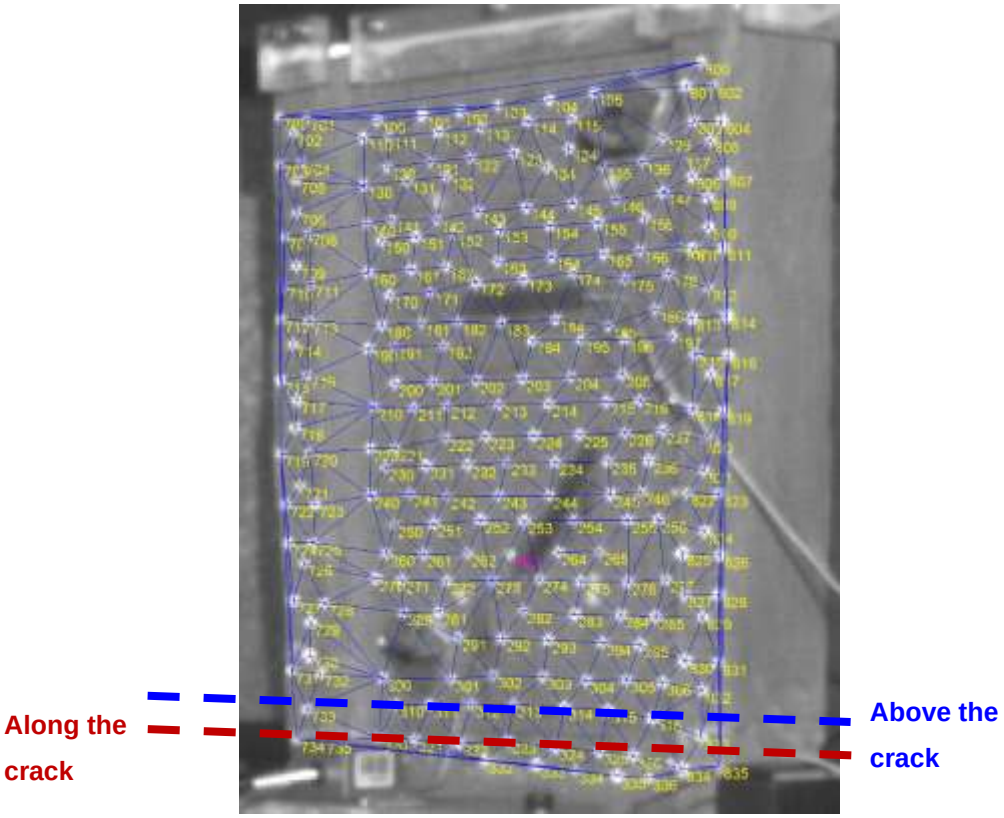

Figure 5.3.6: triangulation computed in EngVis – exp 5

After the completion of the experiment and having observed the crack path (fig. 5.3.3), two groups (fig. 5.3.6) of triangles are decided to be analysed and discussed for their displacement. These are presented in graphs in relation to the specimen's length. The first group is consisted of eleven triangles showing the displacement range of the triangles' centroids located above the crack, as it is observed and monitored during the experimental phase. The second group is consisted of twelve triangles along the same crack.

Figures 5.3.7 – 5.3.9 present the displacement range of the triangles' centroids of these two groups in relation to the specimen's length (x axis) between the four epochs. It does not start at zero on the x axis as the first measurement is the centroid of the first triangle, which is at 12.5mm on the axis of the graph (fig 5.3.7). Figures 5.3.6 – 5.3.8 present the displacement of the triangle's centroids on the x axis ranging from -4.1mm to zero for the groups of triangles above, and along the specimen's crack between epochs 1 and 3. For the same groups of triangles, and between epochs 3 and 4 the displacement range on the x axis has a range of zero to 8.9mm with maximum values being recorded above the crack.

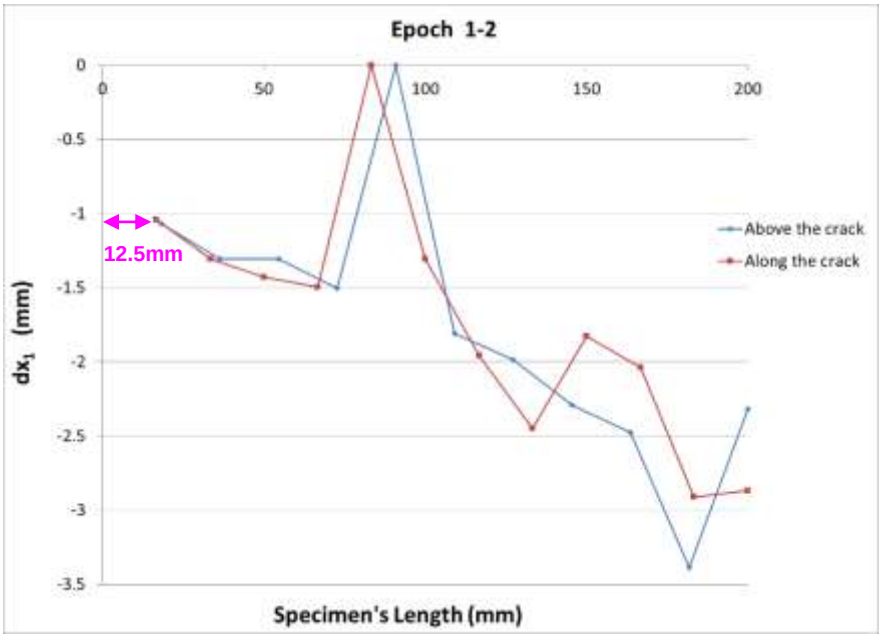

Figure 5.3.7: epoch 1-2 (dx_1 – exp 5)

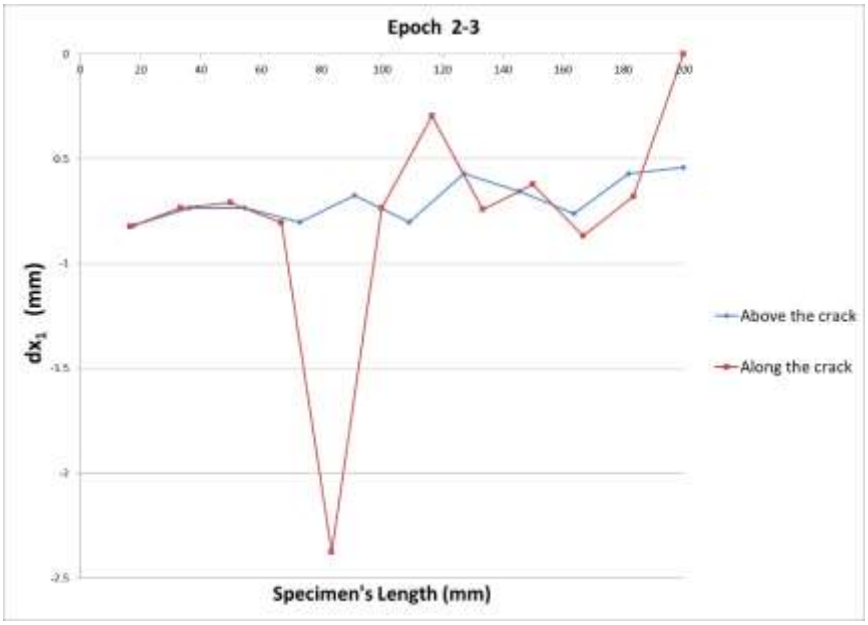

Figure 5.3.8: epoch 2-3 (dx_1 – exp 5)

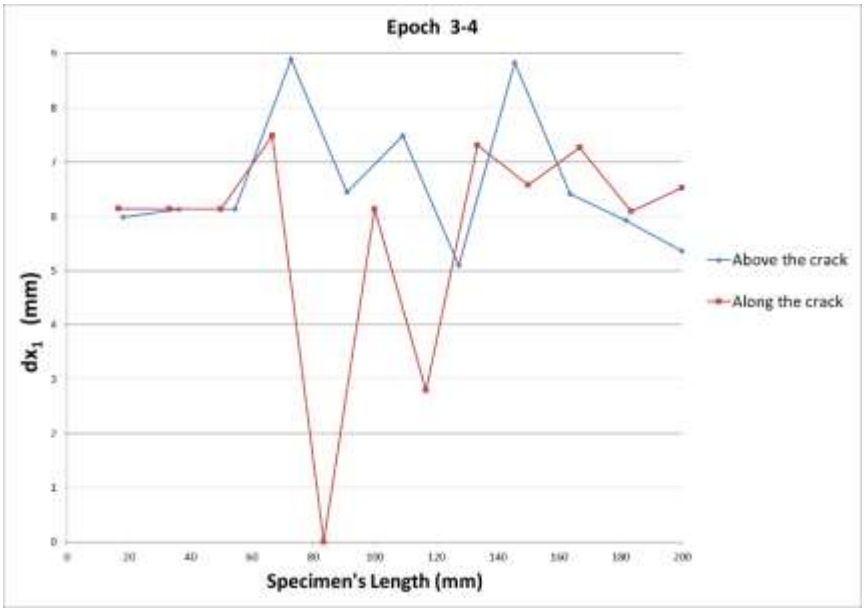

Figure 5.3.9: epoch 3-4 (dx_1 – exp 5)

Figures 5.3.10 – 5.3.12 present the computed shear strain of the measured targets, using the layout of a contour map. These contour maps use for plotting the $x-y-z$ centroid coordinates of each triangle, which is created using the Surfer software. The x-axis represents the length of the tested specimen, the y-axis the height, and the contours the shear strain. Figure 5.3.10 shows shear strain values up to 1.8 mainly at the bottom of the specimen between epochs 1 and 2. Figure 5.3.11 shows the shear strain values up to 2.2, between epochs 2 and 3 and figure 5.3.12 shows the shear strain values up to 6, between epochs 3 and 4. All these figures show the initiation and propagation of the crack at the bottom of the specimen.

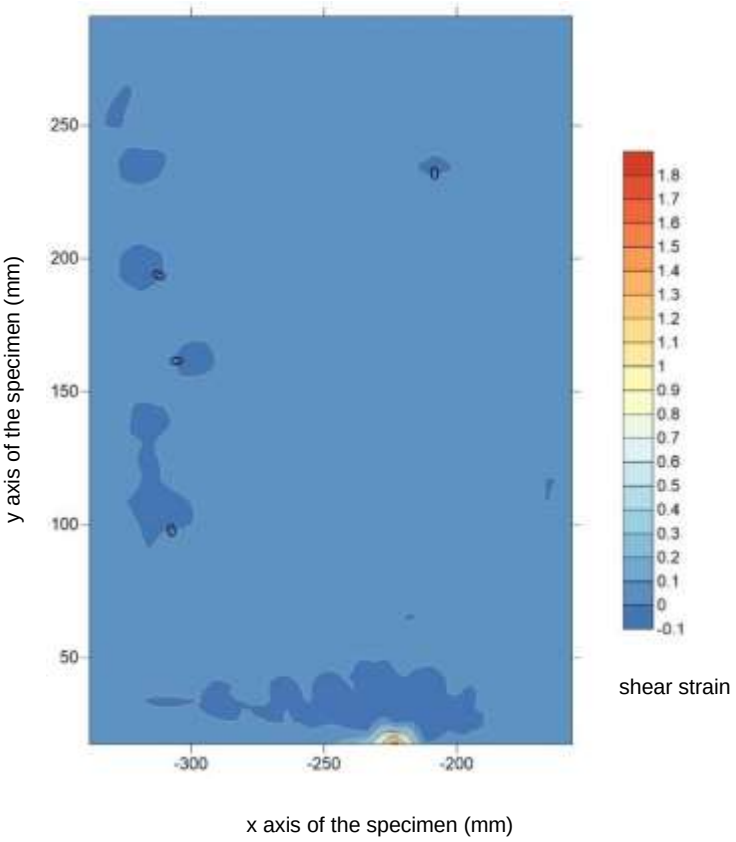

Figure 5.3.10: epoch 1-2 (shear ε – exp 5)

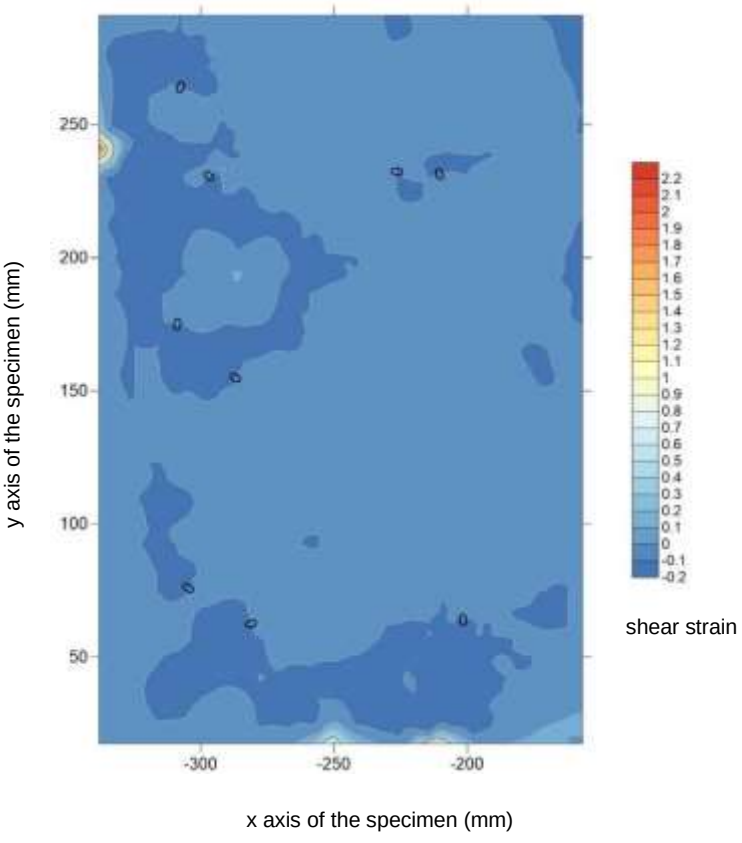

Figure 5.3.11: epoch 2-3 (shear ε – exp 5)

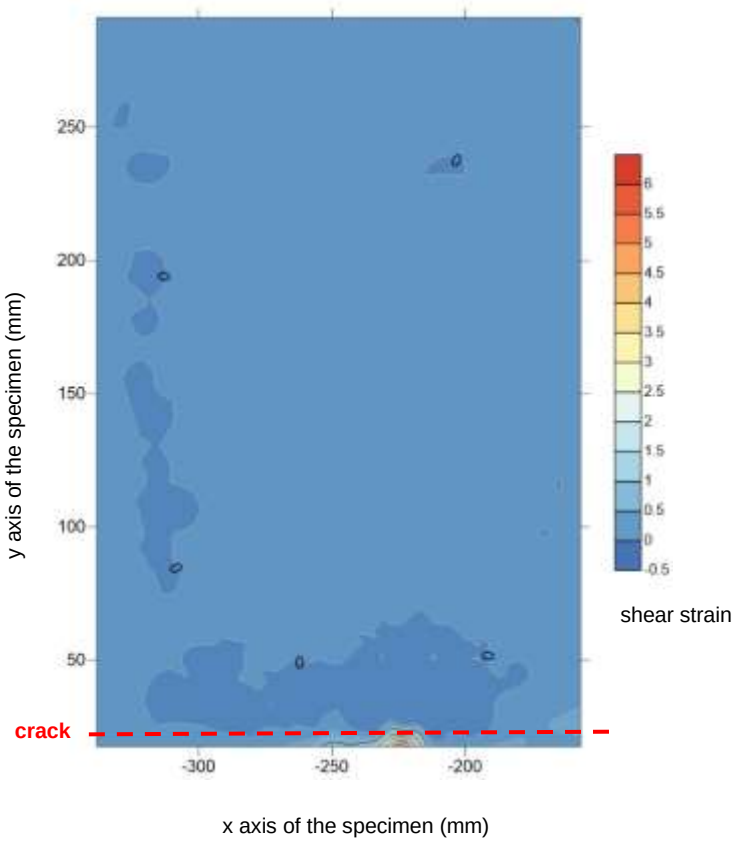

Figure 5.3.12: epoch 3-4 (shear ε – exp 5)

5.4.2 Strain Gauge

Two strain gauges have been installed on the front face of the mini-wall, the one diagonally covering the fourth, fifth and sixth brick layers from the bottom of the specimen and the second one has been installed horizontally between the eighth and ninth brick layers on the mortar area. Both are installed using the same method as described in chapter 4.2.3.3. Figure 5.3.13 shows the SGs' results as recorded during the motion of the specimen. The crack started occurring after the 150 seconds of the monitored motion. As shown on figure 5.3.2, the crack started occurring at 15:08:43.105. At 15:08:52, it was also recorded the largest peak from the diagonal strain gauge showing a value of 0.05. The largest strain reading from the horizontal strain gauge is 0.01 at 15:08:36 (hr:min:sec).

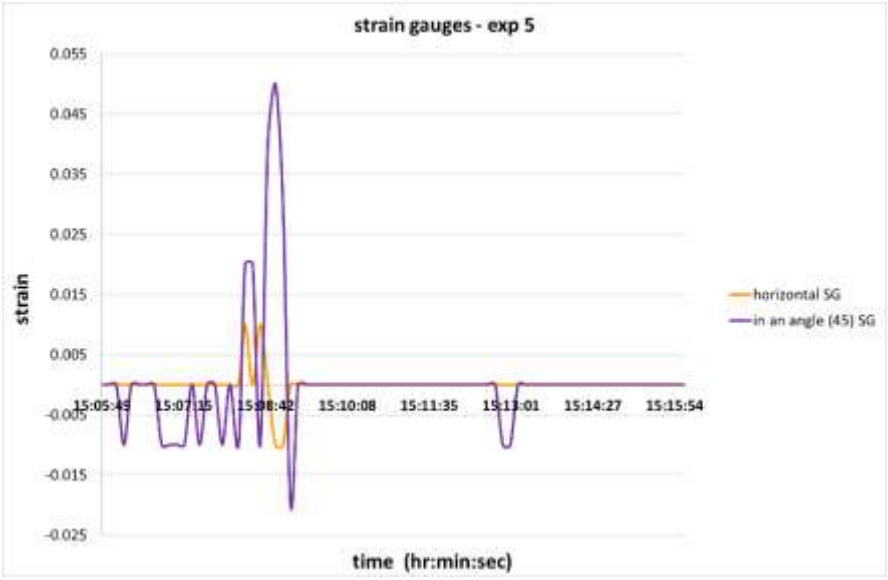

Figure 5.3.13: SG's results – strain over time (hour:minute:second) – exp 5

5.4.3 Comparisons

Figure 5.3.14 presents part of the triangulation picture from the experimental analysis. The triangulation picture is zoomed around the areas of the installed SGs to select the corresponding triangles for the purposes of strain computation using the CRDP method. Each triangle computed one strain value using the CRDP method. In figure 5.3.13 the green line corresponds to the horizontal strain gauge and the pink line to the diagonal strain gauge. The picture also shows the damage localisation as the crack has propagated at the bottom of the specimen.

Therefore, during the experimental analysis, eight triangles were selected along the diagonal strain gauge and seven along the horizontal one (table 5.4). All the negative strain data, computed based on the CRDP method, converted to absolute values, they summed up and divided by the number of triangles. Hence, the four epochs produced three plane strain values for each triangle using the CRDP method and these three strain values, along the strain gauges, were plotted against time as presented in figure 5.3.14. Observing figure 5.3.13, the maximum strain recorded by the horizontal strain gauge is 0.01 at 15:08:36, which is close to 0.013, the strain as computed by the CRDP for epochs 3-4 at 15:08:57.556. Therefore, diagram 5.5 shows the time difference of 21.556 seconds of the recorded strains by the strain gauge and the close-range digital photogrammetry. The strain value, along the triangles of the diagonal strain gauge, computed between epochs 3 and 4, is 0.01 (table 5.4, fig. 5.3.14) recorded at 15:08:57.556 (diagram 5.6). Observing figure 5.3.13, the maximum strain

recorded by the diagonal strain gauge is 0.05 at 15:08:52, which is close to the strain of epochs 3-4 as computed by the CRDP. Therefore, diagram 5.6 shows the time difference of 5.556 seconds of the recorded strains by the strain gauge and the close-range digital photogrammetry.

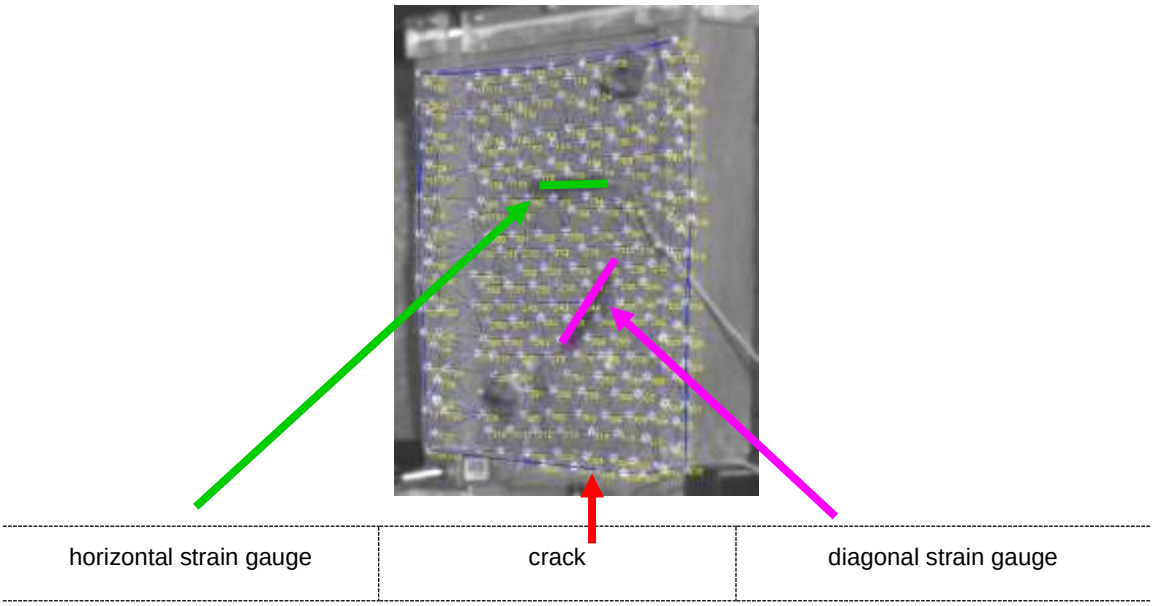

Figure 5.3.14: zoomed area on the triangulation picture – exp 5

					Strain - CRDP		
	triangles along horizontal SG				Strain (1-2)	Strain (2-3)	Strain (3-4)
1	162	171	172		-0.003	0.005	-0.013
2	171	172	182		-0.015	0.005	0.010
3	172	182	183		-0.015	0.004	0.020
4	172	183	173		-0.015	0.004	0.018
5	173	183	184		0.017	-0.001	0.001
6	173	184	174		0.004	-0.007	0.016
7	184	174	185		0.148	-0.141	-0.015
8	174	185	175		-0.394	-0.195	0.197
					0.031	0.024	0.013
	triangles along diagonal SG						
9	215	225	226		0.008	0.000	-0.016
10	225	226	235		-0.012	-0.003	-0.009
11	234	225	235		0.009	-0.005	0.013
12	234	235	245		0.007	-0.004	0.010
13	234	245	244		0.005	-0.003	0.009
14	244	245	254		0.008	-0.002	-0.009
15	244	253	254		0.014	-0.002	0.001
16	253	254	264		-0.010	0.004	-0.009
					0.009	0.003	0.010

time (hr:min:sec:millisec) – epochs	15:08:43.105	15:08:47.589	15:08:57.556

Table 5.4: strains using CRDP method along SGs – exp 5

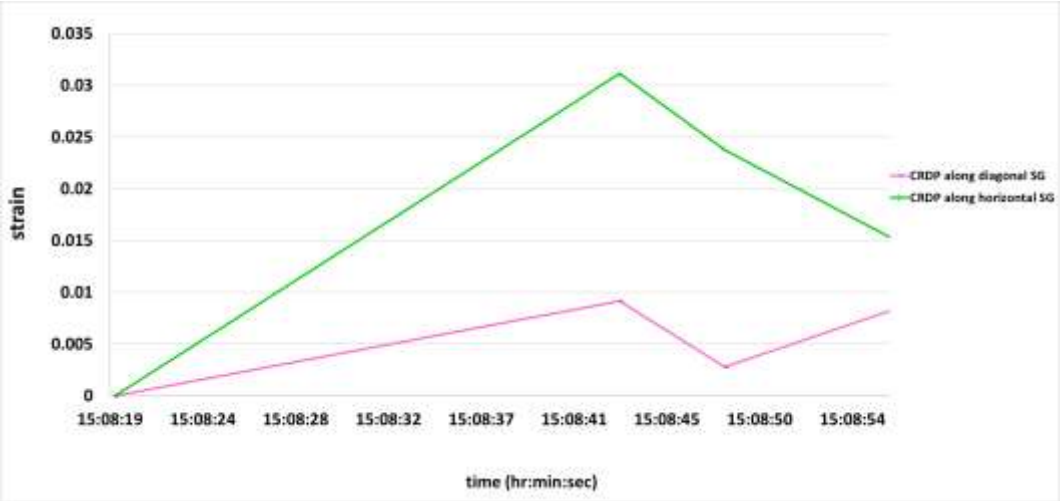

Figure 5.3.15: CRDP strain readings along SGs' sensors – exp 5

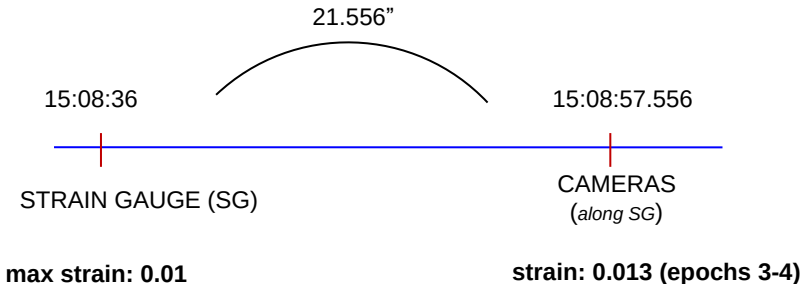

Diagram 5.5: strains along the monitoring methods for experiment 5 – horizontal

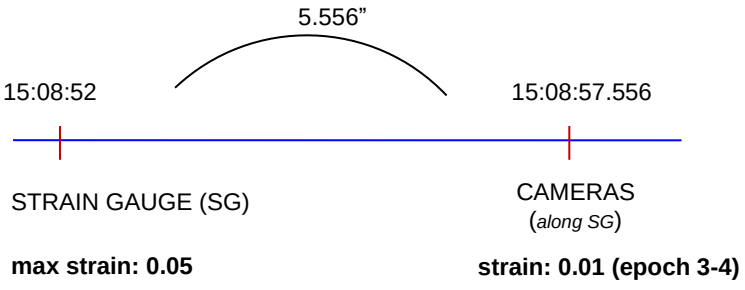

Diagram 5.6: strains along the monitoring methods for experiment 5 – diagonal

5.5 Experiment 6

Experiment 6 carried out on a small-scale masonry specimen excited on a small shaking table. The specimen was built with brick type A and mortar type I and its dimensions were 280mm in height, 240mm in length and 25mm in width. The specimen covered with plaster in order to check if the crack's propagation can be detected by the cameras. The shaking table was turned by 90° and the specimen was vibrated on the z axis in order to check if the application of the CRDP method is efficient when the cameras capture an object being excited on the z axis. 28 control reflected targets were installed on the Π-shape frame attached to the laboratory's wall and 256 free reflected targets installed on the front face of the specimen facing the three redlake cameras and two Nikon ones, installed at a 0.85m distance from the specimen. Each redlake camera collected 300 images and each Nikon ones, 20 images. The test ran for 129 seconds, with an input excitation value to the shaking table of 20Vpp in amplitude and of 25Hz in frequency. The input excitation applied on the z axis was a result of a trial and error with the scope to create cracking to the specimen. For checking the specimen's distortion under different loading, an imposed load of 5.6kg was applied at its top. One strain gauge installed horizontally along the 9th mortar joint (fig. 5.4.1).

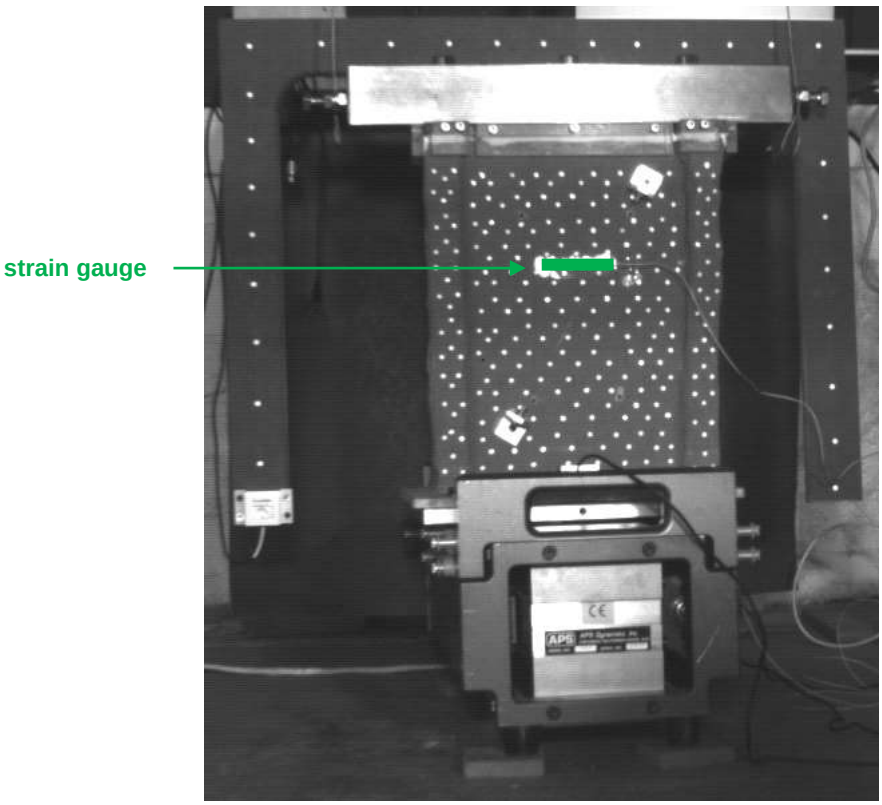

Figure 5.4.1: undamaged small-scale masonry specimen – exp 6

5.5.1 Close Range Digital Photogrammetry

Experiment 6 carried out on a mini-wall specimen on the z axis out of plane direction. For its purposes three redlake and two nikon cameras were used. The three synchronised redlake cameras collected three hundred images per camera and the nikon ones selected twenty images per camera. The analysis of the photogrammetric results is comprised of seventy-five images, nineteen from each redlake camera and nine from each nikon camera. These seventy-five images, one from each camera, are classified into different sets of photographs called epochs, based on the timing synchronisation. In total, nineteen epochs were set up for both the redlake and the nikon cameras and the synchronisation gaps between the two cameras were filled in with black images. For presentation purposes, four images from the nineteen epochs, from both cameras have been selected. Therefore, the four stages of the experiment (fig. 5.4.2) comprised of four epochs (diagram 5.7). Figure 5.4.2a shows the undamaged wall-specimen in epoch 1. Figure 5.4.2b shows the damaged wall-specimen in epoch 2. Figure 5.4.2c and figure 5.4.2d show the damaged wall-specimen in epochs 3 and 4, respectively. Figure 5.4.3 is a zoomed picture of the crack's location.

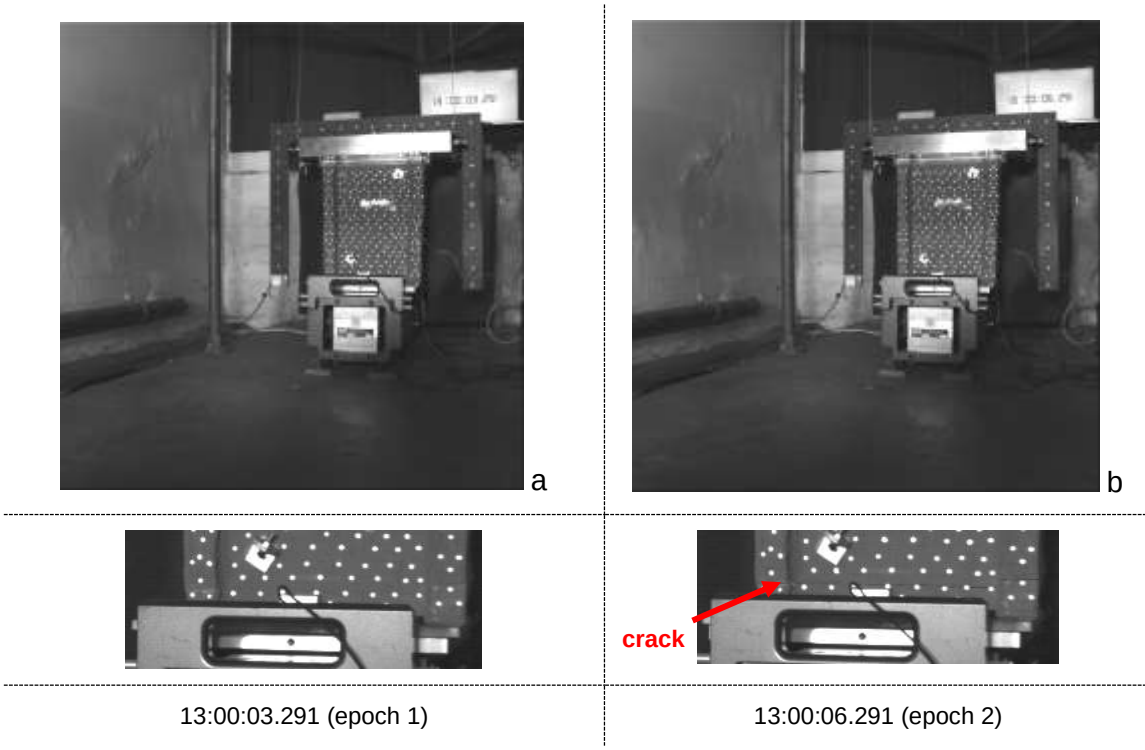

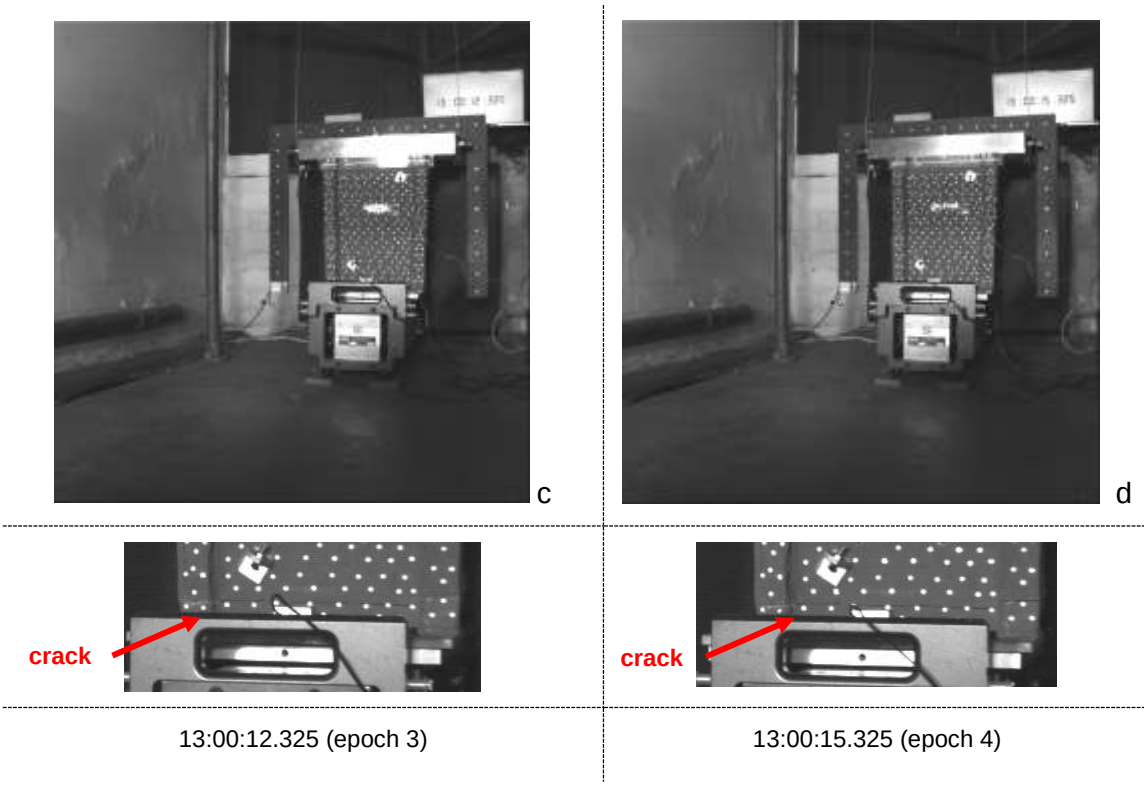

Figure 5.4.2: Images' sequences capturing the actuated tested wall – exp 6

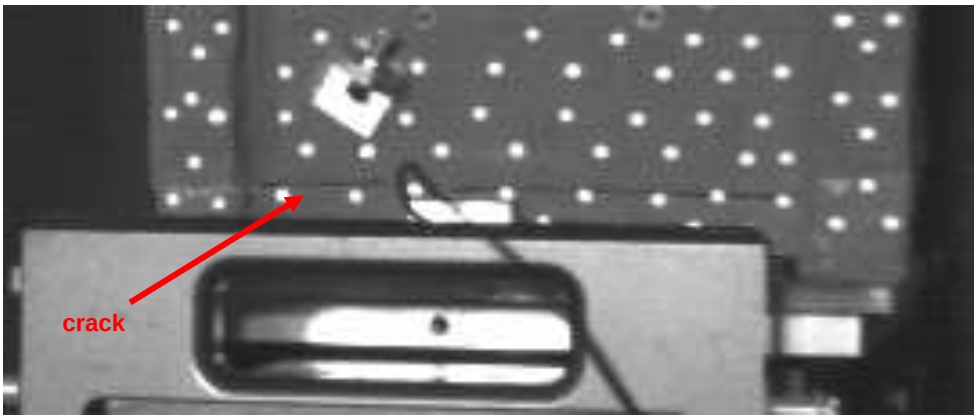

Figure 5.4.3: propagation of the crack – exp 6

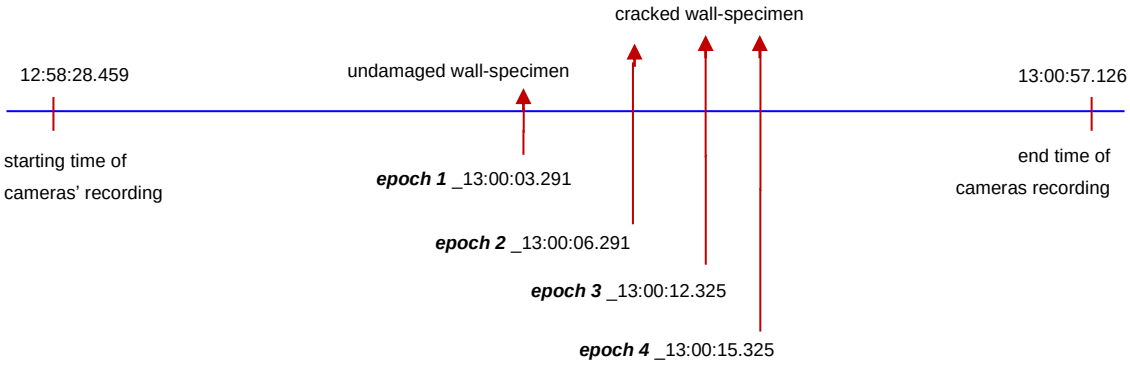

Diagram 5.7: cameras' recording timings for experiment 6 showing both methods (exp 6)

Once the project has been set up on the VMS software and the targets have been inserted, observations are created for both the control and the free targets (fig. 5.4.4). Once the required files have been processed in the VMS environment, data showing the movement of the targets are produced which are inserted further into the EngVis software. This software combines all the measurements from different epochs and can display the target movement in any stage of the experiment. The reason for using EngVis is to generate the triangulation system (fig. 5.4.6), which allows the centroid of any three retro-reflected targets to be determined.

From the seventy-five images, which captured the shaking of the model wall, the $x-y-z$ coordinates of the retro-reflective targets were measured. The standard photogrammetric technique of bundle adjustment was used. From the measured displacements, the strains were calculated based on the basic strain theory (App. IV & Lee *et. al.*, 2006). All the displacements were measured in centimetres within the VMS environment, and these triangles were used as the basis for the strain computation.

Figure 5.4.4a shows the numbered reflected targets (targets ID) on the specimen (green numbers) and on the wooden frame attached to the wall (blue numbers – control points) and the five cameras (green cones). Figure 5.4.4b is the same as figure 5.4.4a along with the observations from the cameras. Figure 5.4.4c is similarly the same as figure 5.4.4a, but on 3D space. Figure 5.4.4d shows the five pictures of the specimen as captured by the five cameras, 3 redlake and 2 nikon ones, in the VMS software.

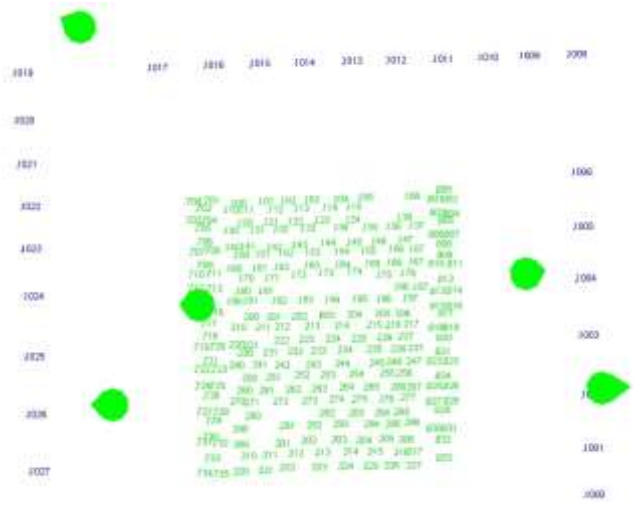

a

object view with target IDs and cameras in 2D

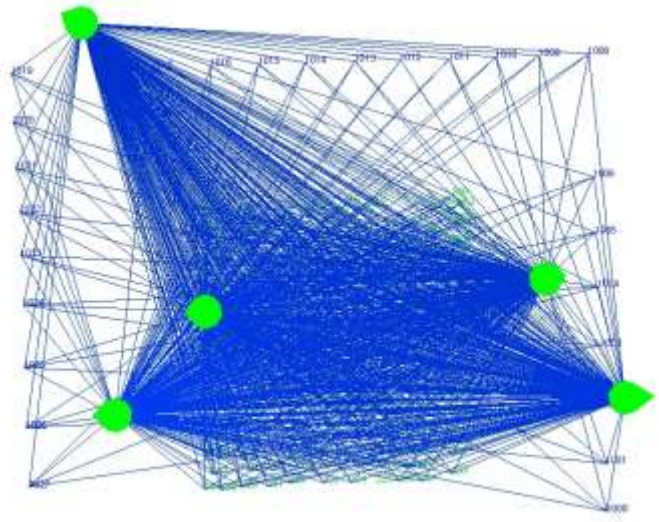

b

object view with observations

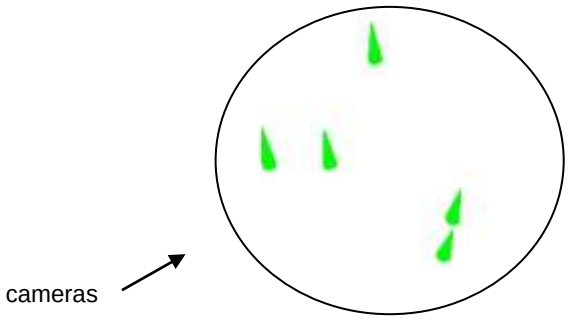

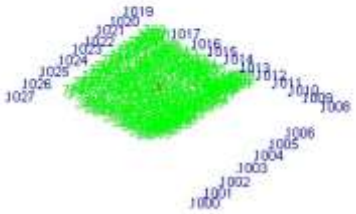

c

object view with target IDs and cameras in 3D

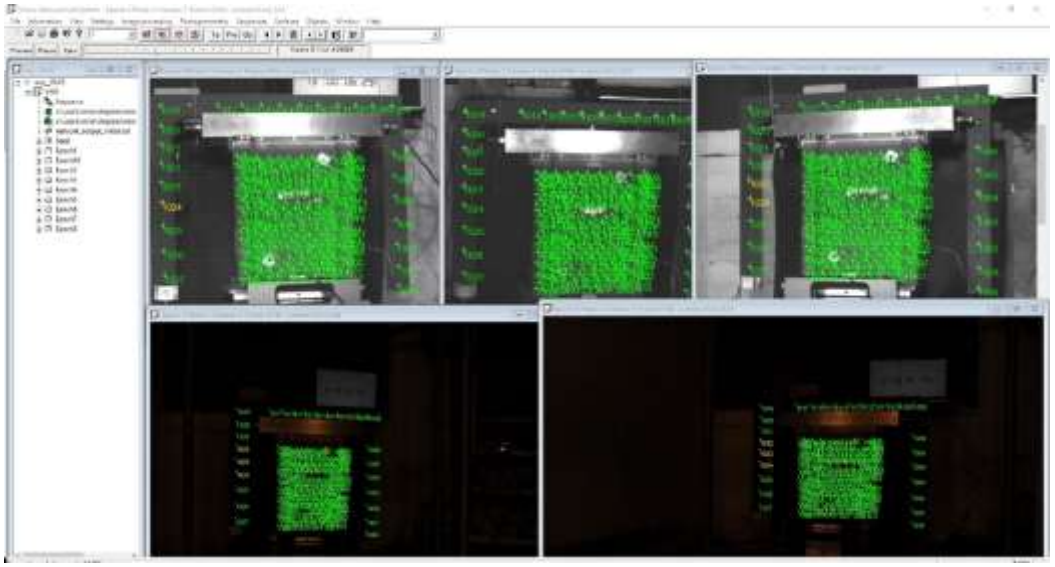

d

VMS analysis photos

Figure 5.4.4: object view of the mini-wall specimen in VMS environment – exp 6

Figure 5.4.5 shows the deformation of all the free reflected targets from epoch 1 to epoch 4. The dots correspond to the monitored reflected targets and figure 5.4.5 verifies figure 5.4.2. Epochs 1 to 2 show very small movement of all the monitored targets on the x axis. However, the overall deformation plots of epochs 1-4 in both 2D and 3D space, confirms the displacement on the z axis resulted due to the out of plane specimen's motion, with a crack being formed at the bottom of the vibrated specimen.

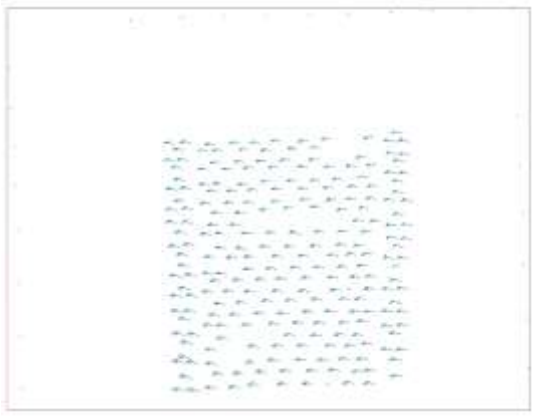

epoch 1

epoch 2

epoch 3

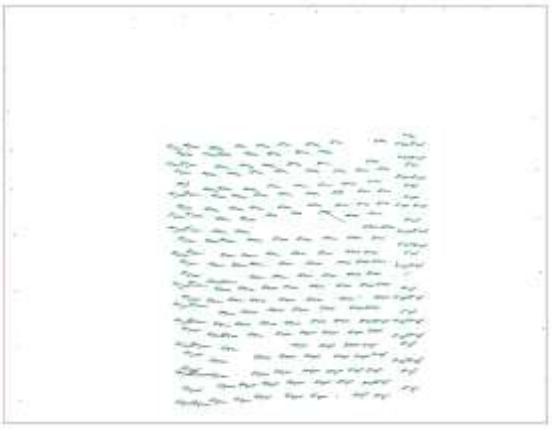

epoch 4

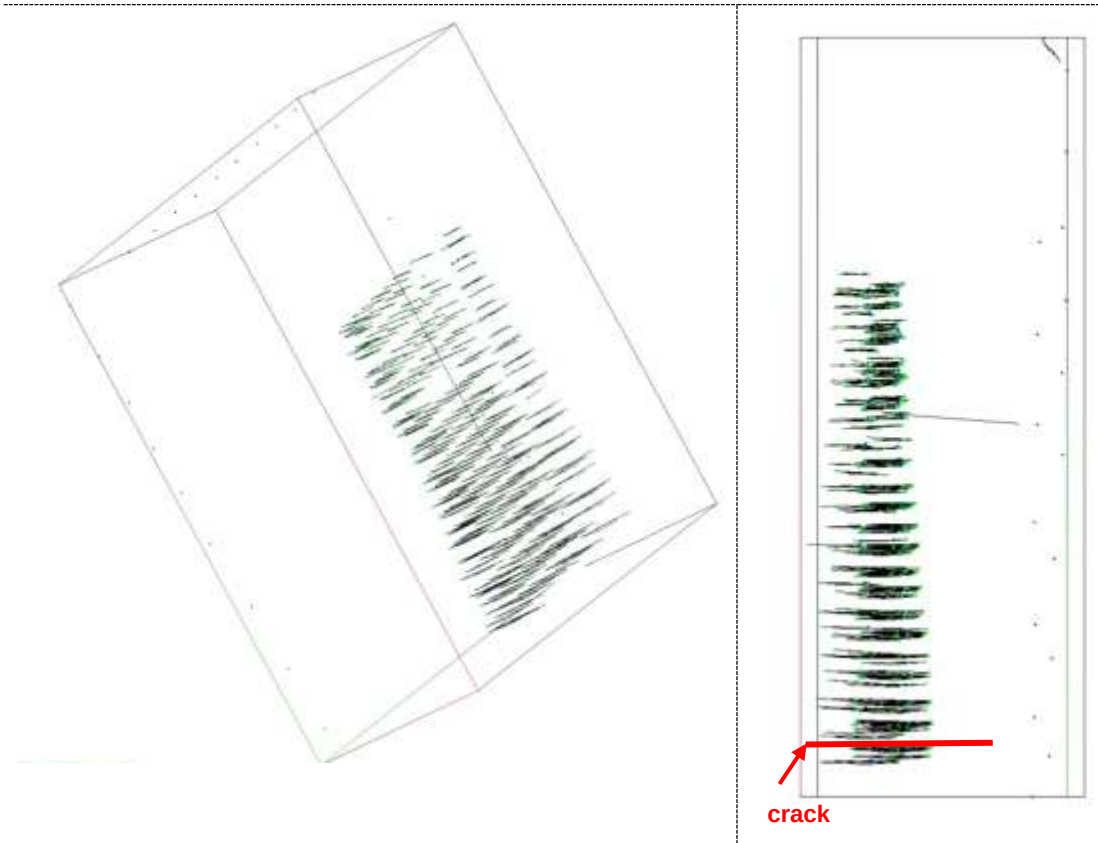

Figure 5.4.5: Deformation of specimen's triangles – exp 6

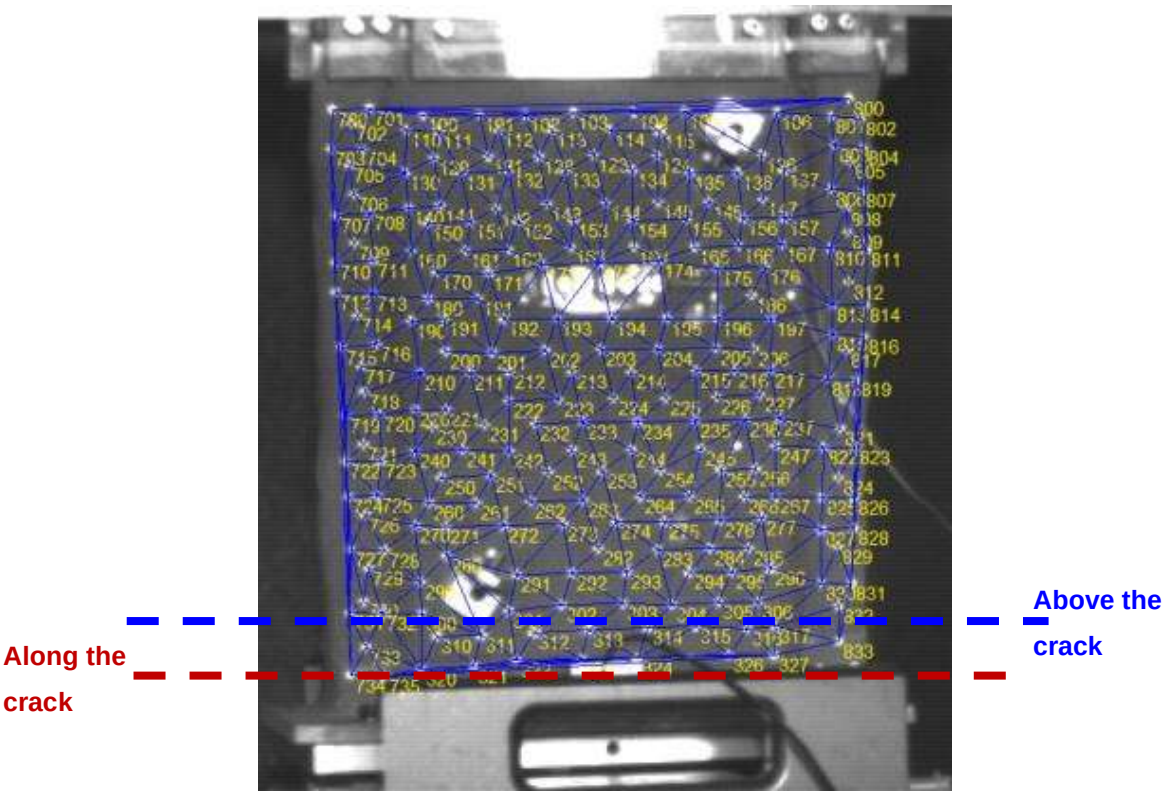

Figure 5.4.6: triangulation computed in EngVis – exp 6

After the completion of the experiment and having observed the crack path (fig. 5.4.3), two groups (fig. 5.4.6) of triangles are decided to be analysed and discussed additionally for their displacement. These are presented in graphs in relation to the specimen's length. The first group is consisted by twenty-three triangles showing the displacement range of the triangles' centroids located above the crack, as it was observed and monitored during the experimental phase. The second group was consisted of fourteen triangles along the same crack.

Figures 5.4.7 – 5.4.9 present the displacement range of the triangles' centroids, on the x axis, of these two groups in relation to the specimen's length (x axis) between the four epochs. Figure 5.4.7 shows the triangles' centroids displacement from epoch 1 to epoch 2 with a range of -2.3 to -1.1mm for the group of triangles above and along the crack, providing a figure of the specimen's distortion during the first 3 seconds of its analysed motion. Figure 5.4.8 has a mirror form with figure 5.4.9, with the triangles' displacements to follow an ascending form along the specimen's x axis between epochs 2 to 3 and a descending form between epochs 3 to 4, and both graphs show very small displacement values. Figures 5.4.10 – 5.4.12 show the triangles' displacement range on the z axis of the specimen's motion, with all the values to be significantly larger to those computed on the x axis. The triangles' displacements on epochs 1 to 2 and 3 to 4, have a mirror form to those computed between epochs 2 to 3. This is observed on both groups of triangles, above and along the specimen's crack. The large displacement values for the group of triangles above and along the specimen between epochs 1 to 2 and 3 to 4, confirms the out of plane motion of the tested mini-wall.

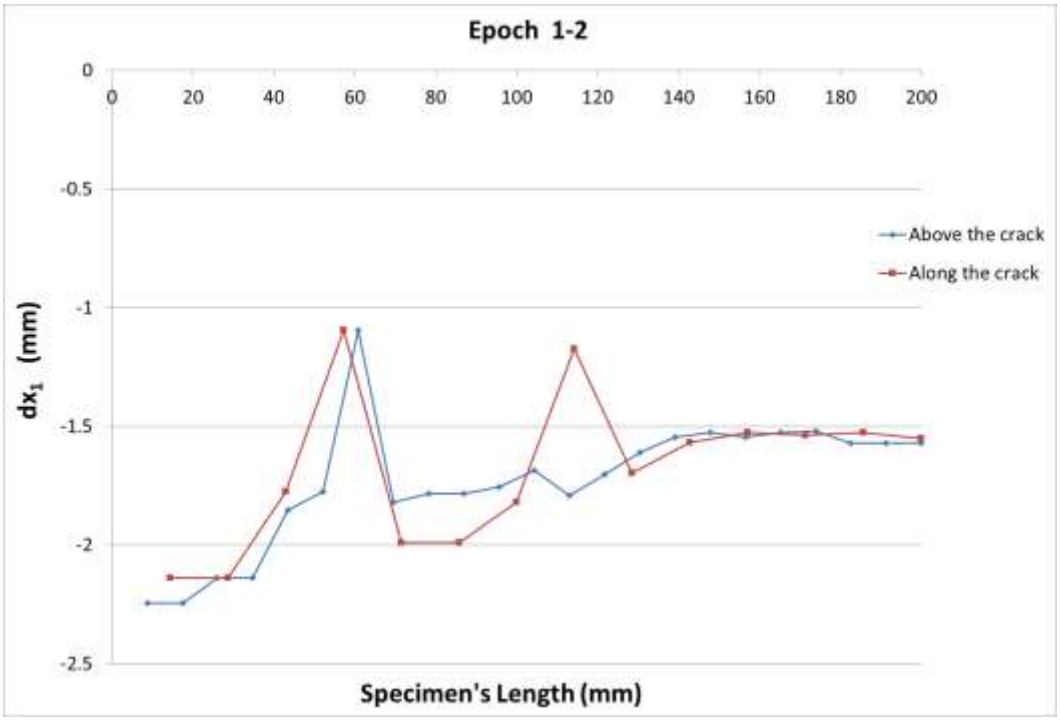

Figure 5.4.7: epoch 1-2 (dx_1 – exp 6)

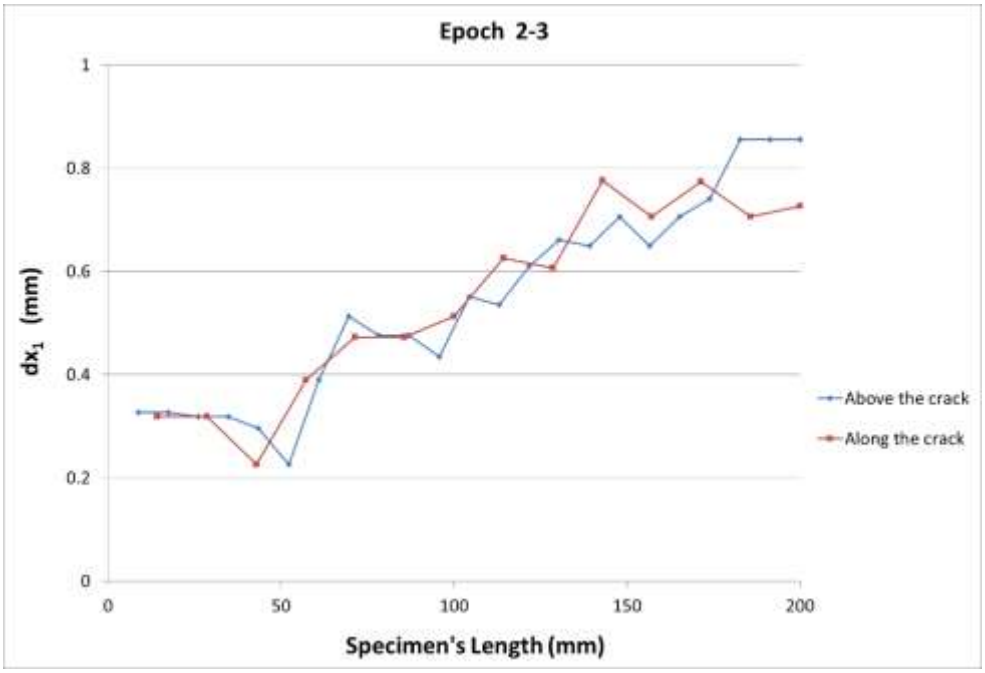

Figure 5.4.8: epoch 2-3 (dx_1 – exp 6)

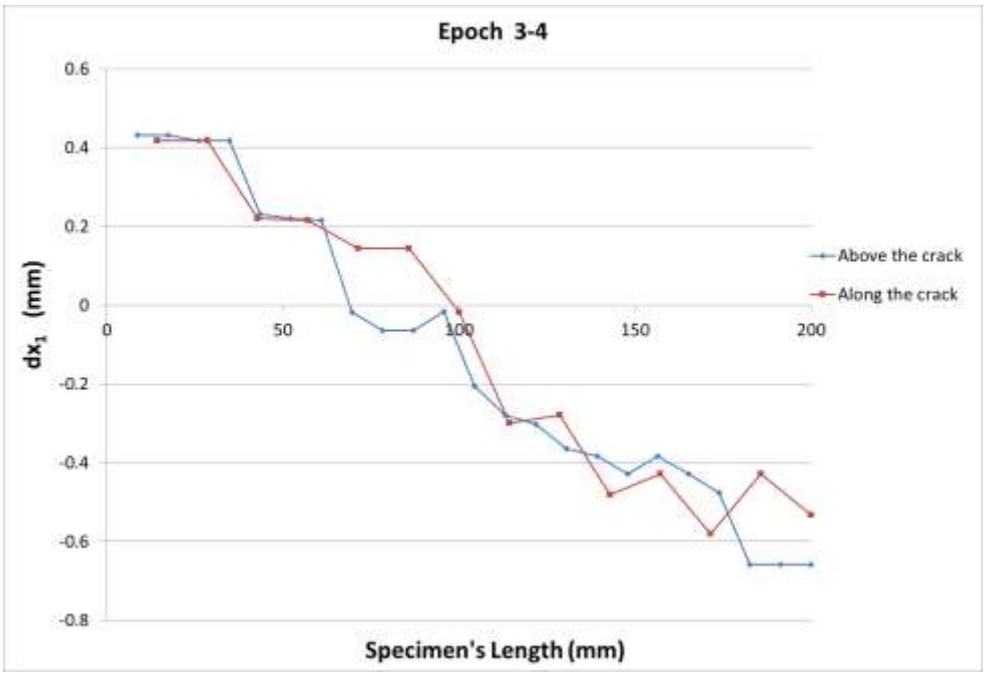

Figure 5.4.9: epoch 3-4 (dx_1 – exp 6)

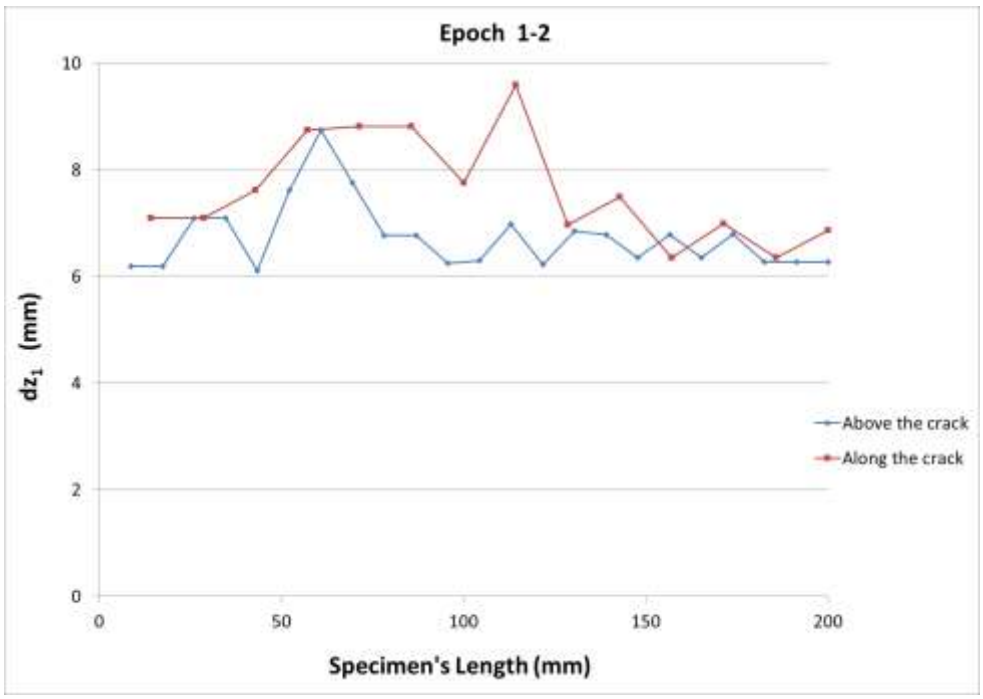

Figure 5.4.10: epoch 1-2 (dz_1 – exp 6)

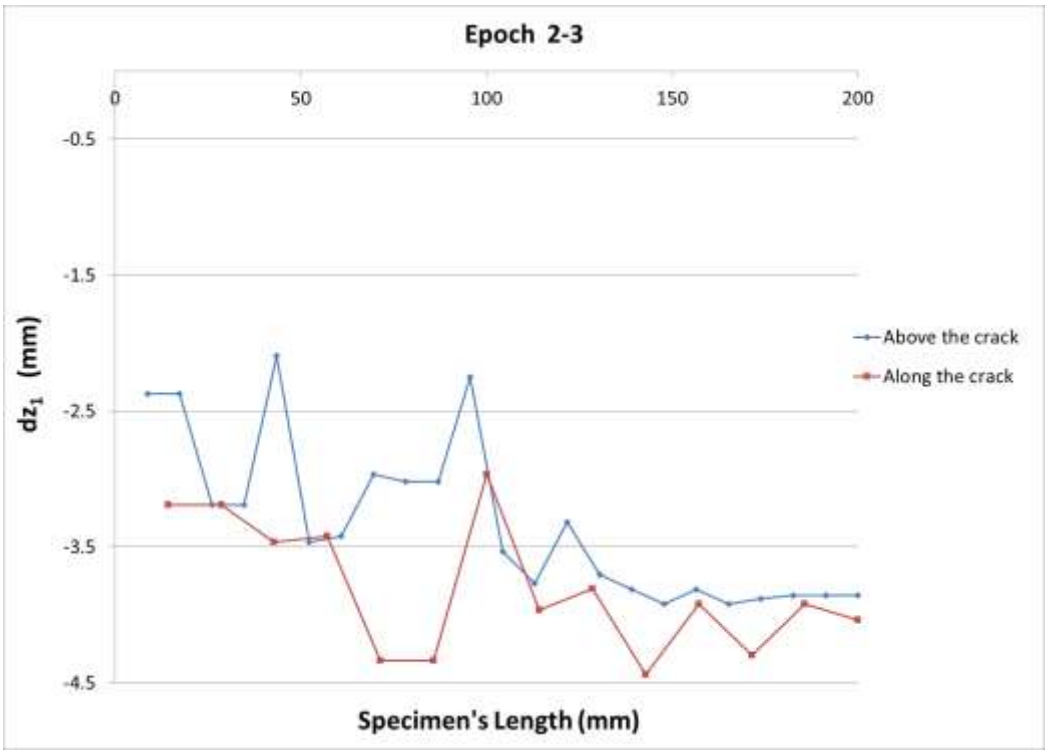

Figure 5.4.11: epoch 2-3 (dx_1 – exp 6)

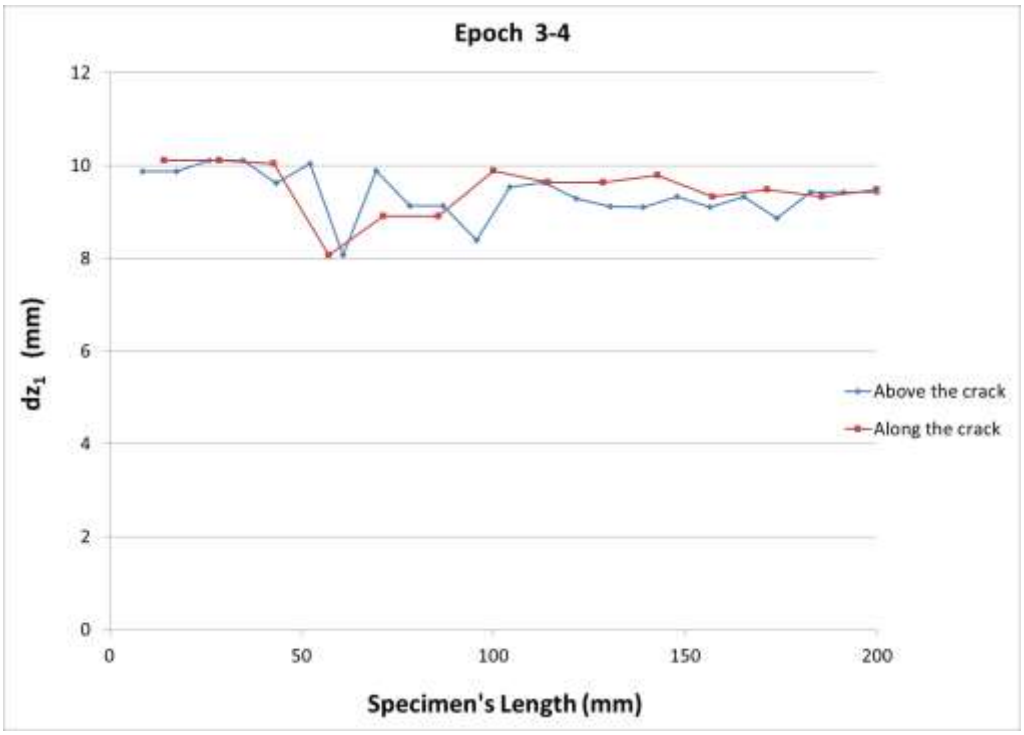

Figure 5.4.12: epoch 3-4 (dx_1 – exp 6)

Figures 5.4.13 – 5.4.15 present the computed shear strain of the measured targets, using the layout of a contour map. These contour maps use for plotting the $x-y-z$ centroid coordinates of each triangle, which is created using the Surfer software. The x-axis represents the length of the tested specimen, the y-axis the height, and the contours the shear strain. Figure 5.4.13 shows shear strain values up to 0.6 between epochs 1 and 2. Figure 5.4.14 shows the shear strain values up to 8, between epochs 2 and 3 and figure 5.4.15 shows the shear strain values up to 12.5, between epochs 3 and 4. These big values show that between epochs 3 and 4, the specimen was undergoing a crack opening at the bottom of the specimen.

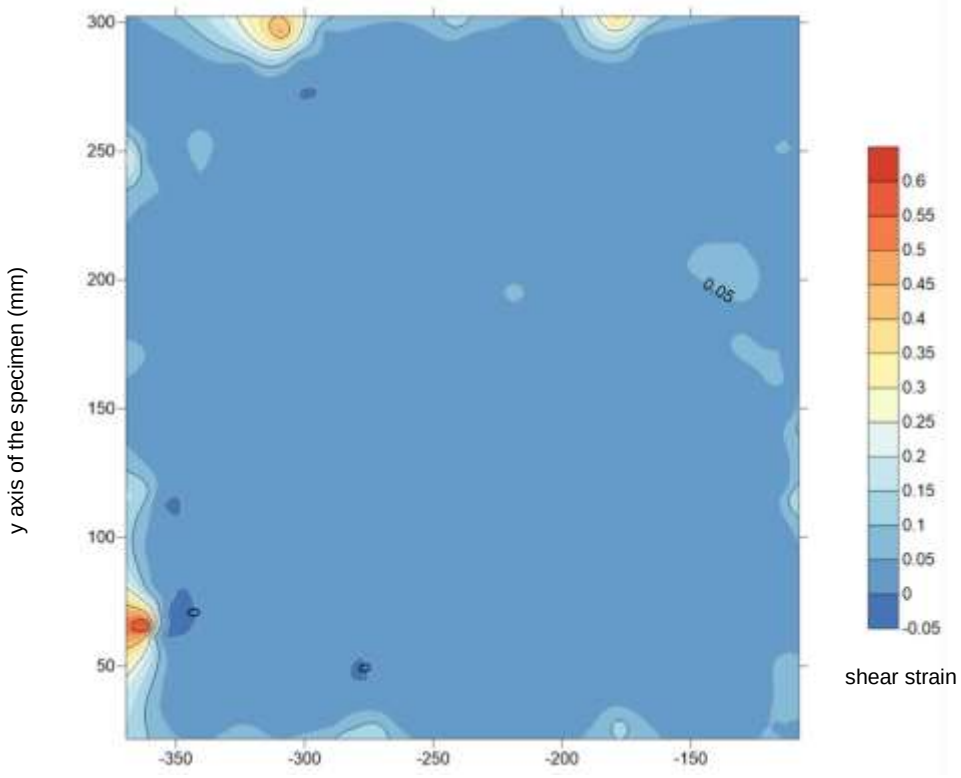

Figure 5.4.13: epoch 1-2 (shear ε – exp 6)

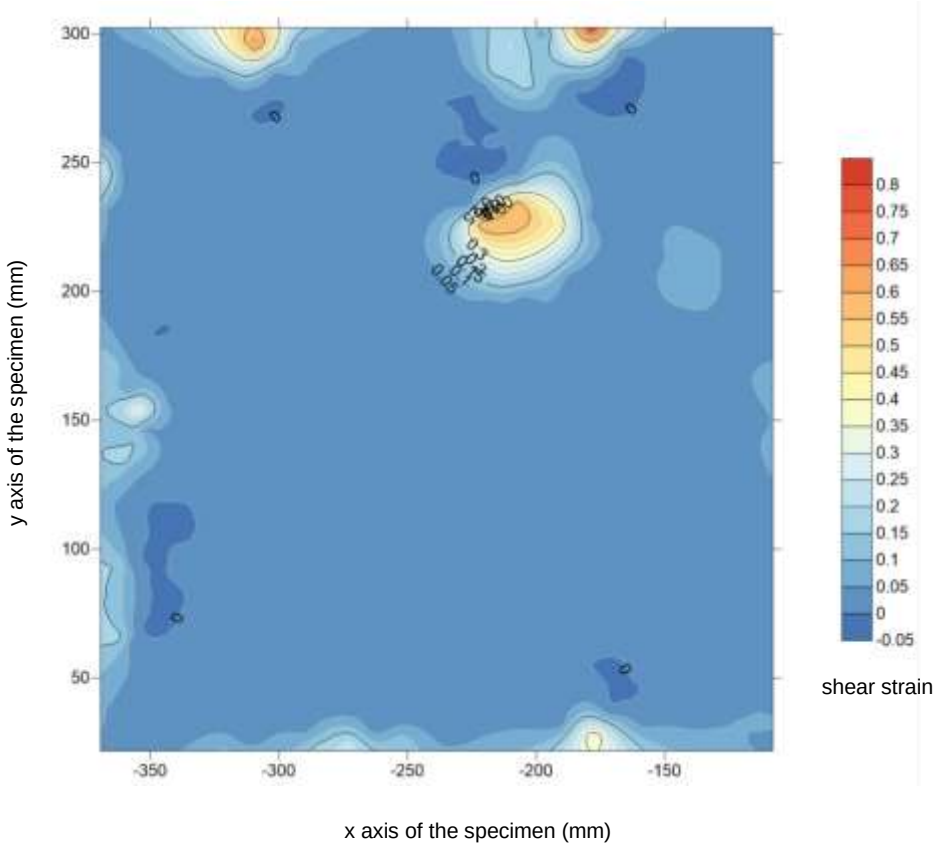

Figure 5.4.14: epoch 2-3 (shear ε – exp 6)

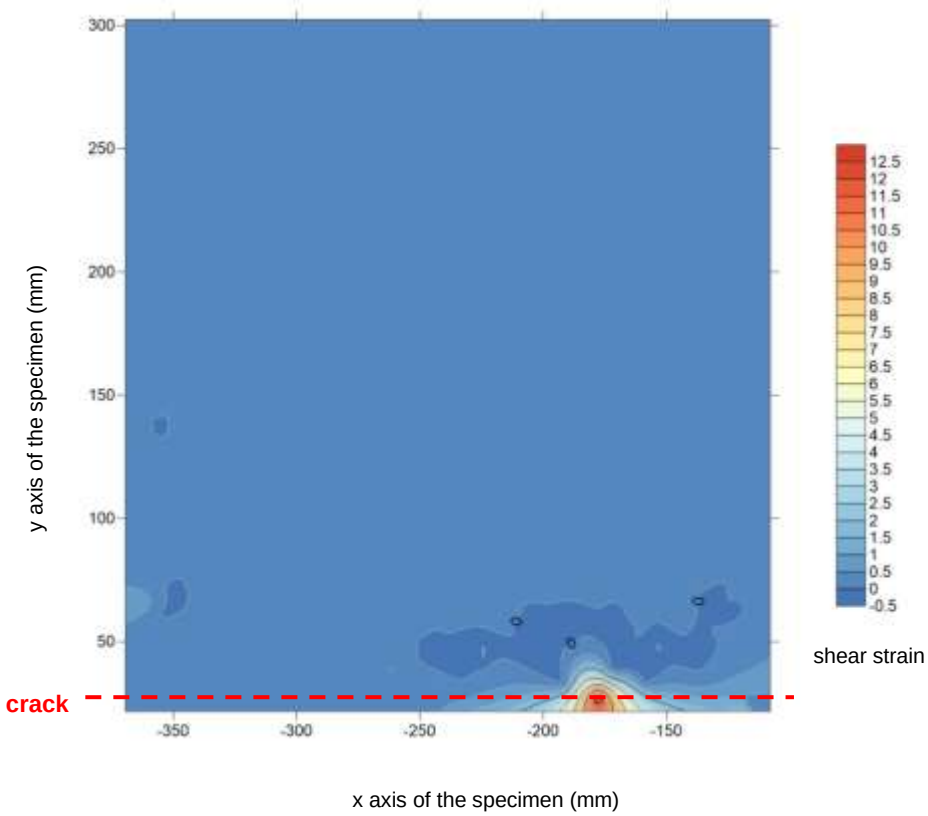

Figure 5.4.15: epoch 3-4 (shear ε – exp 6)

5.5.2 Strain Gauge

One strain gauge was installed at the middle of the mini-wall, horizontally between the eighth and ninth brick row from the bottom of the specimen, on the mortar's location. It was installed using the same method as described in chapter 4.2.3.3. Figure 5.4.16 shows the SG's results as recorded during the motion of the specimen. The largest strain reading recorded by the strain gauge is 0.06 at 13:00:06 (hr:min:sec).

Figure 5.4.16: SG's results – strain over time (hour:minute:second) – exp 6

5.5.3 Comparisons

Figure 5.4.17 presents the triangulation file formed during the experimental analysis. The triangulation picture shows the installed SG to select the corresponding triangles for the purposes of strain computation using the CRDP method. Each triangle computed one strain value using the CRDP method.

Therefore, during the experimental analysis, six triangles were selected along the strain gauge. All the negative strain data, computed based on the CRDP method, converted to absolute values, they summed up and divided by the number of triangles (table 5.5). Hence, the four epochs produced three strain values for each triangle using

the CRDP method, as shown in figure 5.4.18. The maximum strain value computed using the CRDP is 0.023 at 13:00:06. The maximum strain value recorded by the strain gauge is 0.06. Diagram 5.7 shows that the peaks of the maximum strains showing almost no time difference between the strain gauge and the CRDP readings along the SG.

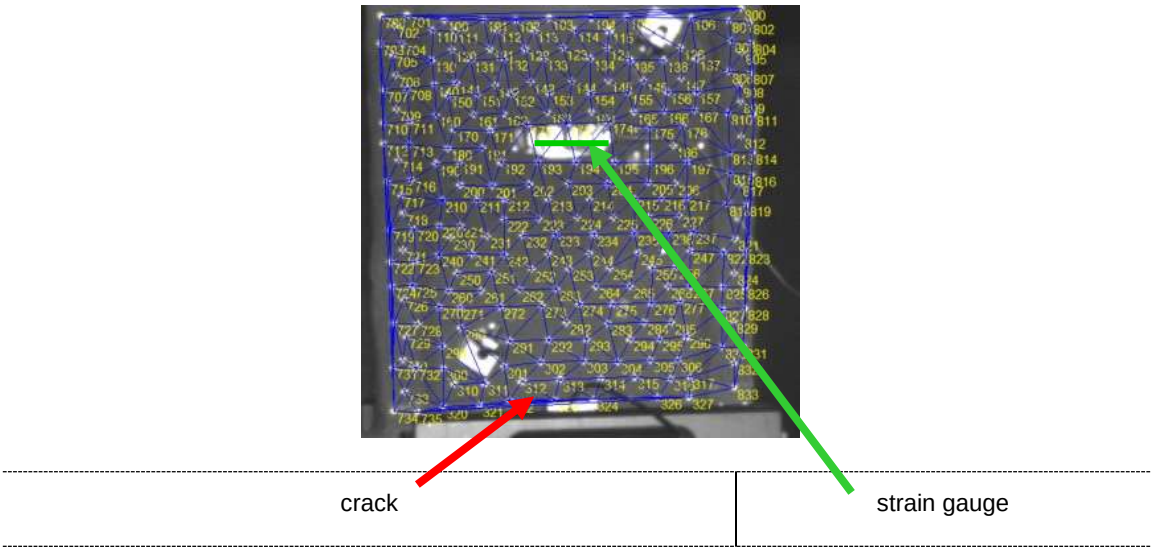

Figure 5.4.17: triangulation picture showing the **crack** and **strain gauge** – exp 6

					Strain - CRDP		
					Strain (1-2)	**Strain (2-3)**	**Strain (3-4)**
	triangles along SG						
1	172	171	192		0.029	0.004	0.001
2	192	193	172		0.029	0.004	0.001
3	172	193	173		0.012	-0.006	-0.001
4	173	193	194		0.037	-0.006	0.009
5	174	194	195		-0.019	0.000	-0.001
6	175	174	195		-0.013	-0.003	-0.014
					0.023	0.004	0.004

time (hr:min:sec:millisec) – epochs	13:00:06.291	13:00:12.325	13:00:15.325

Table 5.5: strains using CRDP method along SG – exp 6

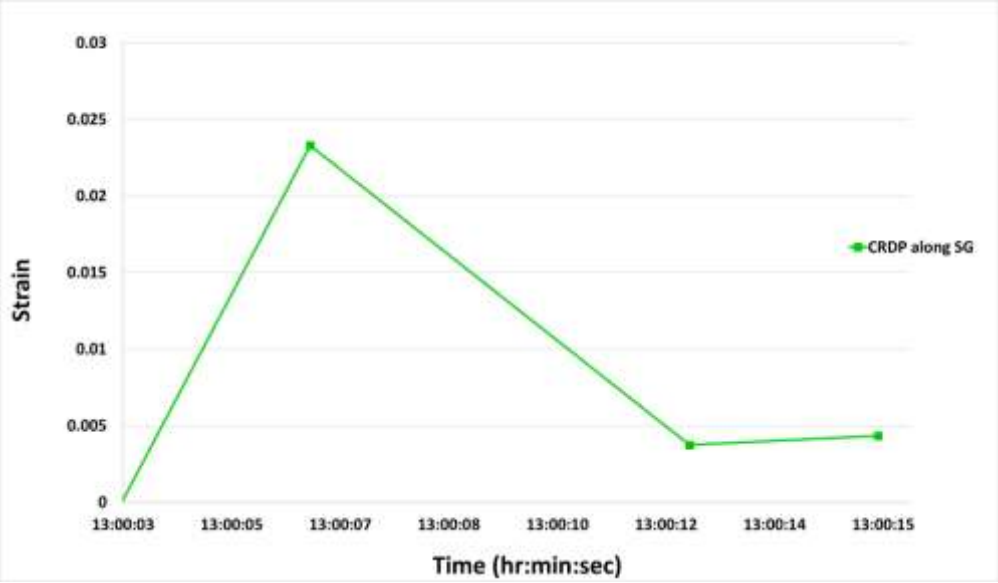

Figure 5.4.18: CRDP's readings along SG sensor – exp 6

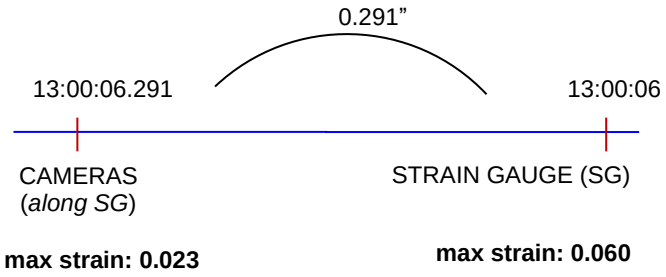

Diagram 5.7: monitoring methods recording sequence for experiment 6 along with their max. strains

5.6 Discussion

Four experiments, dynamically loaded, carried out to one leaf mini-scale masonry specimen and have demonstrated their results for their deformations, their maximum shear strains and the strains obtained by the strain gauges, as they accomplished to record a difference on their readings during the crack propagation. More specifically the technique of close-range digital photogrammetry has been proven sufficient for capturing, monitoring and interpreting the shear failure of the tested specimens, as in all the experiments it captured the initiation, propagation of the crack along with the local and/or global failure of the specimens. The strain gauges managed to present high peaks during the cracks' formations. Following, four critical points are discussed

related to the characteristics and the performance of the experiments as presented in chapters 5.2-5.5.

The results collected with the redlake and the nikon cameras under experiment 4 are obtained using the two different types of cameras, redlake and Nikon ones. The shear strains (5.2.11 & 5.2.17) and the deformation (5.2.5 & 5.2.15) figures show good correlation between the two different cameras, which confirms the fact that CRDP may be applied with any type of cameras. The larger number of frames per second collected, the better for estimating the monitored structural element's pathology.

Two additional experimental set ups have been tested and presented in Chapters 5.4 and 5.5. Under experiment 5, the specimen was positioned at a 45° angle opposite to the monitoring cameras and managed to capture the formation of the crack as shown in Figure 5.3.3. Additionally, under experiment 6, the tested wall was covered with plaster and it was vibrated on the z axis. These parameters did not prevent the CRDP to monitor the formation of the crack at the bottom of the specimen as it is shown in Figure 5.4.3.

Therefore, the CRDP is a sufficient monitoring method under both in plane and out of plane motions, when using experimental (redlake) or commercial (nikon) cameras or when it is plane masonry finish or standard plaster wall finish.

Based on the computed displacements and following the basic strain theory as developed by Lee et. al. (2006), the shear strains for all the experiments have been calculated. The reason for using the Lee et. al. (2006) strain theory is due to the good results the study obtained as presented in chapter 2. Table 5.6 summarises the shear strain from experiments 3 and 4. Experiment 3 has two versions. During version I, the collected image data were split into four epochs. Epoch 2 was the first selected epoch, where the cracking initiated. Epoch 1 was the image where the specimen showed undamaged and before the crack's initiation. Epochs 3 and 4 showed the damaged specimen and the crack's propagation. Version II of experiment 3 is comprised of the same four epochs plus one more epoch before the first one, in order to check if the damage can be detected before it can be seen or shown in the pictures. Therefore, the shear strains computed for versions I and II were similar between epochs 1-2 giving a value of 2.5 and very close for epochs 2-3 giving a value of 8 for version I and a value of 6 for version II. Similarly, the shear strains are very close between epochs 3-4, giving a value of 18 for version I and a value of 21 for version II. Experiment 4 has two versions as well. Version I presents the monitoring using the redlake cameras and version II presents the monitoring using the Nikon cameras. For the redlake version, epoch 2 was the first chosen epoch where the

specimen was slightly damaged. Therefore, the shear strains between epochs 1 and 2 and between 2 and 3 are close to 2. Epoch 3 is the detachment of the small mini brick. Similarly, epoch 2, for the Nikon version, shows the detachment of the mini brick and epoch 1 the undamaged specimen. Therefore, the shear strains between epochs 3 and 4, for the redlake version, and between epochs 1 and 2, for the Nikon version, show close results of 5.2 and 4.8, respectively. This means that both methods are capable in monitoring damage and successfully translate it to shear strain.

However, strain gauges can collect a significant large amount of data and identifying a change on the continuous monitoring strains, once damage occurs. This is well shown under experiments 4 and 5 where the strain gauges have been installed horizontally, diagonally (at 45°) and vertically on the front face of the tested wall. Under all these three different set ups, the collected strains were in good correlation with the computed strains once using the CRDP method.

experiment	epochs	shear strain
exp 3 (I)	1 – 2	2.5
	2 – 3	8
	3 – 4	18
exp 3 (II)	-1 – 1	5.2
	1 – 2	2.5
	2 – 3	6
	3 – 4	21
exp 4 (I – redlake)	1 – 2	2.4
	2 – 3	2.2
	3 – 4	5.2
exp 4 (II – nikon)	1 – 2	4.8

Table 5.6: summary of shear strain results – exp 3 & 4

5.7 Conclusion

The purpose of this chapter was to present the four experiments (3, 4, 5, & 6), which were carried out in the CEGE Laboratories at the University College London to the small scale one-leaf masonry specimens. Their size was the small form of the scaled down church's eastern wall. Experiment 4 was a repetition of experiment 3 to check the performance levels of the two monitoring methods CRDP and SG. Under experiment 5 the wall-specimen was plastered and positioned at an angle of 45° opposite to the cameras and under experiment 6 the wall-specimen was similarly plastered, and it was tested on an out of plane (z axis) motion.

Strain gauges proved capable to monitor a change in their strain recordings once the cracks started propagating during the tests. The CRDP also showed its capability to capture the failure and with the use of the appropriate computation means (Mohr circle) to translate this failure to displacement and strain for a small structural component (i.e. a triangle) of the specimen-walls.

Therefore, for the purposes of the next steps of this research, the two monitoring methods of CRDP and SG, will be applied to the large-scale masonry walls under experiments 7 and 8.

CHAPTER 6

LARGE SCALE EXPERIMENTS

6.1 Overview

This chapter presents, compares and discusses the results of the two experiments carried out in the Earthquake and Large Structures Laboratory (EQUALS) at the University of Bristol. Similarly, to the small scale, two monitoring techniques applied to the tested engineering specimens, close range digital photogrammetry and strain gauges. Table 6.1 summarises these two experiments, with the load being applied at the top of the specimens and the excitation at the bottom.

	duration (sec)	*type of shaking table*	*no. of cameras*	*no. of targets*	*no. of images / camera*	*no. of epochs*
exp 7	239	large shaking table	3	422	300	4
exp 8	179	large shaking table	3	422	300	4
	SG's location			*brick type*	*mortar type*	
exp 7	one along the 4th mortar joint, one along the 8th and one along the 13th			C	II	
exp 8	one along the 4th mortar joint, one along the 8th and one along the 13th			C	II	
	Hz	*applied load (kg)*	*direction of excitation*	*direction of failure*		
exp 7	33.875	148	X axis	out of plane		
exp 8	36.625	148	X axis	out of plane		

Table 6.1: Characteristics of exp 7 & 8

6.2 Experiment 7

Experiment 7 carried out on a large-scale masonry specimen excited on a large shaking table. The specimen was built with brick type C and mortar type II and its dimensions were 1044mm in height, 856mm in length and 208mm in width. 186 control reflected targets were installed on the wall behind the shaking table and on the protected barriers around the shaking table. Also, 422 free reflected targets installed on the front face of the specimen facing the 3 redlake cameras installed at a 2.2m distance from the specimen. Each redlake camera collected 300 images. The test ran for 239 seconds, with an input excitation value to the shaking table of 33.875Hz in frequency. The input excitation applied on the x axis was a result of a trial and error with the scope to create cracking to the specimen. The imposed load applied at the top of the specimen was 148kg (App. II) and the three strain gauges installed horizontally along the 4th, 8th and 13th mortar layers (fig. 6.1.1).

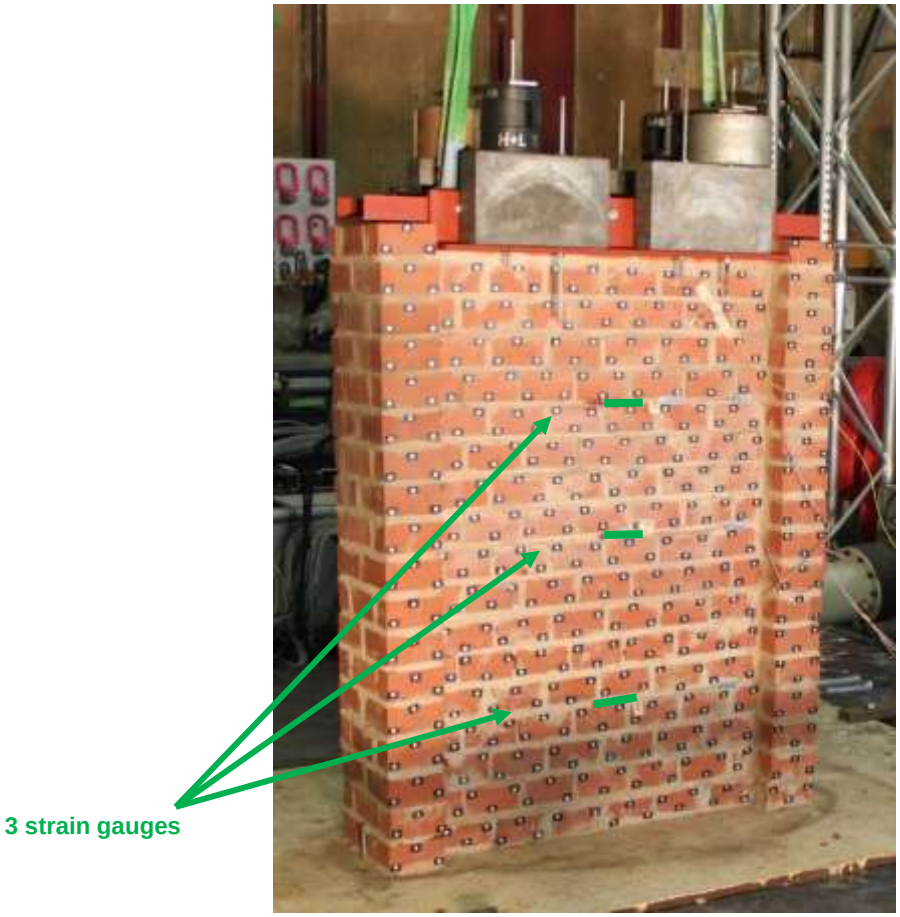

Figure 6.1.1: undamaged large-scale masonry specimen – exp 7

6.2.1 Close Range Digital Photogrammetry

For the purposes of the first large scale experiment three redlake cameras were installed at a distance of 2.2m of the wall specimen. These cameras collected three hundred images per camera. The analysis of the photogrammetric results is comprised of twelve images, one from each camera, which is classified into different sets of photographs called epochs, based on the timing synchronisation. Therefore, the four stages of the experiment (fig. 6.1.2) is comprised of four epochs (diagram 6.1). The first epoch was chosen prior to the damage and epochs 2, 3 and 4 was chosen to show the crack at the bottom of the specimen.

For the purposes of the large-scale experiment three redlake cameras were used, which each of them collected three hundred images. The analysis of the photogrammetric results is comprised of twelve images, one from each camera, which is classified into different sets of photographs called epochs. Therefore, the four stages of the experiment (fig. 6.1.2) is comprised of four epochs (diagram 6.1). Epoch 2 (fig. 6.1.2b) was the first epoch capturing the crack's initiation and epoch 1 (fig. 6.1.2a) was chosen to show the specimen prior to the damage. Epochs 3 and 4 (fig. 6.1.2c & d) were chosen to show the crack at the bottom of the specimen. Figure 6.1.3 shows the tested specimen after its distortion. The cameras' monitoring period successfully captured the initiation of the crack and the specimen's distortion.

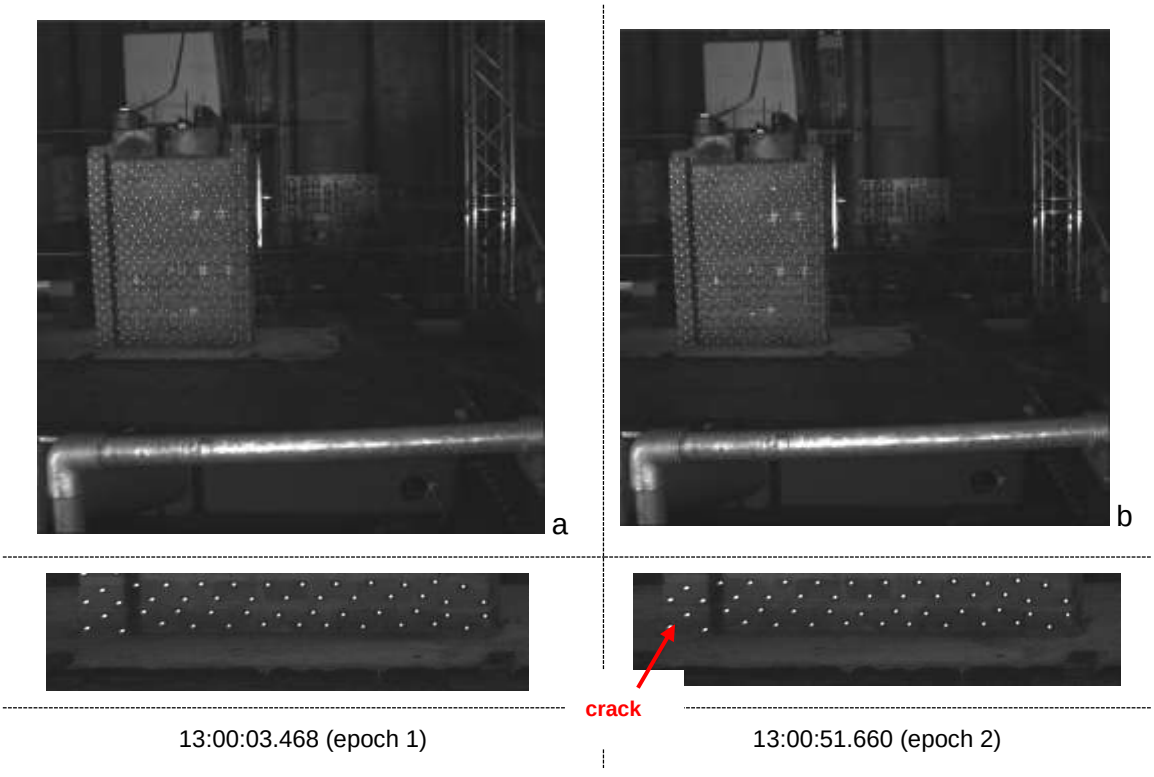

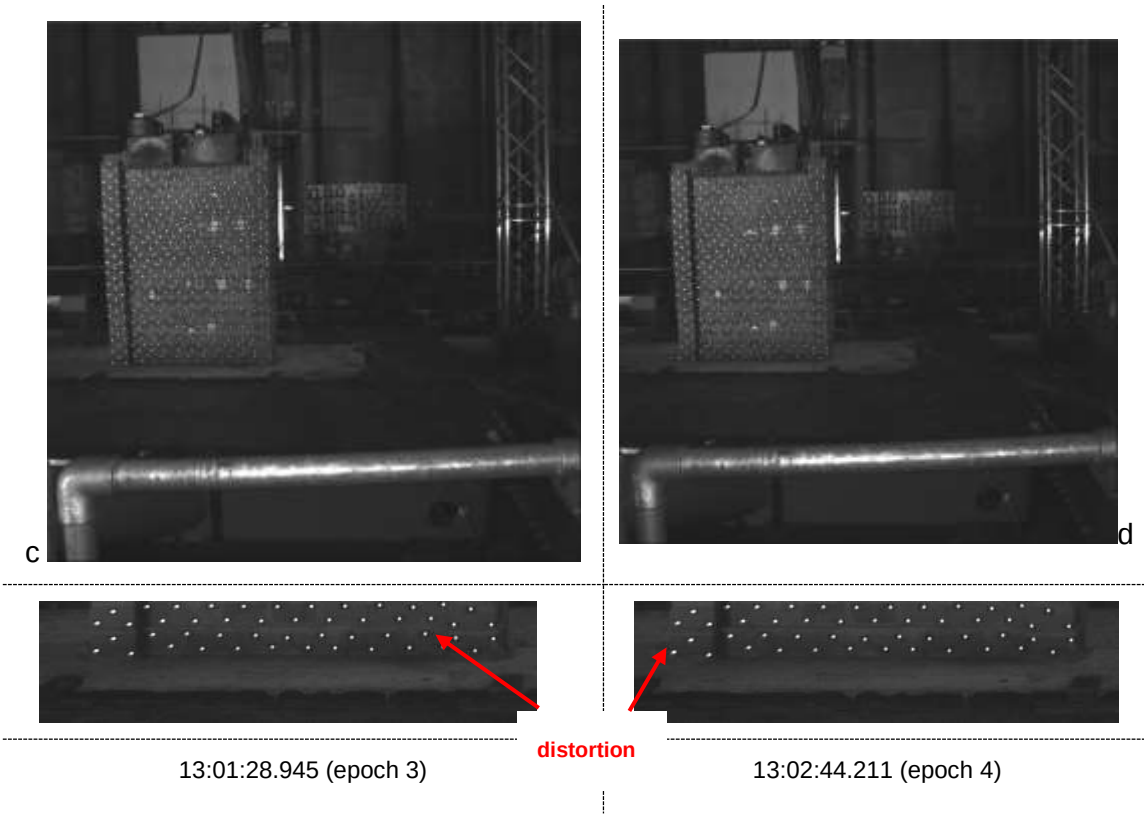

Figure 6.1.2: Images' sequences capturing the actuated tested wall – exp 7

Figure 6.1.3: specimen's distortion – exp 7

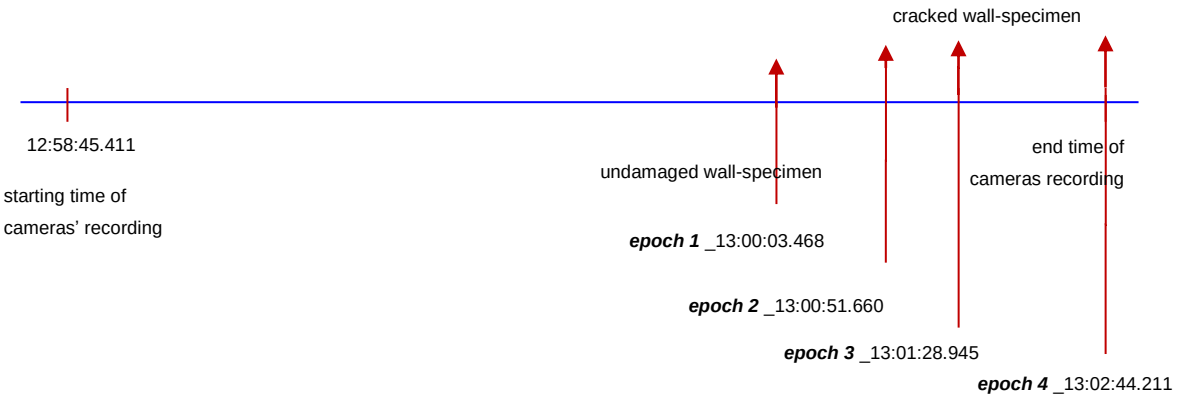

Diagram 6.1: cameras' recording timings for experiment 7

One-hundred eighty-six control points are installed attached to the wall behind the monitored specimen and on the protected barriers around the shaking table. Also, four-hundred twenty-two reflected targets are installed on the face of the specimen which face the three redlake cameras. Once the project has been set up on the VMS software and the targets have been inserted, observations are created for both the control and the free targets (fig. 6.1.4). Once the required files have been processed in the VMS environment, data showing the movement of the targets are produced which are inserted further into the EngVis software. This software combines all the measurements from different epochs and can display the target movement in any stage of the experiment. The reason for using EngVis is to generate the triangulation system (fig. 6.1.6), which allows the centroid of any three retro-reflected targets to be determined.

From the twelve images, which captured the shaking of the model wall, the $x-y-z$ coordinates of the retro-reflective targets were measured. The standard photogrammetric technique of bundle adjustment was used. From the measured displacements, the strains were calculated based on the basic strain theory (App. IV & Lee *et. al.*, 2006). All the displacements were measured in centimetres within the VMS environment, and these triangles were used as the basis for the strain computation.

Figure 6.1.4a shows the numbered reflected targets (targets ID) on the specimen (green numbers), the control points on the rails and on the wall (blue numbers) and the three cameras (green cones). Figure 6.1.4b is the same as figure 6.1.4a along with the observations from the cameras. Figure 6.1.4c is similarly the same as figure 6.1.4a, but on 3D space. Figure 6.1.4d shows the three pictures of the specimen as captured by the three cameras in the VMS software.

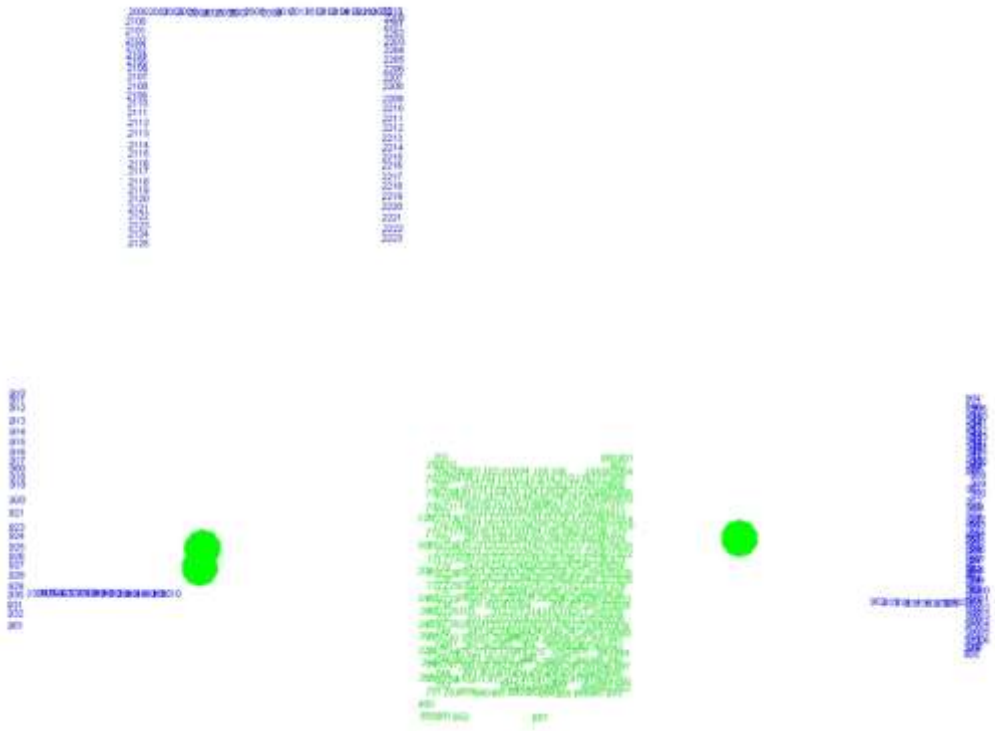

a

object view with target IDs and cameras in 2D

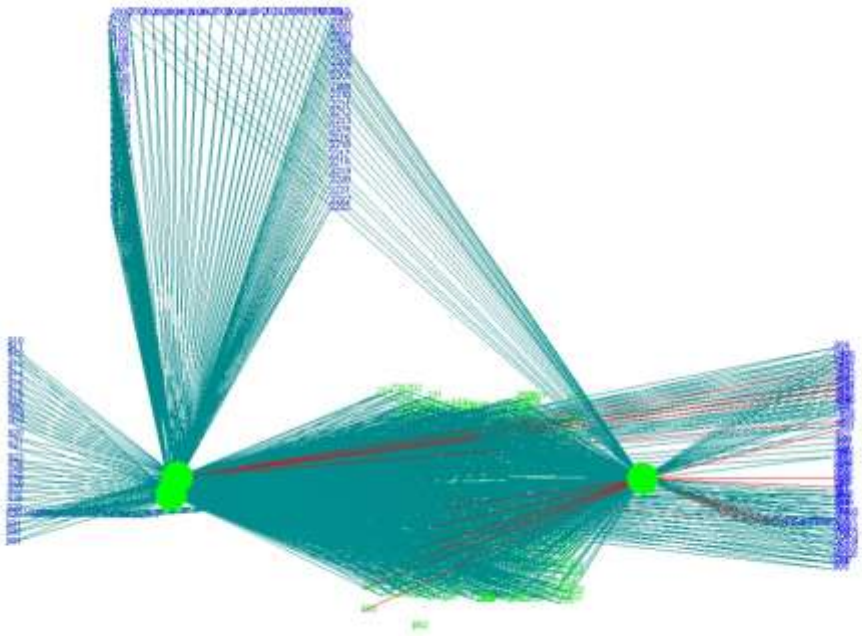

b

object view with observations

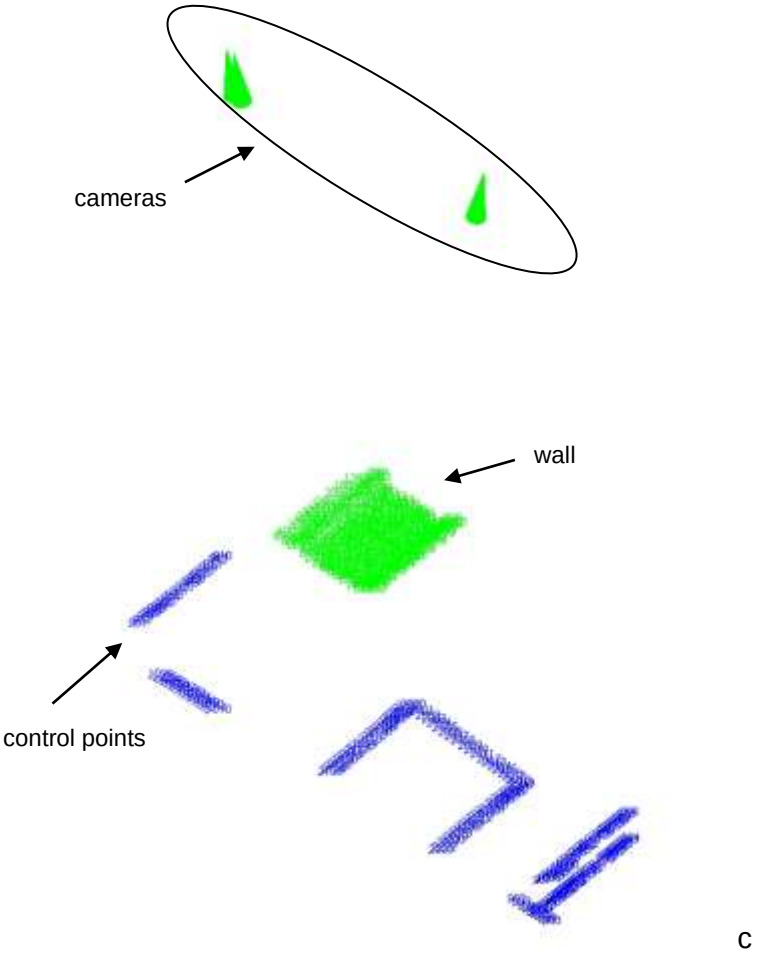

c

object view with target IDs and cameras in 3D

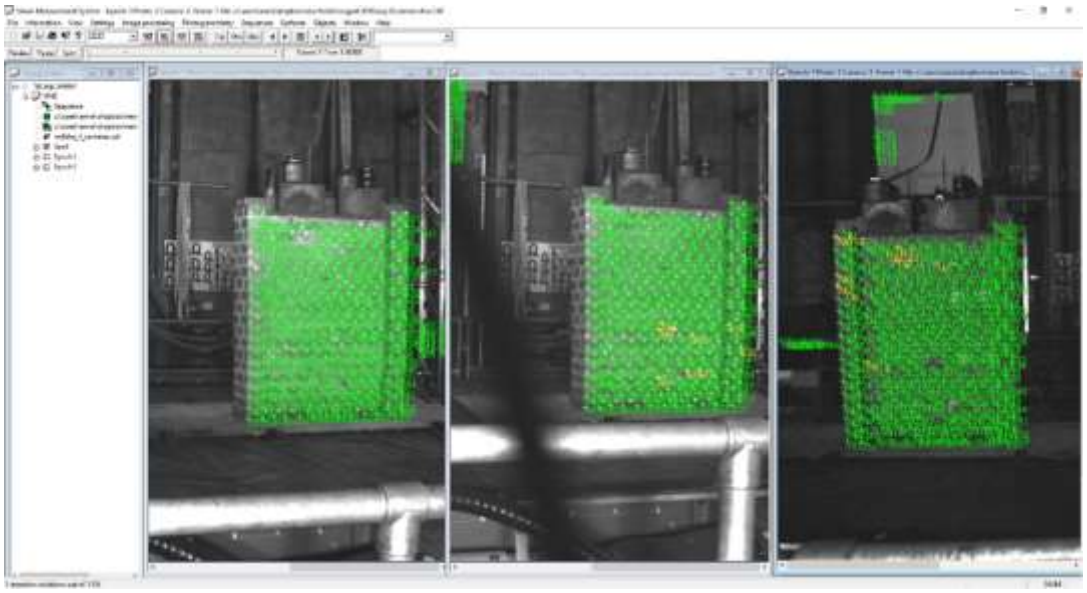

d

VMS analysis photos

Figure 6.1.4: object view of the mini-wall specimen in VMS environment – exp 7

Figure 6.1.5 shows the deformation of all the free reflected targets from epoch 1 to epoch 4. The dots correspond to the monitored reflected targets and figure 6.1.5 verifies figure 6.1.2. Epoch 1 shows the targets on their initial position, epoch 2 presents the same as epoch 1, and epochs 3 and 4 show a minor distortion at the bottom of the wall. The summary of the targets' movement for all the epochs, is also presented in figure 6.1.5, along with the deformation of the tested specimen on the Z axis throughout all the epochs.

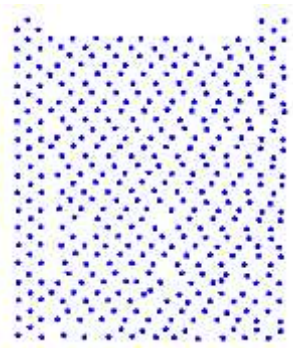

epoch 1

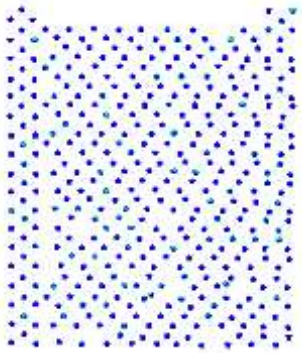

epoch 2

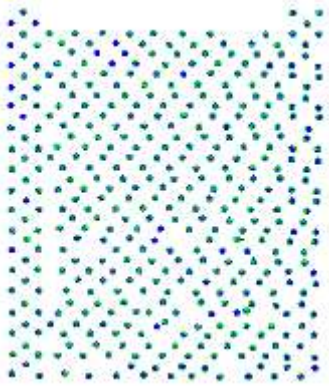

epoch 3

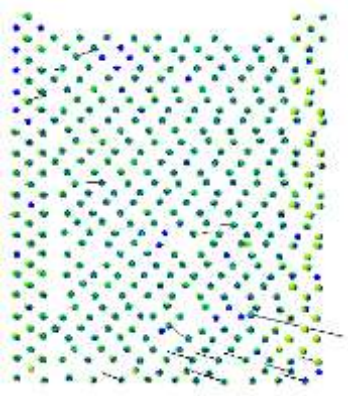

epoch 4

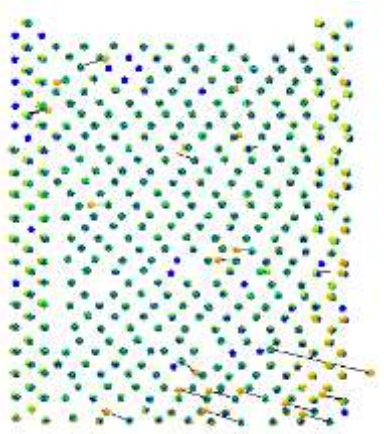

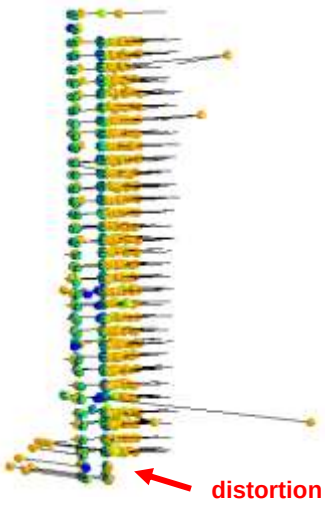

x-y | y-z

epochs 1-4

Figure 6.1.5: Deformation of specimen's triangles – exp 7

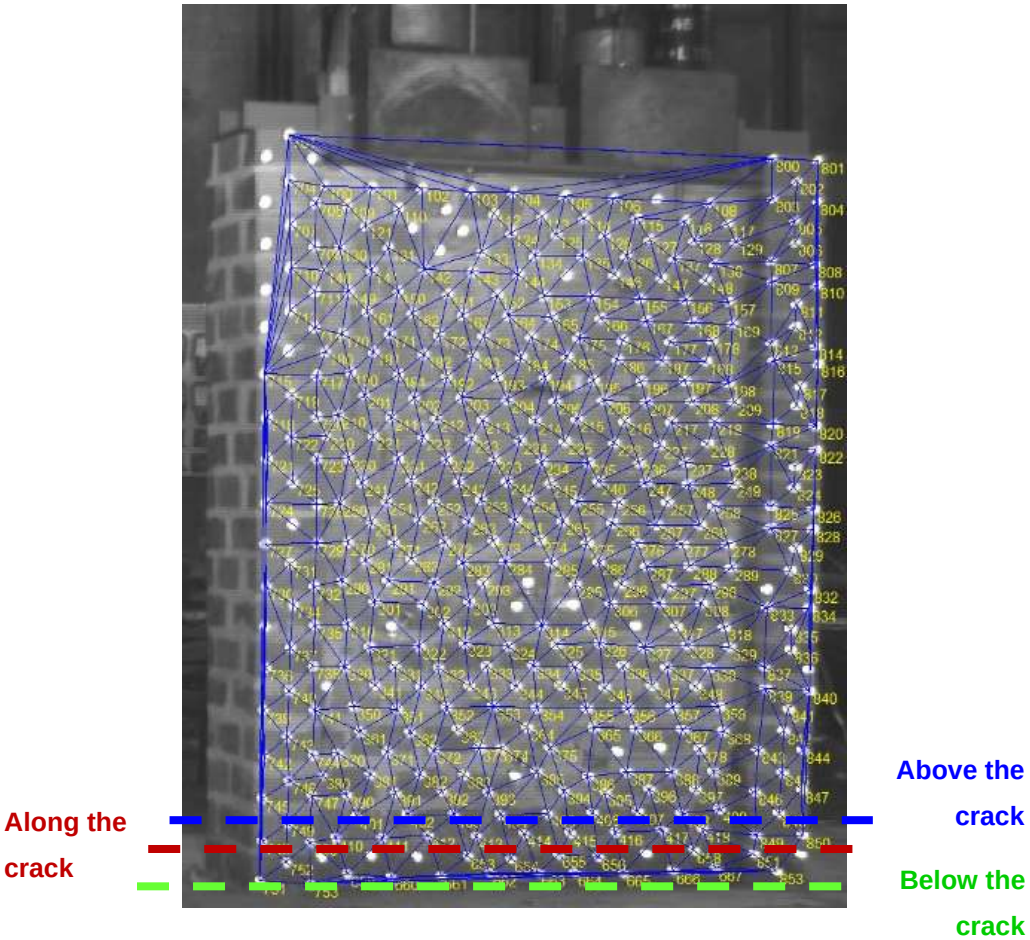

Figure 6.1.6: triangulation computed in EngVis – exp 7

After the completion of the experiment and having observed the crack path (fig. 6.1.3), three groups (fig. 6.1.6) of triangles are decided to be analysed and discussed additionally for their displacement and strain results. These are presented in graphs in relation to the specimen's length. The first group is consisted of fourteen triangles showing the displacement range of the triangles' centroids located below the crack, as it was observed and monitored during the experimental phase. The second group was consisted of twenty-three triangles above the same crack and the third group of thirty-one along the crack.

Figures 6.1.7 – 6.1.9 present the displacement range of the triangles' centroids of these three groups in relation to the specimen's length (x axis) between the four different epochs. Figure 6.1.7 shows the triangles' centroids displacement from epoch 1 to epoch 2 with a range of -0.8 – 0.07mm for the group of triangles above, along and below the crack, providing a figure of the specimen's distortion during the first 48.2 seconds of its monitored motion. Within this timing only seven triangles, four located along the crack and three above the crack which are sited between the 0-40mm along the specimen's x axis show larger peaks, displaced from 0.89mm to 1.5mm. Figure 6.1.8 shows the triangles' centroids displacement from epoch 2 to epoch 3 with a range of -0.3 – 0.6mm providing nine significantly larger peaks than those measured during epochs 1 to 2. These peaks on figure 6.1.8 have been monitored in all the three groups showing a range of 9.8-17.2mm. Figure 6.1.9 shows a small, however significant larger displacement all along the specimen's x axis, with a range of -0.45 – 1.9mm, which proves the damage at the bottom of the specimen. The measurements between epochs 3 to 4 (fig. 6.1.9) also provided six peaks with a range of 3.1-12.5mm. Figures 6.1.10 – 6.1.12 show the triangles' displacement range on the z axis of the specimen's motion, with all the values to be significantly larger to those computed from the x axis. The triangles' displacements on epochs 1 to 2 and 3 to 4, have a mirror form to those computed between epochs 2 to 3. This is observed on the two groups of triangles, above and along the crack. The large displacement values for the group of triangles above and along the specimen between epochs 1 to 2 and 3 to 4, confirms the out of plane failure of the tested wall specimen.

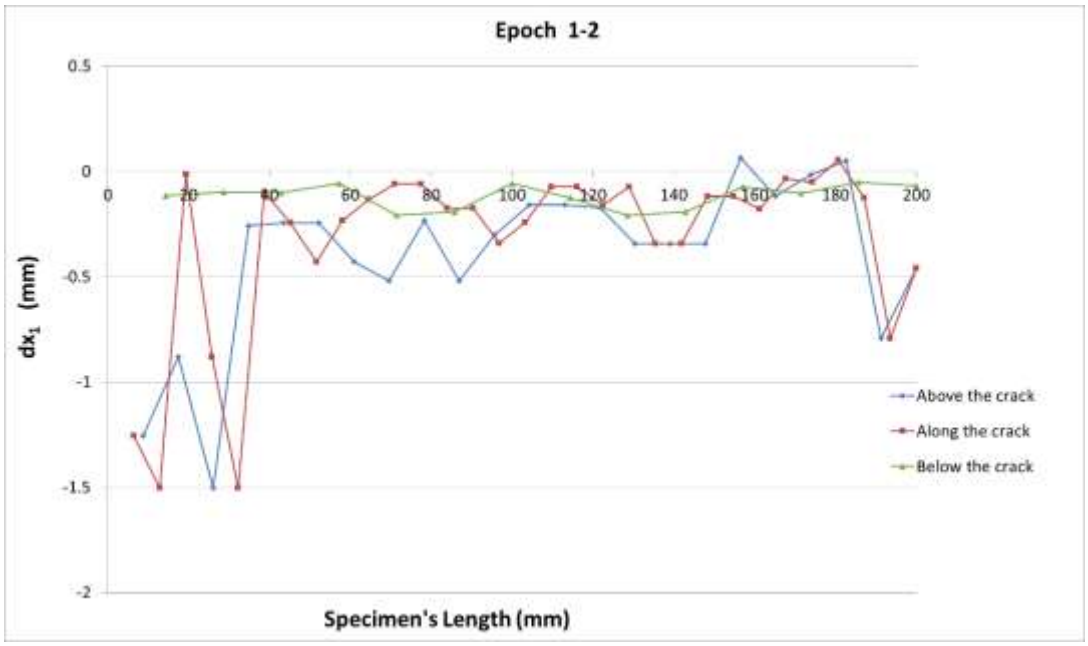

Figure 6.1.7: epoch 1-2 (dx_1 – exp 7)

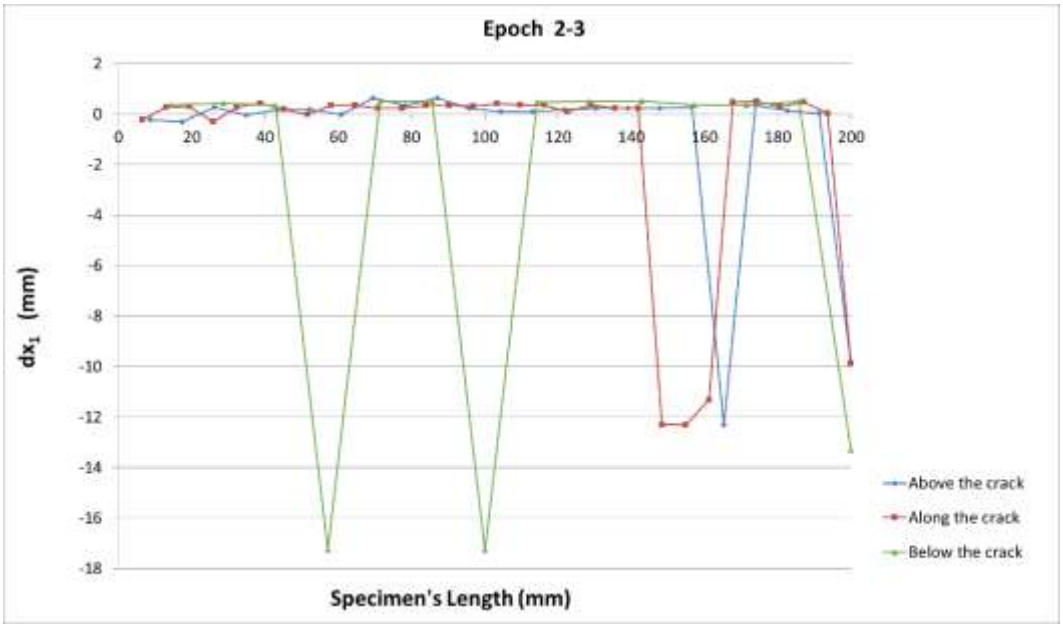

Figure 6.1.8: epoch 2-3 (dx_1 – exp 7)

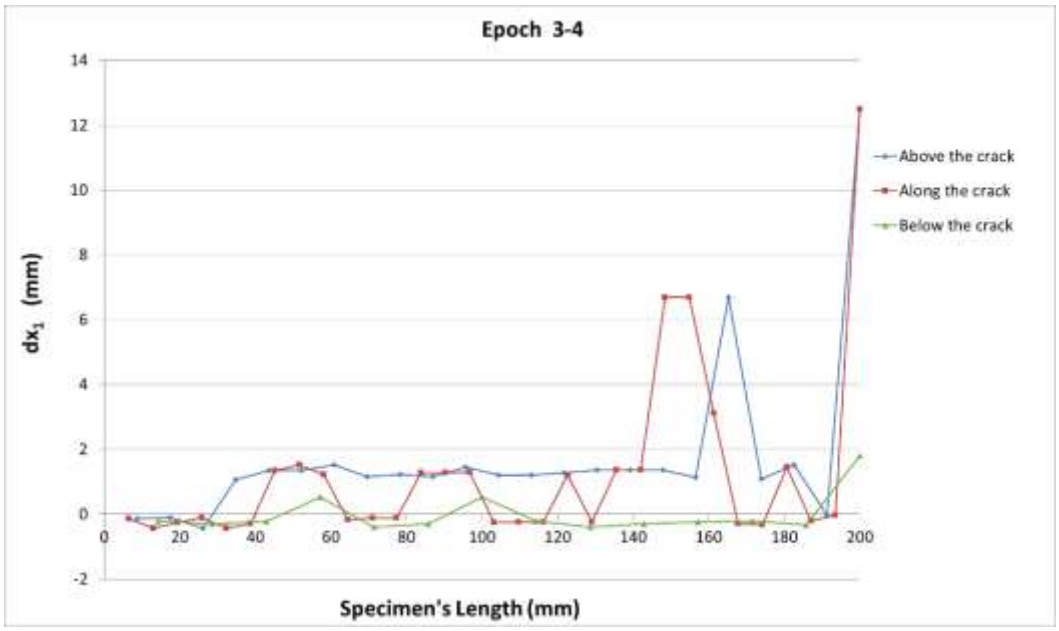

Figure 6.1.9: epoch 3-4 (dx_1 – exp 7)

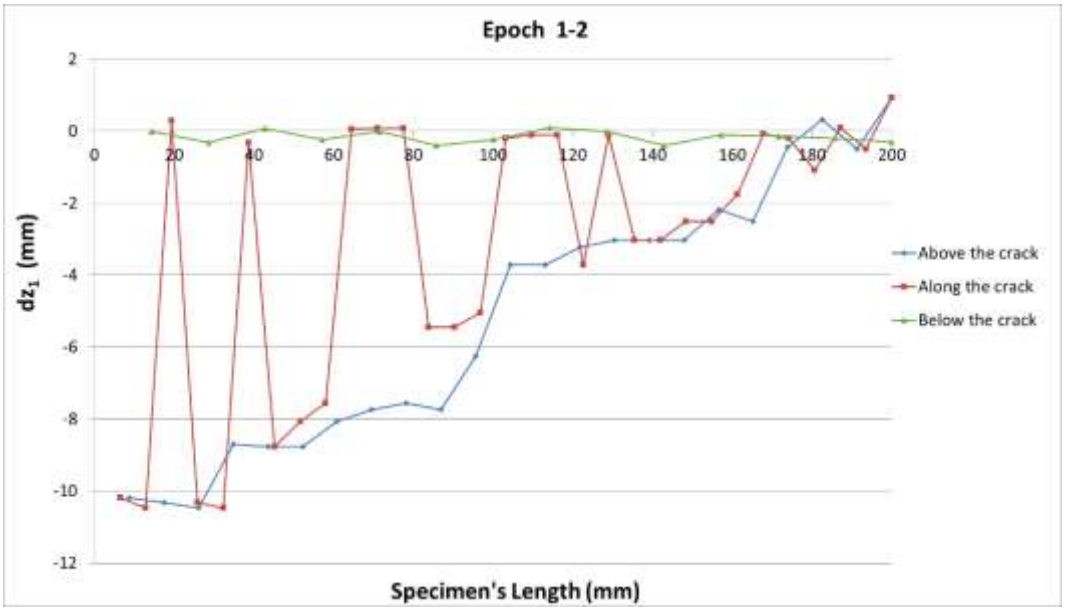

Figure 6.1.10: epoch 1-2 (dz_1 – exp 7)

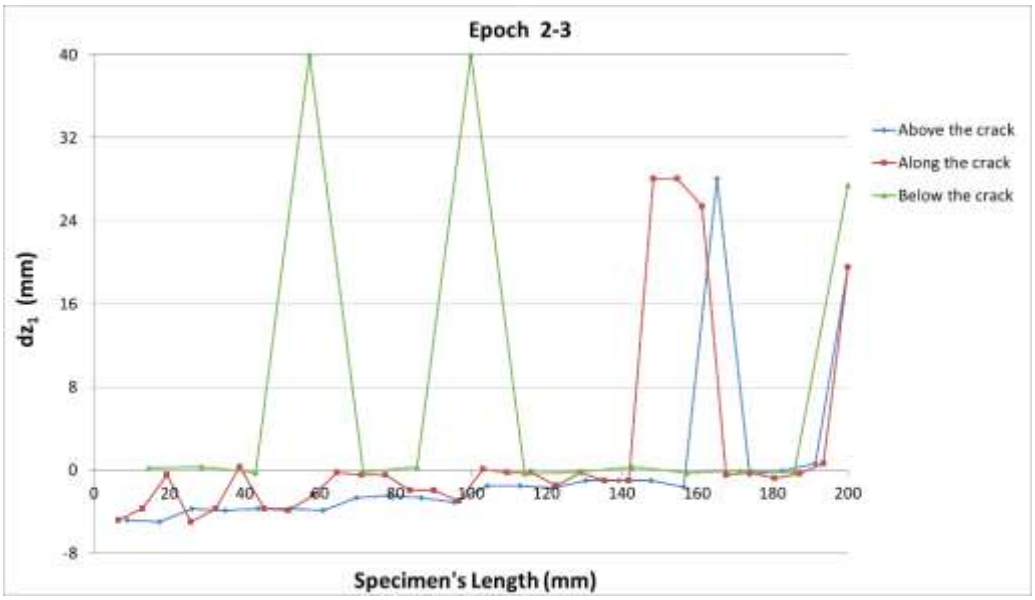

Figure 6.1.11: epoch 2-3 (dz_1 – exp 7)

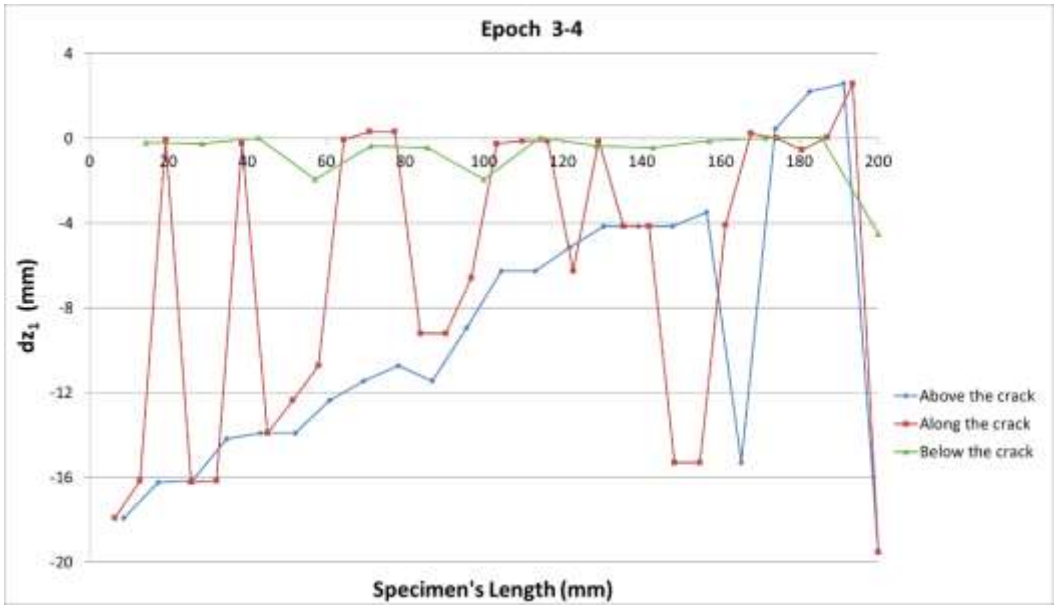

Figure 6.1.12: epoch 3-4 (dz_1 – exp 7)

Figures 6.1.13 – 6.1.15 present the computed shear strain of the measured targets, using the layout of a contour map. These contour maps use for plotting the $x-y-z$ centroid coordinates of each triangle, which is created using the Surfer software. The x-axis represents the length of the tested specimen, the y-axis the height, and the contours the shear strain. Figure 6.1.13 shows shear strain values up to 1 between epochs 1 and 2. Figure 6.1.14 shows the shear strain values up to 1.6, between epochs 2 and 3 and figure 6.1.15 shows the shear strain values up to 2.8, between epochs 3 and 4, where the distortion's presentation is shown at the bottom of the specimen.

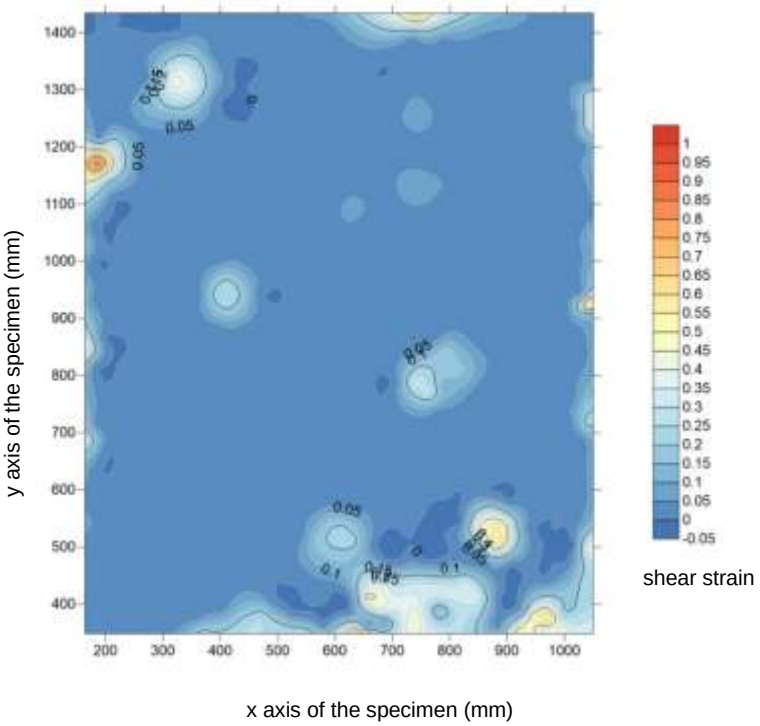

Figures 6.1.13: epoch 1-2 (shear ε – exp 7)

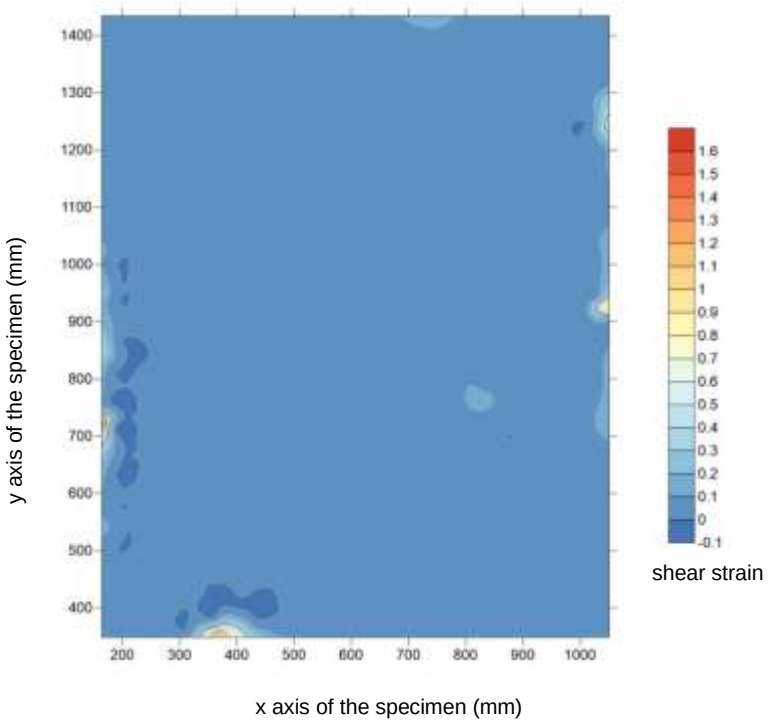

Figure 6.1.14: epoch 2-3 (shear ε – exp 7)

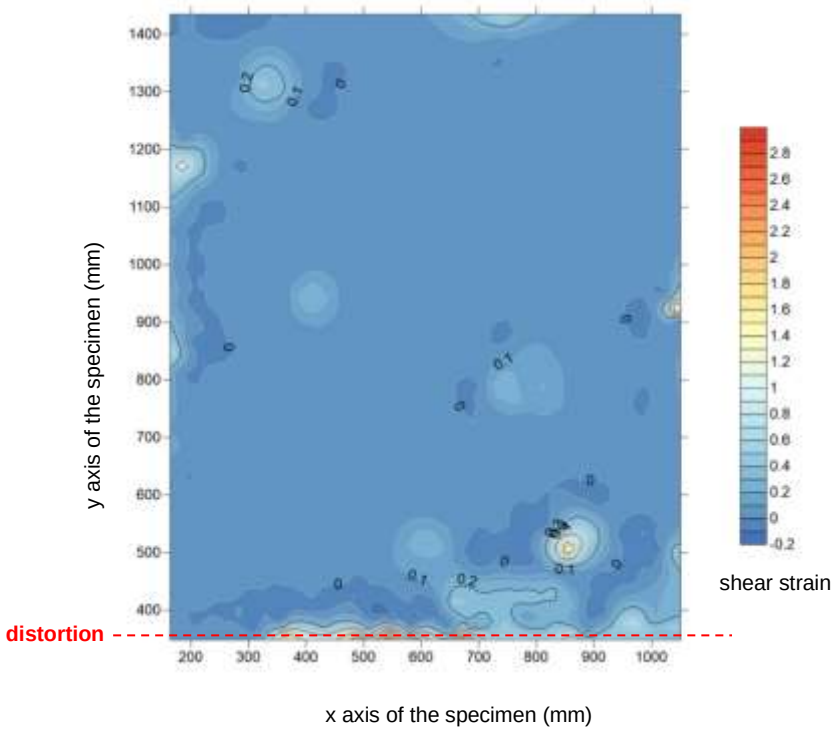

Figure 6.1.15: epoch 3-4 (shear ε – exp 7)

6.2.2 Strain Gauge

Three strain gauges were installed on the front face of the tested wall, all horizontally along the specimen's height. The first one on the mortar area between the third and fourth brick layers, the second one similarly on the mortar area between the seventh and the eighth brick layer and lastly the third strain gauge similarly was installed on the mortar area between the twelfth and thirteenth. All the strain gauges were glued directly on the mortar. Figure 6.1.16 shows the SGs' (top, middle and bottom) results as recorded during the specimen's test. The maximum strain recorded by the top strain gauge is 0.01 and by the middle and the bottom strain gauges is 0.03. As shown in figure 6.1.2, the crack started occurring at 13:00:51.660, which is the timing when most of the peaks appear in figure 6.1.16.

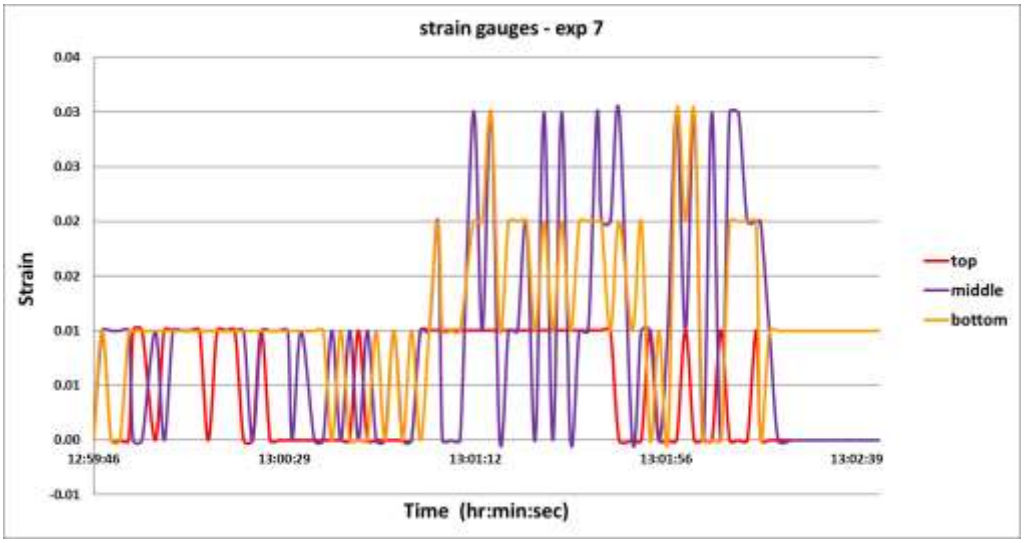

Figure 6.1.16: SG's results – strain over time (hour:minute:second) – exp 7

6.2.3 Comparisons

Figure 6.1.17 presents the triangulation picture from the experimental analysis, showing the installed strain gauges with the view to select the corresponding triangles for the purposes of the strain computation using the CRDP method. Each triangle computed one strain value using the CRDP method. The black horizontal lines correspond to the horizontal installed strain gauges, bottom, middle and top ones. The picture also shows the damage localisation as the crack has propagated at the bottom of the specimen.

Therefore, four triangles have been selected along the top horizontal strain gauge, three along the middle one and ten along the top one (table 6.2). All the negative strain data, computed based on the CRDP method, converted to absolute values, they summed up and divided by the number of triangles. Hence, the four epochs produced three plane strain values for each triangle using the CRDP method (table 6.2). They are also plotted against time as presented in figure 6.1.18. The strain, computed using the CRDP method for the triangles along the bottom strain gauge, is 0.068 at 13:02:44.211 (epochs 3-4). The maximum strain value recorded by the bottom strain gauge, which is close to the formed crack, is 0.03 at 13:02:02. Diagram 6.2 shows that the peaks of the recorded strains show 42.211 seconds time difference between the strain gauge and the CRDP readings along the SG.

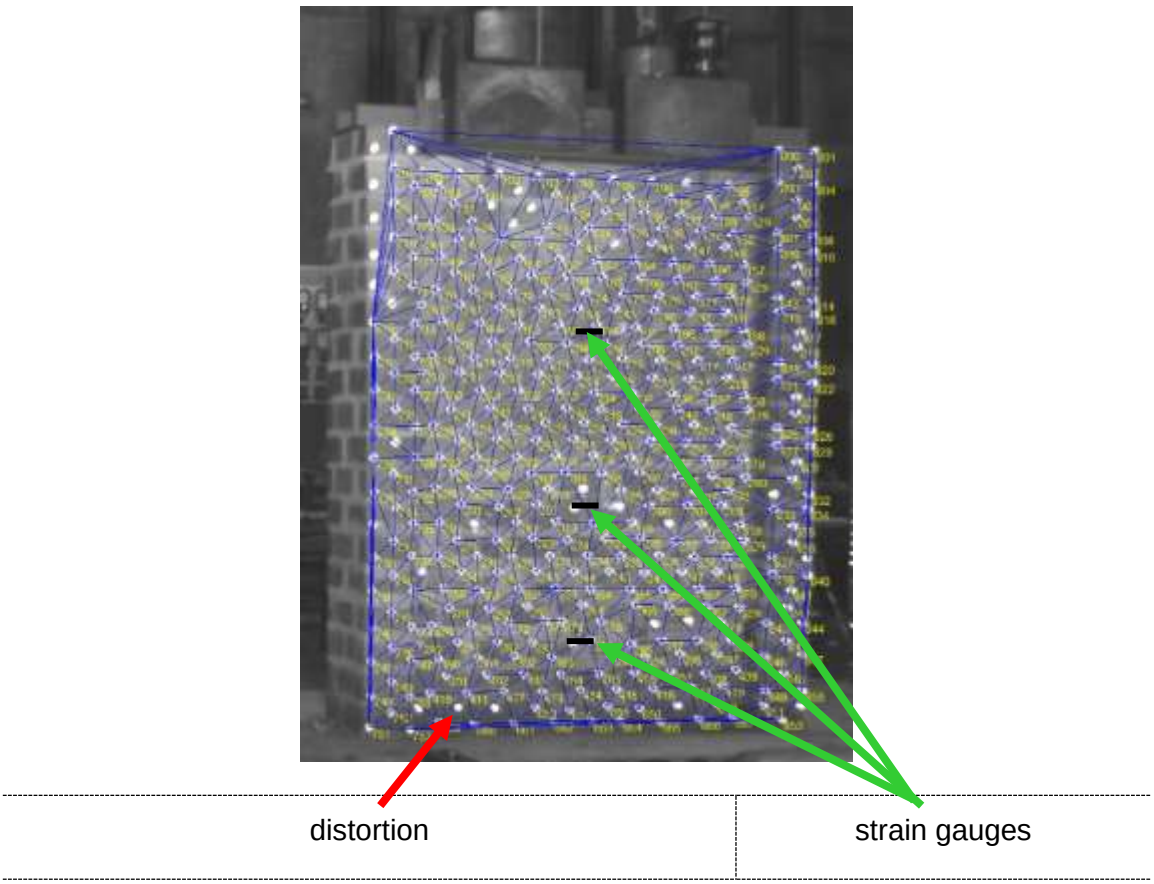

Figure 6.1.17: triangulation picture showing the strain gauges & the damage – exp 7

					Strain - CRDP		
					Strain (1-2)	Strain (2-3)	Strain (3-4)
	triangles along bottom SG						
1	385	374	393		-0.004	0.134	-0.077
2	374	385	364		-0.004	0.091	-0.058
3	375	364	385		0.006	-0.091	0.067
4	375	385	394		-0.001	0.076	-0.069
					0.004	0.098	0.068
	triangles along middle SG						
5	303	313	293		0.003	0.004	-0.005
6	315	295	314		-0.004	0.003	-0.004
7	295	315	306		0.000	0.006	-0.009
					0.002	0.004	0.006
	triangles along top SG						
8	203	204	193		-0.002	0.003	0.001
9	214	194	204		0.005	0.025	0.032
10	205	194	214		0.015	0.031	-0.350
11	185	194	205		-0.010	-0.025	0.323
12	195	185	205		-0.003	0.007	0.090
13	215	195	205		0.002	-0.008	-0.093
14	215	206	195		0.000	0.010	0.000
15	185	195	175		-0.006	0.010	-0.005
16	175	195	186		0.001	-0.018	0.019
17	195	206	186		0.001	0.039	-0.041
					0.005	0.017	0.095

time (hr:min:sec:millisec) – epochs	13:00:51.660	13:01:28.945	13:02:44.211

Table 6.2: strains using CRDP method along SGs – exp 7

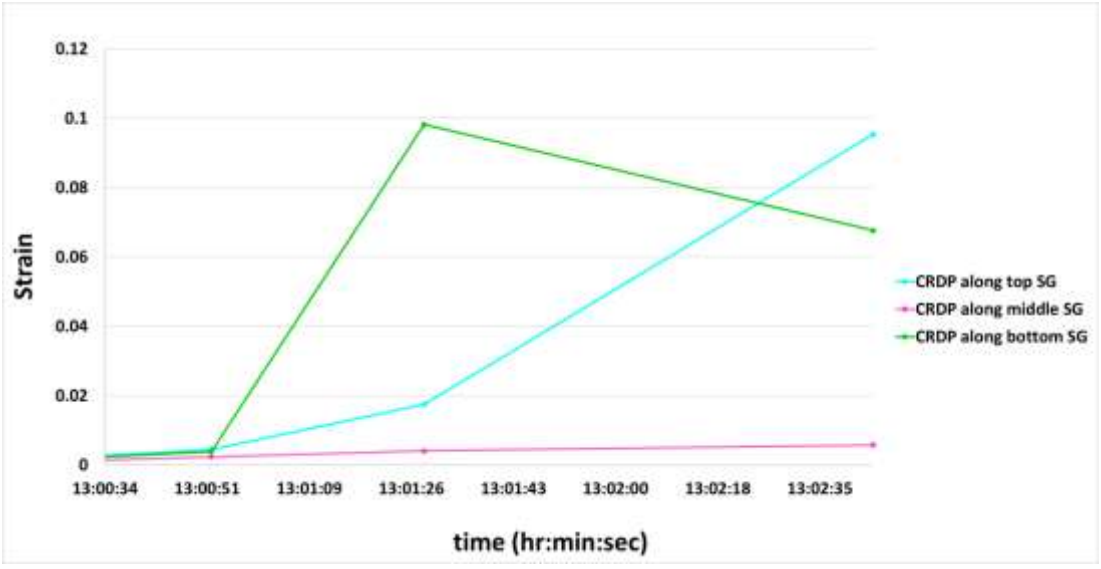

Figure 6.1.18: CRDP's strain readings along SG sensors – exp 7

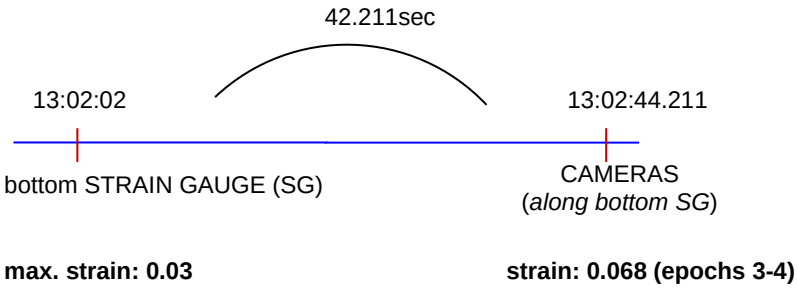

Diagram 6.2: monitoring methods recording sequence for experiment 7 along with their strains

6.3 Experiment 8

Experiment 8 is a replica of experiment 7 with the only difference being the applied excitation. The test ran for 179 seconds, with an input excitation value to the shaking table of 36.625Hz in frequency. The purpose of creating the same sample was to have a backup, in case the first one was damaged. The purpose of re-running the same experiment was to check if there would be any difference in the formed damage.

6.3.1 Close Range Digital Photogrammetry

Similarly, for the purposes of the second large scale experiment three redlake cameras were used, which each of them collected three hundred images. The analysis of the photogrammetric results is comprised of twelve images, one from each camera, which is classified into different sets of photographs called epochs. Therefore, the four stages of the experiment (fig. 6.2.1) is comprised of four epochs (diagram 6.3). Epoch 2 (fig. 6.2.1b) was the first epoch capturing the crack's initiation and epoch 1 (fig. 6.2.1a) was chosen to show the specimen prior to the damage. Epochs 3 and 4 (fig. 6.2.1c & d) were chosen to show the crack at the bottom of the specimen. Figure 6.2.2 shows the tested specimen after its distortion. The cameras' monitoring period successfully captured the initiation of the crack and the specimen's distortion.

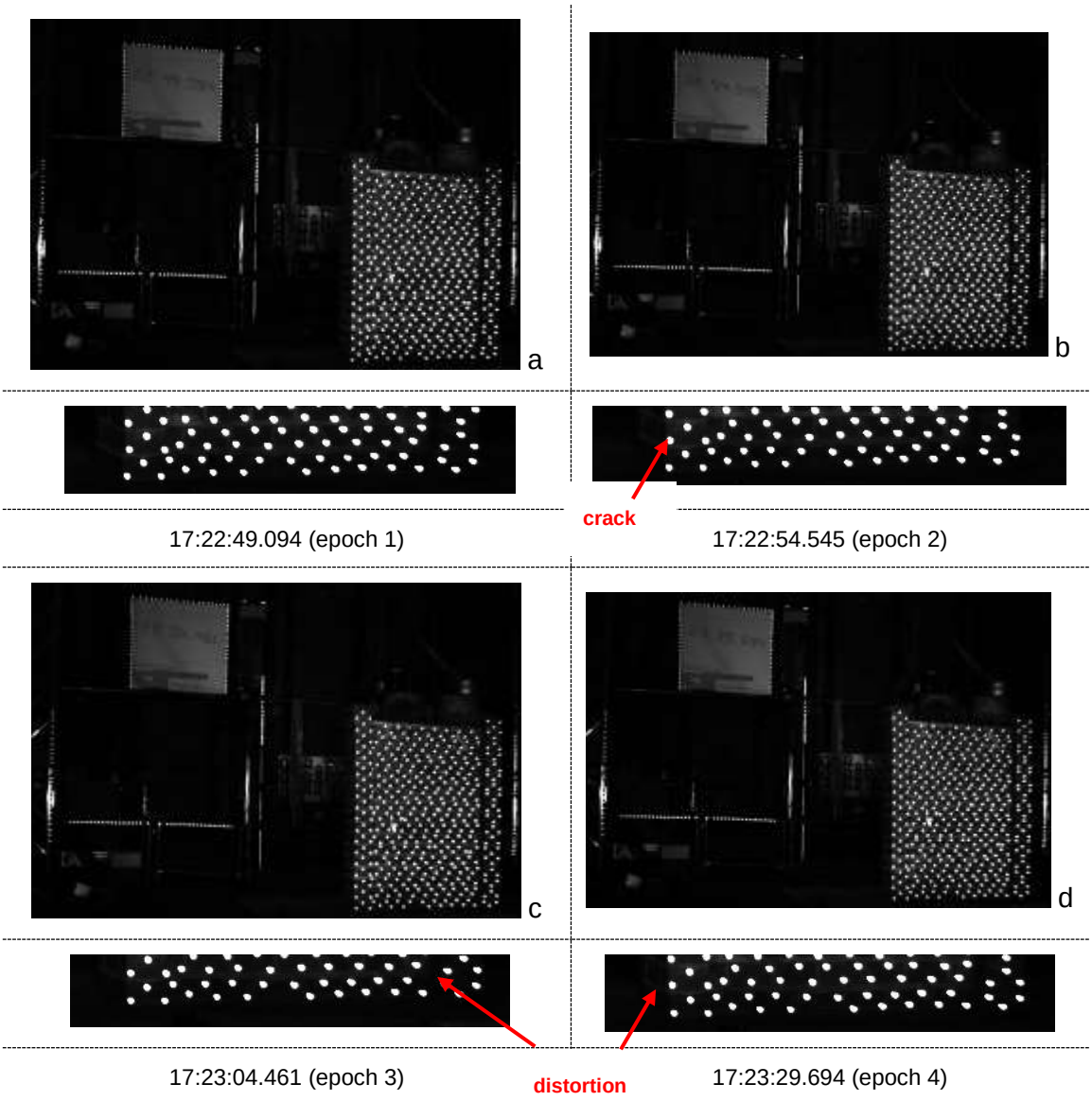

Figure 6.2.1: Images' sequences capturing the actuated tested wall – exp 8

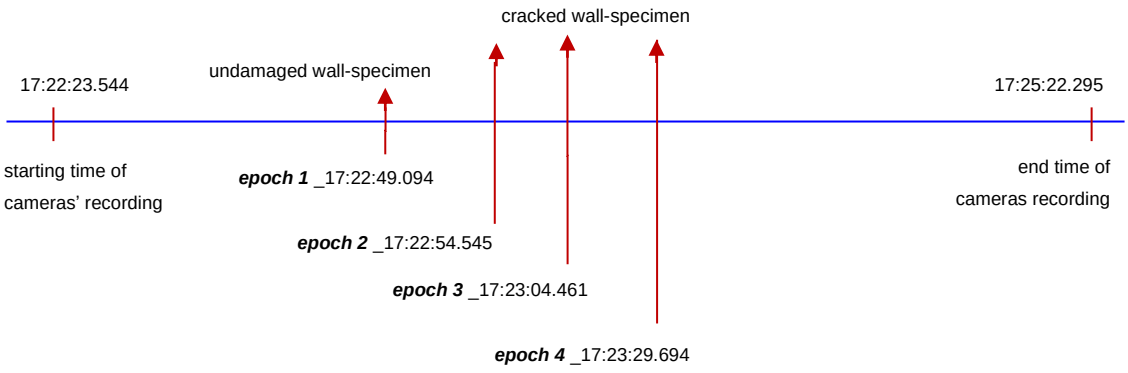

Diagram 6.3: cameras' recording timings for experiment 8

Figure 6.2.2: specimen's distortion – exp 8

Figure 6.2.3 shows the deformation of all the free reflected targets from epoch 1 to epoch 4. The dots correspond to the monitored reflected targets and figure 6.2.3 verifies figure 6.2.1. Epoch 1 shows the targets on their initial position, epoch 2 presents the same as epoch 1, and epochs 3 and 4 show a minor crack initiation at the bottom of the wall. The summary of the targets' movement for all the epochs, is also presented in figure 6.2.3, along with the deformation of the tested specimen on the Z axis throughout all the epochs.

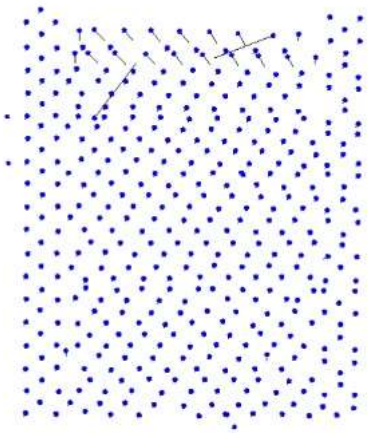

epoch 1

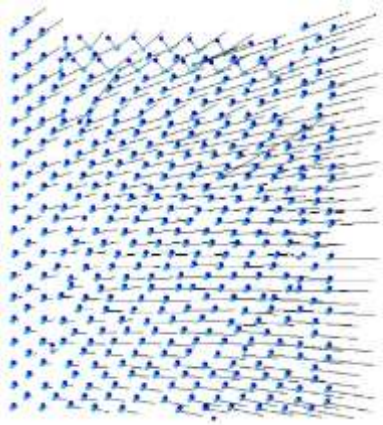

epoch 2

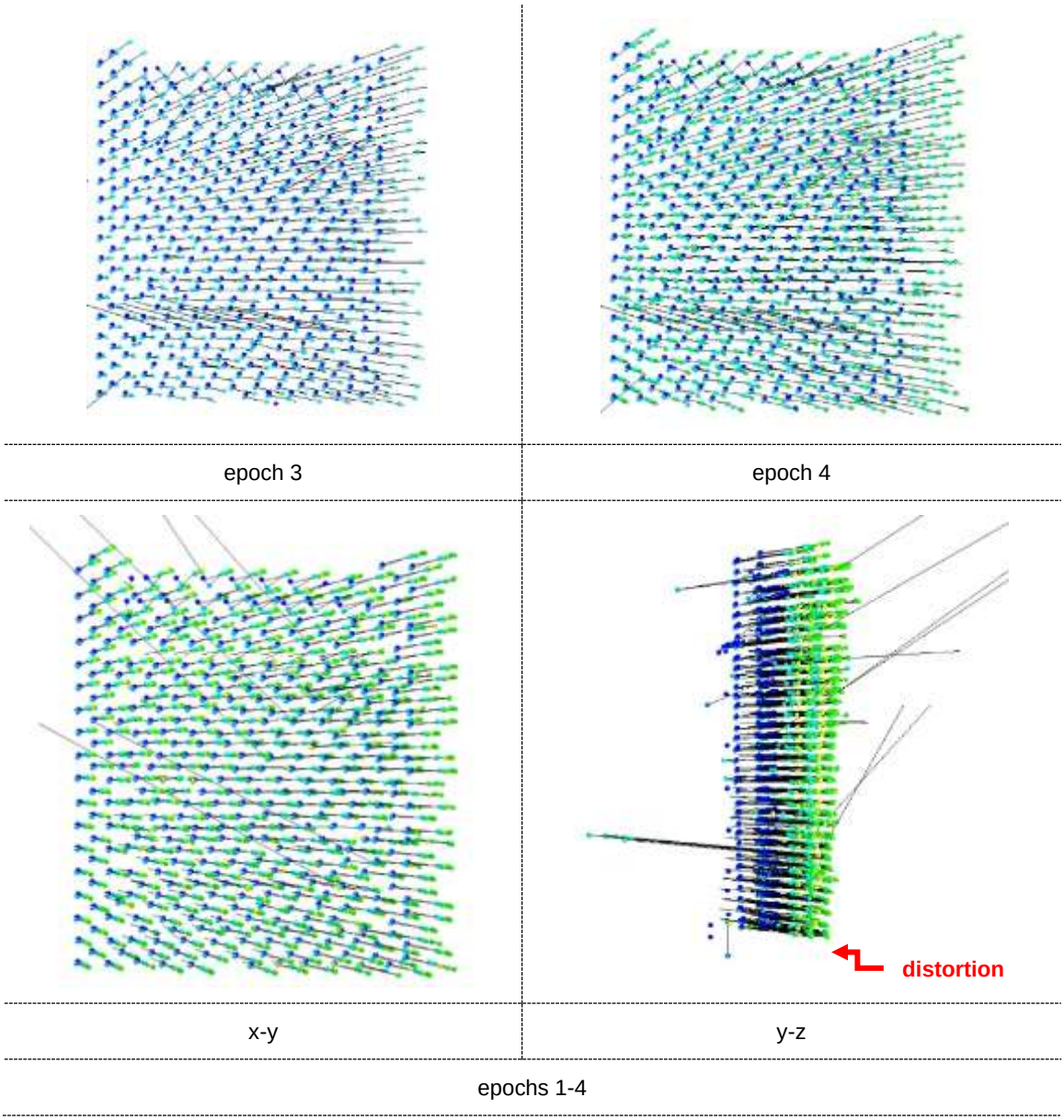

Figure 6.2.3: Deformation of specimen's triangles – exp 8

After the completion of the experiment and having observed the failure (fig. 6.2.2), similar with experiment 7, three groups of triangles are decided to be analysed and discussed additionally for their displacement and strain results. These are presented in graphs in relation to the specimen's length. The first group is consisted of sixteen triangles showing the displacement range of the triangles' centroids located below the crack, as it was observed and monitored during the experimental phase. The second group was consisted of twenty-three triangles above the same crack and the third group of twenty-six along the crack.

Figures 6.2.4 – 6.2.6 present the displacement range of the triangles' centroids of these three groups in relation to the specimen's length (x axis) between the four

different epochs. Figure 6.2.4 shows the triangles' centroids displacement from epoch 1 to epoch 2 with a range of -2.4 – 3.9mm for the group of triangles above, along and below the crack, providing a figure of the specimen's distortion during the first 5.5 seconds of its monitored motion. Within this timing the propagation of the crack shows an ascending form from the left edge of the specimen to the right. Figure 6.2.5 shows the triangles' centroids displacement from epoch 2 to epoch 3 with a range of 6.9 – 14mm and a similar ascending format to figure 6.2.4 with significant larger displacements. Figure 6.2.6 shows the triangles' centroids displacement from epoch 3 to epoch 4 with a mirror format to figure 6.2.4 and a displacement range of -3.5 – 4.6mm. Figures 6.2.7 – 6.2.9 show the triangles' displacement range on the z axis of the specimen's motion, with all the values to be significantly larger to those computed from the x axis. The triangles' displacements on epochs 1 to 2 and 2 to 3, have a mirror form to those computed between epochs 3 to 4. This is observed on all the two groups of triangles, above and along the crack. The large displacement values for the group of triangles above and along the specimen between epochs 1 to 2, confirms the out of plane motion of the tested wall specimen.

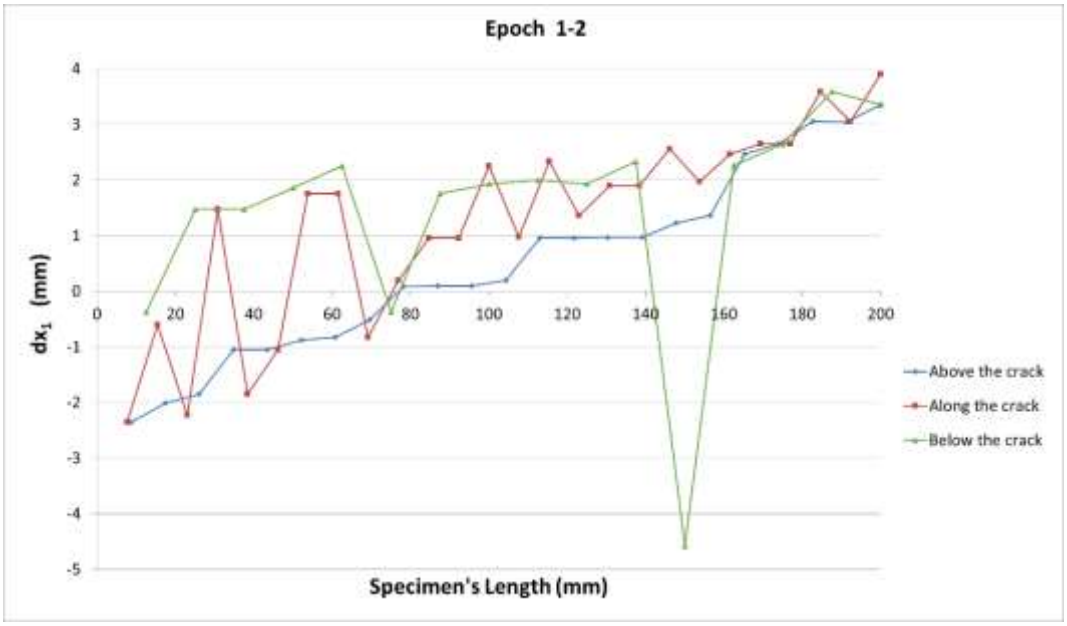

Figure 6.2.4: epoch 1-2 (dx_1 – exp 8)

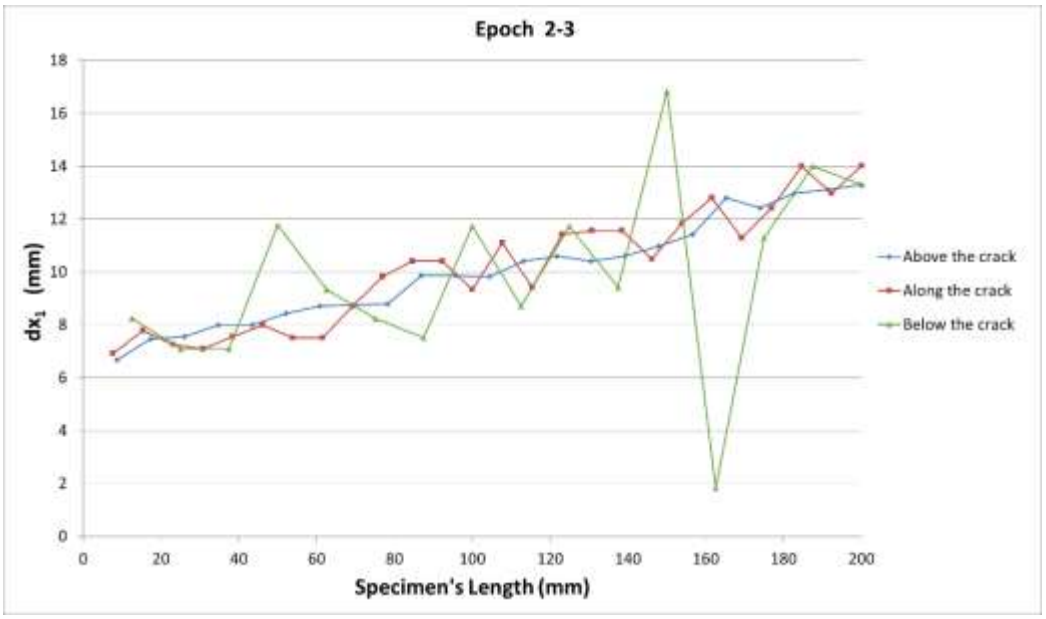

Figure 6.2.5: epoch 2-3 (dx_1 – exp 8)

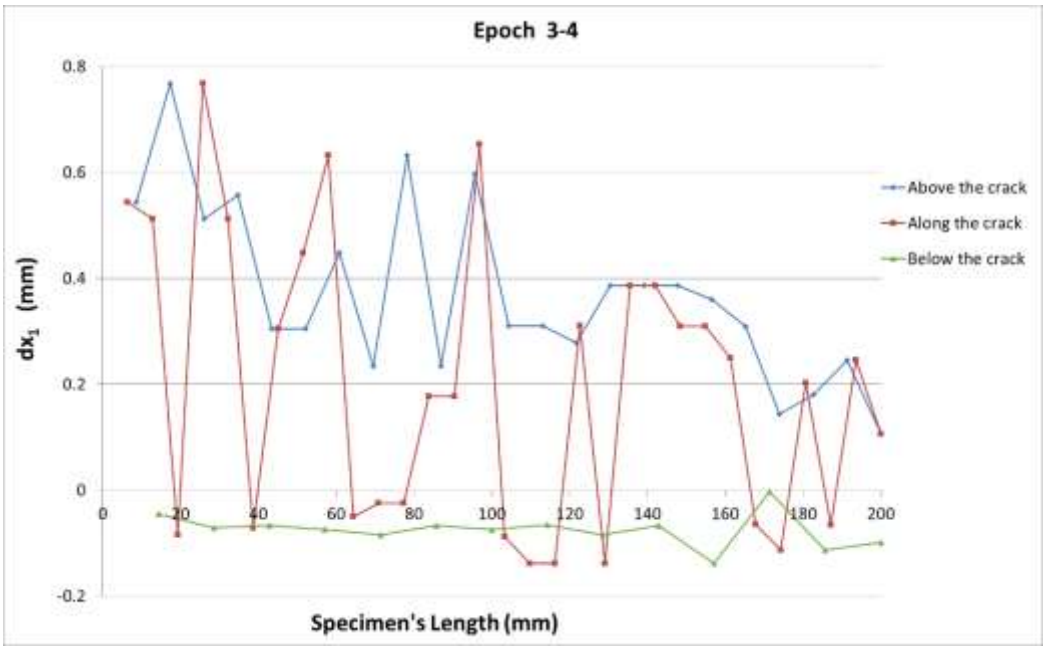

Figure 6.2.6: epoch 3-4 (dx_1 – exp 8)

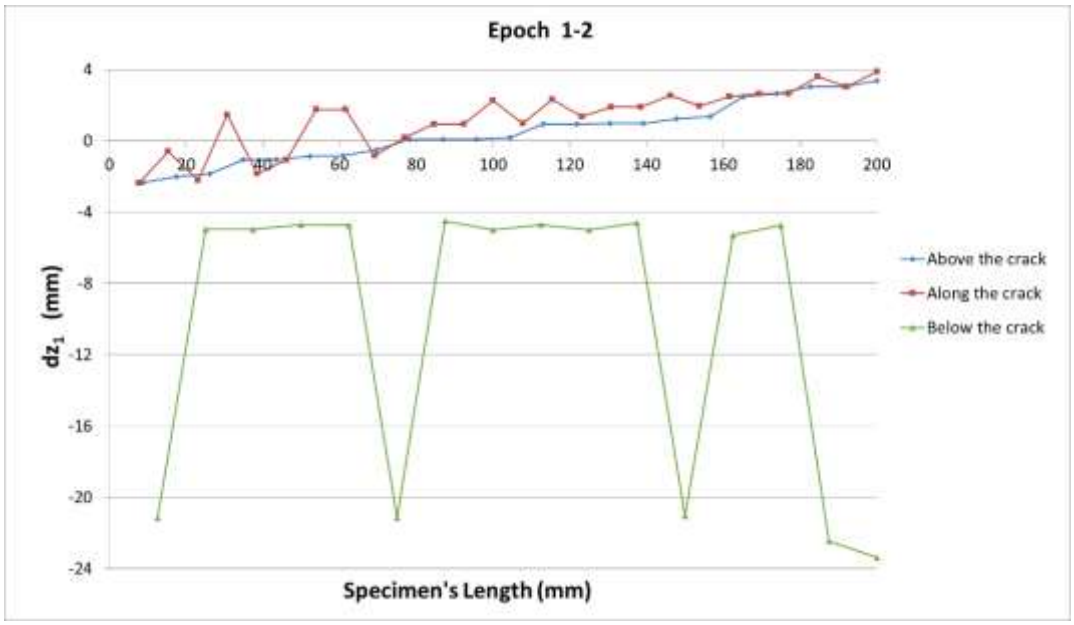

Figure 6.2.7: epoch 1-2 (dz_1 – exp 8)

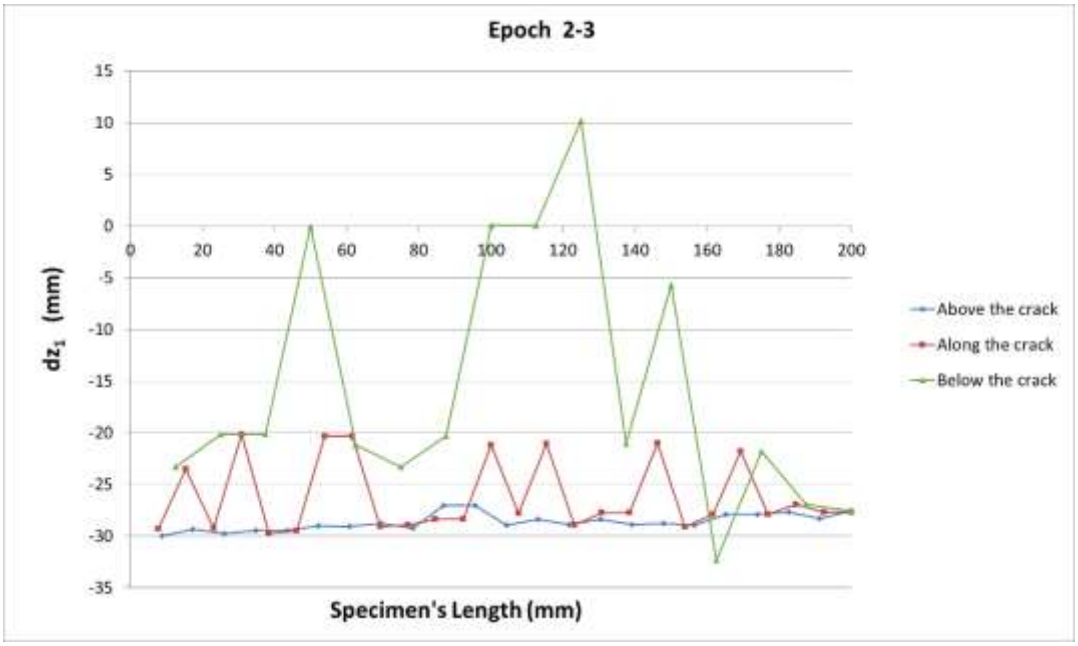

Figure 6.2.8: epoch 2-3 (dz_1 – exp 8)

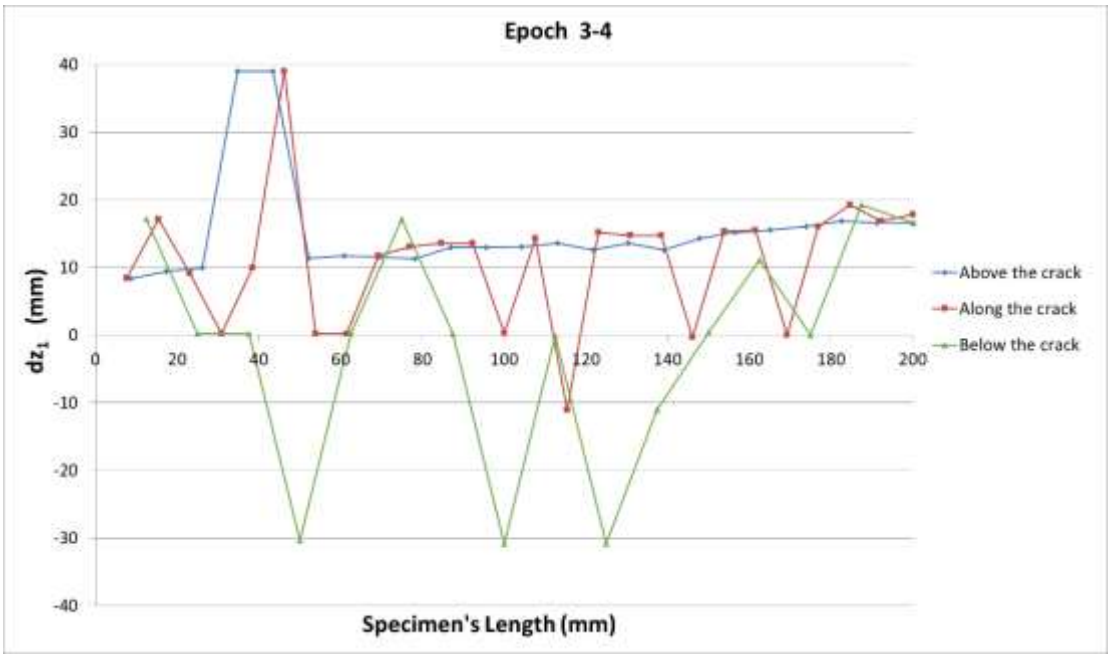

Figure 6.2.9: epoch 3-4 (dz_1 – exp 8)

Figures 6.2.10 – 6.2.12 present the computed shear strain of the measured targets, using the layout of a contour map. These contour maps use for plotting the $x-y-z$ centroid coordinates of each triangle, which is created using the Surfer software. The x-axis represents the length of the tested specimen, the y-axis the height, and the contours the shear strain. Figure 6.2.10 shows shear strain values up to 1 between epochs 1 and 2. Figure 6.2.11 shows the shear strain values up to 1.5, between epochs 2 and 3 and figure 6.2.12 shows the shear strain values up to 2.8, between epochs 3 and 4, where the distortion's presentation is shown at the bottom of the specimen.

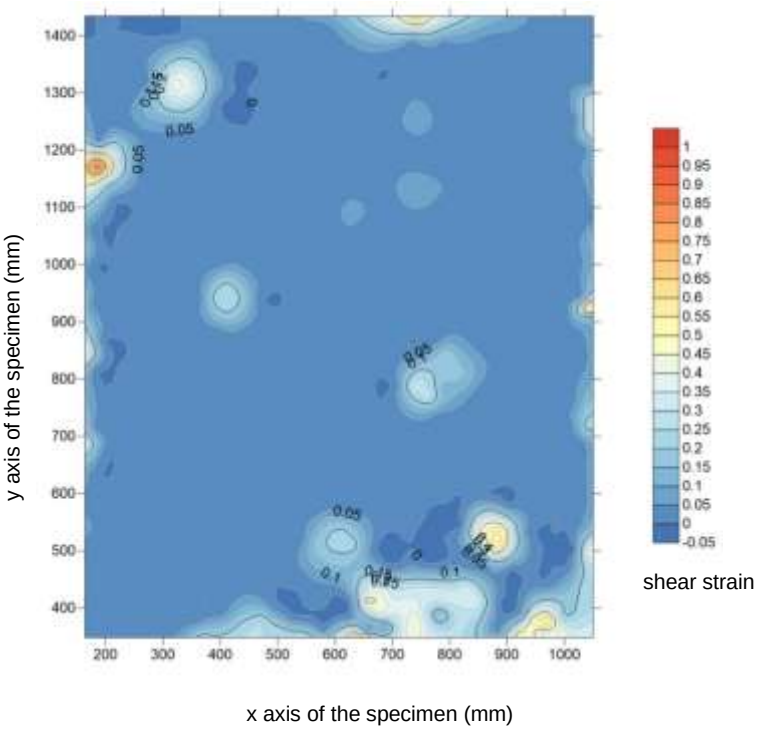

Figures 6.2.10: epoch 1-2 (shear ε – exp 7)

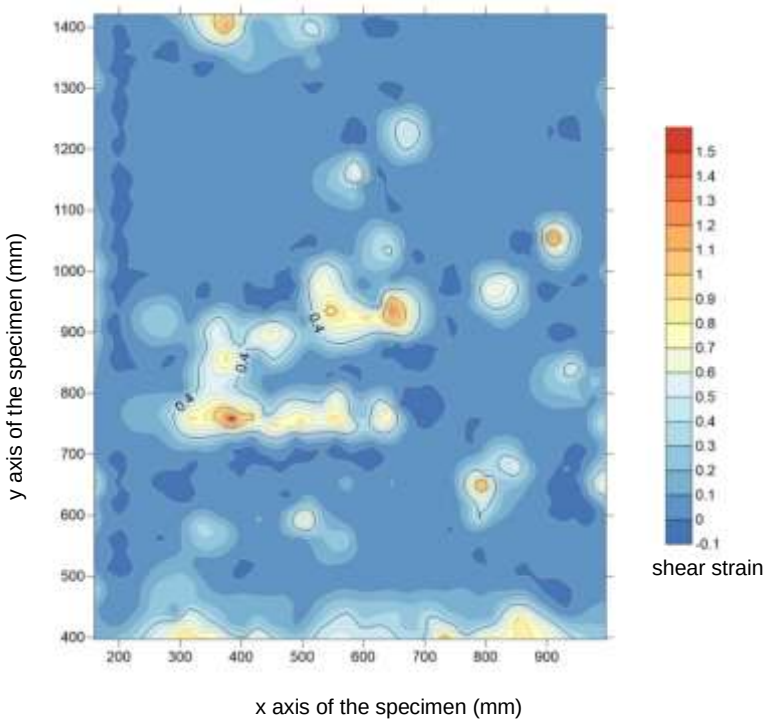

Figure 6.2.11: epoch 2-3 (shear ε – exp 7)

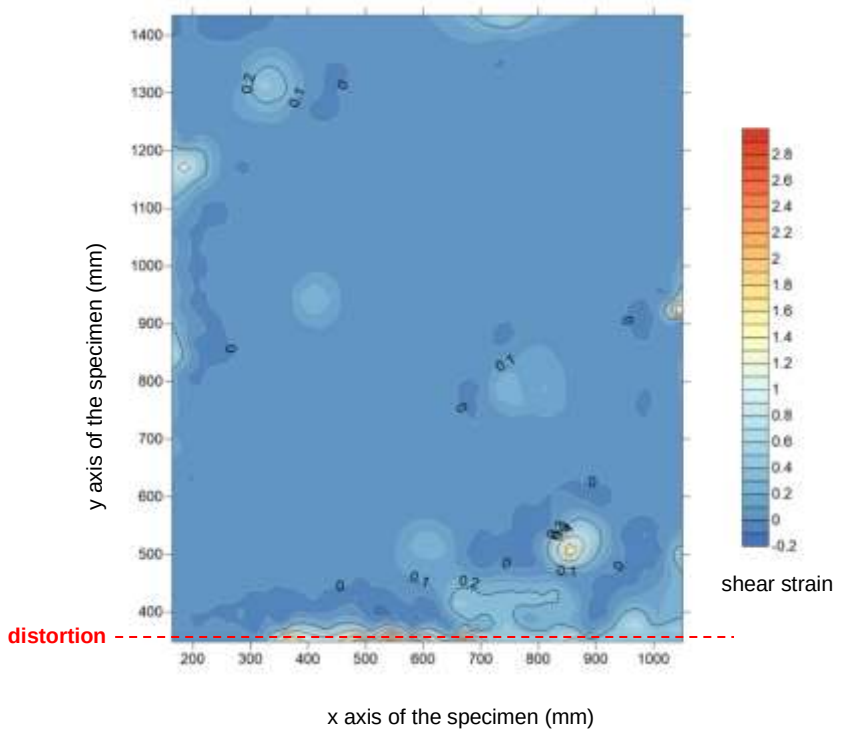

Figure 6.2.12: epoch 3-4 (shear ε – exp 7)

6.3.2 Strain Gauge

Three strain gauges were installed on the front face of the tested wall, all horizontally along the specimen's height. The first one on the mortar area between the fourth and the fifth brick layers, the second one similarly on the mortar area between the ninth and the tenth brick layer and lastly and similarly the third strain gauge was installed on the mortar area between the thirteenth and fourteenth. All the strain gauges were glued directly on the mortar. Figure 6.2.13 shows the SGs' (top, middle and bottom) results as recorded during the specimen's test. The maximum strain recorded by the top strain gauge is 0.03 and by the middle and the bottom strain gauges is 0.02. As shown on figure 6.2.1, the crack started occurring around 17:23:29.694, which is the timing when most of the peaks appear on figure 6.2.13.

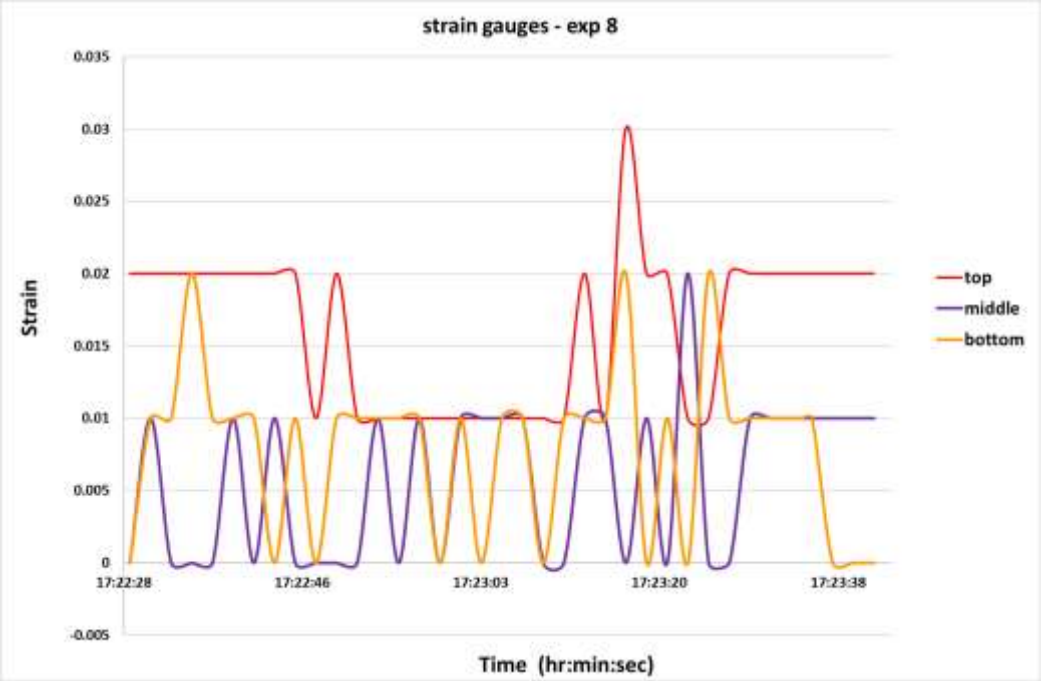

Figure 6.2.13: SG's results – strain over time (hour:minute:second) – exp 8

6.3.3 Comparisons

Figure 6.2.14 presents the triangulation picture from the experimental analysis, showing the installed strain gauges with the view to select the corresponding triangles for the purposes of the strain computation using the CRDP method. Each triangle computed one strain value using the CRDP method. The black horizontal lines correspond to the horizontal installed strain, bottom, middle and top ones. The picture also shows the damage localisation as the distortion has occured at the bottom of the specimen.

Therefore, four triangles have been selected along the bottom horizontal strain gauge, eight along the middle one and eight along the top one (table 6.3). All the negative strain data, computed based on the CRDP method, converted to absolute values, they summed up and divided by the number of triangles. Hence, the four epochs produced three plane strain values for each triangle using the CRDP method (table 6.3). They are also plotted against time as presented in Figure 6.2.15. The strain computed using the CRDP method for the triangles along the bottom strain gauges is 0.043 at 17:23:29.694 (epoch 3-4). The maximum strain value recorded by the bottom strain gauge, which is close to the specimen's distortion, is 0.02 at 17:23:17. Diagram 6.4 shows that the peaks of the recorded strains show 12.694 seconds time difference between the strain gauge and the CRDP readings along the SG.

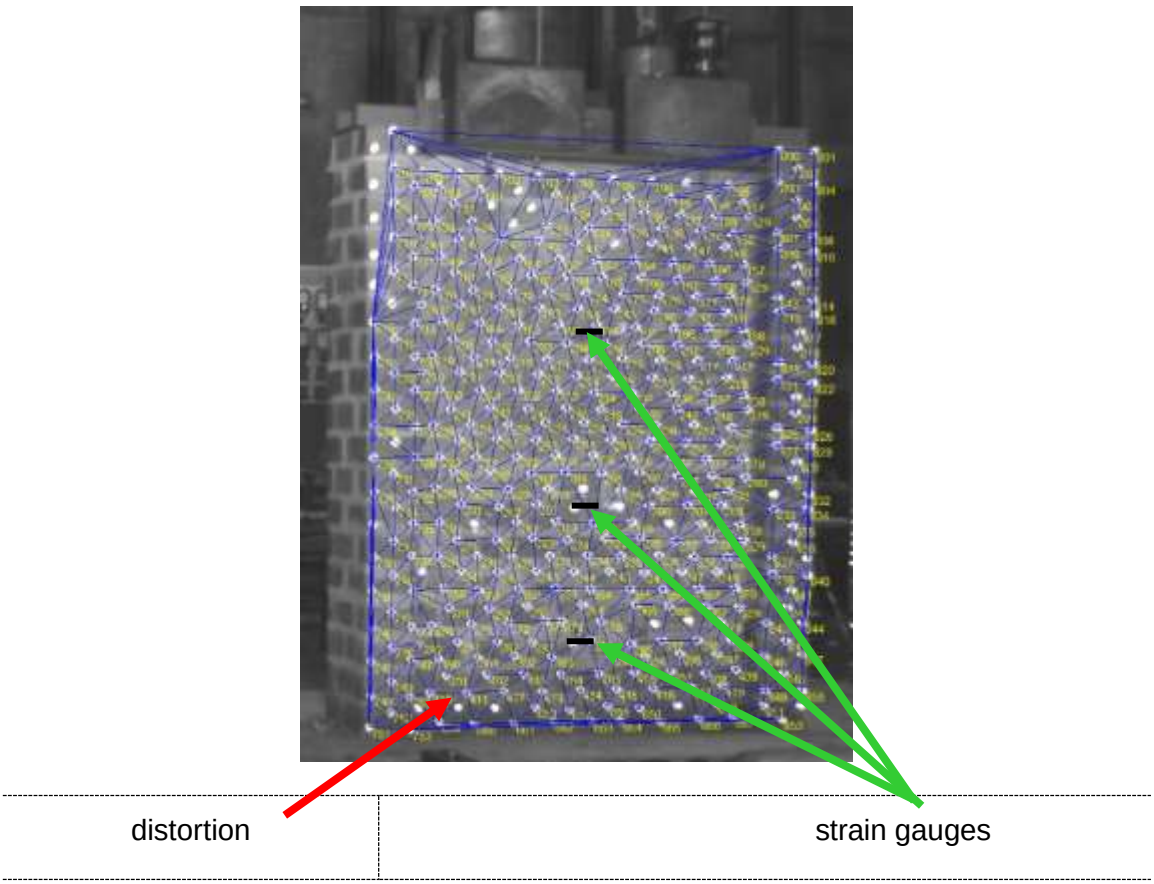

Figure 6.2.14: triangulation picture showing the strain gauges & the damage – exp 8

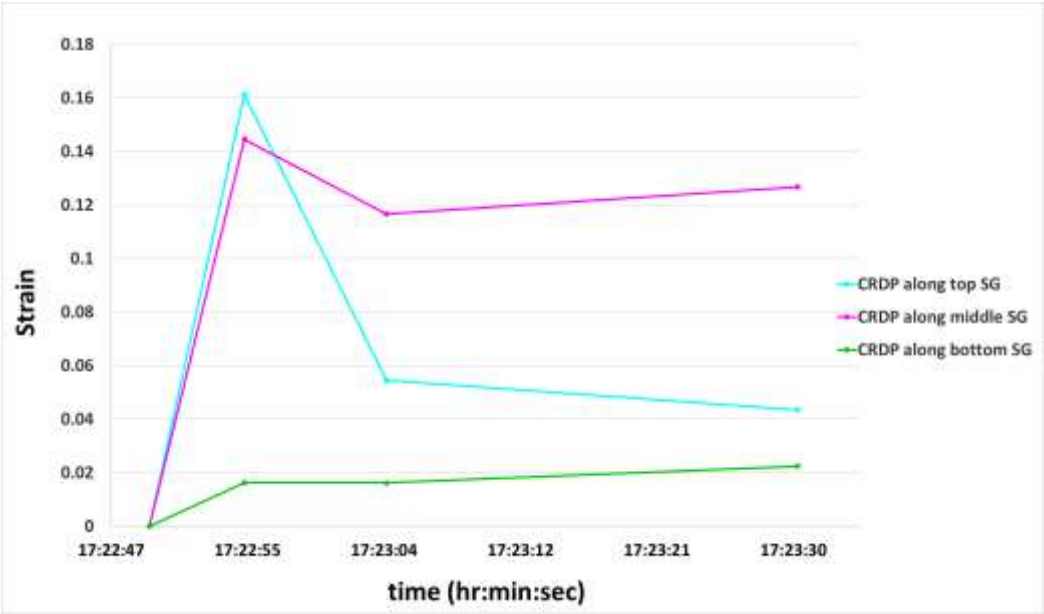

Figure 6.2.15: CRDP's strain readings along SG sensors – exp 8

					Strain - CRDP		
					Strain (1-2)	Strain (2-3)	Strain (3-4)
	triangles along top SG						
1	364	354	374		0.005	0.010	-0.004
2	354	364	345		-0.067	0.077	0.060
3	364	355	345		0.002	-0.002	0.000
4	355	364	365		-0.008	-0.008	0.004
5	335	345	355		-0.002	-0.010	0.010
6	335	355	346		0.001	-0.003	-0.009
7	355	365	346		0.040	0.010	-0.089
8	346	365	356		-0.005	-0.009	0.004
					0.016	0.016	0.022
	triangles along middle SG						
9	264	254	253		-0.014	-0.002	-0.008
10	254	244	253		0.001	0.009	-0.038
11	264	265	254		0.029	0.006	0.472
12	265	245	254		-0.350	-0.124	0.000
13	245	265	255		0.749	-0.684	0.205
14	275	266	255		-0.004	-0.065	-0.171
15	246	245	255		-0.008	0.036	0.108
16	256	246	255		0.001	0.008	0.013
					0.144	0.117	0.127
	triangles along bottom SG						
17	183	184	173		0.141	-0.049	0.014
18	174	184	194		0.489	0.162	-0.149
19	174	194	185		0.005	-0.005	0.009
20	185	175	174		-0.011	-0.002	0.003
					0.161	0.055	0.043

time (hr:min:sec:millisec) – epochs	17:22:54.545	17:23:04.461	17:23:29.694

Table 6.3: strains using CRDP method along SGs – exp 8

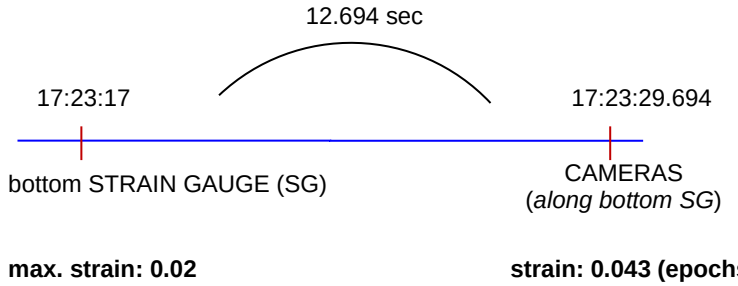

Diagram 6.4: monitoring methods recording sequence for experiment 8 along with their strains

6.4 Conclusion

The purpose of this chapter was to present the two experiments (exp 7 & 8) carried out at the Earthquake and Large Structures Laboratory (EQUALS) of the University of Bristol to the large scale one-leaf masonry specimens. Their size was the large form of the scaled down church's eastern wall. Experiment 8 was a repetition of experiment 7, with the view to double-check the results obtained from experiment 7. Initially, the experiments were scheduled to be carried out in two days, one each day, as the EQUALS is a laboratory with limited access due to its commercial use. The first day was unsuccessful due to lack of synchronization of the monitoring means. Therefore, the second day both experiments carried out, morning and afternoon, and managed to prove good correlation of the strain results among the two monitoring techniques of CRDP and SG, and additionally to attribute the localisation of damage resulted from shear.

CHAPTER 7

CONCLUSION

7.1 Summary Remarks

This research introduces a precise, cost efficient, non-destructive monitoring strategy, continuously applied to structural elements exposed to every day vibrations, with the view to form an online data record which will automatically alter an existing analytical structural model. Such a definition, of the appropriate monitoring strategy, can provide the right timing for the application of the mitigation method. This is an added-up value for the Building Information Modelling (BIM) and the retrofitting industry.

The monitoring strategy is comprised of two monitoring techniques: the photogrammetry and the strain gauge. A part of the Kapnikarea chapel's northern wall is chosen as the prototype structural element to understand and prove the efficiency of the proposed monitoring strategy. This wall is scaled down twice, initially, by seventeen times and thereafter by five times. The scale models are one-leaf masonry specimens built by both mini and normal size bricks.

The small-scale specimens are tested five times under dynamic loading applied at the bottom of the mini-wall on the x axis, one time at the z axis and the last time at the x axis with the specimen facing at 45° degrees the cameras. The large-scale specimen is tested twice, actuated on the x axis. For all the experimental set ups the cameras are positioned opposite to the specimen and the strain gauges installed horizontally or diagonally.

Two different types of failures were resulted, in plane and out of plane, under four experimental set ups. Four specimens, just small ones, were tested in plane (x axis), and the crack was similarly formed on the x axis. Two specimens, both large and small ones, were tested in plane (x axis) and the failure occurred out of plane (z axis). One small specimen was tested out of plane and received an out of plane failure as

well. Under static loading only one specimen was tested, and two cracks were formed, both horizontally and vertically.

SG were proved capable of monitoring a change in their strain recordings once the cracks started propagating during the test. The CRDP showed its capability to capture the failure and with the use of the appropriate computation means (Mohr circle) to translate this failure to displacement and strain for a small structural component (i.e. a triangle) of the specimen-walls.

Therefore, the final conclusions per experiment are:

Experiment 1 was a trial and error experiment to define the experimental workflow. It resulted to an in-plane (x axis) failure caused by an in-plane excitation. The collected image data did not manage to capture the crack propagation and the specimen's failure, however by plotting the shear strain contour maps, using the Surfer software, it was managed to detect the failure's initiation. Thus, the number of images was increased through the following experiments.

Experiment 2 was the only static experiment where the pressure was applied on the y axis. Cracks of the tested wall specimen were formed both horizontally (x axis) and vertically (y axis). The close-range digital photogrammetry (CRDP) method managed to capture the specimen's deformation. The strain gauge also monitored a change in strain with a time lapse of 4 seconds to the CRDP.

Experiment 3 was resulted to an in-plane failure caused by an in-plane excitation. The image data of this experiment were analysed by two methods. The first one comprised of 4 epochs which managed to show the failure and the second method, which was comprised of 5 epochs, managed to predict the crack's initiation. Both the CRDP and the SG managed to record a change in strain, when the specimen was damaged, with a time lapse of 1.175'' seconds.

Experiment 4 was resulted to an in-plane failure, out of plane and a de-attachment of a small brick caused by an in-plane excitation. The image data of this experiment were analysed by two methods. During the first one only redlake cameras were used and during the second one only the nikon cameras. The two installed strain gauges managed to collect data by showing a change in strain the same time with the CRDP method. Both the CRDP and the SG managed to record a change in strain, when the specimen was damaged, with a time lapse of 1,743'' seconds for the redlake cameras and 0.58'' seconds for the nikon ones.

Experiment 5 was resulted to an in-plane failure in the direction of the excitation. It is the only experiment where the wall specimen was placed at an angle of 45°, with the

cameras being able to capture the crack's propagation. Both the CRDP and the SG managed to record a change in strain, when the specimen was damaged, with a time lapse of 21.556'' seconds for the horizontal strain gauge and of 5.556'' seconds for the diagonal strain gauge.

Experiment 6 was resulted to an in-plane and out of plane failure. It is the only experiment, where the excitation was applied on the z axis, with the cameras being able to capture the crack's propagation. Both the CRDP and the SG managed to record a change in strain, when the specimen was damaged, with a time lapse of 0.291'' seconds.

Experiments 7 and 8 are identical and they are the only experiments carried out on a large-scale model wall and at the large shaking table of the University of Bristol. The vibration was applied on the x axis and the failure occurred on the z axis; out of plane failure for both tested specimens. During experiment 7 both the CRDP and the three strain gauges monitored a change in strain with a time lapse of 42.211 seconds. And similarly, during experiment 8 both the CRDP and the three strain gauges monitored a change in strain with a time lapse of 12.694 seconds.

7.2 Future Work

As a next step of the collected monitored data will be transferred directly to a structural software (fig. 7.1) with the view a structural analysis to be carried out by the engineer. Prior to this step, the laser scanning (fig. 7.1) of the structural element or the structure itself may have been carried out and insert it to the structural analysis software to create a model, geometrically close to the real one. For historical structures, such as the Kapnikarea chapel, the Elizabeth Tower (Big Ben), the Duomo Cathedral and others, the geometry is critical as partial collapses occur to bell towers or to thin pillar columns or to other architectural elements.

Once the geometrical and input field data have been inserted to the structural analysis software, the results need to be discussed within a multi-disciplinary team with the view to apply innovative techniques efficient for the structures' rehabilitation.

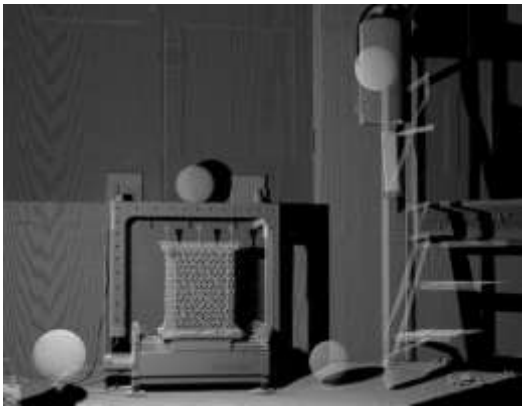

point cloud with laser scanning

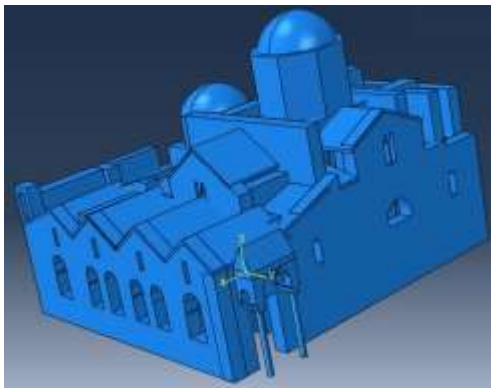

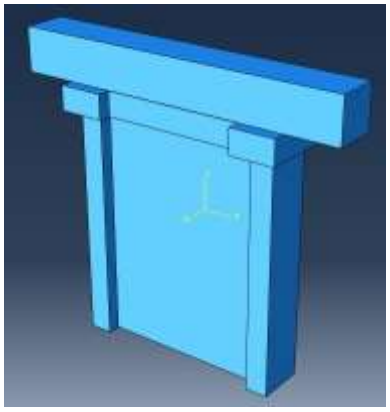

structural analysis modelling

Kapnikarea Chapel's model	small-scale wall model

Figure 7.1: point cloud and FE models for both the Kapnikarea chapel and the scaled down mini-wall

REFERENCES

1. Addison, A.C. & Gaiani, M. (2000), *Virtualized architectural heritage: new tools and techniques*, *MultiMedia, IEEE*, 7(2), 26 – 31, doi: 10.1109/93.848422
2. Alba, M., Roncoroni, L., Barazzetti, A., Giussani, F., Scaioni, M. (2011). Monitoring of the Main Spire of the Duomo Di Milano.
3. Arias, P., Armesto, J., Di-Capua, D., González-Drigo, R., Lorenzo, H., Pérez-Gracia, V. (2007), *Digital photogrammetry GPR and computational analysis of structural damages in a mediaeval bridge, Engineering Failure Analysis*, 14(8), 1444-1457, ISSN 1350-6307, http://dx.doi.org/10.1016/j.engfailanal.2007.02.001.
4. Armesto, J., Arias, P., Roca, J. & Lorenzo, H. (2008). *Monitoring and Assessing Structural Damage in Historic Buildings*. The Photogrammetric Record, 23(121), pp. 36-50.
5. Asten, M.W., and Henstridge, J., D. (1984). *Arrays estimators and the use of microseisms for reconnaissance of sedimentary basins,* Geophysics, 49-11, 1828-1937
6. Atamturktur, S., Bornn, L. & Hemez, F. (2011), *Vibration characteristics of vaulted masonry monuments undergoing differential support settlement*, Engineering Structures, 33(9), 2472-2484, ISSN 0141-0296, http://dx.doi.org/10.1016/j.engstruct.2011.04.020.
7. Atkinson, K. B. (1996), *Close Range Photogrammetry and Machine Vision*. Department of Photogrammetry and Surveying, University College London. Whittles Publishing. Scotland, U.K.
8. Avdelidis, N.P. & Moropoulou, A. (2004), *Applications of infrared thermography for the investigation of historic structures*, Journal of Cultural Heritage, 5(1), 119-127, ISSN 1296-2074, http://dx.doi.org/10.1016/j.culher.2003.07.002.
9. BBC 1: http://news.bbc.co.uk/1/hi/england/2741307.stm
10. BBC 2: http://news.bbc.co.uk/1/hi/england/london/2984955.stm
11. Bistrow, Charles (Jun. 2010). Personal Communication with Reader in Seismology, Faculty of Mathematical & Physical Sciences (MAPS), Department of Earth Sciences, Thermochronometry Research Laboratory, University College London & Birkbeck College.

12. Boehler, W., Heinz, G. & Marbs, A. (2001), *The potential of Non-Contact Close Range Laser Scanners for Cultural Heritage Recording.* XVIII CIPA International Symposium Proceedings, Potsdam, Germany, September 2001.

13. Bolin, Z., Qingyuan, H., Huixin, L. (1986), *Study of microwave remote sensing of the soil moisture*. Scientia Sinica, Sereis B, 29(1), 57-66.

14. Bonnefoy-Claudet, S. (2004). *Nature du bruit de fond sismique: Implications pour les etudes des effects de site*, Ph.D., University Joseph Fourier, France *(in French with English abstract)*

15. Bouras, Ch. (2001). *Byzantine and Middle Byzantine Architecture in Greece*. Melisa Press, Athens, 2001.

16. Brownjohn, J. & Chien, T. (2001), *Response of tall buildings to weak long distance earthquakes*, Earthquake Engineering & Structural Dynamics, 30(5), 709-729, ISSN 1096-9845, http://dx.doi.org/10.1002/ege.32.

17. Bryan, P., Blake, B. & Bedford, J. (2009), *Metric Survey Specifications for Cultural Heritage*. English Heritage.

18. BS EN 998-2:2016 Specification for mortar for masonry. Masonry mortar

19. Camp, J. (2001). *The Archaeology of Athens*, Yale University Press. New Haven and London.

20. Carrasco, E.V.M., Silva, S.R. & Mantilla, J.N.R. (2014), *Assessment of mechanical properties and the influence of the addition of sawdust in soil-cement bricks using the technique of ultrasonic anisotropic inspection*, Journal of Materials in Civil Engineering, 26(2), 219-225, ISSN 0899-1561, http://dx/doi.org/10.1061/(ASCE)MT.1943-5533.0000723.

21. Chae, M.J., Yoo, H.S., Kim, J.Y., Cho, M.Y. (2012), *Development of a wireless sensor network system for suspension bridge health monitoring*, Automation in Construction, 21, 237-252, ISSN 0926-5805, http://dx.doi.org/10.1016/j.autcon.2011.06.008.

22. Coleman, H.W., & Steele, W.G. (1999). *Experimental and Uncertainty Analysis for Engineers*. Chichester: John Wiley & Sons, Inc.

23. Connor, M. & Scott, D. (1998), *Metal Detector Use in Archaeology: An Introduction*, Historical Archeology, 32(4), 76-85, ISSN 0440-9213, http://www.jstor.org/stable/25616646.

24. Cooper, M.L., Chapman, D.N., Rogers, C.D., Chan, A.H. (2002), *Movements in the Piccadilly Line tunnels due to the Heathrow Express construction*, Géotechnique, 52(4), 243-257, ISSN 0016-8505, doi: 10.1680/geot.2002.52.4.243

25. Delikaraoglou, D., Georgopoulos, A., Ioannidis, C., Lambrou, E. & Pantazis, G. (2010), *Using Geodetic and Laser Scanner Measurements for Measuring and Monitoring the Structural Damage of a Post Byzantine Church.* 8th International Symposium on Conservation of Monuments in the Mediterranean Basin, Patras, Greece, June 2010.

26. Derbal, R., Defer, D., Chauchois, A., Antczak, E. (2014), *A simple method for building materials thermophysical properties estimation*, Construction and Building Materials, 63, 197-205, ISSN 0950-0618, http://dx.doi.org/10.1016/j.conbuildmat.2014.04.076.

27. Dunnicliff, J. (1988), *Geotechnical Instrumentation for Monitoring Field Performance,* A Wiley-Interscience Publication, John Wiley & Sons, New York/Chichester/Brisbane/Toronto/Singapore

28. Duran, Z. & Toz, G. (2003), *Photogrammetric Reconstruction and Virtual Presentation of Monastery of Christ Pantepoptes.* XIX CIPA International Symposium Proceedings, Antalya, Turkey, October 2003.

29. Fang, T.P. & Piegle, L.A. (1995), *Delaunay triangulation in three dimensions*, IEEE Computer Graphics and Applications, 15(5), 62-69, ISSN 0272-1716, doi: 10.1109/38.403829.

30. Fortune, S. (1995), *Voronoi diagrams and Delaunay triangulations*, Computing in Euclidean Geometry Singapore, World Scientific.

31. Francke, Jan (Jun. 2010). Private Communication with PhD Candidate in Environmental Modelling and Monitoring, School of Social Science & Public Policy, Department of Geography, Kings College London.

32. Frantii, G. (1963). *The nature of high-frequency earth noise spectra*, Geophysics, 28-4, 547-562

33. Grove, K., and Caskey, S.J., (2005), *Theodolite and total station measurements of creep rates on San Francisco Bay Region faults: National Earthquake Hazards Reduction Program*, NEHRP Final Technical Report Award# 03HQGR0080.

34. Georgopoulos, Andreas (2010), Personal Communication with Professor of Photogrammetry, School of Rural and Surveying Engineering, Department of Topography, Photogrammetry Research Laboratory, National Technical University of Athens (N.T.U.A.).

35. Glišić, B. & Inaudi, D. (2007). *Fibre Optic for Structural Health Monitoring*, John Wiley & Sons, ISBN 978-0-470-06142-8.

36. Gutenberg, B. (1958), Microseisms, Advan, Geophys, 5, 53-92

37. Hall, S.A., de Sanctis, F. & Viggiani, G. (2006). Monitoring fracture propagation in a soft rock (Neapolitan Tuff) using acoustic emission and digital images, Pure and Applied Geophysics, 163(10), 2171-2204, ISSN 0033-4553, http://dx/doi.org/10.1007/s00024-006-0117-z.

38. Harris, C. & Piersol, A. (2002). *Harris' Shock and Vibration Handbook*, McGraw-Hill, London, New York, 5th Edition, ISBN 978-0-071-37081-3.

39. Harris, H. & Sabnis, G. (1999), *Structural Modeling and Experimental Techniques*. CRC Press, 2nd Edition.

40. Harvey, B. (2009), *Monitoring and Measuring Historic Masonry Structures*. Proceedings of the 3rd Australasian Engineering Heritage Conference (Dunedin, New Zealand).

41. Hellenic Ministry of Culture Reports, folders: B, Δ, Z, H & Θ (1979 – 2002)

42. Henriques, M.J. & Casaca, J. (2001). *Monitoring vertical displacements by means of geometric levelling*. 3rd International Conference on Structural Analysis and Historical Construction, Guimarães, Portugal.

43. Hochtief Murphy Joint Venture (2012), Internal Report, Thames Tunnel Plan, Crossrail, DLR Interface, HMJV, Monitoring Plan.

44. Huntley, S. & Valsangkar, A. (2013), *Field monitoring of earth pressure on integral bridge abutments*, Canadian Geotechnical Journal, 50(8), 841-857, ISSN 0008-3674.

45. Imposa, S., Mele, G., Corrao, M., Coco, G. & Battaglia, G. (2014). *Characterization of Decay in the Wooden Roof of the S. Agata Church of Ragusa Ibla (Southeastern Sicily) by Means of Sonic Tomography and Resistograph Penetration Tests*, International Journal of Architectural Heritage: Conservation, Analysis, and Restoration, 8(2), 213-223, ISSN 1558-3058, http://dx.doi.org/10.1080/15583058.2012.685924.

46. Indirli, M., Cami, R., Carpani, B., Algeri, C., Panzeri, P., Rossi, G. & Piova, G. (2006). *The Antiseismic Rehabilitation of Marchesale Castle at San Giuliano di Puglia*. 5th International Conference on Structural Analysis and Historical Construction, New Delhi, India.

47. Indirli, M. & Castellano, M. G. (2008). *Shape Memory Alloy Devices for the Structural Improvement of Masonry Heritage Structures*. International Journal of Architectural

Heritage: Conservation, Analysis, and Restoration, 2(2), 93-119, ISSN 1558-3058, http://dx.doi.org/10.1080/15583050701636258.

48. Jasieńko, J., Tomasz P. Nowak, T. & Bednarz, L. (2014). *Baroque Structural Ceiling Over the Leopoldinum Auditorium in Wrocław University: Tests, Conservation, and a Strengthening Concept*. International Journal of Architectural Heritage: Conservation, Analysis, and Restoration, 8(2), 269-289, ISSN 1558-3058, http://dx.doi.org/10.1080/15583058.2012.692848.

49. Kear, G., Flatley I. & Jones, S. (2006). *Application of polarisation resistance measurements for the estimation of corrosion rates of galvanised steel structures in soils*, No. 127, Corrosion and Protection 06 Conference, ISSN: 0111-7505, Australia.

50. Kee, S.H. & Zhu, J. (2010), *Using air-coupled sensors to determine the depth of a surface-breaking crack in concrete*, The Journal of the Acoustical Society of America, 127(3), 1279-1287, ISSN 0001-496, http://dx.doi.org.libproxy.ucl.ac.uk/10.1121/1.3298431

51. Kiremidjian, A.S., Straser, E.G., Meng, T., Law, K., Sohn, H. (1997). *Structural Health Monitoring Current Status and Perspectives*, Fu-Kuo Chang, edt., Technomic Publishing Co, Stanford Publications.

52. Krawinkler, H., Mills, R.S., Moncarz, P.D., et al. (1978). Scale Modeling and Testing of Structures for Reproducing Response to Earthquake Excitation. Blume Earthquake Engineering Center Department of Civil Engineering, Stanford University.

53. Krstevska, L., Tashkov, L., Gramatikov, K., Landolfo, R., Mammana, O., Portioli, F. & Mazzolani, F. (2010). *Large-Scale Experimental Investigation on Mustafa Pasha Mosque*. Journal of Earthquake Engineering, 14(6), 842-873, ISSN 1363-2469, http://dx.doi.org/10.1080/13632460903338528.

54. Kwok, Y. H. & Sawjani, C. (2001). Precise measurement technique, 3rd year project report, Department of Civil & Environmental Engineering, University College London.

55. Lagomarsino, S., Modaressi Hormoz, Pitilakis, K., Bosiljkov Vlatko, Calderini Chiara, D'Ayala D., Benour D. & Cattari S. (2010). "PERPETUATE Project: The Proposal of a Performance-Based Approach to Earthquake Protection of Cultural Heritage", Advanced Materials Research, Vols. 133-134, pp. 1119-1124, 2010

56. Lee, H., & Ko, D. (2007). *Seismic response characteristics of high-rise RC wall buildings having different irregularities in lower stories*, Engineering Structures, 29(11), 3149-3167, ISSN 0141-0296, http://dx.doi.org/10.1016/j.engstruct.2007.02.014.

57. Lee, H. & Rhee, H. (2013), *3-D measurement of structural vibration using digital close-range photogrammetry*, Sensors and Actuators A: Physical, 196, 63-69, ISSN 0924-4247, http://dx.doi.org/10.1016/j.sna.2013.03.010.

58. Lee, Y.J. & Bassett, R.H. (2006). *Application of a photogrammetric technique to a model tunnel*, Tunnelling and Underground Space Technology 21 (2005), 79-95.

59. Lechner, T., Nowak, T. & Kliger, R. (2014). *In situ assessment of the timber floor structure of the Skansen Lejonet fortification, Sweden*, Construction and Building Materials, 58(15), 85-93, ISSN 0950-0618, http://dx.doi.org/10.1016/j.conbuildmat.2013.12.080.

60. Le Monde: http://www.lemonde.fr/archives/article/2003/02/17/le-creusement-de-tunnels-sous-la-ville-entraine-des-risques-et-des-surcouts_309581_1819218.html?xtmc=le_creusement_de_tunnels_sous_la_ville_entraine_des_risques_et_des_surcouts&xtcr=1

61. Loh, C.H. and Tou, I.C. (1995). *A System Identification Approach to the Detection of Changes in Both Linear and Nonlinear Structural Parameters*, International Journal Earthquake Engineering and Structural Dynamics, 24, 85-97, ISSN 1096-9845, http://dx.doi.org/10.1002/eqe.4290240107.

62. Luhmann, T., Robson, S., Kyle, S. and Boehm J. (2013). Close-Range Photogrammetry and 3D Imaging. 2nd edition, De Gruytter.

63. Lynch, J.P., Wang, Y., Loh, K.J., Yi , J.H., Yun, C.B. (2006), *Performance monitoring of the Geumdang Bridge using a dense network of high-resolution wireless sensors*, Smart Materials and Structures, 15(6), 1561-1575, doi:10.1088/0964-1726/15/6/008

64. Mair, R. J. & Harris, D. (2001). Innovative engineering to control Big Ben's tilt. *Ingenia*, 9, August, 23 – 27.

65. Matteis, G. & Mazzolani, F. (2010). *The Fossanova Church: Seismic Vulnerability Assessment by Numeric and Physical Testing*. International Journal of Architectural Heritage: Conservation, Analysis, and Restoration, 4(3), 222-245, ISSN 1558-3058, http://dx.doi.org/10.1080/15583050903078903.

66. Martin – Perez, B., Deif, A., Cousin, B., Zhang, C., Bao, X., Li, W. (2010), *Strain monitoring in a reinforced concrete slab sustaining service loads by distributed Brillouin fibre optic sensors*, Canadian Journal of Civil Engineering, 37(10), 1341-1349, ISSN 0315-1468, http://dx.doi.org/10.1139/L10-080.

67. Marques, F., Moutinho, C. & Cunha, Á. (2012). *Local Fatigue Analysis using a Long-Term Monitoring System at the Trezói Railway Bridge*. Proceedings of the Eleventh International Conference on Computational Structures Technology, Paper 110, Stirlingshire, Scotland.

68. Michael, I. (2011). *Novel applications of distributed fibre-optic sensing in geotechnical engineering*, ETH, http://dx.doi.org/10.3929/ethz-a-6559858.

69. Nakamura, Y. (1989). *A method for dynamic characteristics estimation of subsurface using ambient noise on the ground surface,* Geotechnical Engineering & Disaster Prevention Laboratory, Quarterly Report of Railway Technical Research Institute, 30(1), 25-33

70. Nakamura, Y., Gurler, E. D., Saita, J. (1999). *Dynamic Characteristics of Leaning Tower of Pisa using Microtremor –Preliminary result–*, Proceedings of the 25th JSCE Earthquake Engineering Symposium, 921-924.

71. Nakamura, Y., Gurler, E. D., Saita, J., Rovelli, A. & Donati, S. (2000). *Vulnerability Investigation of Roman Colosseum using Microtremor*, Proceedings of 12th WCEE, Auckland, New Zealand, #2660.

72. Nassif, H., Gindy, M., Davis, J. (2005). *Comparison of laser Doppler vibrometer with contact sensors for monitoring bridge deflection and vibration*, NDT & E International, 38(3), 213-218, ISSN 0963-8695, http://dx.doi.org/10.1016/j.ndteint.2004.06.012.

73. Newspaper “KATHIMERINI” (Mar. 2002). Monthly inset “Seven Days” of the Greek press: *Wells and cisterns*.

74. O' Reilly, M. P. & New, B. M. (1983). *Settlement above tunnels in the United Kingdom – their magnitude and prediction*. Transport and Road Research Laboratory, Crowthorne, England.

75. Ottoni, F. (2015). *Dome Strengthening By Encircling Ties: A Monitored Experiment*. International Journal of Architectural Heritage: Conservation, Analysis, and Restoration, 8(1), 82-95, ISSN 1558-3058, http://dx.doi.org/10.1080/15583058.2013.793436.

76. Palacio, A.G., Hernández J.D. & Aldasoro, J.J. (2001). *Monitoring and structural analysis of the chuch "Santa Maria de Elexondo (Zeanuri)*. 3rd International Conference on Structural Analysis and Historical Construction, Guimarães, Portugal.

77. Papadopoulos, N.G., Sarris, A., Parkinson, W.A., Gyucha, A., Yerkes, R.W., Duffy, P.R., Tsourlos, P. (2014). *Electrical resistivity tomography for the modelling of cultural deposits and geomophological landscapes at neolithic sites: A case study from southeastern Hungary*, Archaeological Prospection, ISSN1075-2196, doi: 10.1002/arp.1480.

78. Plagge, R. (2006). *Moisture and Salt Mapping by TDR in the Historical Stonework of the Finca Marina-Manresa in Mallorca*. 5th International Conference on Structural Analysis and Historical Construction, New Delhi, India.

79. Riegl, Laser Measurement Systems. Retrieved 2011-04-15 from http://www.riegl.com/

80. Robson, S. (2007). "Vision Metrology", Lecture Notes, Department of Civil, Environmental and Geomatic Engineering, University College London.

81. Satoh, T., Kawase, H. & Matsushima, S. (2001). *Differences between site characteristics obtained from microtremors, S-waves, P-waves, and codas*, Bulletin of the Seismological Society of America, 91, 313-334

82. Simões, A., Gago, A., Lopes, M. & Bento, R. (2012). *Characterization of Old Masonry Walls: Flat-Jack Method*, 15th World Conference on Earthquake Engineering, Lisbon.

83. Smith, S.W. (2003). *Digital Signal Processing: A practical Guide for Engineers and Scientists*. London: Newnes – An Imprint of Elsevier Science.

84. Snell, L. & Cheek, M. (2006). *Estimating Fresh Concrete Temperatures: Infrared Thermometers Provide Rapid Check*. Concrete International, American Concrete Institute, 6 (6), pp. 49-52, ISSN 0162-4075.

85. Solla, M., Caamaño, J.C., Riveiro, B., Arias, P. (2012). *A novel methodology for the structural assessment of stone arches based on geometric data by integration of photogrammetry and ground-penetrating radar*, Engineering Structures, 35, 296-306, ISSN 0141-0296, http://dx.doi.org/10.1016/j.engstruct.2011.11.004.

86. Song, G., Olmi, C. & Gu, H. (2007). *An overheight vehicle-bridge collision monitoring system using piezoelectric transducers*, Smart Materials & Structures, 16(2), 462-468, ISSN 0964-1726, http://dx/doi.org/10.1088/0964-1726/16/026.

87. Squeglia, N. & Bentivoglio, B. (2015). *Role of Monitoring in Historical Building Restoration: The Case of Leaning Tower of Pisa*. International Journal of Architectural Heritage: Conservation, Analysis, and Restoration. 9(1), 38-47, ISSN 1558-3058, http://dx.doi.org/10.1080/15583058.2013.865813.

88. Tabbagh, A., Hesse, A. & Grard, R. (1993). *Determination of electrical properties of the ground at shallow depth with an electrostatic quadrupole: filed trials on archaeological sites*. Geophysical Prospecting, 41(5), 579-597, ISSN 1365-2478, http://dx.doi.org/10.1111/j.1365-2478.1993.tb00872.x.

89. Thériault, S., O. Hill, K., Bilodeau, F., Johnson, D.C., Albert, J., Drouin, G., Béliveau, A. (1997). *High*-g *accelerometer based on an in-fiber bragg grating sensor*, Optical Review, 4(1), A145-A147, ISSN 1340-6000, http://dx.doi.org/10.1007/BF02936013.

90. Tsakiri, M., Ioannidis, C., Papanikos, P. & Kattis, M. (2004). *Load Testing Measurements for Structural Assessment Using Geodetic and Photogrammetric Techniques*, 1st FIG International Symposium on Engineering Surveys for Construction Works and Structural Engineering, Nottingham, U.K.

91. Tsokas, G.N., Tsourlos, P.I., Vargemezis, G. & Novack, M. (2008). *Non-destructive Electrical Resistivity Tomography for Indoor Investigation: the Case of Kapnikarea Church in Athens*. Archaeological Prospection, 15 (1), 47-61. ISSN 1075-2196, http://dx.doi.org/10.1002/arp.321.

92. Tsung-Pao, F. & Les A. P. (1995). Delaunay Triangulation in Three Dimension. IEEE Computer Graphics and Applications

93. Wasil, B. A., Merchant, D. C. & Del Vecchio, Jr. (1965). *Photogrammetric Measurements of Dynamic Displacements*, Experimental Mechanics, 5(10), 332 – 339, ISSN 0014-4851, doi: 10.1007/BF02327536.

94. Watters, D.G., Jayaweera, P., Bahr, A.J., Huestis, D.L., Priyantha, N., Meline, R., Reis, R., Parks, D. (2003). *Smart Pebble: wireless sensors for structural health monitoring of bridge decks*. Proc. SPIE 5057, Smart Structures and Materials 2003: Smart Systems and Non-destructive Evaluation for Civil Infrastructures, http://dx.doi.org/10.1117/12.482397.

95. Wiberg, J. & Karoumi, R. (2009). *Monitoring dynamic behaviour of a long-span railway bridge*, Structure and Infrastructure Engineering: Maintenance, Management, Life-Cycle Design and Performance, 5(5), 419-433, ISSN 1573-2479, http://dx.doi.org/10.1080/15732470701478.

96. Wilson, J. (2005). Sensor Technology, Elsevier, ISBN 978-0-7506-7729-5

97. Xia, Y., Zhang, P., Ni, Y., Zhu, H. (2014). *Deformation monitoring of a super-tall structure using real-time strain data*, Engineering Structures, 67, 29-38, ISSN 0141-0296, http://dx.doi.org/10.1016/j.engstruct.2014.02.009.

98. Yamanaka, H., Dravinski, M. & Kagami, H. (1993). *Continuous measurements of microtremor on sediments and basement in Los Angeles*, California, Bulletin of the Seismological Society of America, 63, 1227-1253

99. Yu Qi-feng, Fu Si-hua, Jiang Guang-wen, Lei Zhi-hui (2010). *Pose-relay videometric method and ship deformation measurement system with camera-series*, Optomechatronic Technologies (ISOT), 2010 International Symposium, 1-5, ISBN 978-1-4244-7684-8, doi: 10.1109/ISOT.2010.5687350.

Appendices

APPENDIX I

CASE STUDY

Figure App. I – 1: Kapnikarea Chapel (google)

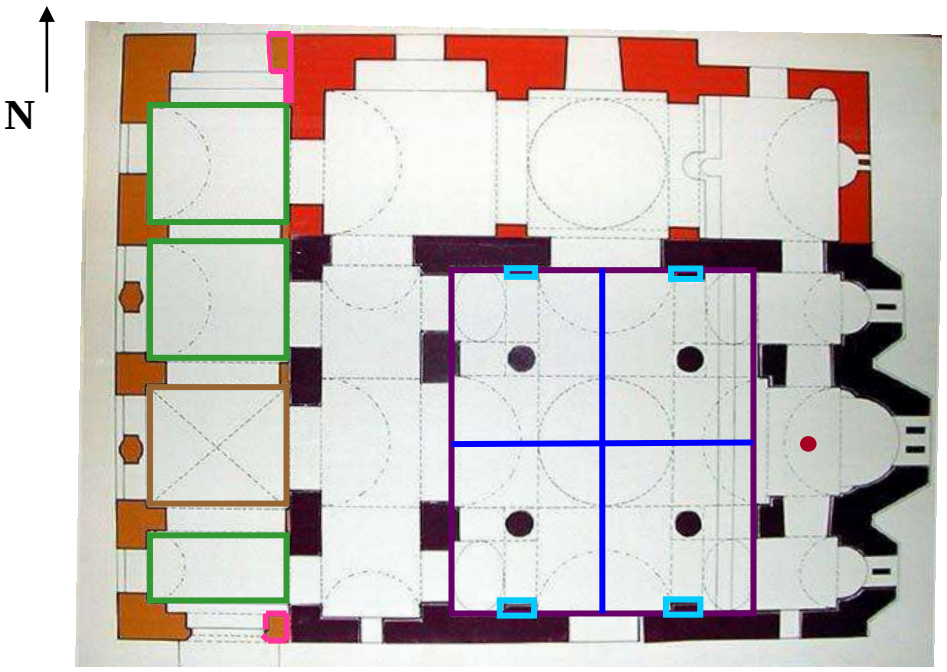

LEGEND:

Cross, square, pilasters, approximate position of the priest standing point during the Mass, barrel shaped vaults, cross shaped vault, marble projected columns

Figure App. I – 2: Plan view of the Kapnikarea Chapel showing its three parts; the nave (black colour), the "oratory" dedicated to Saint Barbara (red colour) and the exo-narthex (orange colour) (PANORAMIO)

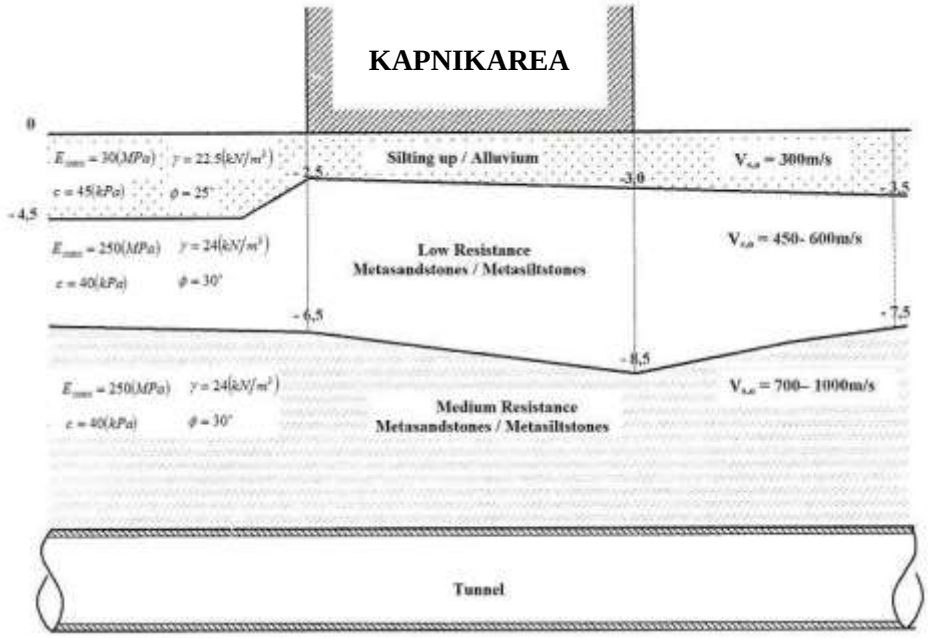

Figure App. I – 3: Ground Profile related to the Tunnel showing the composition, the geological characteristics and the S waves' velocity (Hellenic Ministry of Culture Report, folder H, 29/04/2002)

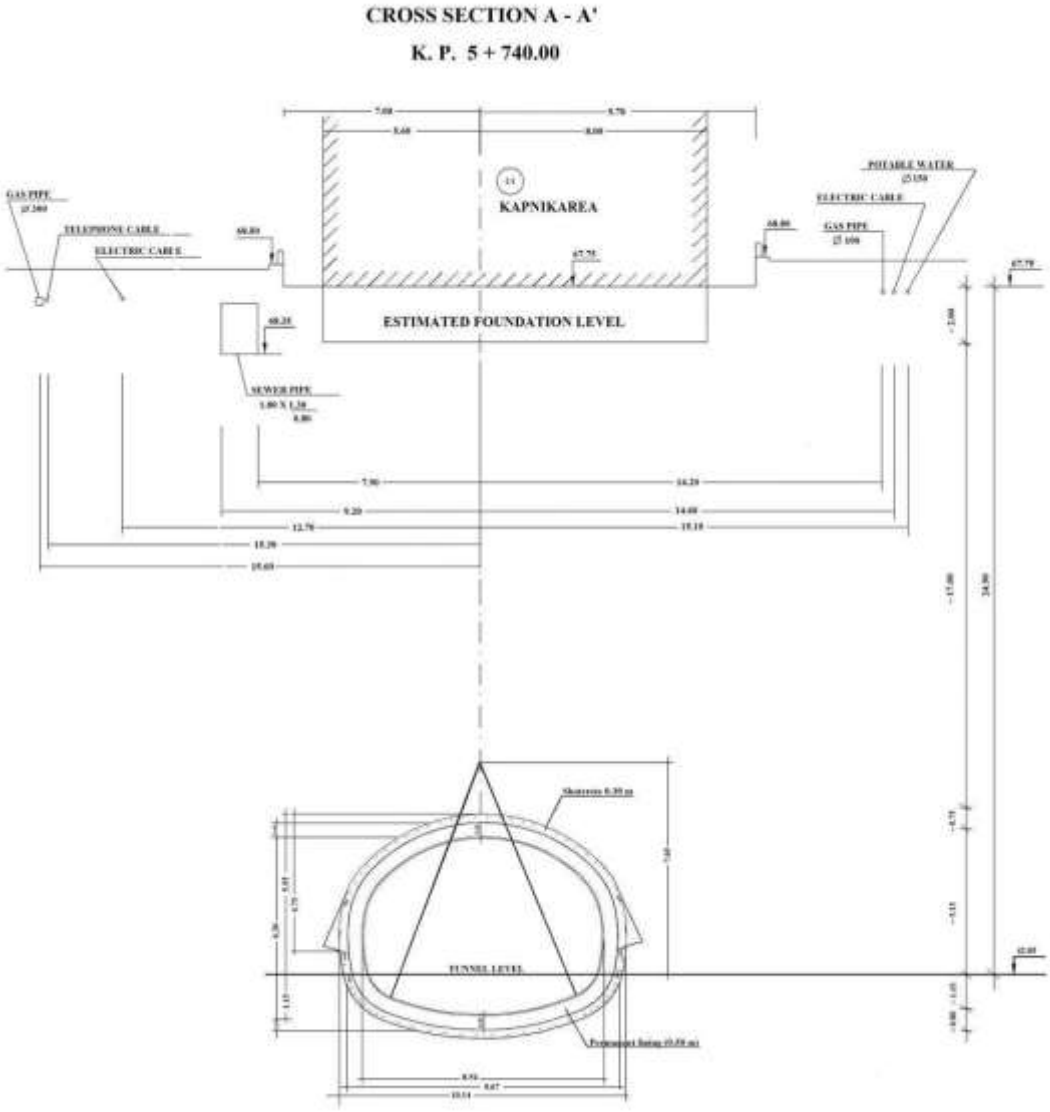

Figure App. I – 4: Tunnel's Cross Section underneath the Kapnikarea chapel (Hellenic Ministry of Culture Report, folder Z, 09/2000)

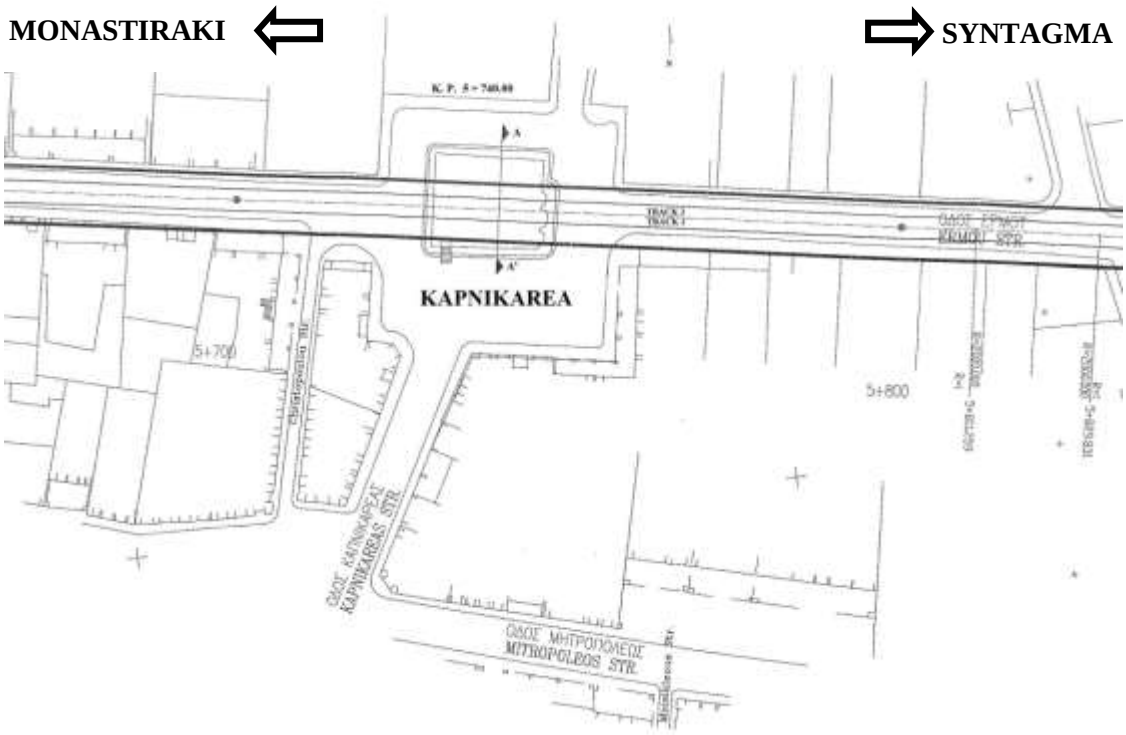

Figure App. I – 5: Plan of the Tunnel & the Kapnikarea chapel (Hellenic Ministry of Culture Report, folder Z, 09/2000)

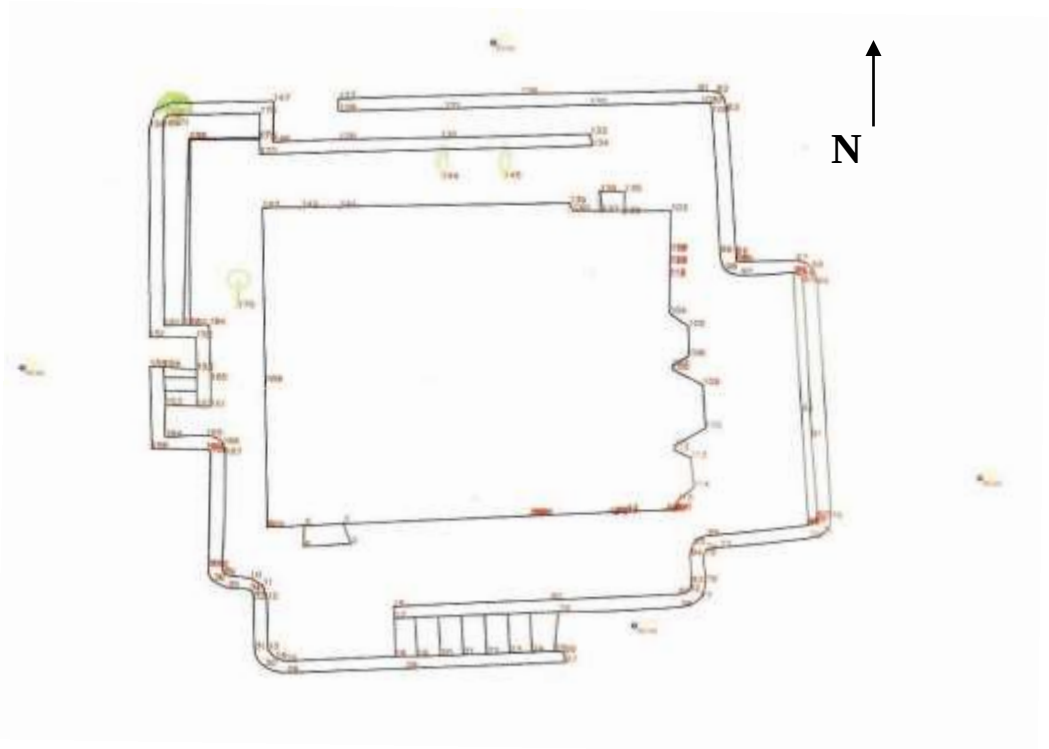

Figure App. I – 6: generated a map of the surveyed area around the Kapnikarea chapel (Metheniti, 2008)

Figure App. I – 7: Crack 1, South Side
(Metheniti, 2008)

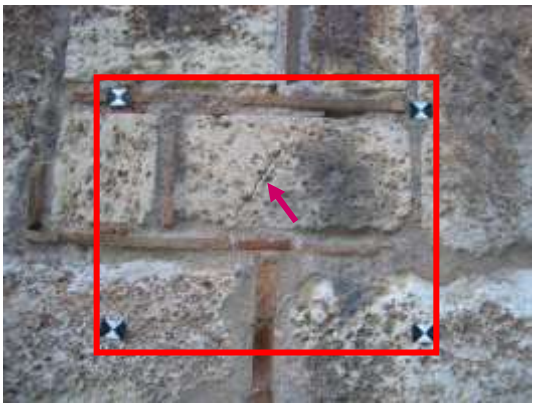

Figure App. I – 8: Crack 2, South Side
(Metheniti, 2008)

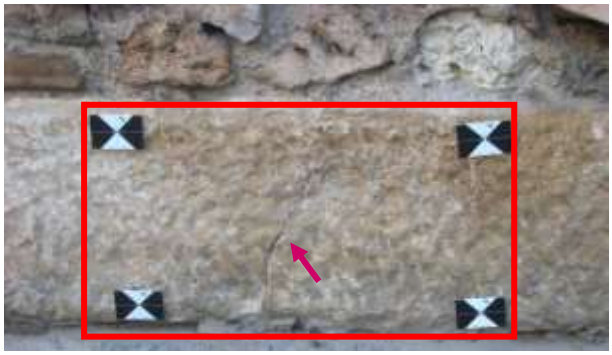

Figure App. I–9: Crack 3, South Side
(Metheniti, 2008)

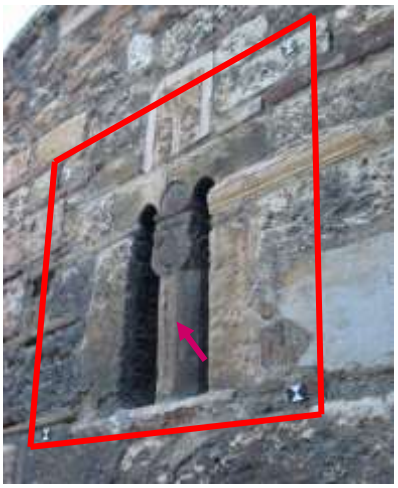

Figure App. I – 10: Crack 4, East Side
(Metheniti, 2008)

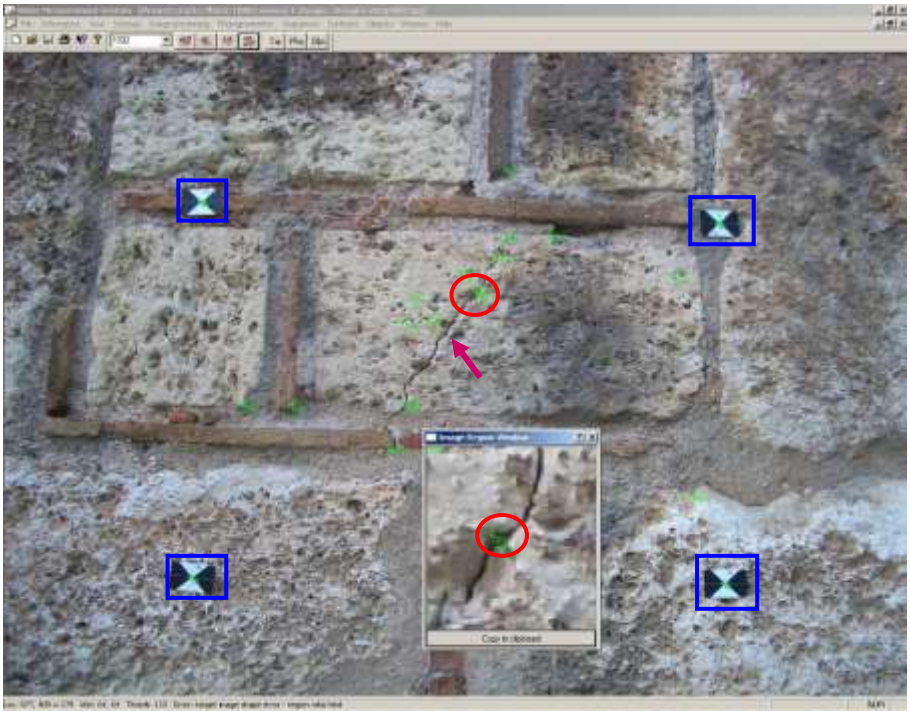

Figures App. I – 11: Crack 2 analysed in the VMS environment to determine the **free points** **2004** & **2005**; **control points** (Metheniti, 2008)

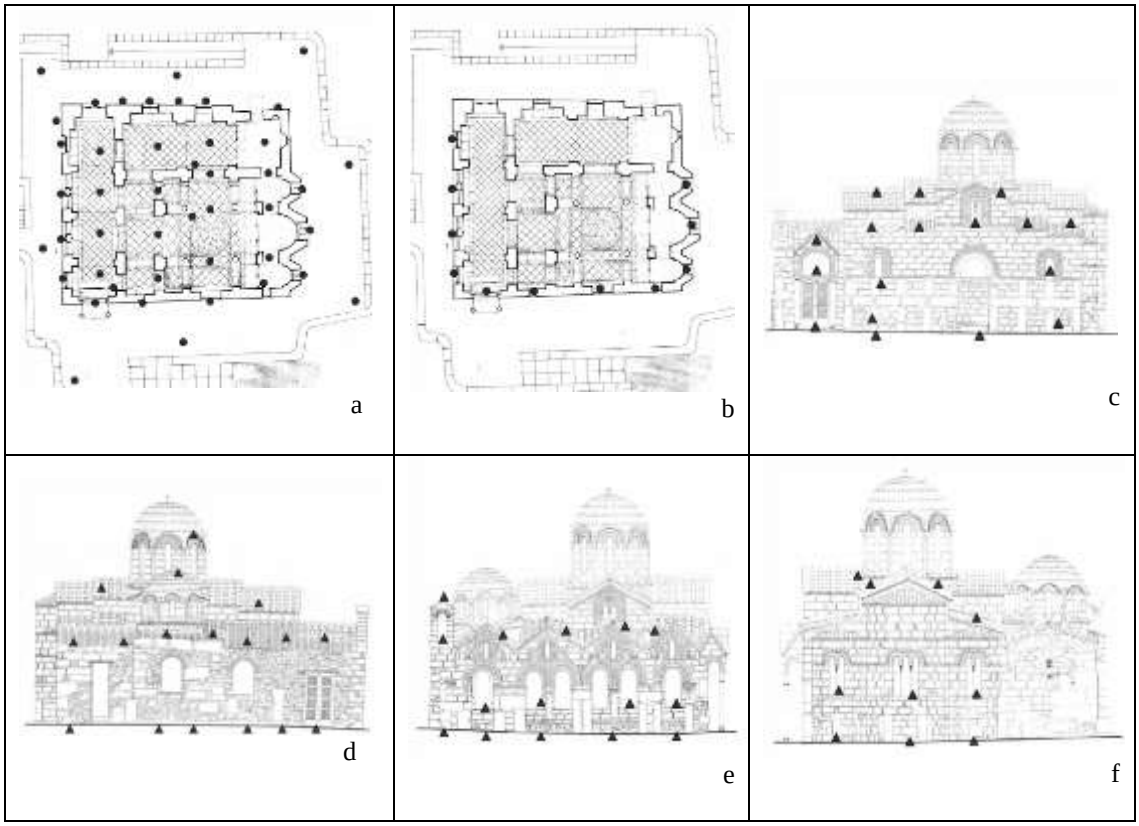

Figure App. I – 12: Locations of the measurement points: a) on the ground) b) on the windows c) on the southern face d) on the northern face e) on the western face f) on the eastern face.

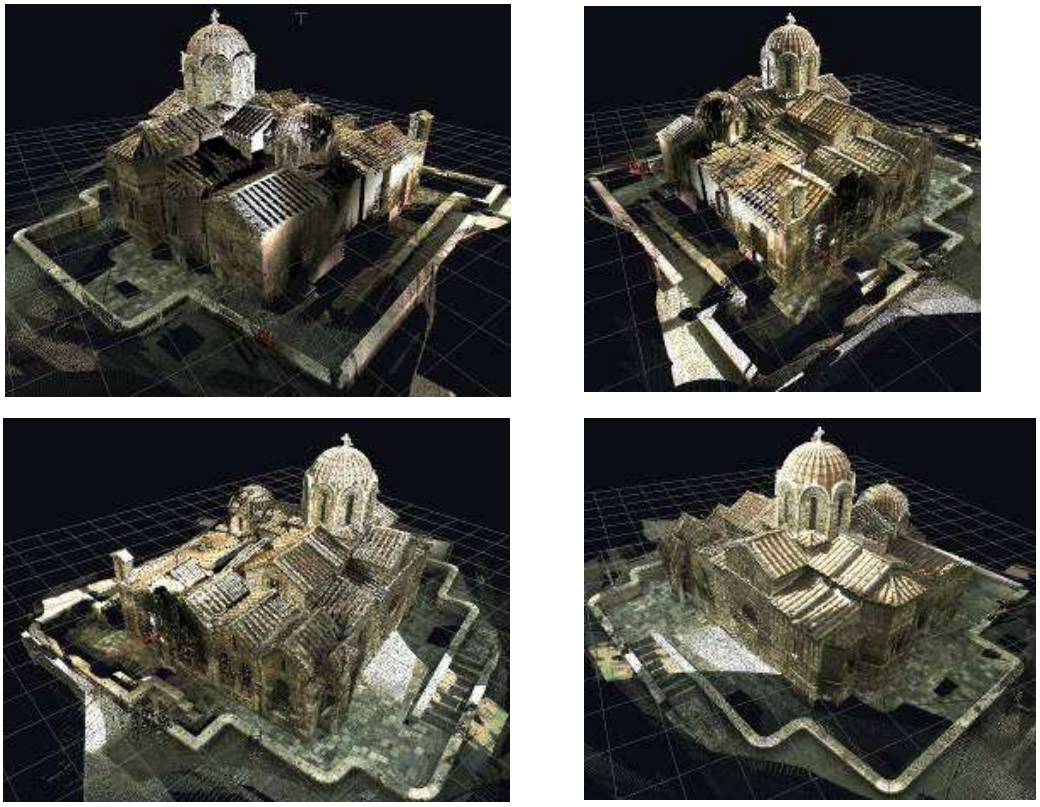

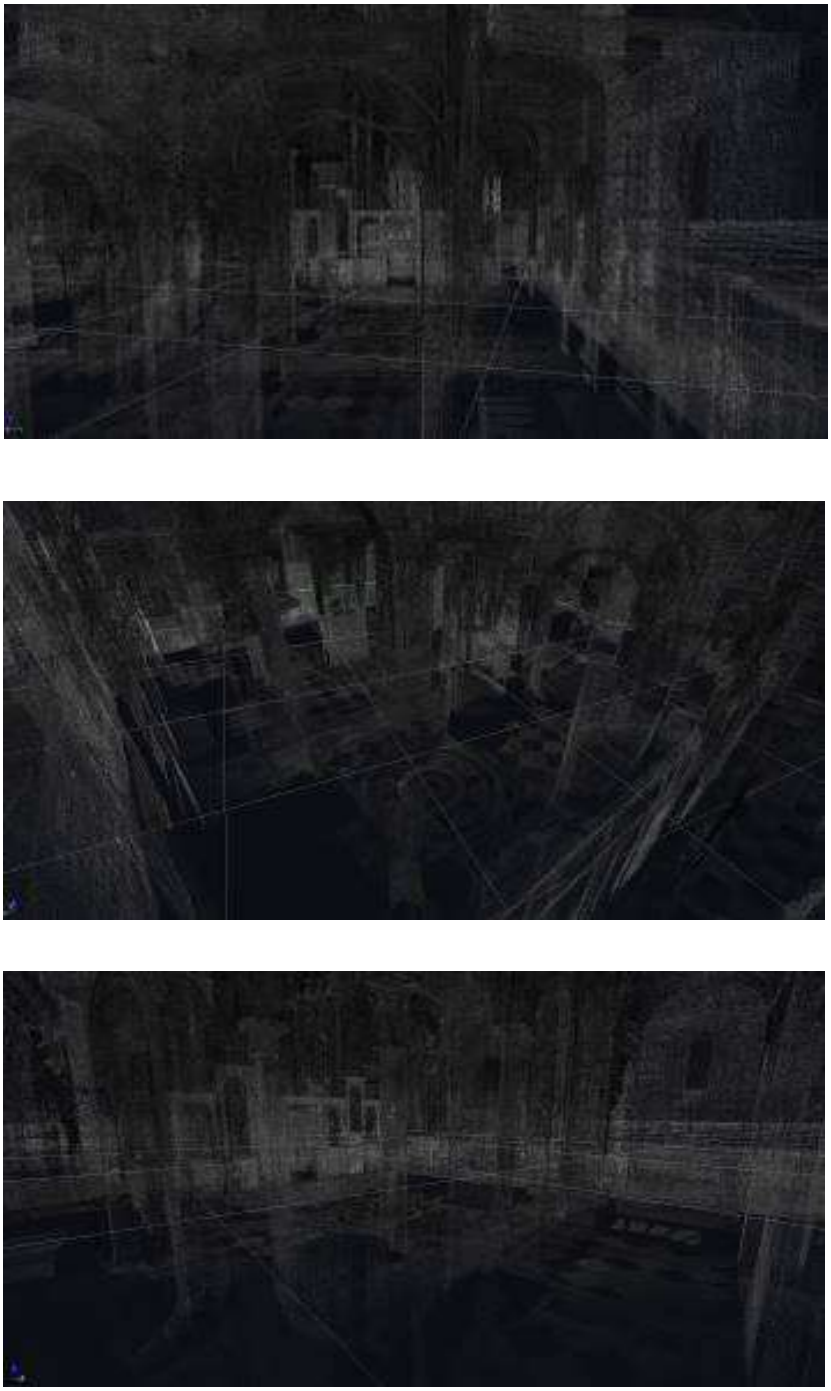

Figure App. I – 13: Different views of the Kapnikarea chapel's point cloud, outside & inside

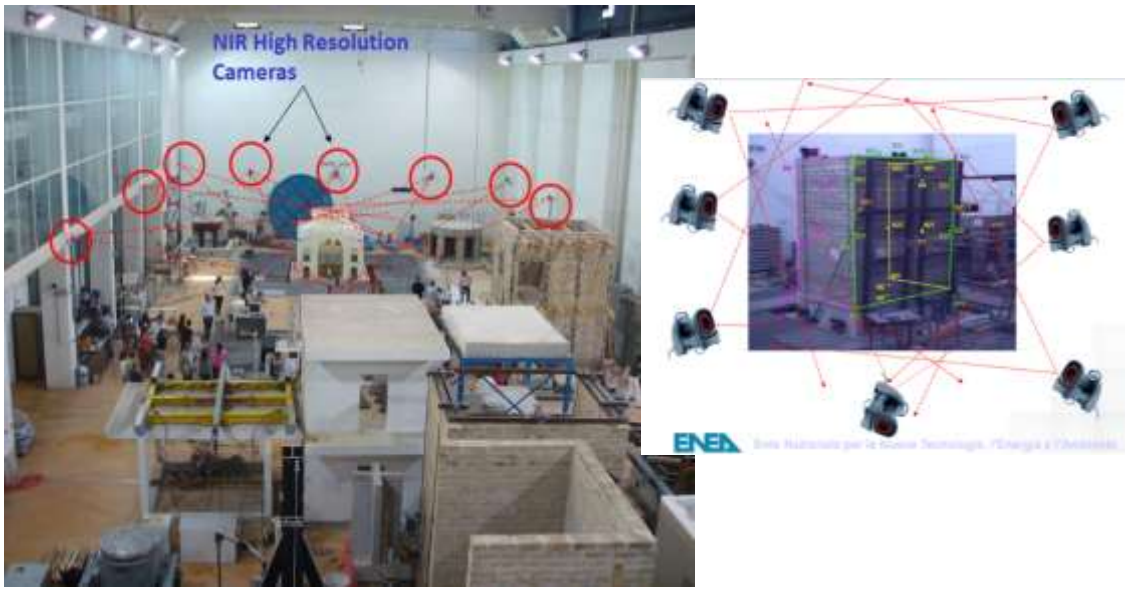

Figure App. I – 14: A full-scale tuff masonry (right hand) wall reinforced with external bonded composites has been monitored with nine infrared (NIR) cameras at the ENEA Casaccia Research Centre under the PERPETUATE project. The created cameras system is able to track the dynamic displacement of hundred selected points (markers) of the structures during shaking table tests (Lagomarsino, 2010).

APPENDIX II

LOADING CALCULATIONS

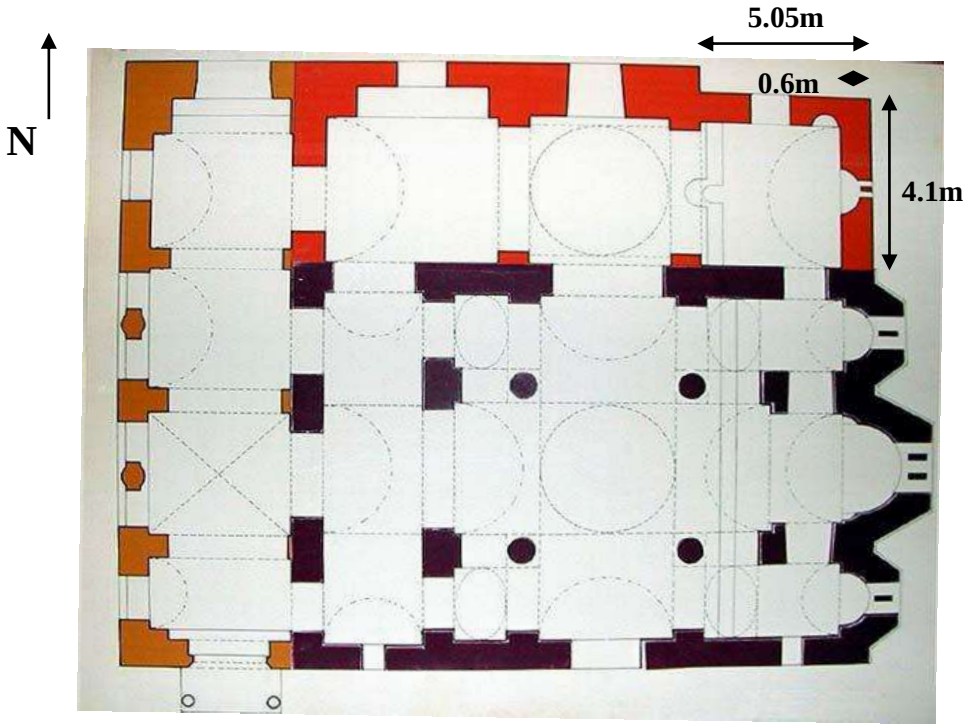

Figure App. II – 1: Plan view of the Kapnikarea Chapel showing its three parts (PANORAMIO)

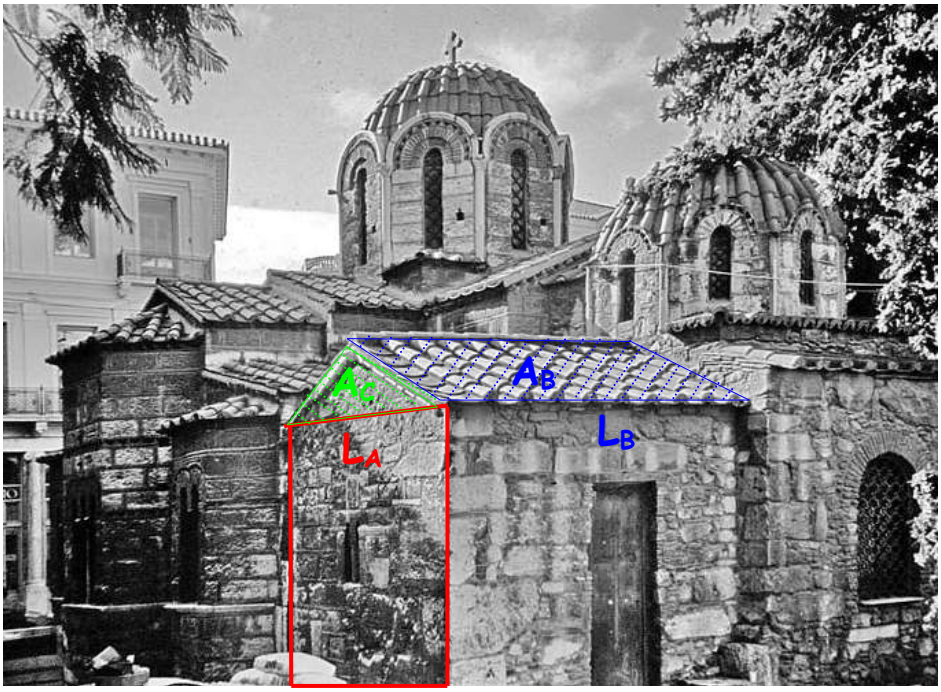

Figure App. II – 2: North-eastern side of the Kapnikarea Chapel, scaled-down wall (red) (Hellenic Ministry of Culture Report, folder A, 05/12/1996)

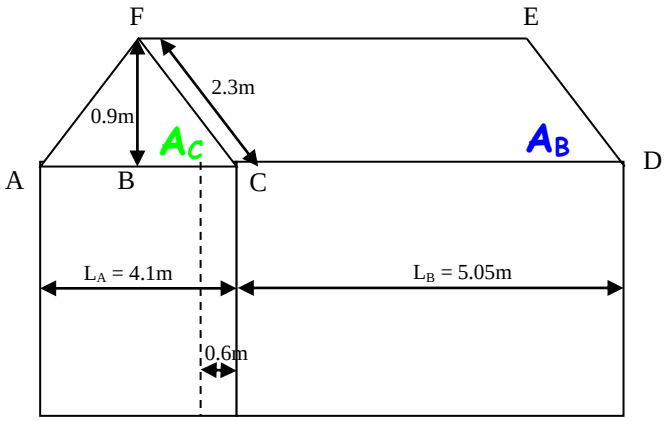

Figure App. II – 3: Sketch of the North-eastern side of the Kapnikarea Chapel

Assumptions: 1.) masonry dead load: $g_A = 26 kN/m^3$ (British Standards)

2.) tiles dead load: $g_B = 0.7 kN/m^3$ (British Standards)

3.) modulus of Elasticity: $E_{PROTOTYPE} = E_{MODEL} = 1$

The following calculations are made to compute the applied load on top of the tested specimens, small-scale and large-scale wall specimens. For that purpose, the applied load at the top on the chapel's north-eastern wall should be computed. Therefore, the

quantities of Area (*A*), Volume (*V*), applied load (*W*), applied load per metre (*Q*), scaling factor (*λ*) and weight (*R*) will be computed.

$$A_{CDEF} = A_B = (CF)\times(CD) \Rightarrow A_B = (2.3m)\times(5.05m) \Rightarrow A_B = 11.615m^2$$

$$A_{ACF} = A_C = (1/2)\times(FB)\times(AC) \Rightarrow A_C = (1/2)\times(0.9m)\times(4.1m) \Rightarrow A_C = 1.845m^2$$

$$V_{ACF} = (A_C)\times(depth) \Rightarrow V_{ACF} = (1.8m^2)\times(0.6m) \Rightarrow V_{ACF} = 1.107m^3$$

$$W_A = (g_A)\times(V_C) \Rightarrow W_A = (26kN/m^3)\times(1.107m^3) \Rightarrow W_A = 28.782kN$$

$$Q_1 = (W_A)/(L_A) \Rightarrow Q_1 = (28.782kN)/(4.1m) \Rightarrow Q_1 = 7.02\,kN/m$$

$$W_B = (2)\times(g_B)\times(A_B) \Rightarrow W_B = (2)\times(0.7\,kN/m^2)\times(11.615m^2) \Rightarrow W_B = 16.261kN$$

$$Q_2 = (W_B)/\{(2)\times[(L_A)+(L_B)]\} \Rightarrow Q_2 = (16.261kN)/\{(2)\times[(4.1m)+(5.05m)]\} \Rightarrow Q_2 \approx 0.9\,kN/m$$

$$Q = Q_1 + Q_2 \Rightarrow Q = (7.02\,kN/m)+(0.9\,kN/m) \Rightarrow Q = 7.92\,kN/m$$

$$R = (Q)\times(L_A) \Rightarrow R = (7.92\,kN/m)\times(4.1m) \Rightarrow R = 31.68kN$$

$$L_{PROTOTYPE} = L_A = 4.1m$$

$$L_{SMALL..MODEL} = L_I = 0.2354m$$

$$L_{BIG..MODEL} = L_{II} = 0.856m$$

$$\lambda_I = L_A/L_I \Rightarrow \lambda_I = (4m)/(0.2354m) \Rightarrow \lambda_I \approx 17$$

$$\lambda_{II} = L_A/L_{II} \Rightarrow \lambda_{II} = (4m)/(0.856m) \Rightarrow \lambda_{II} \approx 4.673$$

$$\lambda_I^2 = R_{PROTOTYPE}/R_{MODEL..I} \Rightarrow R_{MODEL..I} = (31.68kN)/[(17)^2] \Rightarrow R_{MODEL..I} \approx 11.2kg$$

$$\lambda_{II}^2 = R_{PROTOTYPE}/R_{MODEL..II} \Rightarrow R_{MODEL..II} = (31.68kN)/[(4.673)^2] \Rightarrow R_{MODEL..II} \approx 148kg$$

APPENDIX III

EXPERIMENTAL SET UP / SKETCHES

Figure App. III – 1: Equipment apparatus for the UCL based experiments

Figure App. III – 2: Equipment apparatus for the UCL based experiments

Figure App. III – 3: Equipment apparatus for the UCL based experiments

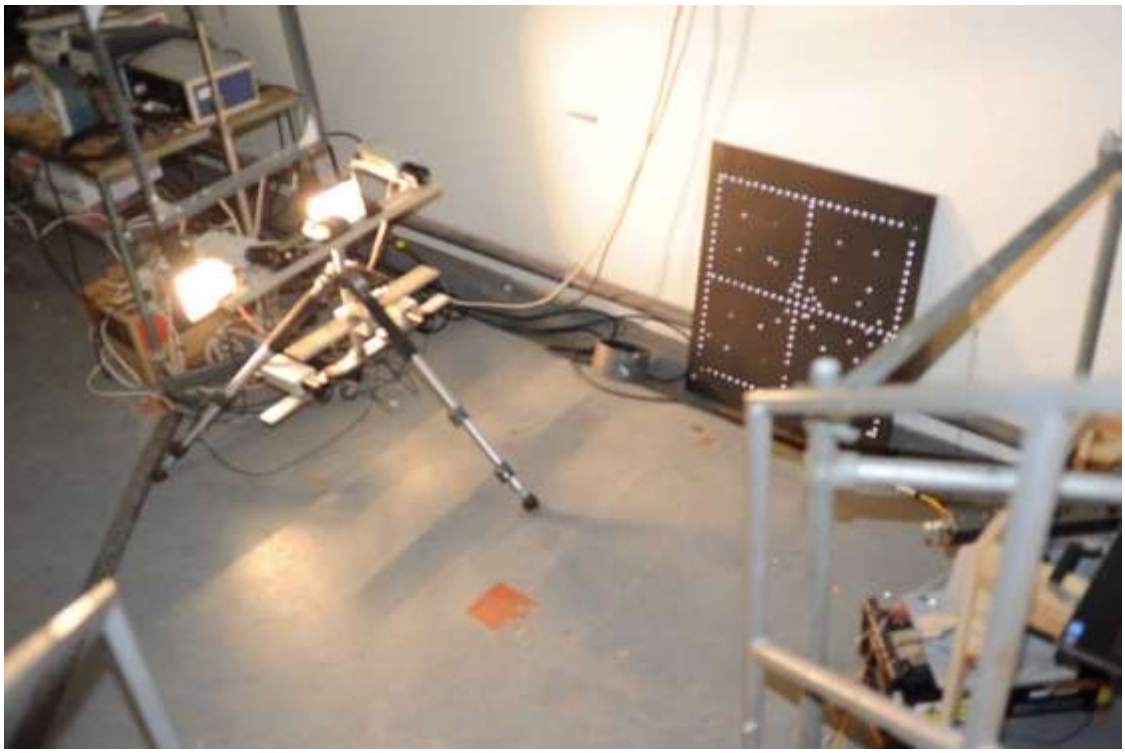

Figure App. III – 4: Head-lights, 4 RedLake cameras and the blackened glass calibration plate

Figure App. III – 5: Two large-wall specimens at the laboratory yard of the University of Bristol

Figure App. III – 6: First large-wall specimen during its positioning on the shaking table with the use of the laboratory's crane, at the University of Bristol

Figure App. III – 7: First large-wall specimen during its positioning on the shaking table with the use of the laboratory's crane being driven by the two technicians, at the University of Bristol

Figure App. III – 8: First large-wall specimen positioned on the shaking table along with the loadings fixed at the top of the large wall with the use of the stainless-steel loading case and the appropriate steel rods, at the University of Bristol

Figure App. III – 9: First large-wall specimen positioned on the shaking table along with the loadings; head-lights, cameras and computers placed on a desk opposite to the shaking table, at the University of Bristol

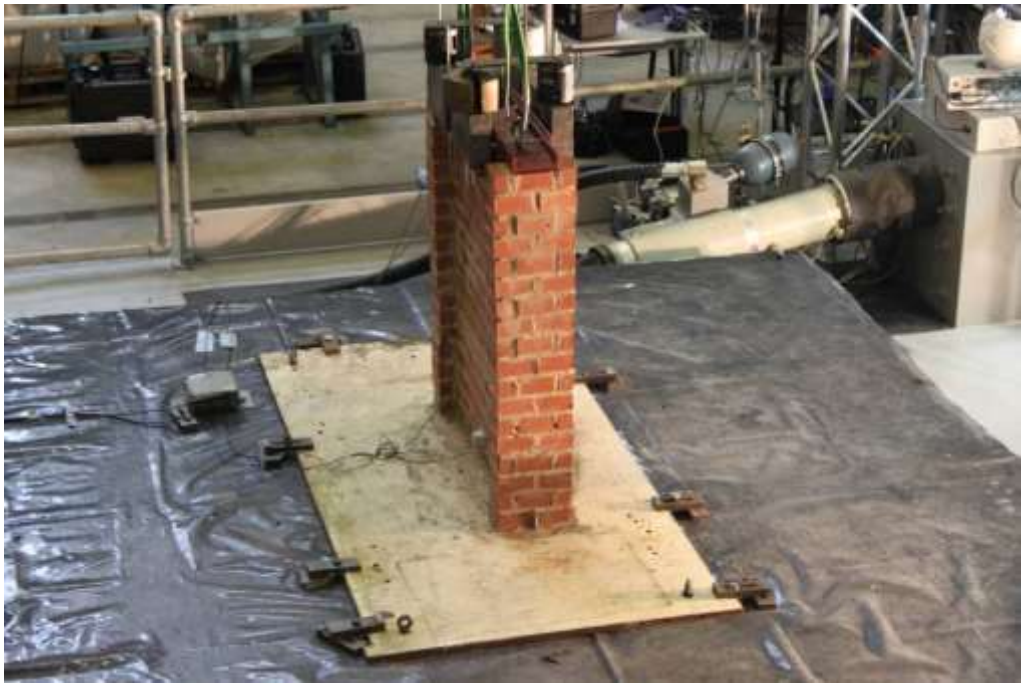

Figure App. III – 10: First large-wall specimen positioned on the shaking table along with the loadings at the University of Bristol

Figure App. III – 11: Front face of the large-wall specimens at the laboratory yard of the University of Bristol

APPENDIX IV

TRIANGULATION – MOHR CIRCLE

All the following calculations are used as computed and presented on the 3rd year project of two undergraduate students.

Kwok, Y. H. & Sawjani, C. (2001), Precise measurement technique, 3rd year project report, Department of Civil & Environmental Engineering, University College London.

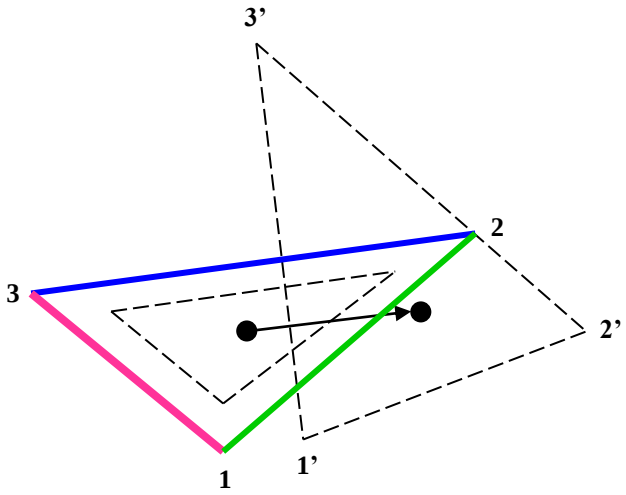

$$\varepsilon_{12} = \frac{(2-1)-(2'-1')}{(2-1)} \qquad \varepsilon_{23} = \frac{(3-2)-(3'-2')}{(3-2)} \qquad \varepsilon_{31} = \frac{(3-1)-(3'-1')}{(3-1)}$$

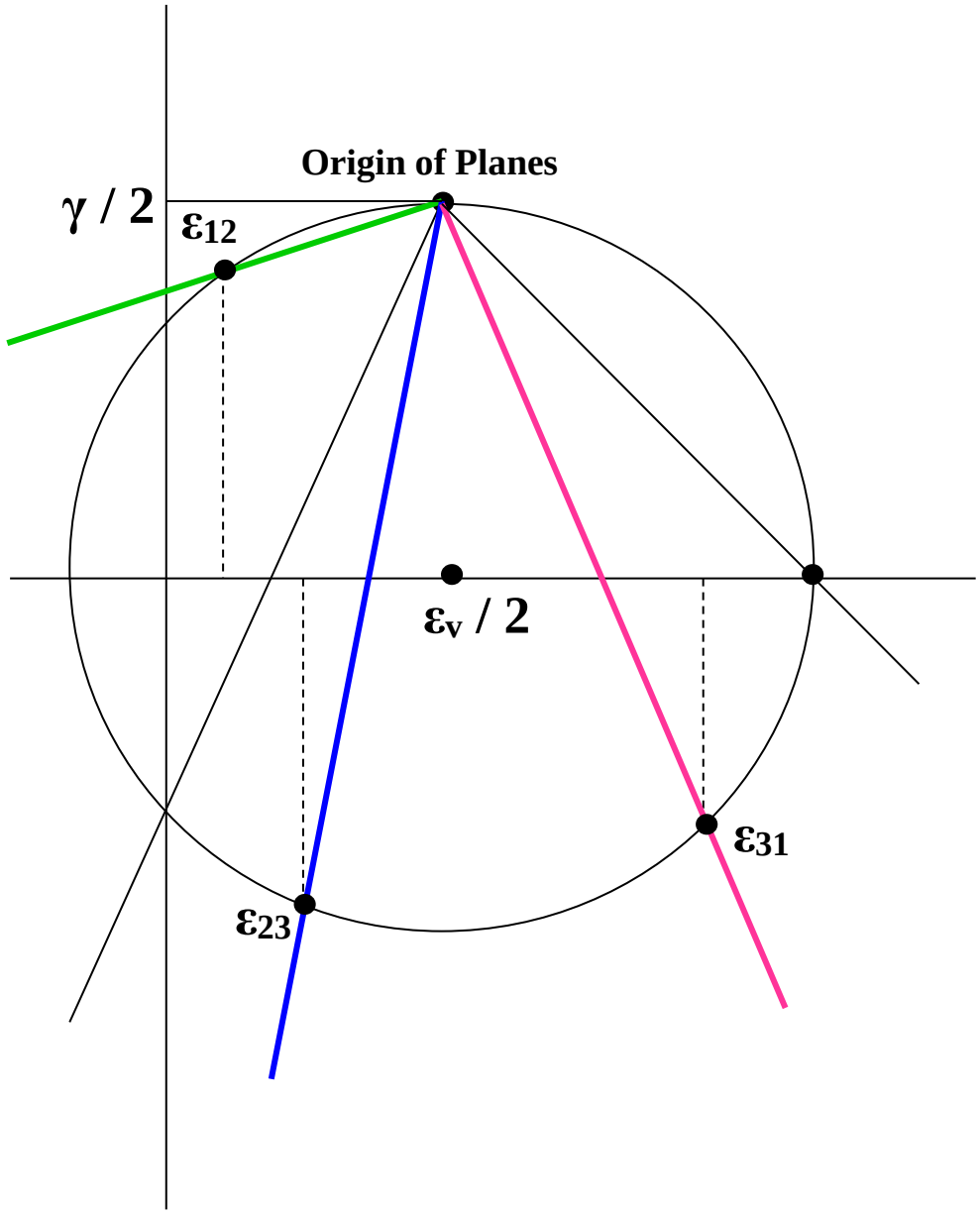

$$\varepsilon_{12} = \frac{\varepsilon_v}{2} + \frac{\gamma}{2}\cos 2(\theta_{12} - \alpha)$$

$$\varepsilon_{23} = \frac{\varepsilon_v}{2} + \frac{\gamma}{2}\cos 2(\theta_{23} - \alpha)$$

$$\varepsilon_{31} = \frac{\varepsilon_v}{2} + \frac{\gamma}{2}\cos 2(\theta_{31} - \alpha)$$

$$\varepsilon_{12}-\varepsilon_{23}=\left[\frac{\varepsilon_\nu}{2}+\frac{\gamma}{2}\cos 2(\theta_{12}-a)\right]-\left[\frac{\varepsilon_\nu}{2}+\frac{\gamma}{2}\cos 2(\theta_{23}-a)\right]\Rightarrow$$

$$\Rightarrow \varepsilon_{12}-\varepsilon_{23}=\frac{\varepsilon_\nu}{2}+\frac{\gamma}{2}\cos(2\theta_{12}-2\alpha)-\frac{\varepsilon_\nu}{2}-\frac{\gamma}{2}\cos(2\theta_{23}-2a)\Rightarrow$$

$$\Rightarrow \varepsilon_{12}-\varepsilon_{23}=\frac{\gamma}{2}\{[\cos(2\theta_{12}-2\alpha)]-[\cos(2\theta_{23}-2a)]\}$$

$$\varepsilon_{12}-\varepsilon_{31}=\left[\frac{\varepsilon_\nu}{2}+\frac{\gamma}{2}\cos 2(\theta_{12}-a)\right]-\left[\frac{\varepsilon_\nu}{2}+\frac{\gamma}{2}\cos 2(\theta_{31}-a)\right]\Rightarrow$$

$$\Rightarrow \varepsilon_{12}-\varepsilon_{31}=\frac{\varepsilon_\nu}{2}+\frac{\gamma}{2}\cos(2\theta_{12}-2\alpha)-\frac{\varepsilon_\nu}{2}-\frac{\gamma}{2}\cos(2\theta_{31}-2a)\Rightarrow$$

$$\Rightarrow \varepsilon_{12}-\varepsilon_{31}=\frac{\gamma}{2}\{[\cos(2\theta_{12}-2\alpha)]-[\cos(2\theta_{31}-2a)]\}$$

Set $A=\varepsilon_{12}-\varepsilon_{23}$ and $B=\varepsilon_{12}-\varepsilon_{31}$

$$\cos P-\cos Q=-2\sin\frac{P-Q}{2}\sin\frac{P+Q}{2}$$

$$\sin P+\sin Q=2\sin\frac{P+Q}{2}\cos\frac{P-Q}{2}$$

$$\frac{\varepsilon_{12}-\varepsilon_{23}}{\varepsilon_{12}-\varepsilon_{31}}=\frac{\gamma/2\{[\cos(2\theta_{12}-2a)]-[\cos(2\theta_{23}-2a)]\}}{\gamma/2\{[\cos(2\theta_{12}-2a)]-[\cos(2\theta_{23}-2a)]\}}\Rightarrow$$

$$\Rightarrow \frac{A}{B}=\frac{\cos 2\theta_{12}\cos 2a+\sin 2\theta_{12}\sin 2a-\cos 2\theta_{23}\cos 2a+\sin 2\theta_{23}\sin 2a}{\cos 2\theta_{12}\cos 2a+\sin 2\theta_{12}\sin 2a-\cos 2\theta_{31}\cos 2a+\sin 2\theta_{31}\sin 2a}\Rightarrow$$

$$a=\frac{1}{2}\tan^{-1}\left\{\frac{[-(\varepsilon_{12}-\varepsilon_{23})\sin(\theta_{12}-\theta_{31})\sin(\theta_{12}+\theta_{23})]+[-(\varepsilon_{12}-\varepsilon_{31})\sin(\theta_{23}-\theta_{12})\sin(\theta_{23}-\theta_{12})]}{[-(\varepsilon_{12}-\varepsilon_{23})\sin(\theta_{31}+\theta_{12})\cos(\theta_{31}-\theta_{12})]+[(\varepsilon_{12}-\varepsilon_{31})\sin(\theta_{12}-\theta_{23})\sin(\theta_{12}-\theta_{23})]}\right\}\Rightarrow$$

$$\gamma = \frac{2(\varepsilon_{12} - \varepsilon_{23})}{\cos(2\theta_{12} - 2a) - \cos(2\theta_{23} - a)}$$

$$\varepsilon_{12} = \frac{\varepsilon_\nu}{2} + \frac{\gamma}{2}\cos 2(\theta_{12} - \alpha) \Rightarrow \varepsilon_{12} = \frac{\varepsilon_\nu + \gamma\cos(2\theta_{12} - 2a)}{2} \Rightarrow$$

$$\Rightarrow 2\varepsilon_{12} = \varepsilon_\nu + \gamma\cos(2\theta_{12} - 2a) \Rightarrow \varepsilon_\nu = 2\varepsilon_{12} - \gamma\cos(2\theta_{12} - 2a)$$